UNIVERSITY OF CALIFORNIA

Santa Barbara

Understanding and optimizing the interactions of functional species in mesostructured materials with diverse transport properties

A dissertation submitted in partial satisfaction of the

requirements for the degree Doctor of Philosophy

in Chemical Engineering

by

Matthew Nels Idso

Committee in charge:

Professor Bradley F. Chmelka, Chair

Professor Songi Han

Professor M. Scott Shell

Professor Michael Gordon

September 2017

The dissertation of Matthew Nels Idso is approved.

_____

Songi Han

_____

Michael Gordon

_____

M. Scott Shell

_____

Bradley F. Chmelka, Committee Chair

August 2017

Understanding and optimizing the interactions of functional species in mesostructured materials with diverse transport properties

Matthew Nels Idso

ACKNOWLEDGEMENTS

I would first like to thank my research advisor, Prof. Brad Chmelka, for the outstanding mentorship, encouragement and support that has forged me into the researcher and teacher that I am today. I also want to express deep gratitude to Prof. Songi Han for the research advice, opportunities, and mentorship that she's provided me over the years. My sincere appreciation also extends to all the members of the Chmelka and Han groups, past and present, who have provided both technical and personal support throughout my doctoral studies at UCSB; being one of your colleagues was a pleasure and an honor. I'd like to specifically thank Dr. Justin Jahnke and Dr. Sunyia Hussain for being fantastic research mentors. I am also particularly grateful for Niels Zussblatt, who was a close colleague and supporter throughout my doctoral studies; I'll certainly miss your presence as a co-worker when our paths diverge, though I'm certain our adventures together are far from over. I also feel blessed to have worked with several talented and competent undergraduate researchers, Sirish Narayanan, Naomi Baxter and David Phan; it was an absolute pleasure and privilege to work with each of you. I consider the support from broader research community at UCSB a key driver of my research. I'd like to thank the technical support from the user facilities at UCSB, especially Dr. Jerry Hu, Jaya Nolt and Shaman Walker of the spectroscopy facility, Dr. Youli Li, Philip Kohl and Miguel Zepeda of the X-ray facilities, and Amanda Strom of the TEMPO facilities. I'd also like to thank my direct research collaborators, both within the United States and abroad; my experiences with you propelled my research and taught me long-lasting lessons, both personal and technical.

My sincere thanks also extends to my family and friends, who provided unwavering support in my pursuits in scientific research. I am overwhelmingly grateful for my mom and dad who inspired and enabled me to become a scientist in the first place, and encouraged me

through all the set-backs and triumphs along the way. To my brother, Zach, I'd like to express thanks for continually reminding me that actions speak louder than words ever can. Additionally, I thank my aunt Candace whose persistent support, optimism and thoughtfulness spurred me on throughout my graduate studies, and my grandma Carolyn who always reminds me to persevere. To my grandpa Lloyd and grandma Kathy, thank you for your support in pursuing a graduate degree and, of course, your openness and helpfulness in discussing scientific issues. Also, I'm also grateful for Papa and Nana for teaching me to always think big and to strive to become the "best damn" researcher that I could be. Finally, to all my friends in Santa Barbara, thank you for all the great experiences and support over these years that have made my time during graduate school an absolute blast; I look forward to all the adventures and engineering challenges that we'll undertake together in the future. Finally, to Shannon Walker, I thank you for your extraordinary patience, kindness, support, and love, which has had a singular and pervasive positive effect on me that reflects in every aspect of my life.

Matthew Nels Idso

matt.idso@gmail.com

360.631.3159

EDUCATION

Doctor of Philosophy, Chemical Engineering 2012 – 2017 (expected)

University of California, Santa Barbara, with Certificate in Technology Management

Bachelor of Science, Chemical Engineering 2008 –2012

University of Washington, Seattle, Departmental honors, Magna Cum Laude

RESEARCH

PhD Research 2013 – 2017

University of California, Santa Barbara, Department of Chemical Engineering

Advisor: Dr. Bradley Chmelka

Thesis: Understanding and controlling interactions in nanostructured inorganic-organic hybrid materials with photo-responsive molecular guests

Developed a general synthetic protocol for assembling functionally-active membrane proteins into nanostructured surfactant-silica membranes

Analyzed inter-protein and surfactant-protein interactions that influence membrane protein function

Determined molecular interactions responsible for the adsorption and release of pharmaceuticals from surface-functionalized porous silicas

Improved understanding of intermolecular interactions in polymer-fullerene blends that enhance solar energy conversion

Undergraduate Research 2009 – 2012

University of Washington, Seattle, Department of Chemical Engineering

Research advisor: Dr. Qiuming Yu

Surface enhanced Raman scattering with gold nanostructures to detect marine bacteria and pesticides

EMPLOYMENT

British Petroleum, Cherry Point, WA - Process Engineering intern, Coker Unit 2011

Mentor: Kieth Zinc, Process Engineer

Assessed the viability of coker antifoams to provide product recommendations for unit operations

SERVICE

9th annual Clorox-Amgen Graduate Student Symposium co-organizer 2016

University of California, Santa Barbara, Department of Chemical Engineering

UCSB College of Engineering Executive committee: Graduate student representative 2014-2015

Engineers Without Borders: University of Washington 2009–2012

Fundraising Director, Grant Writing Co-lead

AWARDS

Warren K. Schlinger Fellowship for Excellence in Chemical Engineering Research, UCSB 2016

Outstanding Teaching Assistant Award – UCSB, Dept. of Chemical Engineering 2014/16

Heslin Fellowship for promising first-year graduate students in Chem. Eng. UCSB 2012

Emerging Leader in Engineering Scholarship, University of Washington 2011

Chemical Engineering Scholarship, University of Washington 2010, 2011

PUBLICATIONS

Idso, M.; Baxter, N.; Narayanan, S.; Chang, E.; Fisher, J.; Chmelka, B.; Han, S., "Functional significance of interactions at the transmembrane interface of the light-responsive membrane protein proteorhodopsin," to be submitted to *J. Mol. Biol.*

Lalli, D.; Idso, M.; Andreas, L.; Baxter, N.; Han, S.; Chmelka, B.; Pintacuda, G.; "Protons as structural NMR reporters throughout a heptahelical membrane protein in lipid bilayers," accepted, *JACS*.

Jahnke, J.; Idso, M.; Hussain, S.; Junk, M.; Phan, D.; Han, S.; Chmelka, B., "Functionally active membrane protein proteorhodopsin incorporated in mesostructured silica films," submitted, *JACS*.

Gebbie, M.; Wei, W.; Schrader, A.; Cristiani, T.; Dobbs, H.; Idso, M.; Waite, H.; Chmelka, B.; Israelachvili, J. "Tuning underwater adhesion with cation-π interactions," *Nat. Chem.*, 2017, 9, 473-479.

Morales, V.; Idso, M.; Balabasquer, M.; *et al.*, "Correlating Surface-functionalization of mesoporous silica with adsorption and release of pharmaceutical guest species," *J. Phys. Chem. C*, 2016, 120, 16887-17898.

Graham, K. R.; Cabanetos, C.; Jahnke, J.; Idso, M.; *et al.* "Importance of Donor:Fullerene Intermolecular Arrangement for High-Efficiency Organic Photovoltaics," *JACS*, 2015, 136, 9608-9618.

Deng, Y.; Idso, M.; Galvan, D.; Yu, Q., *et al.* "Optofluidic microsystem with quasi-r dimensional gold plasmonic nanostructure arrays for online sensitive and reproducible SERS detection," Analytical Chimica Acta, 2015, 863, 41-48.

Xu J.; Turner J.; Idso, M. N.; *et al*. "Quasi-3D Plasmonic Nanostructures for Strain Specific Identification of Marine Bacteria Vibrio Parahaemolyticus Using SERS," *Analytical Chemistry*, 2013, 85, 2630-2637.

Xu, J.; Kvasnička, P.; Idso, M.; *et al*. "Understanding the effects of dielectric medium, substrate, and depth on electric fields and SERS of quasi-3D plasmonic nanostructures", *Optics Express*, 2011, 19, 20493-20505.

SELECTED PRESENTATIONS

M. Idso; J. Fisher; D. Lalli; L. Andreas; N. Baxter; Matthias Junk; G. Pintacuda; S. Han; B. Chmelka. 58th Experimental NMR conference, "*Structural insight into nanostructured silica-surfactant composites that incorporate the membrane protein proteorhodopsin using solid-state NMR spectroscopy*" March 26, 2017. Asilomer, CA. Poster presentation.

M. Idso; J. Fisher; S. Han; B. Chmelka. Silicon-containing Polymers and Composites conference. "*Nanocomposite silica-surfactant materials containing hydrophobic membrane proteins*," December 14, 2016. San Diego, CA. Oral presentation.

M. Idso; N. Baxter; S. Han; B. Chmelka. 2016 American Institute of Chemical Engineers annual meeting, "*Understanding the roles of surfactants and oligomeric assembly on the functionality of the light-activated membrane protein proteorhodopsin*" November 18, 2016. San Francisco, CA. Oral presentation.

M. Idso; N. Zussblatt; D. Lalli; N. Baxter; G. Pintacuda; S. Han; B. Chmelka. 2016 American Institute of Chemical Engineers annual meeting. *Incorporation of photo-responsive membrane protein species into nanostructured silica for light-driven ion transport*. November 14, 2016. San Francisco, CA. Oral presentation.

M. Idso; D. Lalli; L. Andreas; N. Baxter; S. Hussain; L. Emsley; G. Pintacuda; S. Han; B. Chmelka. 57th Experimental Nuclear Magnetic Resonance conference. *Understanding local environments of the membrane protein proteorhodopsin in nanostructured silica hosts*. April 13, 2016. Pittsburgh, PA. Oral presentation.

M. Idso; S. Hussain; N. P. Zussblatt; D. Lalli; L. Andres; L. Herwig; N. Baxter; F. Arnold; G. Pintacuda; S. Han; B.F. Chmelka. Centre de Resonance Magnetique Nucleaire a Tres Hauts Champs, École Normal Supérieure de Lyon. *Incorporation of photo-responsive membrane proteins into mesostructured silica for light-driven ion transport*. November 25, 2015. Lyon, France. Seminar talk.

M. Idso; S. Hussain; N. Zussblatt; D. Lalli; L. Andreas; L. Herwig; N. Baxter; F. Arnold; G. Pintacuda; S. Han; B. Chmelka. Chemical Sciences Student Seminar UCSB, *Incorporation of photo-responsive membrane proteins into mesostructured silica for light-driven ion transport*. October 25, 2015. Santa Barbara, CA. Seminar talk.

M. Idso; J.P. Jahnke; K.R. Graham; A. Amassian; P.M. Beaujuge; M. D. McGehee; B.F. Chmelka. 56th annual Experimental NMR Conference, *Assessing fullerene proximities to donor and acceptor moieties in bulk heterojunction materials using solid-state NMR spectroscopy*. April 20, 2015. Asilomar, CA. Poster presentation.

M. Idso; S. Hussain; J. P. Jahnke; S. Han; B. F. Chmelka. 4th bilateral UCSB-Chalmers workshop on Materials Science and Engineering, *Incorporation of the membrane protein proteorhodopsin in inorganic-organic nanocomposites for light activated ion-transport*. June 30, 2014. Chalmers University, Gothenburg, Sweden. Invited talk.

J. P. Jahnke; M. Idso; K. R. Graham; A. Amassian; P. M. Beajuge; M. D. McGehee; B. F. Chmelka. 2013 Annual Center for Advanced Molecular Photovoltaics, *Assessing fullerene proximities to donor and acceptor moieties in bulk heterojunction materials*. August 23, 2013. Stanford University, Stanford, CA. Poster presentation.

ABSTRACT

Understanding and optimizing the interactions of functional species in mesostructured materials with diverse transport properties

by

Matthew Nels Idso

Mesostructured inorganic-organic hybrid materials have high interfacial areas, through-connecting mesoscale (2-50 nm) channels, and high mechanical and chemical robustnesses that can be exploited for diverse technological applications, especially those that involve the transport of charges, ions or molecules. These materials can, moreover, accommodate a broad assortment of functional molecular species that can mediate or instill transport properties. One interesting example is membrane proteins, which are biomacromolecules that transport ions or molecules across biological lipid bilayers at high rates and selectivities; for instance, the membrane protein proteorhodopsin actively transports H^+-ions in response to light, which might be harnessed for solar-to-electrochemical energy conversion. Mesostructured inorganic-organic hybrid materials that include macroscopically aligned proteorhodopsin species are expected to generate bulk ion gradients across host materials under illumination. Here, a solution-based synthetic protocol is presented that allows high concentrations (up to 15 wt%) of active proteorhodopsin species to be incorporated within mesostructured silica membrane hosts. Synthesis conditions and compositions were selected to stabilize proteorhodopsin molecules in the presence of the structure-directing surfactant and soluble network-forming

silica species that co-assemble to form mesostructured silica host matrices, as established by small-angle X-ray diffraction analyses. Multidimensional solid-state NMR spectra show that proteorhodopsin molecules incorporated within mesostructured silica hosts retain native-like structures, though with some interesting differences. The optical absorbance behaviors of proteorhodopsin guests in the synthetic mesostructured silica hosts correspond to the photochemical reaction cycles of proteorhodopsin in near-native environments that are associated with the active transport of H^+-ions. The collective synthetic, structural and functional understanding developed here is leveraged to synthesize durable and optically transparent self-supporting mesostructured silica films that include high loadings of proteorhodopsin, as well as other membrane proteins. In separate mesostructured material systems, functional guest species at the mesostructure interfaces are shown to dramatically influence bulk material performances. Specifically, aminoalkyl-fullerene functionalities at the mesochannel surfaces of mesoporous silica can substantially modify the sorption and release behaviors of pharmaceutical species from these materials, while interfacial alkyl functionalities in polymer:fullerene heterojunctions can promote efficient separation of photo-generated charges.

Table of Contents

Introduction

Mesostructured materials

Mesostructured materials have structures with characteristic dimensions on the mesoscale (2-50 nm) that impart high interfacial areas, which can be exploited for a broad variety of engineering technologies, especially the transport of molecules, ions and charges. For example, in conventional organic photovoltaic cells the presence of mesostructured interface among the conjugated polymer and fullerene phases supports high interfacial contact that enhances charge separation and overall device efficiency, versus heterojunctions with planar bilayer interfaces. Separately, porous mesostructured materials, or "mesoporous" materials, exhibit high surface areas and porous volumes that can be functionalized with high quantities of diverse molecular species to facilitate mass transport. For instance, mesoporous silica membranes with multiple acidic organic species promoted the conduction of H^+-ions within the material, making these materials useful as proton-exchange membranes for hydrogen fuel cells.[1]

An important subset of mesostructured materials are mesostructured inorganic-organic composites that have long-ranged mesoscale ordering, high mechanical and chemical robustnesses and facile processabilities. Mesostructured inorganic-organic composites are synthesized from solutions by the co-assembly of amphiphilic surfactant aggregates with inorganic oxide precursor species. In particular, interactions among silica-surfactant aggregates drive their assembly into structures with long-ranged periodic mesoscale ordering, similar to in binary lyotropic liquid crystals;[2–4] subsequent cross-linking of the inorganic species yields a dense inorganic framework that imparts mechanical and chemical robustness

to the mesostructured material. Judicious selection of synthesis compositions and conditions enables control over the rates of mesostructure assembly, inorganic cross-linking kinetics, and solvent evaporation that can be adjusted to yield various mesostructure topologies and dimensions.[3,5,6] Many such topologies are anisotropic (*e.g.*, hexagonal, lamellar) and can be aligned over macroscopic length scales by external fields,[2,7] shear forces,[8] electrochemical potentials,[9] or by tuning the interfacial energies at the solvent evaporation or substrate interface.[10,11] Removal of the structure-directing surfactant species, by calcination or solvent extraction, produces ordered mesoporous materials with high pore volumes and surface areas that can be easily functionalized.[1,12] Moreover, the solution-based processing conditions of mesostructured inorganic-organic composites enable these materials to be processed into several macroscopic morphologies, including free-standing membranes, monoliths,[13] thin films[14,15] and powders.[16] Moreover, the versatile synthesis conditions, structures and chemistries of mesostructured inorganic-organic composites allow these materials to accommodate and exploit a wide range of functional molecular guests.

Functional molecular species can be incorporated into mesostructured inorganic oxide materials either by post-synthetic adsorption or direct co-assembly. Post-synthetic adsorption involves exposing mesoporous materials to solutions containing the functional guest species, which intercalate into the porous material volumes and undergo physical or chemical surface adsorption. While the high surface areas and pore volumes enable high guest loadings, molecular species with dimensions comparable to or larger than the mesopore diameters can be sterically hindered from entering pores, which leads to pore blockage, low guest loadings, and inhomogeneous distributions of guests in the host material.[17] Alternatively, molecular guests of arbitrary molecular sizes can be co-assembled into mesostructured hosts during

material synthesis, by solubilizing the guest in the material precursor solution. Synthesis compositions and conditions can be adapted to allow the incorporation of guest species of a variety of chemistries and sizes, such as small molecular dyes,[18,19] conjugated polymers,[20,21] nanoparticles[22] and proteins.[23] On macroscopic scales the guest species co-assemble homogeneously throughout the material, but on the mesoscale the guest molecules partition into either the relatively hydrophobic surfactant or hydrophilic inorganic regions, based on hydrophobicity of the guest. For example, Jahnke et al showed that highly hydrophobic conjugated polymers co-assemble into the relatively hydrophobic block-copolymer regions, rather than the titania framework, of mesostructured titania materials;[21] by comparison, water-soluble glucose oxidase proteins incorporate in the hydrophilic silica matrix of mesostructured silica-surfactant composite materials.[23] The versatility to incorporate diverse functional species into particular regions of mesoporous oxide materials make these materials useful to exploit functional guests for selective or enhanced mass transport.

Membrane proteins as molecular guests

An interesting and technologically relevant class of functional guest species with transport properties are membrane proteins. Transmembrane proteins are highly hydrophobic biomacromolecules that span the lipid bilayers of biological cells and perform versatile functionalities that include the transport of ions, molecules and signals across the lipid membrane to support cellular viabilities. Such functionalities are often rapid, highly specific to particular molecules or ions, and can be passive or activated by external stimuli, *e.g.* light, which would be useful to harness for technological applications. For example, the transmembrane protein aquaporin can selectively transport water at a rate of $3x10^9$ molecules

per second per protein;[24] with such high water transport rates, membranes with aquaporin could achieve water permeabilities that are approximately two orders of magnitude higher than current reverse osmosis membranes used to desalinate seawater.[25,26] Other membrane proteins have useful activated functionalities, such as proteorhodopsin and bacteriorhodopsin that absorb green light to transport an H^+-ion across the lipid bilayer as part of cellular metabolism. Proteorhodopsin in particular can be found ubiquitously in marine bacteria, such as picoplankton, at populations of up to 2.0×10^4 per cell,[27] or approximately 16% of the area of the lipid membrane for a ~1.5 μm diameter cell. Assuming that a picoplankton cell requires between 3×10^{11}–3×10^{12} adenosine triphosphate (ATP) molecules every cell division (estimated here as ten hours[28]), as each H^+-ion pumped by proteorhodopsin yielding one ATP and with a H^+-ion pumping frequency of ~50 Hz[27] the proteorhodopsin species would supply approximately 1-13% of a picoplankton cell's energy. This provides a context to explore proteorhodopsin and bacteriorhodopsin for applications in macroscopic solar-to-chemical energy conversion.[29] Besides solar energy conversion, the unique light-activated properties of bacteriorhodopsin could be useful for optoelectronics[30,31] or security dyes.[32] While membrane proteins in lipid bilayers cannot easily harness protein function on macroscopic scales, synthetic materials that incorporate high membrane protein concentrations could enable protein function to be integrated with and exploited in macroscopic devices. However, the high hydrophobicities and limited stabilities of membrane proteins in synthetic environments have made it exceedingly challenging to incorporate functionally-active membrane proteins into synthetic materials. As a result, to-date membrane proteins have been incorporated into only few synthetic environments, which include supported lipid bilayers,[33–35] lipid arrays,[36,37] block

copolymers,[38–40] or silica sol gels[41–44] that either lack the mechanical robustness or processabilities needed to harness membrane proteins in macroscopic devices.

By comparison, mesostructured inorganic-organic oxides appear a promising host material to exploit the selective transport properties of membrane proteins. It is hypothesized that the synthesis compositions and conditions could be adapted for compatibility with membrane protein stabilities, which could allow high concentrations of functionally-active membrane proteins to be co-assembled into mesostructured inorganic-organic oxide hosts. Moreover, the resulting mesostructure can include interconnecting mesochannels along which molecules or ions could diffuse and, under appropriate synthesis conditions, can be oriented over macroscopic length scales to reduce tortuosity. The solution-based synthesis conditions also permit these materials to be processed as thin films or self-supporting membranes that serve as semi-permeable membranes and easily integrated into macroscopic devices.

This thesis describes a detailed understanding of the co-assembly of functionally-active membrane proteins into mesostructured silica-surfactant hybrid materials, focusing mainly on the membrane protein proteorhodopsin that functions as a light-activated H^+-ion pump.[45] Judiciously selected surfactants are shown to serve dual roles of stabilizing proteorhodopsin and directing the formation of the mesostructure (Chapters 1 and 6). Investigations using state-of-the-art proton-detected nuclear magnetic resonance methods[46–49] establish that the structures of proteorhodopsin guests bear high similarities to those in lipids, but with a few differences (Chapters 2 and 3). Complementary time-resolved absorbance spectroscopy establishes that proteorhodopsin species in the synthetic mesostructured hosts undergo native photochemical reaction cycles, indicating that the proteorhodopsin guests pump H^+-ions in response to light. A detailed investigation of how surfactants and oligomerization influence

proteorhodopsin function and stability (Chapter 4) yield insights useful in preparing transparent free-standing mesostructured silica materials with high loadings of highly active monomeric proteorhodopsin (Chapter 5).

Interfacial interactions in mesostructured materials

The interfaces of mesostructured materials mediate molecular-level interactions and processes that are important for molecular, ionic and charge transport in these materials. For instance, the sorption and diffusion of pharmaceutical species in surface-functionalized mesoporous silica depends on the types of surface functionalities;[12] separately, the close proximities of photo-activated conjugated polymers to titania mesochannel surfaces of mesostructured titania materials can facilitate photo-generated charge separation necessary for photovoltaic energy conversion.[21] Furthermore, perfluorosulfonic acid and aluminum surface functionalities in mesoporous silica membranes enhanced H^+-ion conduction in the materials under low humidities and high temperatures, imparting these materials with superior H^+-ion conductivities versus conventional Nafion-117 proton exchange membranes at high-temperatures.[1] Such interfacial processes in mesostructured materials rely strongly on the chemistries, proximities and distributions of moieties at the interface, which can typically be adjusted through synthesis.

The high interfacial areas and facile surface functionalization of mesoporous inorganic oxide materials permit high fractions of their surfaces to be decorated with a variety of functional moieties. Surface functionalization in these materials can be achieved by co-condensing functionalized inorganic precursors during material co-assembly, which yields materials with surface functionalities distributed homogenously on the material interface. An

alternative method is to post-synthetically graft functional species to the reactive surface sites of mesoporous inorganic oxide materials, usually hydroxyl groups.[12,50,51] While this method can provide significant extents of surface functionalization, mass transport limitations can lead to inhomogenous distributions of functional species within the material.

The general significance of interfaces to mesostructured material performance has garnered much interested in understanding, controlling and exploiting the interactions among guest species and surface functionalities. Though, the inherently low masses of these interfaces compared to the bulk material make them challenging to interrogate experimentally. Solid-state NMR spectroscopy lends itself well for such investigations due to its atomic-level resolution and sensitivity to the proximities, dynamics and chemistries of molecular moieties, especially using dynamic-nuclear polarization techniques that substantially (>100x) enhance NMR.[20,52,53] This thesis describes new insights about the interfacial interactions in several mesostructured systems, which include: surface-functionalized mesoporous silicas that inorporate pharmaceutical guests (Chapter 7) and photovoltaic polymer:fullerene heterojunctions (Chapter 8). For each system, the molecular-level insights are correlated with and explain the macroscopic molecular or charge transport properties.

Overview

This dissertation is organized into chapters that each describe new understanding about the interactions of functional guest species in mesostructured hosts that are useful for diverse transport applications. The chapters of this thesis are modular, and each includes an introduction and references that motivate the results discussed. Below is an overview that briefly describes the contents of each chapter.

Chapter 1 - Functionally active membrane proteins incorporated into mesostructured silica films for light-activated H^+-ion transport: This chapter describes a novel synthetic method for incorporating high loadings of membrane proteins into mesostructured surfactant-silica composite materials. Judicious selection of synthesis compositions and conditions enables high loadings of the light-activated transmembrane protein proteorhodopsin to be incorporated into mesostructured silica materials with retained protein function. The synthetic protocol appears to be general and was adapted to incorporate other functional membrane proteins, including rhodopsin and cytochrome c.

Chapter 2 - Proton-based structural analysis of a heptahelical transmembrane protein in lipid bilayers: The molecular structure of fully protonated proteorhodopsin in near-native lipid membranes is characterized by using state-of-the-art nuclear magnetic resonance spectroscopic methods. Such analyses yield resonance assignments for the backbone regions of 146 residues and approximately 57% of the ^{1}H and ^{13}C moieties aliphatic side-chains, which are exploited to establish numerous ^{1}H-^{1}H proximities useful in determining protein structure. These novel structural insights about proteorhodopsin in near-native environments enable valuable comparisons with proteorhodopsin guests in synthetic mesostructured silica materials.

Chapter 3 - Structure and photo-kinetics of the membrane protein proteorhodopsin in a synthetic mesostructured host material: The local environments of proteorhodopsin guests in mesostructured surfactant-silica hosts are probed at atomic level resolution and correlated with light-activated H^+-ion pumping function. The structures of proteorhodopsin in synthetic

mesostructured silica and native-like lipids are highly similar, but with several interesting differences attributable to interactions with the structure-directing surfactants and silica moieties. These structural differences are correlated with and used to interpret functional differences among proteorhodopsin in synthetic hosts, surfactant, and lipid environments.

Chapter 4 - Tuning the function of proteorhodopsin by oligomerization in different surfactant environments: This chapter compares the influences of oligomerization and surfactant environment on the light-activated functionalities of proteorhodopsin in micellar solutions. The functionalities of monomeric and oligomeric proteorhodopsin are probed in different micellar surfactant environments, which are subsequently analyzed to identify whether surfactants or oligomerization predominantly modify proteorhodopsin function. These insights provide useful guidelines for stabilizing monomeric proteorhodopsin species, which appear to pump H^+-ions at higher rates than oligomeric proteorhodopsin species and, thus, would support more potent light-activated responses as guests in mesostructured silica.

Chapter 5 - Co-assembly of proteorhodopsin molecules into mesostructured silica-surfactant composites: A deep understanding of the co-assembly and properties of proteorhodopsin in mesostructured silica hosts are developed. These insights are exploited to synthesize transparent self-supporting mesostructured silica membranes that include record-high (20 wt%) protein loadings. Powerful solid-state NMR spectroscopy is employed to interrogate the structures and interactions of surfactant mesochannels into which proteorhodopsin species are co-assembled. The structures and functionalities of proteorhodopsin guests in mesochannel environments are highly sensitive to hydration and are

correlated. The synthetic, structural, and functional insights are exploited to selectively incorporate monomeric and oligomeric proteorhodopsin into self-supporting mesostructured silica films.

Chapter 6 - Correlating surface-functionalization of mesoporous silica with adsorption and release of pharmaceutical guest species: This chapter describes molecular-level insights into how surface aminopropyl-C_{60}-fullerene functionalities of mesoporous silicas influence the sorption and subsequent release of the pharmaceutical guest species methylprednisolone. Powerful two-dimensional solid-state NMR analyses are used to identify intermolecular interactions responsible for methylprednisolone sorption to the functionalized surfaces of mesoporous silicas. This information correlates with and explains macroscopic release of methylprednisolone species from the surface-functionalized mesoporous silica hosts.

Chapter 7 - Importance of donor:fullerene intermolecular arrangement in high-efficiency organic photovoltaics: This chapter discusses the molecular interactions and arrangements at the interfaces of polymer and fullerene phases in polymer:fullerene heterojunction materials. Two-dimensional solid-state NMR spectroscopy techniques are exploited to discern proximities of moieties on fullerene and polymer species in bulk polymer:fullerene heterojunctions. Analyses reveal that polymer side chains can sterically direct fullerene species to interact different polymer backbone moieties, which has substantial consequences for photovoltaic conversion efficiency of organic photovoltaic devices.

Chapter 8 - Conclusions and outlook: This chapter summarizes the main conclusions of this thesis and briefly discusses directions of future research**.**

References

(1) Athens, G. L.; Kim, D.; Epping, J. D.; Cadars, S.; Ein-eli, Y.; Chmelka, B. F. *J. Am. Chem. Soc.* **2011**, *133*, 16023.

(2) Firouzi, A.; Schaefer, D. J.; Tolbert, S. H.; Stucky, G. D.; Chmelka, B. F. *J. Am. Chem. Soc.* **1997**, *119* (40), 9466.

(3) Alberius, P. C. A.; Frindell, K. L.; Hayward, R. C.; Kramer, E. J.; Stucky, G. D.; Chmelka, B. F. *Chem. Mater.* **2002**, *14*, 3284.

(4) Firouzi, A.; Kumar, D.; Bull, L. M.; Besier, T.; Sieger, P.; Huo, Q.; Walker, S. A.; Zasadzinski, J. A.; Glinka, C.; Nicol, J.; et, al.; Margolese, D.; Stucky, G. D.; Chmelka, B. F. *Sci.* **1995**, *267* (5201), 1138.

(5) Palmqvist, A. E. C. **2003**, *8*, 145.

(6) Firouzi, A.; Atef, F.; Oertli, A. G.; Stucky, G. D.; Chmelka, B. F. *J. Am. Chem. Soc.* **1997**, *7863*, 3596.

(7) Tolbert, S. H.; Firouzi, A.; Stucky, G. D.; Chmelka, B. F. *Science* **1997**, *278*, 1.

(8) Melosh, N. A.; Davidson, P.; Feng, P.; Pine, D. J.; Chmelka, B. F. *J. Am. Chem. Soc.* **2001**, *123* (6), 1240.

(9) Walcarius, A.; Sibottier, E.; Etienne, M.; Ghanbaja, J. *Nat. Mater.* **2007**, *6*, 602.

(10) Jahnke, J. P.; Wildemuth, D.; Nolla, J.; Kim, D.; Neyshtadt, S.; Segel-Peretz, T.; Frey, G. L.; Chmelka, B. F. *Prep. Sci.* **2017**.

(11) Freer, E. M.; Krupp, L. E.; Hinsberg, W. D.; Rice, P. M.; Hedrick, J. L.; Cha, J. N.;

Miller, R. D.; Kim, H.-C. *Nano Lett.* **2005**, *5*, 2014.

(12) Morales, V.; Idso, M. N.; Balabasquer, M.; Chmelka, B.; García-Muñoz, R. A. *J. Phys. Chem. C* **2016**, *120*, 16887.

(13) Melosh, N. a.; Lipic, P.; Bates, F. S.; Wudl, F.; Stucky, G. D.; Fredrickson, G. H.; Chmelka, B. F. *Macromolecules* **1999**, *32* (13), 4332.

(14) Lebeau, B.; Fowler, C. E.; Hall, S. R.; Mann, S. *J. Mater. Chem.* **1999**, *9* (10), 2279.

(15) Hayward, R. C.; Alberius, P. C. a; Kramer, E. J.; Chmelka, B. F. *Langmuir* **2004**, *20* (14), 5998.

(16) Kresge, C. T.; E., L. M.; Roth, W. J.; Vartuli, J. C.; Beck, J. S. *Nature* **1992**, *359*, 710.

(17) Schlipf, D. M.; Rankin, S. E.; Knutson, B. L. *ACS Appl. Mater. Interfaces* **2013**, *5*, 10111.

(18) Phan, H.; Jahnke, J. P.; Chmelka, B. F.; Nguyen, T.-Q. *Appl. Phys. Lett.* **2014**, *104*, 233305.

(19) Steinbeck, C. a.; Ernst, M.; Meier, B. H.; Chmelka, B. F. *J. Phys. Chem. C* **2008**, *112* (7), 2565.

(20) Segal-peretz, T.; Jahnke, J. P.; Berenson, A.; Neeman, L.; Oron, D.; Rossini, A. J.; Chmelka, B. F.; Frey, G. L. *J. Phys. Chem. C* **2014**, *118*, 25374.

(21) Neyshtadt, S.; Jahnke, J. P.; Messinger, R. J.; Rawal, A.; Peretz, T. S.; Huppert, D.; Chmelka, B. F.; Frey, G. L. *J. Am. Chem. Soc.* **2011**, *133*, 10119.

(22) Granja, L. P.; Martínez, E. D.; Troiani, H.; Sanchez, C.; Soler Illia, G. J. A. A. *ACS Appl. Mater. Interfaces* **2017**, *9*, 965.

(23) Blin, J. L.; Gérardin, C.; Carteret, C.; Rodehüser, L.; Selve, C.; Stébé, M. J. *Chem. Mater.* **2005**, *17*, 1479.

(24) Zeidel, M. L.; Ambudkar, S. V.; Barbara, S. L.; Agre, P. *Biochemistry* **1992**, *31*, 7436.

(25) Tang, C. Y.; Zhao, Y.; Wang, R.; Hélix-nielsen, C.; Fane, A. G. *Desalination* **2013**, *308*, 34.

(26) Tang, C. Y.; Kwon, Y.; Leckie, J. O. *Desalination* **2009**, *242*, 168.

(27) Béjà, O.; Spudich, E. N.; Spudich, J. L.; Leclerc, M.; DeLong, E. F. *Nature* **2001**, *411* (6839), 786.

(28) Fogg, G. E. *Aquat. Microb. Ecol.* **1995**, *9*, 33.

(29) Singh, K.; Caplan, S. R. *Trends Biochem. Sci.* **1980**, 62.

(30) Hampp, N. *Chem. Rev.* **2000**, *100*, 1755.

(31) Bräuchle, C.; Hampp, N.; Oesterhelt, D. *Adv. Mater.* **1991**, *3*, 420.

(32) Hampp, N.; Fischer, T.; Neebe, M.; Chemistry, P.; Meerwein, H.; Geb, S. *Proc. SPIE* **2017**, *4677* (6421), 121.

(33) Nordlund, G.; Boon Sing Ng, J.; Ng, S.; Bergström, L.; Brzezinski, P. *ACS Nano* **2009**, *3*, 2639.

(34) Rao, S.; Guo, Z.; Liang, D.; Chen, D.; Wei, Y.; Xiang, Y. *Phys. Chem. Chem. Phys.* **2013**, 1.

(35) Yang, T. (Calvin); Yee, C. K.; Amweg, M. L.; Singh, S.; Kendall, E. L.; Dattelbaum, A. M.; Shreve, A. P.; Brinker, C. J.; Parikh, A. N. *Nano Lett.* **2007**, *7*, 2446.

(36) Liang, H.; Whited, G.; Nguyen, C.; Stucky, G. D. *Proc. Natl. Acad. Sci. U. S. A.* **2007**, *104*, 8212.

(37) Liang, H.; Whited, G.; Nguyen, C.; Okerlund, A.; Stucky, G. D. *Nano Lett.* **2008**, *8*, 333.

(38) Hua, D.; Kuang, L.; Liang, H. *J. Am. Chem. Soc.* **2011**, *133*, 2354.

(39) Kuang, L.; Fernandes, D. A.; O'Halloran, M.; Zheng, W.; Jiang, Y.; Ladizhansky, V.; Brown, L. S.; Liang, H. **2014**, No. 1, 537.

(40) Ma, D.; Zhao, Y.; Wu, J.; Cui, T.; Ding, J. *Soft Matter* **2009**, *5*, 4635.

(41) Luo, T.-J. M.; Soong, R.; Lan, E.; Dunn, B.; Montemagno, C. *Nat. Mater.* **2005**, *4*, 220.

(42) Bromley, K. M.; Patil, a. J.; Seddon, a. M.; Booth, P.; Mann, S. *Adv. Mater.* **2007**, *19* (18), 2433.

(43) Wu, S.; Ellerby, L. M.; Cohan, J. S.; Dunn, B.; El-Sayed, M. A.; Valentine, J. S.; Zink, J. I. *Chem. Mater.* **1993**, *5*, 115.

(44) Besanger, T. R.; Brennan, J. D. *J. Sol-Gel Sci. Technol.* **2006**, *40*, 209.

(45) Béjà, O.; Spudich, E. N.; Spudich, J. L.; Leclerc, M.; DeLong, E. F. *Nature* **2001**, *411*, 786.

(46) Barbet-Massin, E.; Pell, A. J.; Retel, J. S.; Andreas, L. B.; Jaudzems, K.; Franks, W. T.; Nieuwkoop, A. J.; Hiller, M.; Higman, V.; Guerry, P.; Bertarello, A.; Knight, M. J.; Felletti, M.; Le Marchand, T.; Kotelovica, S.; Akopjana, I.; Tars, K.; Stoppini, M.; Bellotti, V.; Bolognesi, M.; Ricagno, S.; Chou, J. J.; Griffin, R. G.; Oschkinat, H.; Lesage, A.; Emsley, L.; Herrmann, T.; Pintacuda, G. *J. Am. Chem. Soc.* **2014**, *136* (35), 12489.

(47) Andreas, L. B.; Le Marchand, T.; Jaudzems, K.; Pintacuda, G. *J. Magn. Reson.* **2015**, *253*, 36.

(48) Lalli, D.; Idso, M. N.; Andreas, L. B.; Hussain, S.; Baxter, N.; Emsley, L.; Han, S.; Chmelka, B. F.; Pintacuda, G. *Submitt. J. Am. Chem. Soc.* **2017**.

(49) Andreas, L. B.; Jaudzems, K.; Stanek, J.; Lalli, D.; Bertarello, A.; Le Marchand, T.; Cala-De Paepe, D.; Kotelovica, S.; Akopjana, I.; Knott, B.; Wegner, S.; Engelke, F.;

Lesage, A.; Emsley, L.; Tars, K.; Herrmann, T.; Pintacuda, G. *Proc. Natl. Acad. Sci. U. S. A.* **2016**, *113*, 9187.

(50) Athens, G. L.; Shayib, R. M.; Chmelka, B. F. *Curr. Opin. Colloid Interface Sci.* **2009**, *14*, 281.

(51) Lee, C.; Lin, T.; Lin, H.; Zhao, Q.; Liu, S.; Mou, C. *Microporous mesoporous Mater.* **2003**, *57*, 199.

(52) Sangodkar, R. P.; Smith, B. J.; Gajan, D.; Rossini, A. J.; Roberts, L. R.; Funkhouser, G. P.; Lesage, A.; Emsley, L.; Chmelka, B. F. **2015**.

(53) Rossini, A. J.; Zagdoun, A.; Lelli, M.; Lesage, A.; Coperet, C.; Emsley, L. *Acc. Chem. Res.* **2014**, *46*.

Chapter 1 : Functionally active proteorhodopsin membrane proteins incorporated in mesostructured silica films

Abstract

A versatile synthetic protocol is reported that allows high concentrations of functionally active membrane proteins to be incorporated in mesostructured silica materials. Judicious selections of solvent, surfactant, silica precursor species, and synthesis conditions enable membrane proteins to be stabilized in solution and during subsequent co-assembly into silica-surfactant composites with nano- and mesoscale order. This was demonstrated by using a combination of non-ionic (*n*-dodecyl-β-D-maltoside or Pluronic P123) and lipid-like (1,2-diheptanoyl-*s,n*-gycero-3-phosphocholine) surfactants under mild acidic conditions to co-assemble the light-responsive transmembrane protein proteorhodopsin at concentrations up to 15 wt% into the hydrophobic regions of mesostructured silica materials in film or monoliths. Small-angle X-ray scattering, electron paramagnetic resonance spectroscopy, and transient UV-visible spectroscopy analyses established that proteorhodopsin molecules in mesostructured silica films exhibited native-like function, as reflected in their light absorbance properties and light-activated conformational changes that are consistent with the native H^+-pumping mechanism of these biomolecules, as well as enhanced thermal stabilities compared to in surfactant or lipid environments. The synthetic protocol is expected to be general, as demonstrated also for the incorporation of functionally-active transmembrane protein rhodopsin and cytochrome c, a peripheral membrane protein involved in electron transport, into mesostructured silica-cationic surfactant films.

Introduction

Proteins are versatile biomolecules that are tailored for particular functions in biological systems, many of which would be desirable to harness for technological applications. The compositions and structures of proteins within cellular environments have evolved under biological selection criteria for diverse functionalities, including highly selective reactions, molecular or ion transport, and signaling, which often occur at high rates and support the viabilities of biological organisms. Recently, there has been significant progress in the engineering of proteins to have functionalities that are different from those of wild-type analogs by judiciously adjusting protein compositions through biomolecular mutagenesis processes (e.g., directed evolution).[1,2] Many such functionalities could be attractive for technological uses, such as chemical or biological sensing,[3] catalysis,[4,5] separations,[6,7] bioanalytics,[8] or energy conversion,[9] though they are typically highly specific for certain substrates over a narrow range of conditions. The effective exploitation of proteins for non-biological purposes often requires that proteins be extracted from native biological environments and stabilized in active forms within synthetic host materials. Such synthetic hosts should provide robust local environments for the protein molecules to function under abiological conditions, over length scales larger than a single cell, and be integrable into technologically relevant processes or devices.

Membrane proteins in particular offer many technological opportunities based on their diverse functionalities, though incorporating them into synthetic host materials has been challenging due to their limited stabilities and high hydrophobicities that require robust amphiphilic host environments. Consequently, in contrast to water-soluble globular proteins, membrane proteins are generally located within or interact with the amphiphilic lipid bilayers

that separate the interiors of cells from their surroundings. At these complicated interfaces, individual monomers or oligomeric assemblies[10–12] of membrane proteins regulate intracellular conditions in a variety of functional roles that include sensing, signal transduction, and the selective transport of ions or molecules,[13] many of which might be exploited for a variety of practical purposes. One interesting example is the membrane protein proteorhodopsin (PR), which is found ubiquitously in oceanic organisms[14–20] and which absorbs green light to actively transport H^+-ions (protons) across cell membranes as part of cellular metabolic cycles.[19] Based on the photo-responsive transport activities of PR, synthetic materials that include PR molecules have been proposed for a variety of energy conversion and optical applications, similar to those suggested for the homologous and well-characterized membrane protein bacteriorhodopsin of the archaea *Halobacterium salinarium*.[21–26] However, preparing synthetic hosts that contain membrane proteins with native or native-like activities is difficult, given the highly specific conditions required to support the generally complex protein structures[27,28] and dynamics[29,30] that are necessary for protein function. In most cases, membrane proteins can remain functional outside of the native lipid membranes only in the presence of membrane-mimetic surfactants or lipids[31–35] and over narrow ranges of solvent compositions and temperatures.[36] Such stability considerations have limited the incorporation of membrane proteins into only a few types of synthetic materials, including hydrogels,[37] block copolymers,[38–40] silica gels or glasses,[41,42] self-assembled lipid bilayer arrays,[43,44] and supported lipid bilayers.[45] These materials, however, exhibit poor processabilities and only modest mechanical, thermal, and chemical stabilities that have limited their suitabilities for harnessing the functionalities of membrane proteins.[38,39,43–45]

The solution processabilities, amphiphilic properties, mechanical and thermal stabilities, and wide range of synthesis conditions of mesostructured silica make these materials advantageous to stabilize and exploit the functionalities of membrane proteins. Compared to lipid bilayers, mesostructured oxides are physically and chemically robust and can be synthesized in a wide range of macroscopic morphologies, including films, fibers, powders, and monoliths.[46] Furthermore, their mesoscale channel dimensions (3-12 nm) and specific volumes (1-2 cm^3/g) are suitable for macromolecular or colloidal guests, such as proteins,[5,8,47–51] conjugated polymers,[52,53] or nanoparticles.[54,55] For example, by adjusting the mesochannel diameters of mesoporous silica hosts to be within approximately 1 nm of the dimensions of a folded protein, such protein species could be stabilized within the host;[48,56] for the case of the water-soluble enzyme protein lipase, higher activities were observed for lipase molecules incorporated in mesoporous silica hosts with optimized mesochannel dimensions.[57] In addition, mesochannel surface compositions can be modified during syntheses or by post-synthetic treatments to facilitate the incorporation of such guests, e.g., by introducing protein binding sites[47] or by adjusting the hydrophobicity of the channel surfaces to promote interactions with proteins.[9,58] Despite such beneficial properties of mesostructured oxides, only a few types of membrane proteins, such as the light-harvesting photosynthetic complexes of the bacterium *Thermochratium tepidum*, have been incorporated in active forms into them, which has generally been achieved by the post-synthetic adsorption of proteins onto powders of these materials.[9,58,59] These approaches, however, lead to particles that often have composition gradients of proteins, small sizes (<10 μm diameters), and low inter-particle connectivities, which limit the usefulness of powders in exploiting the molecular or ion transport properties of membrane proteins over macroscopic length scales.

Here, we present a general solution-based synthetic protocol for co-assembling high concentrations of functional membrane proteins into surfactant-directed mesostructured silica materials as self-supporting films and monoliths. This is achieved by appropriate selection of solution compositions and conditions, including pH, solvent and surfactant species, that serve dual roles: to stabilize the large, highly hydrophobic, and relatively fragile membrane protein molecules and to direct their assembly with network-forming silica precursor species into a mesostructured silica composite. Proteorhodopsin was selected for incorporation, because its structure with seven α-helices represents a broad category of transmembrane proteins and because its light-activated functional properties are of potential technological interest. The structures, dynamics, stabilities, and distributions of PR guest molecules in synthetic mesostructured silica hosts are probed by a combination of complementary X-ray diffraction, electron paramagnetic resonance (EPR) spectroscopy, and optical absorbance analyses for comparison with those in native-like micellar solution (aq.) and lipid environments. Insights into the light-responsive functionalities of PR species in mesostructured silica films are established from time-resolved EPR and visible absorbance analyses, following by pulsed illumination of the films with green light. The synthesis protocol was adapted to incorporate rhodopsin transmembrane proteins and the peripheral membrane protein cytochrome c oxidase into mesostructured silica membranes to demonstrate the generality of the approach.

Materials and methods

Materials. Reagent grade tetraethoxysilane (TEOS, Aldrich Chemicals) was used as the silica precursor and all acidic solutions were prepared by diluting concentrated hydrochloric acid (Fisher) with the appropriate amounts of deionized water. Amphiphilic surfactants were used to stabilize proteorhodopsin molecules in solution and to direct the formation of the PR-

containing mesostructured silica composites. These included the non-ionic surfactant *n*-dodecyl-β-D-maltoside (DDM, Anatrace), the triblock copolymer Pluronic^{TM} P123 (poly(ethyleneoxide)$_{20}$-*b*-poly(propyleneoxide)$_{70}$-*b*-poly(ethyleneoxide)$_{20}$, $(EO)_{20}(PO)_{70}(EO)_{20}$ (obtained as a gift from BASF, Mount Olive, New Jersey, USA), the zwitterionic lipid 1,2-diheptanoyl-*sn*-glycero-3-phosphocholine (diC_7PC, Avanti Polar Lipids), and the cationic surfactant tetradecyltrimethylammonium chloride (TTACl, TCI America, Portland, Oregon, USA). Ethanol (>99.5% purity, Gold Shield Distributors, Hayward, California, USA) was used as a co-solvent to incorporate PR into synthetic materials that used triblock copolymers as structure-directing species. Cytochrome c from equine heart was purchased from Sigma. The low-molecular-weight fluorinated surfactant, sodium perfluoro-octanoate (PFO, Oakwood Products, Inc., West Columbia, South Carolina, USA) was used as an NMR probe molecule. The chemical formulas for these surfactants are shown in Figure 1A. All chemicals were used as-received.

Proteorhodopsin preparation. The basic methodologies for expression, purification, and nitroxide spin-labeling of proteorhodopsin were implemented as described previously,[60,61] with further details given in the Supporting Information. The proteorhodopsin gene used here was the BAC31A8 sequence, modified such that the three natural cysteines were substituted with serine residues. The slowed-photocycle E108Q mutant was employed in light-triggered spectroscopic studies, and additional mutants with single cysteines were used for site-specific nitroxide-labelling and subsequent EPR characterization. Such cysteine residues, obtained by site-directed mutagenesis, were labeled with the commonly used methanethiosulfonate (MTSL) nitroxide moiety,[62,63] commonly termed R1, the structure of which is shown in Figure 1B. The two spin-labeled proteorhodopsin residues exploited in this study were located

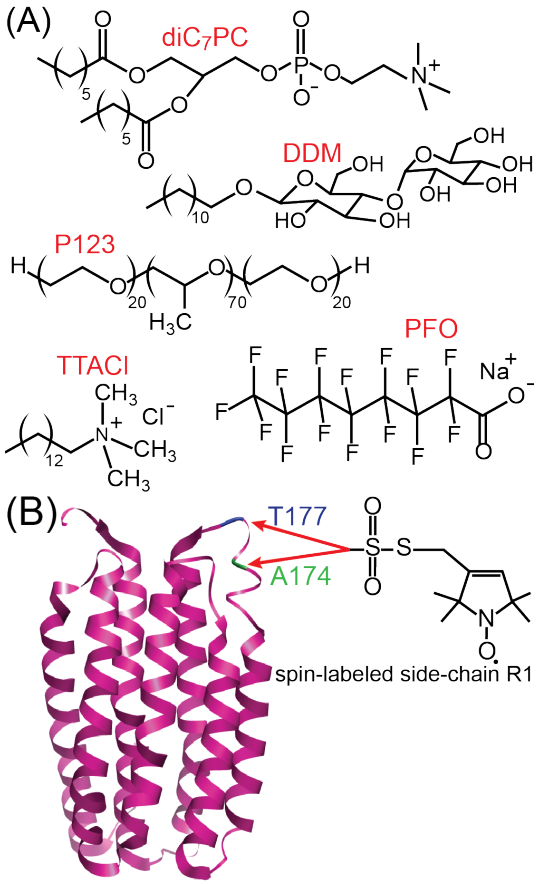

Figure 1. (A) Molecular structures of the structure-directing agents 1,2-diheptanoyl-3-glycero-sn-phosphocholine (diC$_7$PC), n-dodecyl-β-D-maltoside (DDM), PluronicTM P123, and tetradecyltrimethylammonium chloride (TTACl) and the surfactant sodium perfluoro-octanoate (PFO) used as a NMR probe molecule. **(B)** Schematic structure[68] of a proteorhodopsin monomer with the two specific residues A174 and T177 indicated to which nitroxide spin-labels (R1) were attached for EPR characterization.[60]

on the intracellular E-F loop of proteorhodopsin, as depicted schematically in Figure 1B, and characterized in detail elsewhere.[60] Proteorhodopsin species spin-labeled at either residue A174 or T177 were chosen, as they are associated with two modes of intra-protein contact (interfacial and exposed, respectively) and exhibit characteristic spectral signatures of light-driven conformational change, with those of A174R1 being larger in amplitude.[60]

For this study, size-exclusion Fast Protein Liquid Chromatography (FPLC) was used to purify and isolate predominantly monomeric proteorhodopsin and to remove salt from the proteorhodopsin-containing solution to reduce the effects of excess ions on subsequent

surfactant-directed co-assembly of the mesostructured silica host. The separation of monomeric and oligomeric complexes of proteorhodopsin solubilized within DDM micelles has been previously demonstrated using a Superdex 200 FPLC column.[61] For the current investigations, before elution of the proteorhodopsin through the FPLC column, the proteorhodopsin was incubated overnight in buffer containing 2 wt% of the zwitterionic lipid-like diC_7PC, which was observed to enrich the monomeric fraction of PR when FPLC-purified with a 0.05% DDM buffer.[10] After separation of the proteorhodopsin species by FPLC, the low-molecular-weight fractions corresponding to monomeric proteorhodopsin (with associated diC_7PC and DDM surfactants) were collected and concentrated by using 50,000 MWCO Amicon centrifugal filters (Millipore). All buffer compositions, up to and including the elution step of the purification, were 50 mM K_2HPO_4 and 150 mM KCl. To remove buffering salts, the monomeric PR solution was eluted through a Sephadex PD-10 buffer exchange column (GE Healthcare) equilibrated with millipore water (18.2 MΩ•cm) containing 0.05 wt% DDM and adjusted to pH 4 using dilute HCl (aq). This was followed by centrifugation of the PR-surfactant solution using 50,000 MWCO Amicon centrifugal filters (Millipore) to obtain 60-1750 μM PR in solutions with volumes of 200-500 μl, as determined by optical absorbance.[32] Subsequent analyses of the resulting solutions by Blue-Native Polyacrylamide Gel Electrophoresis (BN-PAGE) revealed the presence of predominantly monomeric and dimeric proteorhodopsin species (63%, as estimated from the areas of the BN-PAGE signals, data not shown). To synthesize materials with high (>10 wt%) protein loadings required the removal of excess DDM and diC_7PC surfactants from the monomeric PR FPLC fractions, which was achieved by binding the monomeric PR to Ni-NTA resin and subsequently washing the PR-bound resin with 200 mL of an aqueous buffer containing 0.05

wt% DDM buffer and 20 mM imidazole. After eluting PR from the Ni-NTA resin using 500 mM imidazole buffer, the K_2HPO_4, KCl and imidazole salts were removed from the PR sample by eluting the PR through a Sephadex PD-10 buffer exchange column (GE Healthcare) equilibrated with millipore water (18.2 MΩ•cm) containing 0.05 wt% DDM and adjusted to a pH of ~4 using dilute aqueous HCl. The PR was then concentrated using 50,000 kDa MWCO Amicon centrifugal filters (Millipore) to the desired PR concentration.

Preparation of protein-containing mesostructured silica films. DDM+diC_7PC-directed mesostructured silica materials without or with proteorhodopsin guests were typically synthesized by adding 0.05 g tetraethoxysilane (TEOS) to 1 g of 4 mM HCl (aq.) at room temperature. The mixture was stirred at room temperature for 2 h to allow the TEOS to hydrolyze, after which appropriate amounts of DDM and diC_7PC were added, which both direct the assembly of the mesostructured silica framework and stabilize monomeric proteorhodopsin species. After dissolution of these surfactants, the precursor solution was cast directly onto a suitable substrate (typically glass for optical characterization, a polymer, e.g. Kapton^{TM}, for SAXS measurements, or PDMS to yield free-standing films) and allowed to dry under ambient humidity and temperature conditions for 2 days to generate the DDM+diC_7PC-directed mesostructured silica films before characterization. For materials that incorporate proteorhodopsin, the precursor solution was mixed in an approximately 1:1 ratio with an aqueous solution containing DDM+diC_7PC-solubilized proteorhodopsin monomers (60-1750 μM), prepared as described above, and subsequently cast onto a desired substrate and also allowed to dry for 2 days under ambient conditions. The film thickness could be varied from a few microns (typically supported on a substrate) to that of a free-standing monolith with thicknesses ranging from approximately 50 μm to more than a millimeter. The film area could

also be controlled over arbitrary dimensions; films have been routinely prepared with areas of several square centimeters, with scaling to significantly larger film areas expected to be possible. High PR concentrations, relatively low (H_2O:TEOS mass ratio of <15:1) solvent quantities during synthesis and the presence of PFO promoted the assembly of mesostructured silica films with macroscopically uniform thicknesses and PR distributions. DDM+diC_7PC-directed silica materials with 40% DDM, 20% diC_7PC and 40% SiO_2 were calcined by ramping the temperature at a rate of 0.5 °C/min to 550 °C, holding this temperature for 8 h, and subsequently decreasing the temperature to 25 °C at a rate of 4°C/min.

Pluronic^{TM} P123-directed mesostructured silica materials were similarly synthesized by first dissolving 0.7 g of P123 in 0.7 g of ethanol mixed with 0.6 g of 0.02 M HCl (aq.). Following the dissolution of P123, 1.47 g of TEOS were added to this solution and allowed to hydrolyze for 2 h, after which 2.5 g of an aqueous solution containing the desired amount of proteorhodopsin (typically 80 μM) were added. This solution was then cast on a suitable substrate and allowed to dry at room temperature under a vacuum of 36 kPa to promote more rapid solvent evaporation.

To prepare mesostructured silica materials containing cytochrome c, 0.1 g of the structure-directing surfactant, TTACl, and 0.2 g of TEOS were mixed with 2 g of 5 mM HCl (aq.), and the TEOS was allowed to hydrolyze for 2 h at ambient temperature. The pH of the resulting solution was approximately 4. After hydrolysis, 13.5 mg of cytochrome c were added. This mixed solution was then cast on a suitable substrate and allowed to dry under ambient temperature and humidity for 2 days.

Characterization. Small-angle X-ray scattering (SAXS) patterns were acquired from mesostructured silica-surfactant materials without or with proteorhodopsin to establish the

degree of mesostructural order in the films. Powders of DDM+diC_7PC-directed mesostructured films were characterized on a Rigaku Smartlab High-Resolution Diffractometer (λ = 1.542 Å, voltage 40 keV, current 44 mA). SAXS measurements of PR-containing P123-directed materials were conducted using a XENOCS Genix 50W X-ray microsource with Cu K_α radiation (λ = 1.542 Å, voltage 50 keV, current 1 mA) and a MAR345 image plate area detector (located 1.4 m behind the sample) in a transmission geometry.

2D HYperfine Sublevel CORrelation (HYSCORE) pulsed EPR analyses were conducted to establish the proximities among the nitroxide spin-labels attached to E-F loop residue 174 of proteorhodopsin molecules and the ^{19}F moieties of sodium perfluoro-octanoate molecules in the mesostructured silica film. These pulsed-EPR experiments were performed at υ_L = 9.2492 GHz on an X-band Bruker Elexsys 580 spectrometer that was equipped with a Bruker Flexline split-ring resonator ER4118X-MS3. The temperature was set to 50 K by cooling with a closed-cycle cryostat (ARS AF204, customized for pulsed EPR, ARS, Macungie, Pennsylvania, USA). First, an electron spin-echo (ESE)–detected spectrum was recorded with the primary echo sequence $\pi/2$–τ–π–τ–echo. The lengths of the $\pi/2$ and π pulses were 16 ns and 32 ns, respectively, and τ was set to 200 ns. 2D HYSCORE spectra were recorded with the pulse sequence $\pi/2$– τ –π /2– t_1 –π – t_2 –$\pi/2$– τ –echo[64,65] at a magnetic field of 329.3 mT, corresponding to the maximum amplitude of the nitroxide EPR signal. The lengths of all pulses were set to 16 ns, and the time intervals t_1 and t_2 were varied from 300 ns to 4396 ns in increments of 16 ns. A standard eight-step phase cycle was used to eliminate unwanted echoes. To avoid substantial "blind spot" artifacts, two separate HYSCORE spectra were recorded with a τ value of either 148 ns or 180 ns. The time traces of each HYSCORE spectrum were baseline corrected with a third-order polynomial, apodized with a Gaussian

window, and zero-filled with 1024 points along each dimension. After applying a two-dimensional (2D) Fourier transformation, the absolute-value spectra recorded for τ = 148 ns and 180 ns were then added to achieve an artifact-reduced spectrum.

Solution-state ^{1}H NMR measurements were conducted at 11.7 T on a Bruker AVANCE 500 MHz spectrometer operating at a ^{1}H frequency of 500.2 MHz. Single-pulse ^{1}H NMR spectra were acquired using a 90° pulse of 13.8 μs, an acquisition time of 6 s, and a recycle delay of 10 s for each of the 64 signal-averaged transients. The surfactant quantities in the desalted PR-surfactant solution were established by acquiring a solution-state single-pulse ^{1}H NMR spectrum on a solution containing 50 μl of the as-purified PR-surfactant sample and 950 μl of D_2O containing 0.1 wt% of DDM, which corresponds to a 1-in-20 dilution of the PR-surfactant solution. The quantity of DDM in the diluted proteorhodopsin sample was obtained by comparing the integrated areas of the ^{1}H signals at 0.84, 3.5 and 5.4 ppm, assignable to the ^{1}H moieties of DDM,[66] to those from an external reference of 0.1 wt% of DDM in D_2O.

Solid-state NMR ^{1}H{^{19}F} rotational-echo, double-resonance (REDOR) MAS NMR spectra were acquired at 9.4 T by using a variable-temperature 2.5-mm triple-resonance Bruker MAS probehead on a Bruker ASCEND-III NMR spectrometer operating at frequencies of 400.02 MHz for ^{1}H and 376.32 MHz for ^{19}F. Samples were packed into 2.5 mm zirconia rotors with VELSPAR™ caps. The ^{1}H{^{19}F} REDOR NMR spectra were acquired under MAS conditions of 15 kHz at approximately -20 °C, using a 6 s delay time, and 250 ms acquisition time for each of the 256 signal-averaged transients. A train of 15 rotor-synchronized π-pulses, corresponding to a 0.11 ms recoupling time, was applied to the ^{19}F channel to recouple the ^{19}F-^{1}H dipolar couplings during the ^{1}H evolution period. Differences among the signal intensities

of spectra acquired without and with ^{19}F-^{1}H dipolar recoupling arise from the dipolar couplings among ^{1}H and ^{19}F moieties, providing insights about their proximities.

Continuous-wave (cw) EPR spectra were collected at room temperature with a 0.35 T Bruker EMXplus spectrometer equipped with a Bruker TE011 high-sensitivity cylindrical microwave cavity (ER 4119HS-LC High Sensitivity Probehead). The spectra were acquired using 20 mW incident microwave power, 1 G modulation amplitude, and 150 G sweep width on PR-containing mesostructured silica films or micellar solutions contained in 0.6 mm ID, 0.84 mm OD quartz capillaries (VitroCom) and placed into 4 mm diameter quartz EPR tubes (Wilmad). Multiple 40-s scans were averaged to enhance the signal-to-noise of the EPR spectra.

Light-activation of proteorhodopsin within the EPR microwave cavity was carried out by illumination through the cavity optical window using a ~5 mW green (532 nm) diode laser (DPS20 Midwest Laser Products, LLC) that was mounted on an aluminum stage secured to the front of the electromagnet. Time-resolved laser-triggered cw EPR measurements were performed by synchronizing EPR data acquisition to a 500 ms laser flash from the green diode laser source, using a Hewlett-Packard 8116A pulse generator that provided TTL pulses to the external trigger port of the EMX-plus spectrometer and the diode laser with the desired timing. Transient changes of a specific cw EPR peak were tracked by fixing the magnetic field to resonate at the frequency of interest and observing the cw EPR spectral amplitude for 10-15 s during and after laser illumination by a 500 ms green laser pulse. Such measurements were repeated and averaged for 4 h or longer (1000 scans or more) to improve signal-to-noise.

Time-resolved optical absorbance measurements were conducted on a home-built apparatus previously described[60] and used to monitor the absorbance changes of

proteorhodopsin guests induced by the green laser pulse. The same ~5 mW green laser used for cw EPR experiments was used to illuminate the samples (silica films or solution), which were contained in a flat sample cell or a 1 mm square cuvette. A tungsten light source (Ocean Optics, LS-1) and a charge-coupled device (CCD) camera (Andor Idus) were used to collect absorbance difference spectra every 80-100 ms after a 500 ms laser pulse. Buffers of identical compositions and monomeric proteorhodopsin were used to ensure that the photocycle kinetics measurements were comparable among all the samples that were characterized.

Steady-state absorbance measurements were conducted on a Shimadzu UV3600 UV-Vis-NIR spectrometer with an integrating-sphere detector to determine the thermal stability of proteorhodopsin molecules within the mesostructured silica films and in the lipid bilayer samples, as well as to examine the oxidation state of cytochrome c. The thermal stabilities of the various PR-containing samples were probed by heating samples for 24 h at the temperatures specified in the text (70-105 ^{o}C) in a Fisher Scientific IsoTemp oven. Ex situ absorbance measurements were performed following treatments at different temperatures and normalized to absorbance measurements on the same sample prior to heating. Since negligible denaturation of PR was observed at 70 ^{o}C, these samples were also used for assessing denaturation at 80 ^{o}C, but otherwise previously unheated samples were used in all tests. Samples of PR in lipid bilayers were prepared by the following procedure: overexpressing PR in *E. coli*, lysing these cells, using centrifugation to isolate the lipid membrane fragments, and then resuspending the lysed PR-containing membranes in a phosophate-buffered solution, as described in the Supporting Information.

UV-visible absorption analyses were also conducted to characterize the oxidation and reduction of cytochrome c guests in TTACl-directed mesostructured silica materials.

For the UV-visible absorption measurements, the samples were prepared by placing a free-standing film of the material into a plastic cuvette and the incubating the film for 10 min in 2 mL of 0.1 M tris-acetate buffered solution that was titrated to pH 7.0 by using 1 M HCl and without ethylenediaminetetraacetic acid. To reduce the cytochrome c guests in the mesostructured silica hosts, the tris-acetate-buffered solution in the cuvette was removed and the film was subsequently incubated in 2 mL of a fresh tris-acetate-buffered solution with an otherwise identical composition, except with 30 mM ammonium iron(II) sulfate.

Results and discussion

Mesoscale order in proteorhodopsin-containing silica films. The surfactants that stabilize proteorhodopsin molecules outside of the native lipid environments can also direct the assembly of mesostructured silica materials with or without proteorhodopsin. Surfactants such as the non-ionic *n*-dodecyl-β-*D*-maltoside (DDM) and zwitterionic 1,2-diheptanoyl-*sn*-glycero-3-phosphocholine (diC_7PC) interact with PR species and enable the native structures, dynamics, and functionalities of these biomolecules to be preserved in non-native environments. We hypothesized that the PR-stabilizing surfactant species DDM and diC_7PC could direct the assembly of mesostructured silica materials, resulting in synthetic hosts into which functionally-active PR guests could be incorporated. The structure-directing roles of DDM and diC_7PC surfactants, individually and in mixtures, were probed by small-angle X-ray scattering, which is sensitive to long-range order within the materials; for the X-ray wavelength used (1.54 Å), Bragg's Law stipulates that small-angle ($<5^o$) reflections correspond to periodicities larger than 1.5 nm, thereby providing information about mesoscale (2-50 nm) order within the surfactant-directed silica materials. For example, the SAXS pattern (Figure 2A) of a silica film synthesized with a mixture of DDM and diC_7PC surfactants in a 2:1 mass

ratio shows a broad primary *(100)* reflection at 1.9° (full-width-at-half-maximum, fwhm 0.4°), corresponding to a *d*-spacing of 4.6 nm, that establishes the presence of mesostructural order within DDM+diC_7PC-directed silica. The broadness of this reflection and the absence of higher-order Bragg reflections indicate the relatively modest long-ranged mesostructural organization of this material. Based on the proclivity of DDM surfactants to assemble into cylindrical aggregates,[67] the SAXS and BET results suggest that DDM and diC_7PC surfactants form wormlike mesochannels within the mesostructured silica, as shown schematically in the inset of Figure 2A. The surfactant and silica compositions of DDM+diC_7PC-directed materials can be adjusted to produce materials with characteristic ordering length scales between 3.5 and 7.0 nm (Appendix B, Figure B1), with the smaller mesoscale dimensions observed for materials with higher diC_7PC contents, consistent with the shorter alkyl chains of the diC_7PC molecules compared to the DDM surfactant species. The worm-like mesostructural order represents a tradeoff among the stabilizing effects of the relatively short-chain surfactants on proteorhodopsin guest molecules, the moderate hydrophilic-hydrophobic contrast of the short surfactants, and the solution conditions (pH, solvent, temperature) required for co-assembly of the surfactants with the network-forming silica and functionally active PR species.

Mesostructured silica synthesized with a 2:1 mass ratio of DDM to diC_7PC was selected to incorporate proteorhodopsin guest species, as these materials were expected to have surfactant mesochannel dimensions (~3 nm) similar to those of proteorhodopsin monomers (~4 nm in length x ~3 nm in diameter, Figure 1B).[68] These DDM+diC_7PC-directed silica films synthesized with 5 wt% of PR (Figure 2B, inset) are transparent with an intense purple color, consistent with that of photo-active and functional PR under acidic conditions.[69] The SAXS pattern of this material shows a single, somewhat broader primary *(100)* reflection at 1.7° (0.5°

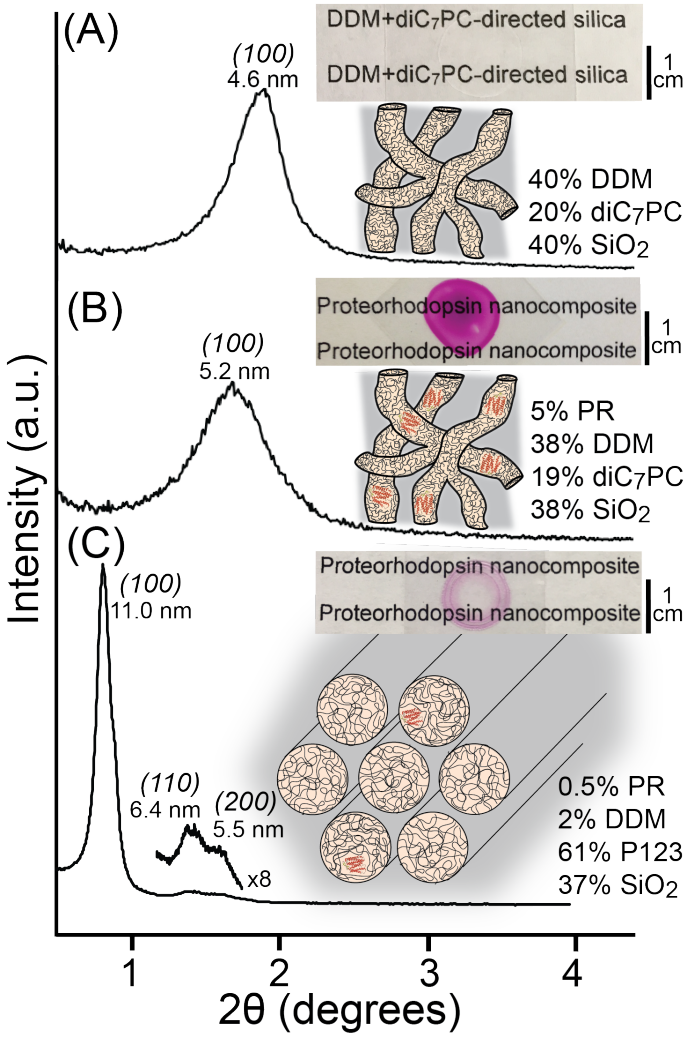

Figure 2. Small-angle X-ray scattering (SAXS) patterns for 50-μm-thick DDM+diC$_7$PC-directed mesostructured silica films **(A)** without and **(B)** with 5 wt% proteorhodopsin incorporated. The position of the characteristic *(100)* reflection changes from 1.9° to 1.7°, corresponding to a 0.6 nm difference in the *d*-spacing upon inclusion of PR. **(C)** SAXS pattern for P123-directed mesostructured silica film that contains 0.5 wt% PR. The schematic diagrams depict the relative dimensions of the silica mesochannels and proteorhodopsin in the different mesostructured silica materials. The insets adjacent to each SAXS pattern show optical images of the respective mesostructured silica films on glass substrates.

fwhm), corresponding to a *d*-spacing of 5.2 nm (Figure 2B), that is displaced to a smaller scattering angle compared to otherwise identical silica films without PR guest species (Figure 2A). These observations are consistent with the incorporation of predominantly monomeric PR species in the DDM+diC$_7$PC-directed mesostructured silica host, which is expected to be

associated principally with hydrophobic surfactant moieties in the silica mesochannels, owing to the high hydrophobicities of the membrane protein guests. DDM+diC_7PC-directed silica materials prepared with 15 wt% PR yield *(100)* SAXS reflections (Appendix B, Figure B2) at the same 2θ positions of 1.7° but with even larger widths (fwhm ~1.0°), reflecting a broader distribution of mesochannel dimensions and order for materials with higher PR contents.

Synthesis compositions and conditions can be adapted to adjust the intermolecular interactions among the co-assembling species and the resulting periodic ordering and dimensions of proteorhodopsin-containing mesostructured silica hosts. This is demonstrated for materials prepared by using the triblock-copolymer Pluronic^{TM} P123, $(EO)_{20}(PO)_{70}(EO)_{20}$, as the primary structure-directing surfactant species. For example, the SAXS pattern in Figure 2C for P123-directed mesostructured silica containing 0.5 wt% PR shows three well-resolved reflections at 0.8° (0.1° fwhm), 1.3°, and 1.5° that are indexable to the *(100)*, *(110)*, and *(200)* reflections, respectively,[70] of a well-ordered hexagonal (*p6mm*) mesostructure with a unit cell-parameter of 13.2 nm. Similar reflections are observed for otherwise identical P123-directed mesostructured silica film, except without PR (Appendix B, Figure B3), consistent with the low PR content of the material and the relatively large mean mesochannel dimensions (ca. 8 nm diameter),[70] compared to the size of the PR monomers (Figure 2C). Higher concentrations (>0.5 wt%) of PR yielded pink powders that precipitated out of solution, exhibited no SAXS reflections (i.e., no mesostructural order was present), and from which macroscopic films could not be formed. Such behavior is likely due to the more hydrophilic characters of the ethyleneoxide and propyleneoxide blocks of the structure-directing P123 surfactant species compared to DDM or diC_7PC, the former of which are less compatible with and therefore less

effective in incorporating the highly hydrophobic PR molecules under the synthesis conditions used.

Stability of proteorhodopsin molecules in mesostructured silica. The absorbance properties of proteorhodopsin guest species lend insight into their photo-activities and stabilities in synthetic mesostructured silica hosts. Under acidic conditions, the retinal chromophore within functional PR absorbs maximally at ~546 nm,[69] which differs from the absorbance of free (non-PR-associated) retinal in aqueous solution at ~380 nm.[71] This is a result of the different local environments of the retinal moieties within PR, including covalent and hydrogen bonding, as well as interactions with moieties in the H^+-ion channel of PR. The UV-visible absorbance spectrum in Figure 3A of a DDM+diC_7PC-directed silica film containing 5 wt% PR shows a broad (110 nm fwhm) absorption peak centered at 541 nm, which is characteristic of the retinal moieties in functionally active PR molecules under acidic conditions and accounts for the purple coloration of such films (Figure 2B, inset). Absorbance intensity is also observed in the range of 350-450 nm, which likely originates from scattered light from the mesostructured silica film and the beta-band absorbance of the retinal chromophore in PR;[32,72] for bacteriorhodopsin, absorbance in this region is associated with high-energy transitions in the retinal that are separate from those associated with the chromophore absorbance above 500 nm.[73] Under ambient and dark storage conditions, the PR-containing mesostructured silica films retain purple colorations for at least several months, with no perceptible changes in absorbance detected by the human eye. Collectively, these results demonstrate the stabilities of photo-active PR guests in DDM+diC_7PC-directed mesostructured silica host materials under ambient conditions.

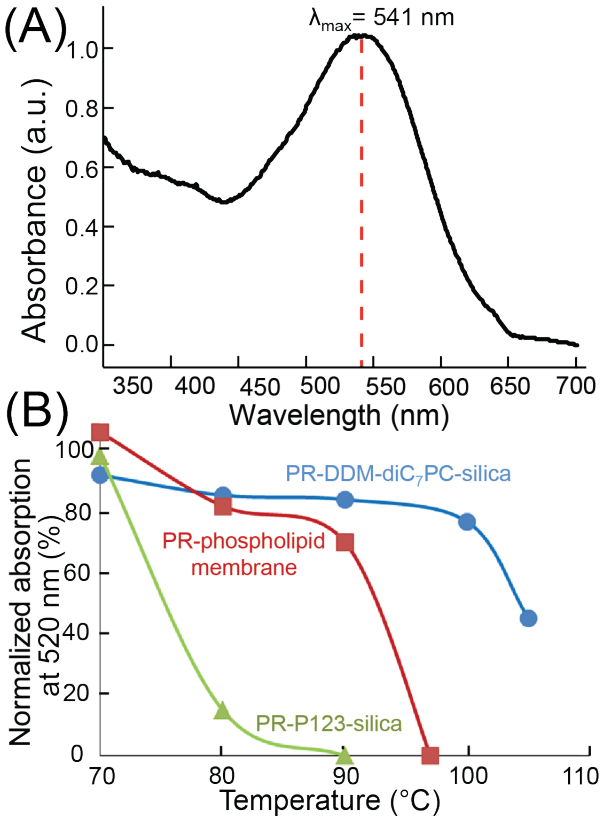

Figure 3. (A) UV-visible absorption spectrum of DDM+diC$_7$PC-directed mesostructured silica film containing 5 wt% PR. **(B)** Normalized UV-visible absorbance intensity at 520 nm of proteorhodopsin in a mesostructured DDM+diC$_7$PC-silica film (blue circles), a mesostructured P123-silica film (green triangles), or in phospholipid membranes (red squares) after heating for 24 h at temperatures between 70 and 105 °C. For each heat-treated sample, the visible absorbance at 520 nm was measured and normalized to the absorbance intensity at 520 nm of the same sample measured before heating. The uncertainty in normalized absorption is expected to be 5-10% based on variations in film thicknesses and measurement limitations.

In addition, proteorhodopsin guest molecules in DDM+diC$_7$PC-directed mesostructured silica films maintained high photo-activities even after exposure to elevated temperatures (up to 105 °C). The thermal stabilities of photo-active PR guest species were assessed by measuring the absorbance intensities at 520 nm of PR-containing mesostructured DDM+diC$_7$PC- or P123-directed silica films after exposure to elevated temperatures up to 105 ^{o}C for 24 h. By Beer's law, these absorbance intensities are proportional to the concentration of photo-active PR guests; thus, their normalization to the 520 nm absorbance of each respective sample prior to thermal treatment yields an estimate for the percentage of PR guests

that remain photo-active after each thermal treatment. For comparison, identical measurements and analyses were conducted on PR in native-like phospholipid membranes of *E. coli* cells. As shown in Figure 3, after thermal treatment at 70 °C, all three PR-containing materials retained at least 90% of the absorbance intensity at 520 nm, indicating a loss of <10% of photo-active PR species after heating to this moderately elevated temperature. After treatments at higher temperatures, however, significant differences are observed: there was no detectable absorbance at 520 nm from the PR-containing P123-directed silica film and *E. coli* membranes after heating to 90 °C and 97 °C, respectively, establishing that the PR guests in these materials were fully denatured within the sensitivity limits of the UV-visible absorbance analyses. By comparison, after heating to an even higher temperature of 100 °C, the PR-containing DDM+diC_7PC-directed silica films retained 77% of the 520-nm absorbance observed in the film before thermal treatment, and 45% after heating at 105 °C for 24 h. The relatively high thermal stabilities of photo-active PR guests in the DDM+diC_7PC-directed silica, compared to the P123-directed films and phospholipid membranes, likely results from the combined benefits of the narrower DDM+diC_7PC-directed mesochannel dimensions (~3 nm) that physically constrain the PR species from unfolding and the favorable interactions between PR molecules and hydrophobic DDM and diC_7PC surfactant moieties.

Local proteorhodopsin environments within silica mesochannels. Insight into the local distributions of proteorhodopsin guest molecules within the mesostructured silica hosts is provided by two-dimensional (2D) electron paramagnetic resonance (EPR) spectroscopy. EPR methods, such as hyperfine sublevel correlation (HYSCORE) experiments, are sensitive to hyperfine interactions between an electron spin and proximal (<1 nm) nuclear spins. Consequently, by exploiting a nitroxide spin-label ("R1") covalently attached to the exterior

moieties of PR molecules (here, at the E-F loop site 174, "A174R1", Figure 1B) the local proximities of the spin-labels, and thus the attached PR molecules, to nearby nuclei can be probed. In the high-frequency (+,+) quadrant of a 2D HYSCORE spectrum, correlated intensities along the frequency diagonal arise from nuclear spins that are weakly coupled by hyperfine interactions to unpaired electrons, while the lineshape of the correlated signal along the corresponding frequency *anti*-diagonal is related to the anisotropy associated with these interactions.

For example, the high-frequency quadrant of the 2D HYSCORE spectrum (Figure 4A) acquired on a DDM+diC_7PC-directed mesostructured silica film containing 5 wt% of spin-labeled PR-A174R1 and 5 wt% PFO shows correlated signal intensity along the diagonal at (14.0, 14.0) MHz. This corresponds to the ^{1}H nuclear Larmor frequency and establishes the close (<1 nm) proximities of ^{1}H moieties to the unpaired electrons of the nitroxide spin-labels attached to PR molecules. The anti-diagonal lineshape that intersects near (14.0, 14.0) MHz (labeled "^{1}H" in Figure 4) is similar to that of a characteristic powder pattern for an axially symmetric ^{1}H-electron hyperfine coupling tensor, the anisotropic parts of which result in the two less intense correlations separated evenly about the frequency diagonal at ca. (14.3, 14.3) MHz. The large ~1 MHz separation of these two signals about the frequency diagonal indicates that these signals arise from ^{1}H species that experience strong hyperfine couplings, allowing these signals to be confidently attributed to the strong *intramolecular* hyperfine interactions among the ^{1}H moieties and unpaired electron spin on each nitroxide spin label. By comparison, the more intense and narrower frequency distribution near (14.0, 14.0) MHz likely originates from both intra- and intermolecular hyperfine interactions among a large number of ^{1}H

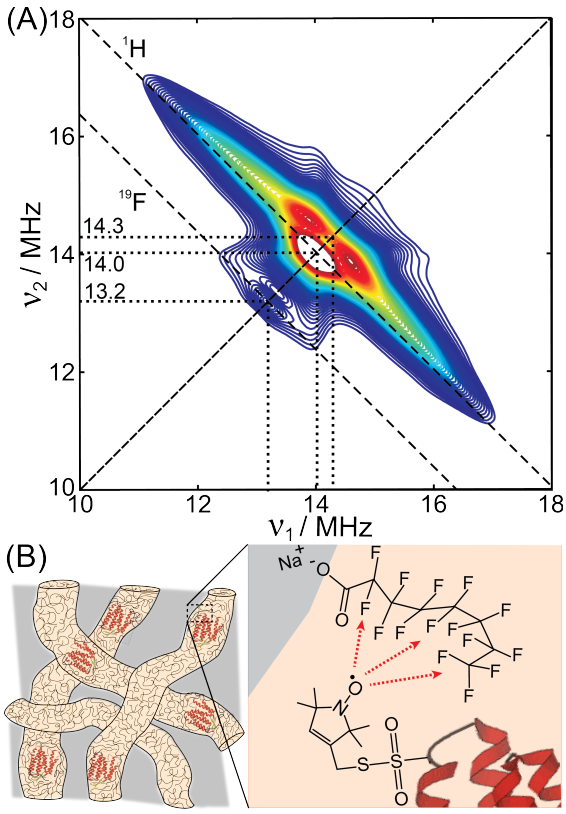

Figure 4. High-frequency region **(A)** of the 2D HYSCORE spectrum acquired from a DDM+diC$_7$PC-directed mesostructured silica film containing 5 wt% proteorhodopsin with a nitroxide spin-label at the E-F loop residue A174R1. Intensity at (13.2, 13.2) MHz is associated with the ^{19}F Larmor frequency at 0.3293 T and indicates the presence of ^{19}F spins, and thus PFO molecules, within 1 nm of the nitroxide spin-labels on the PR-A174 species, as shown in the schematic diagram in **(B).** This spectrum was acquired at a temperature of 50 K at a field strength of 0.3293 T and using a microwave frequency of υ_L = 9.2492 GHz.

moieties of the protein and the surrounding environment that are more distant from the unpaired electrons.

The HYSCORE spectrum also provides detailed information about *intermolecular* interactions among the proteorhodopsin guest molecules with the surfactant and silica species of the mesostructured silica host material. In particular, the weaker correlated signal on the frequency diagonal at (13.2, 13.2) MHz, corresponding to the Larmor frequency of ^{19}F, unambiguously establishes the close proximities of the nitroxide spin-labels with ^{19}F nuclear spins of the PFO surfactant probe species, which are the only fluorinated molecules in this

material. Separate solid-state $^{1}H\{^{19}F\}$ REDOR NMR experiments (Appendix B, Figure B4) on mesostructured silica hosts without PR reveal the close (<1 nm) proximities of the hydrophobic perfluorinated chains of the PFO molecules and the alkyl chains of the stabilizing and structure-directing DDM and diC_7PC surfactant species. The HYSCORE and $^{1}H\{^{19}F\}$ REDOR analyses together indicate that spin-labeled PR species are close to and interact with the hydrophobic alkyl chains of the DDM and diC_7PC surfactant species that form the mesochannels of the mesostructured silica host. No correlated intensities are observed that suggest the close (<1 nm) proximities of the unpaired nitroxide electron spins and ^{29}Si nuclear spins (4.7% natural abundance) of the silica framework. These analyses affirm that spin-labeled PR guest species are distributed within the DDM- and diC_7PC-rich surfactant channels of the mesostructured silica host, as depicted schematically in Figure 4B.

Dynamics of proteorhodopsin within mesostructured silica. The light-activated H^+-transporting functionalities of proteorhodopsin molecules, whether within native lipid bilayers or within the mesostructured surfactant-silica host materials, rely on the dynamics of the biomolecules. Native cell membrane environments provide ample water, salts, and lipids to enable the conformational changes of PR molecules, specifically the pico- to nanosecond dynamics of protein structural elements that are thought to be generally necessary to support protein activities and biological functions.[74] Continuous-wave (cw) EPR is sensitive to such motions and therefore enables insight into the dynamics of PR within non-native host environments, which can have different length scales and compositions in than native lipids.

Based on the native-like optical absorption properties (Figure 3A) of proteorhodopsin molecules in synthetic mesostructured silica, we hypothesized that the surfactant-rich mesochannel environments would also support the native-like structural dynamics of

proteorhodopsin guests. To test this hypothesis, cw EPR spectroscopy was used to examine the dynamics of nitroxide spin-labels attached to PR at residues A174 or T177 of the □-helical E-F loop (yielding PR-A174R1 or PR-T177R1, Figure 1B), the motions of which are highly correlated with the light-activated H^+-transport mechanism of PR.[60] The cw EPR spectra in Figure 5A of these spin-labeled PR species in powders of as-synthesized DDM+diC_7PC-directed mesostructured silica films exhibit lineshapes that are characteristic of nitroxide radicals, with three distinct EPR peaks. Lineshape analyses of the EPR spectra can provide site-specific information on the local dynamics of the spin-labelled moieties under different conditions. Specifically, the linewidth of the central peak (characterized by H_0) is broader for less mobile species, while the intensities of the "*m*" and "*i*" components of the low-frequency peak (leftmost in Figure 5A) reflect the relative populations of nitroxide spin-labels that are relatively mobile and immobile, respectively, on the nanosecond time scale.[75,76] The "*m*" and "*i*" components may arise from spin labels in two conformations that exchange slowly on the EPR timescale or not at all, due to differences in local PR structure or local molecular environments.

In particular, the dynamics of the E-F loop of proteorhodopsin in synthetic mesostructured silica hosts were evaluated by comparing the cw EPR lineshapes of spin-labeled PR in DDM+diC_7PC-directed silica powders and in aqueous micellar solutions. The EPR spectra in Figure 5A acquired from PR-A174R1 or PR-T177R1 in as-synthesized DDM+diC_7PC-directed mesostructured silica both show center-peak linewidths in the range of 0.88-0.92 mT, which are broader than the 0.23-0.31 mT linewidths (Figure 5B,C, insets) of identically-spin-labeled PR in alkaline-buffered DDM+diC_7PC micellar solutions. These differences reflect the slower dynamics of the A174R1 and T177R1 side-chains of PR guest

molecules confined in mesostructured silica, compared to in DDM+diC_7PC micellar solutions. The slower side-chain dynamics for PR guest species in as-synthesized silica films are also qualitatively borne out in Figure 5A by the significantly greater EPR intensity of the low-frequency immobile "*i*" component over the mobile "*m*" component,[75,76] which is in contrast to the EPR spectra of otherwise identical PR in alkaline-buffered micellar solutions (Figure 5B,C insets) for which the reverse is observed. These results collectively indicate the slower dynamics of the E-F loop of proteorhodopsin molecules incorporated in as-synthesized DDM+diC_7PC-directed mesostructured surfactant-silica hosts, compared to native-like surfactant environments, consistent with physical confinement of the sidechains of PR molecules within the ca. 5-nm silica mesochannels.

The side-chain dynamics of proteorhodopsin guest species in synthetic mesostructured silica depend strongly on the extent of hydration of the host material, as well. The EPR spectra (Figure 5B,C) of PR-containing mesostructured silica films hydrated by exposure to excess amounts of alkaline-buffered solutions (Figure 5B,C) show significantly higher relative signal intensities associated with the mobile "*m*" component (versus the immobile "*i*" component), compared to those of PR in as-synthesized films (Figure 5A). Nevertheless, the relative intensities of the mobile moieties in Figure 5 B,C are still slightly less than those in spectra acquired from identically spin-labeled PR molecules in alkaline-buffered DDM+diC_7PC micellar solutions (Figure 5B,C insets). While these data reveal that the average side-chain dynamics of incorporated PR guests increase with hydration, native-like PR dynamics are not completely obtained even in fully hydrated films, likely due in part to the effects of confinement within the silica mesochannels. Nonetheless, the EPR lineshape analyses reveal that the sidechain mobilities of PR molecules in hydrated mesostructured silica host films are

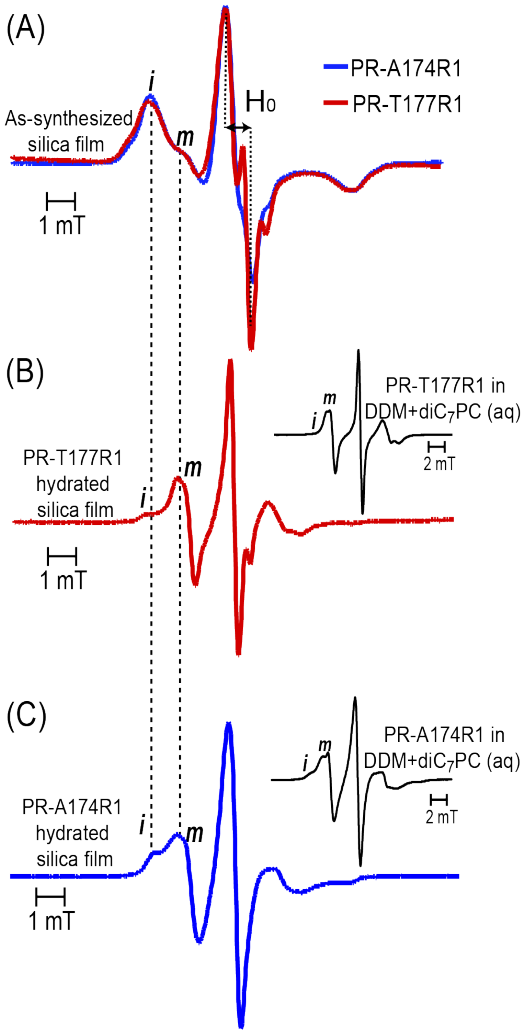

Figure 5. Continuous-wave EPR spectra of powders of DDM+diC$_7$PC-directed mesostructured silica films containing 5 wt% proteorhodopsin with nitroxide spin-labels at residues A174R1 or T177R1: **(A)** overlain spectra acquired from as-synthesized films, (B,C) spectra of the same mesostructured silica films containing either **(B)** PR-T177R1 or **(C)** PR-A174R1 hydrated in alkaline-buffer (50 mM potassium phosphate, with 150 mM KCl, pH 9). The insets of (B) and (C) show the EPR spectra of the corresponding spin-labeled proteorhodopsin in alkaline-buffered DDM+diC$_7$PC micellar solutions under the same pH and buffer conditions.

only slightly lower than PR in micellar solutions, suggesting that the proteorhodopsin guests maintain their predominant functional form.

The different sensitivities of the spin-labelled A174R1 and T177R1 sidechain residues to hydration level yield structural information about the E-F loop of proteorhodopsin guests in

the DDM+diC$_7$PC-directed mesostructured silica films. For PR with native folding, the amphiphilic E-F loop has an α-helical structure that is oriented along the cytoplasmic protein surface, with one side nearer to the protein-bilayer and the other more exposed to solvent;[60,77] as a consequence, E-F loop residues closer to the bilayer, such as A174, show lower mobilities compared to residues farther from the bilayer, such as the solvent-exposed T177.[60] Upon hydrating as-synthesized PR-containing DDM+diC$_7$PC-directed mesostructured silica films, the spectral linewidths (H_0, Figure 5B,C) decrease by factors of 2.1 and 3.4 for films containing PR-A174R1 and PR-T177R1, respectively, indicating that the T177R1 residue is more solvent-exposed than the A174R1 residue. This trend is consistent with the relatively greater solvent exposure for the T177R1 residue, versus the A174R1 residue, of PR molecules in native-like micellar solutions,[43] suggesting that the E-F loop of PR in hydrated mesostructured silica hosts retains its native-like fold.

Photo-activated responses of proteorhodopsin in silica mesochannels. The light-activated transient absorbance behaviors of proteorhodopsin species in mesostructured silica relate to and provide information about the H^+-pumping functionalities of these biomolecular guests. After excitation by green light, PR molecules in native environments undergo a photochemical reaction cycle that involves several changes in isomerization, protein conformation, and the protonation states of various residues that result in the net transport H^+ ions across the transmembrane region of PR.[78] As some of these changes yield different chemical and physical environments for the retinal chromophore, several intermediates in the reaction cycle have characteristic optical absorbance signatures.[32,79] For example, PR in the important "*M*" intermediate state, in which the Schiff base linkage of the retinal chromophore is deprotonated, absorbs maximally at 405 nm,[80] manifesting a significant blue-shift from the ~520 nm

absorbance maximum of PR prior to light activation, referred to as the "*PR*" state. Additional photocycle intermediates include the "*K*" and "*N*" intermediates, which have characteristic absorbances that are red-shifted compared to the *PR* state.[69,80] As a result, after activation by green light, the transient absorbance responses of PR-containing mesostructured silica can provide insights into the photochemical reaction cycle, and thus the H^+-ion pumping function, of PR guest species.

Light-triggered transient absorption analyses were conducted on PR-containing DDM+diC_7PC-directed mesostructured silica and compared with the light-activated absorbance responses of PR in DDM+diC_7PC micellar solutions, as well as in *E. coli* membranes. In this study, measurements were conducted using PR with the "proton donor" glutamate (E108) residue substituted to glutamine (Q), which prolongs the *M* photo-intermediate lifetime to seconds, compared to milliseconds in wild-type PR,[79] and enables the transient absorbance responses of PR to be observed by using conventional laser and optical spectroscopy analyses. In particular, key information about intermediates in the photochemical reaction cycle of proteorhodopsin species in the synthetic mesostructured silica films can be obtained from optical-absorbance difference spectra.[80] Such spectra are obtained by subtracting an absorbance spectrum collected for a sample 130 ms after activation by a 500 ms green laser pulse (~5 mW) from a spectrum acquired immediately prior to illumination; the intensities in such difference spectra manifest absorption changes that are associated with photo-activation. For example, the difference spectra in Figure 6A of 5 wt% PR-E108Q in both the mesostructured DDM+diC_7PC-silica films hydrated in alkaline buffers and alkaline-buffered DDM+diC_7PC micellar solutions show negative intensities at wavelengths near 520 nm, where the *PR* state absorbs, and positive intensities near wavelengths of 410 nm, where

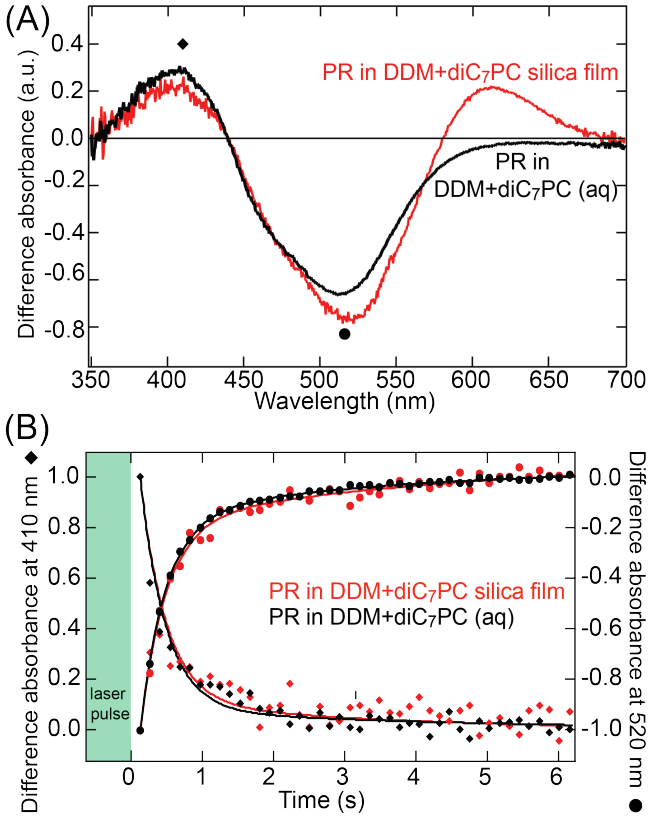

Figure 6. (A) Optical-absorbance difference spectra of the proteorhodopsin mutant PR-E108Q (also with the nitroxide R1 at residue A174C) in a DDM+diC$_7$PC-directed mesostructured silica film hydrated in alkaline buffer (red) and in an alkaline-buffered DDM+diC$_7$PC micellar solution (black). Each spectrum was obtained from the difference of spectra acquired from the PR-E108Q sample before and 130 ms after illumination with a 500 ms green (532 nm) laser pulse at ~5 mW. **(B)** Transient absorbances at 410 nm (diamonds) and 520 nm (circles) from PR-E108Q in the hydrated DDM+diC$_7$PC-directed mesostructured silica film (red circles and diamonds) and in alkaline-buffered DDM+diC$_7$PC solution (black circles and diamonds), following a green laser pulse. The solid red and black lines in (B) are biexponential fits of the transient absorption data. The alkaline buffer was composed of 50 mM potassium phosphate and 150 mM KCl at pH 9.

the *M* intermediate absorbs. These spectral features are consistent with a depleted population of PR species in *PR* state, accompanied by an increased population of PR molecules in the *M* intermediate state at 130 ms after the green laser pulse. However, the spectrum (Figure 6A, red) of PR-E108Q in the hydrated mesostructured DDM+diC$_7$PC-silica film shows positive intensity at approximately 620 nm, where the red-shifted *K* or *N* intermediates absorb, while no such intensities are observed for PR-E108Q in alkaline-buffered DDM+diC$_7$PC micellar

solutions (Figure 6A, black) in this wavelength region. These different transient absorbance behaviors reflect the different rates of accumulation and decay of the *K* and/or *N* intermediates[80] of PR in DDM+diC$_7$PC-mesostructured silica, compared to the micellar solution, possibly due to the somewhat lower extent of hydration and/or more acidic local environments of PR guests in the mesostructured silica. Collectively, the transient optical absorbance analyses provide evidence, after illumination, of transient PR photo-intermediates in hydrated mesostructured silica hosts that are associated with light-activated H^+-pumping activity.

The photocycle kinetics of proteorhodopsin guests in synthetic mesostructured silica hosts also show similarities to monomeric proteorhodopsin in micellar solutions. Importantly, the timescales of the photo-intermediates determine the H^+-pumping rate of PR, with shorter timescales yielding higher proton-pumping rates that would be desirable for photo-electrochemical energy conversion applications. Here, the apparent interconversion kinetics of the *M* intermediate and *PR* states are estimated from the transient absorbances at wavelengths of 520 nm and 410 nm, respectively, at times 130 ms after green-laser excitation. As shown in Figure 6B, after illumination, the transient optical absorbance spectra of PR-E108Q in a DDM+diC$_7$PC-directed mesostructured silica film hydrated with alkaline buffer and monomeric PR-E108Q in an alkaline-buffered DDM+diC$_7$PC micellar solution both show transient decreases in intensities at 410 nm and concomitant increases in intensities at 520 nm. These results indicate a transient decrease in the population of PR in the *M* intermediate state and corresponding accumulation of the *PR* state, the interconversion timescales of which can be estimated by mathematical fitting of transient absorbance spectra. The *M* photo-intermediate states of PR and bacteriorhodopsin are commonly observed to decay bi-

exponentially, with the two timescales arising from separate *M* intermediates, M_1 and M_2, that exhibit similar absorbances, but are thought to have distinct conformations with different proton accessibilities at the cytoplasmic interfaces of cell membranes.[80,81] Bi-exponential fits to the 410 nm absorbances shown in Figure 6B yield decay timescales for the respective M_1 and M_2 intermediates of 0.36 ± 0.01 s and 3.2 ± 0.2 s for PR in the hydrated mesostructured DDM+diC_7PC surfactant-silica film and 0.36 ± 0.03 s and 4.3 ± 0.7 s for PR in the alkaline-buffered DDM+diC_7PC micellar solution. The similar timescales of these transient absorbance behaviors imply similar H^+-ion transport rates for PR molecules in the mesostructured silica films and in native-like micellar solutions. Furthermore, as prior studies showed that the *M* intermediate decay rate is significantly different for monomeric and oligomeric PR species, with a 5x faster decay for PR monomers, the similar absorbance behaviors strongly suggest that predominantly monomeric PR species are incorporated in the mesostructured silica films.[10] The close correlation of the photo-cycle kinetics of PR in mesostructured silica films and in native-like micellar solutions thus indicate that PR guest molecules in mesostructured films are functionally active and perform comparably to PR in near-native environments.

EPR lineshape analyses can provide additional and complementary information regarding the nature of the conformational changes far from the retinal chromophore that proteorhodopsin undergoes in mesostructured silica hosts upon light-activation. To mediate the light-activated H^+-transport mechanism, PR molecules have been suggested to undergo a number of large-scale conformational changes that involve movements and torsions of secondary structural elements,[78] including the α-helical E-F loop that exhibit characteristic rigid-body movements associated with the *M* intermediate state decay.[60] Insights into these E-F loop motions can be obtained by monitoring the EPR lineshapes of spin-labeled A174R1

residues of the E-F loop, which change significantly after photo-activation, due to the distinctively hindered dynamics of this residue caused by interactions with nearby residues at the cytoplasmic interface.[60] For example, the EPR spectrum of PR-A174R1 in a hydrated DDM+diC_7PC-directed mesostructured silica film under constant illumination by green light (Figure 7A, green traces) exhibits increased intensity associated with the relatively immobile "*i*" component and decreased intensity from the more mobile "*m*" component, compared to spectra acquired without light-activation (Figure 7A, black traces, also shown in Figure 5C). These results indicate that the A174R1 residues, as part of the E-F loop of PR guests in mesostructured silica, are on average more confined during light-activation, consistent with the twisting and partial immobilization of the α-helical E-F loop of proteorhodopsin in response to light, as reported in previous studies of PR molecules incorporated in lipid bilayers.[60]

Kinetic information about the E-F loop movements of proteorhodopsin can be obtained by transiently monitoring the EPR amplitudes of the relatively immobile "*i*" spectral component during and after light-activation. As shown in Figure 7B (black trace), for PR-A174R1-E108Q in a DDM+diC_7PC-directed mesostructured silica film the amplitude of the immobile EPR component increases during illumination by the green laser and subsequently decays after the laser is turned off. Similar transient EPR changes are observed for PR-A174R1-E108Q in an alkaline-buffered DDM+diC_7PC micellar solution (Figure 7B, gray trace). However, the decay of the immobile EPR component of PR-A174R1 after the laser pulse is faster for PR in the DDM+diC_7PC-directed mesostructured silica, reflecting faster E-F loop motions than in micellar solution. The faster E-F loop movements of PR molecules in the synthetic silica host may originate from confinement or interactions of PR molecules in the

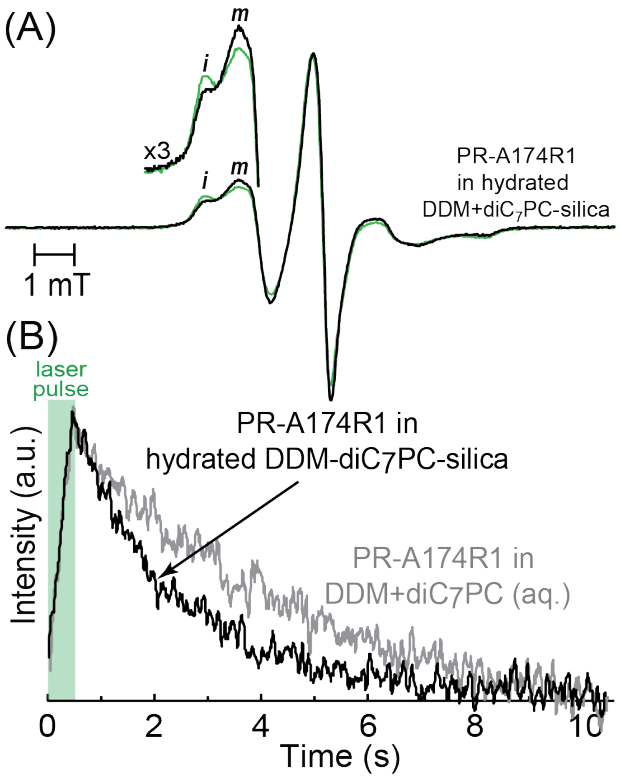

Figure 7. (A) Continuous-wave EPR spectrum acquired from powders of a DDM+diC$_7$PC-directed mesostructured silica film with 5 wt% PR-A174 hydrated with an alkaline (pH 9) buffered solution (50 mM potassium phosphate, 150 mM KCl) under continuous green laser illumination (green trace) and without illumination (black trace, also in Figure 5C). The inset in (A) shows is a zoomed in view of the spectral region with the immobile ("*i*") and mobile ("*m*") spectral components. **(B)** Transient EPR amplitudes at the frequency corresponding to the relatively immobile (*i*) component of the EPR spectra of PR-A174R1 in hydrated DDM+diC$_7$PC-directed mesostructured silica films (grey line) and in the alkaline-buffered (pH 9) DDM+diC$_7$PC micellar solution (black line), directly following illumination of these samples with a green laser (~5 mW) pulse for 500 ms.

mesochannel environments that make the non-activated PR state energetically more favorable than those of the photo-cycle intermediates. Such effects on the spin-labels of residue A174 of light-activated PR in the mesostructured silica hosts are consistent with those of non-illuminated PR guests discussed above (Figure 5). Given the native-like transient absorbances of PR in hydrated DDM+diC$_7$PC-directed mesostructured silica (Figure 6B), these data suggest that the large-scale E-F loop motions of light-activated PR guests are more sensitive to confinement in the mesochannel environment than changes that occur near the retinal

chromophore. The detailed time-resolved EPR spectroscopy results show that site-specifically-labeled PR molecules in synthetic mesostructured silica host materials undergo large-scale native-like conformational changes associated with the light-induced H^+-transport properties of PR, the kinetics of which may be enhanced by confinement.

Incorporation of rhodopsin proteins for broader solar absorption

The synthetic protocol for DDM+diC_7PC-directed mesostructured materials can be applied to incorporate other functionally active transmembrane proteins. The transmembrane protein rhodopsin of *Gloeobacter Violaceus* (GR) exhibits similar light-activated H^+-ion pumping function and absorbance properties compared to proteorhodopsin. However, by using directed evolution techniques can introduce mutations nearby the retinal chromophore that modify the absorption properties of GR, enabling these species exploit different wavelengths of light to pump H^+-ions.[22] Mesostructured silica membranes include such GR variants could convert different and complementary ranges of the solar spectrum compare to those with proteorhodopsin. Using the same synthesis protocol as used for PR, two different rhodopsin variants, GR/T125N and GR/G162L, were incorporated at 1 wt% loadings into mesostructured silica, as shown in Figure 8A. The transmission UV-visible absorbance spectra of these films (Figure 8A) exhibit absorption maxima at 515 nm or 567 nm for mesostructured silica films containing GR/T125N or GR/G162L, respectively, that are distinct from the 540 nm absorbance maxima of films of otherwise identical composition but with 1 wt% PR These absorbance characteristics compare well with those of these species in micellar DDM solutions, indicating the retained native-like structures of three incorporated protein guests.

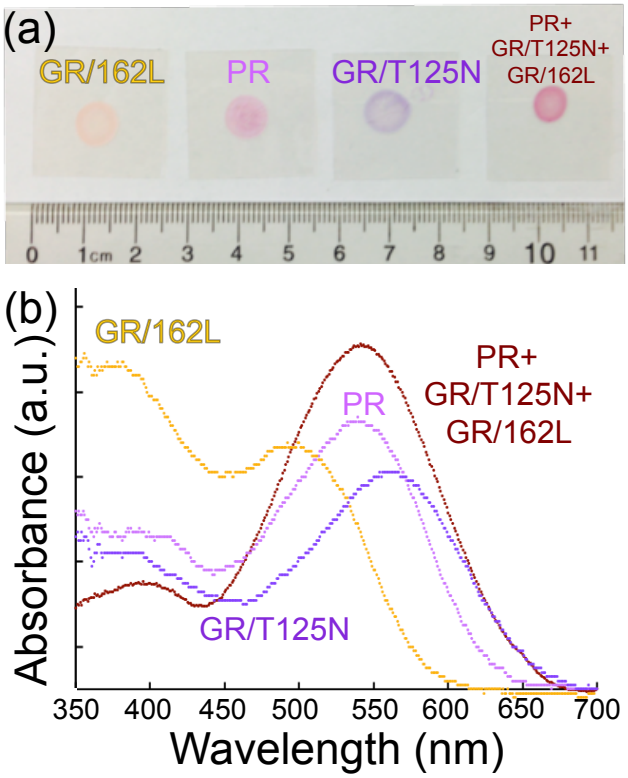

Figure 8. (A) Images of 50-μm thick DDM-diC_7PC-directed mesostructured silica films containing 1 wt% of either proteorhodopsin or different rhodopsin variants: (left-to-right) GR/G162L (orange), wild type PR (pink), GR/T125N (purple), and a mixture of all three proteins (dark red). Their different colors and **(B)** transmission UV-visible absorbance spectra reveal their distinct light-absorption properties.

Moreover, all three membrane proteins can be incorporated into a single mesostructured silica film, shown in Figure 8A, which shows a broader absorbance (Figure 8B) than any of the films with only one protein. The ability to incorporate several different PR and GR species individually and in mixtures into mesostructured silica hosts enables broader fractions of the solar spectrum to be converted by these mesostructured silica materials. Additionally, it indicates a generality of DDM+diC_7PC-directed mesostructured silica materials to incorporate different transmembrane proteins.

Incorporation of cytochrome c in mesostructured silica hosts. The synthetic protocol presented here can be adapted to incorporate other functionally active membrane proteins within synthetic mesostructured silica hosts. To demonstrate this, we adjusted the synthesis

protocol to incorporate the more hydrophilic protein cytochrome c, an iron-containing biomacromolecule (~12 kDa) associated with the mitochondria in cells. In contrast to proteorhodopsin, which is a transmembrane protein that spans the lipid bilayer, cytochrome c is a peripheral membrane protein that is water soluble and, thus, is not found within lipid bilayers, but rather associates with integral membrane proteins at lipid bilayer surfaces.[82] Cytochrome c molecules were incorporated into surfactant-directed mesostructured silica host materials by using the cationic surfactant tetradecyltrimethylammonium chloride (TTACl). The SAXS pattern in Figure 9A of a TTACl-directed mesostructured silica film without cytochrome c shows two reflections at 2.3° (0.15° fwhm) and 3.9° that are indexable to the *(100)* and *(110)* reflections, respectively, of a well-ordered hexagonal mesostructured material with a lattice parameter of 4.6 nm. By comparison, the SAXS pattern for an otherwise identical TTACl-directed silica film containing 8 wt% cytochrome c exhibits a single broad reflection at 2.1° (0.5° fwhm) that corresponds to a *d*-spacing of 4.2 nm, a 0.3 nm increase with respect to the *(100) d*-spacing (3.9 nm) of materials without cytochrome c. As cytochrome c molecules are approximately spherical in shape with a diameter of 3 nm, the observed 0.3 nm increase in the characteristic ordering length scale is consistent with the expansion of the mesostructured silica framework upon incorporation of cytochrome c guests. In addition, the *(100)* reflection is substantially broader for the mesostructured silica containing 8 wt% cytochrome c, reflecting less mesostructural order, compared to the material without protein. The amphiphilic globular cytochrome c molecules likely reside near the mesochannel surfaces of the relatively hydrophilic silica framework and trimethylammonium moieties of the TTACl-directed mesostructured host, as depicted schematically in the inset of Figure 9A. These results are similar to those for proteorhodopsin guest species in DDM+diC_7PC-directed mesostructured

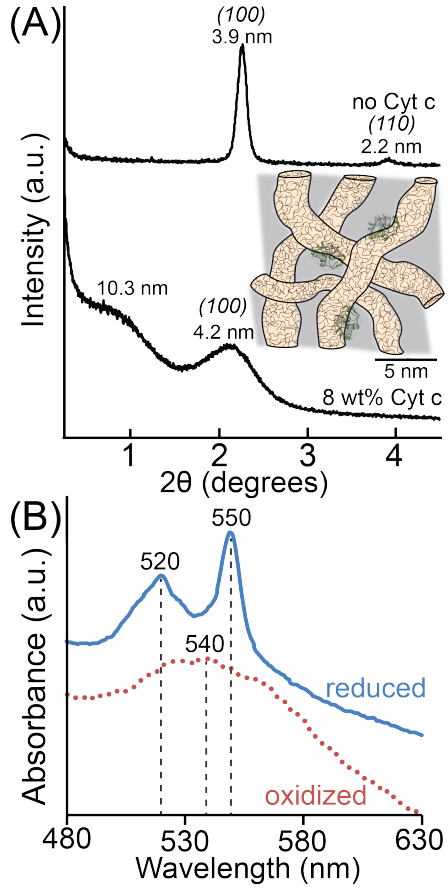

Figure 9. (A) Small-angle X-ray scattering patterns for a TTACl-directed silica film without (top) and with (bottom) 8 wt% cytochrome c that shows one reflection assigned to the *(100)* reflection of a worm-like mesostructure with a *d*-spacing of 4.2 nm. **(B)** Visible absorbance spectra collected from the same cytochrome-c-containing mesostructured silica film soaked in a tris-acetate buffer solution at neutral pH before (dotted red) and 10 min after (solid blue) the addition of 30 mM ammonium iron(II) sulfate.

silica, in which increased extents of membrane protein incorporation are associated with larger *d*-spacings and reduced mesostructural order. Interestingly, the TTACl-directed mesostructured silica with 8 wt% cytochrome c shows an additional broad reflection at 0.85°, which corresponds to a *d*-spacing of 10.3 nm that is significantly larger than the 4.2 nm *d*-spacing of the assigned *(100)* reflection. This low-angle reflection may originate from the incorporation of cytochrome c oligomers, which have been reported to readily form in the

presence of ethanol,[83] which is produced by hydrolysis of TEOS precursor species during co-assembly of TTACl-directed mesostructured silica.

The activities of cytochrome c guests in the mesostructured silica hosts were assessed by using optical absorbance spectroscopy, which is sensitive to the oxidation states of the iron centers of cytochrome c molecules. Cytochrome c oxidase species are capable of undergoing oxidation or reduction as part of the electron transport processes in mitochondria.[84] The oxidized and reduced states of cytochrome c in aqueous solutions notably manifest distinct optical absorbance signatures, with the reduced state exhibiting absorption maxima at ca. 520 and 550 nm and the oxidized state at ca. 532 nm.[85,86] Accordingly, the optical absorbance spectrum in Figure 9B of a TTACl-directed silica film exposed to a buffered solution at neutral pH (Figure 9B, dotted red) shows broad absorbance maximum at ca. 540, characteristic of the oxidized state of cytochrome c. By comparison, after soaking the film in the same buffer, but containing 30 mM ammonium iron(II) sulfate (aq), the broad absorbance near 540 nm disappears and new narrower absorbances are observed at ca. 520 and 550 nm (Figure 8B, blue), characteristic of the reduced state of cytochrome c. These results demonstrate that cytochrome c molecules in TTACl-directed mesostructured silica films are accessible to diffusing species within the host channels, adopt native-like oxidation and reduction states, and retain their functional activities.

Conclusions

The judicious selection of material compositions and processing conditions enabled high concentrations (up to 15 wt%) of the light-activated membrane protein proteorhodopsin (PR) to be incorporated in functionally active forms in mesostructured surfactant-silica host materials. Mixtures of DDM surfactants with either diC_7PC zwitterionic lipids or P123 triblock

copolymers were shown to serve jointly to both stabilize the hydrophobic PR molecules in aqueous solutions and to direct their assembly and that of network-forming silica species into mesostructured silica composites. The solution processing conditions enabled PR-containing mesostructured silica materials to be prepared as transparent, colored, free-standing, mechanically stable films or monoliths of up to 1 mm thickness and arbitrary lateral macroscopic dimensions. Proteorhodopsin in DDM+diC_7PC-silica mesostructured silica materials were shown to exhibit comparable optical absorbance properties as native-like PR, but with significantly enhanced thermal stabilities compared to photo-active PR in native-like phospholipid bilayers of *E. coli* or P123-directed silica hosts. Small-angle X-ray scattering and 2D EPR HYSCORE spectroscopy results showed that hydrophobic PR guest molecules were distributed within the hydrophobic surfactant mesochannels, as opposed to the hydrophilic silica framework. The dynamics of the functionally important E-F loop of the PR guests in DDM+diC_7PC-directed silica materials depended on the extent of hydration and confinement within the mesochannel environments, with fully hydrated materials supporting E-F loop dynamics similar to those in native-like DDM+diC_7PC micellar solutions. The transient photo-responses of PR guest molecules in the hydrated mesostructured silica host materials were demonstrated to be similar to those associated with light-activated H^+-ion transport by PR in near-native environments under alkaline conditions. The synthetic protocol enabled mixtures of rhodopsin and proteorhodopsin transmembrane proteins to be incorporated into mesostructured silica membranes, which exhibited distinct optical absorbances versus materials that included only proteorhodopsin. Adaptation of synthesis compositions and conditions (e.g., structure-directing surfactant type) enabled high (8 wt%) concentrations of the relatively hydrophilic membrane protein cytochrome c oxidase to be incorporated into

hexagonally ordered mesostructured silica materials, while maintaining native-like oxidation and reduction activities. The generality of this synthetic approach is expected to open new opportunities for developing materials that exploit the high-selectivities and diverse functions of membrane proteins for applications in separations, sensors, catalysis, regulated delivery, and ion transport, including by photo-activation.

References

(1) Engqvist, M. K. M.; McIsaac, R. S.; Dollinger, P.; Flytzanis, N. C.; Abrams, M.; Schor, S.; Arnold, F. H. *J. Mol. Biol.* **2015**, *427*, 205.

(2) Kan, S. B. J.; Lewis, R. D.; Chen, K.; Arnold, F. H. *Science* **2016**, *522*, 1048.

(3) Swift, B. J.; Shadish, J. A.; DeForest, C. A.; Baneyx, F. *J. Am. Chem. Soc.* **2017**, *139*, 1958.

(4) Shieh, F.-K.; Wang, S.-C.; Yen, C.-I.; Wu, C.-C.; Dutta, S.; Chou, L.-Y.; Morabito, J. V.; Hu, P.; Hsu, M.-H.; Wu, K. C.-W.; Tsung, C.-K. *J. Am. Chem. Soc.* **2015**, *137*, 4276.

(5) Hudson, S.; Cooney, J.; Magner, E. *Angew. Chemie Int. Ed.* **2008**, *47*, 8582.

(6) Wang, M.; Wang, Z.; Wang, X.; Wang, S.; Ding, W.; Gao, C. *Environ. Sci. Technol.* **2015**, *49*, 3761.

(7) Fane, A. G.; Wang, R.; Hu, M. X. *Angew. Chemie Int. Ed.* **2015**, *54*, 3368.

(8) Ispas, C.; Sokolov, I.; Andreescu, S. *Anal. Bioanal. Chem.* **2009**, *393*, 543.

(9) Oda, I.; Hirata, K.; Watanabe, S.; Shibata, Y.; Kajino, T.; Fukushima, Y.; Iwai, S.; Itoh, S. *J. Phys. Chem. B* **2006**, *110*, 1114.

(10) Hussain, S.; Kinnebrew, M.; Schonenbach, N. S.; Aye, E.; Han, S. *J. Mol. Biol.* **2015**, *427*, 1278.

(11) Maciejko, J.; Mehler, M.; Kaur, J.; Lieblein, T.; Morgner, N.; Ouari, O.; Tordo, P.; Becker-Baldus, J.; Glaubitz, C. *J. Am. Chem. Soc.* **2015**, *137*, 9032.

(12) Edwards, D. T.; Huber, T.; Hussain, S.; Stone, K.; Kinnebrew, M.; Kaminker, I.; Matalon, E.; Sherwin, M. S.; Goldfarb, D.; Han, S. *Biophys. J.* **2013**, *104* (2), 406a.

(13) Yoshizawa, S.; Kumagai, Y.; Kim, H.; Ogura, Y.; Hayashi, T.; Iwasaki, W.; Delong, E. F.; Kogure, K. *Proc. Natl. Acad. Sci.* **2014**, *111*, 6732.

(14) Béjà, O.; Aravind, L.; Eugene, V.; Suzuki, M. T.; Hadd, A.; Nguyen, L. P.; Jovanovich, S. B.; Gates, C. M.; Feldman, R. A.; Spudich, J. L.; Spudich, E. N.; DeLong, E. F. *Science* **2000**, *289*, 1902.

(15) DeLong, E. F.; Béjà, O. *PLoS Biol.* **2010**, *8*, e1000359.

(16) DeLong, E. F. *Nat. Rev. Microbiol.* **2005**, *3*, 459.

(17) de la Torre, J. R.; Christianson, L. M.; Béjà, O.; Suzuki, M. T.; Karl, D. M.; Heidelberg, J.; DeLong, E. F. *Proc. Natl. Acad. Sci. U. S. A.* **2003**, *100*, 12830.

(18) Sabehi, G.; Massana, R.; Bielawski, J. P.; Rosenberg, M.; DeLong, E. F.; Beja, O. *Environ. Microbiol.* **2003**, *5*, 842.

(19) Béjà, O.; Spudich, E. N.; Spudich, J. L.; Leclerc, M.; DeLong, E. F. *Nature* **2001**, *411*, 786.

(20) Moran, M. A.; Miller, W. L. *Nat. Rev. Microbiol.* **2007**, *5*, 792.

(21) Jensen, R. B.; Kelemen, B. R.; McAuliffe, J. C.; Smith, W. C. Method for preparing solid materials comprising immobilized proteorhodopsin U.S. Patent 7,745,066.

(22) Luo, T.-J. M.; Soong, R.; Lan, E.; Dunn, B.; Montemagno, C. *Nat. Mater.* **2005**, *4*, 220.

(23) Bräuchle, C.; Hampp, N.; Oesterhelt, D. *Adv. Mater.* **1991**, *3*, 420.

(24) Chen, Z.; Birge, R. R. *Trends Biotechnol.* **1993**, *11*, 292.

(25) Bertoncello, P.; Nicolini, D.; Paternolli, C.; Bavastrello, V.; Nicolini, C. *IEEE Trans. Nanobioscience* **2003**, *2*, 124.

(26) Hampp, N. *Chem. Rev.* **2000**, *100*, 1755.

(27) Andreas, L. B.; Le Marchand, T.; Jaudzems, K.; Pintacuda, G. *J. Magn. Reson.* **2015**, *253*, 36.

(28) Andreas, L. B.; Jaudzems, K.; Stanek, J.; Lalli, D.; Bertarello, A.; Le Marchand, T.; Cala-De Paepe, D.; Kotelovica, S.; Akopjana, I.; Knott, B.; Wegner, S.; Engelke, F.; Lesage, A.; Emsley, L.; Tars, K.; Herrmann, T.; Pintacuda, G. *Proc. Natl. Acad. Sci. U. S. A.* **2016**, *113*, 9187.

(29) Becker-baldus, J.; Bamann, C.; Saxena, K.; Gustmann, H.; Brown, L. J. *Proc. Natl. Acad. Sci. U. S. A.* **2015**, *112*, 9896.

(30) Good, D. B.; Wang, S.; Ward, M. E.; Struppe, J.; Brown, L. S.; Lewandowski, J. R.; Ladizhansky, V. *J. Am. Chem. Soc.* **2014**, *136*, 2833.

(31) Lenz, M. O.; Huber, R.; Schmidt, B.; Gilch, P.; Kalmbach, R.; Engelhard, M.; Wachtveitl, J. *Biophys. J.* **2006**, *91*, 255.

(32) Friedrich, T.; Geibel, S.; Kalmbach, R.; Chizhov, I.; Ataka, K.; Heberle, J.; Engelhard, M.; Bamberg, E. *J. Mol. Biol.* **2002**, *321*, 821.

(33) Shi, L.; Lake, E. M. R.; Ahmed, M. A. M.; Brown, L. S.; Ladizhansky, V. *Biochim. Biophys. Acta* **2009**, *1788*, 2563.

(34) Yang, J.; Aslimovska, L.; Glaubitz, C. *J. Am. Chem. Soc.* **2011**, *133*, 4874.

(35) Ranaghan, M. J.; Schwall, C. T.; Alder, N. N.; Birge, R. R. *J. Am. Chem. Soc.* **2011**, *133*, 18318.

(36) Scharnagl, C.; Reif, M.; Friedrich, J. *Biochim. Biophys. Acta* **2005**, *1749*, 187.

(37) Jeon, T.-J.; Malmstadt, N.; Schmidt, J. J. *J. Am. Chem. Soc.* **2006**, *128*, 42.

(38) Hua, D.; Kuang, L.; Liang, H. *J. Am. Chem. Soc.* **2011**, *133*, 2354.

(39) Ma, D.; Zhao, Y.; Wu, J.; Cui, T.; Ding, J. *Soft Matter* **2009**, *5*, 4635.

(40) Yang, Y. J.; Holmberg, A. L.; Olsen, B. D. *Annu. Rev. Chem. Biomol. Eng.* **2017**, *8*, 549.

(41) Ellerby, L. M.; Nishida, C. R.; Nishida, F.; Yamanaka, S. A.; Dunn, B.; Valentine, J. S.; Zink, J. I. *Science* **1992**, *255*, 1113.

(42) Wu, S.; Ellerby, L. M.; Cohan, J. S.; Dunn, B.; El-Sayed, M. A.; Valentine, J. S.; Zink, J. I. *Chem. Mater.* **1993**, *5*, 115.

(43) Liang, H.; Whited, G.; Nguyen, C.; Stucky, G. D. *Proc. Natl. Acad. Sci. U. S. A.* **2007**, *104*, 8212.

(44) Liang, H.; Whited, G.; Nguyen, C.; Okerlund, A.; Stucky, G. D. *Nano Lett.* **2008**, *8*, 333.

(45) Janshoff, A.; Steinem, C. *Anal. Bioanal. Chem.* **2006**, *385*, 433.

(46) Athens, G. L.; Shayib, R. M.; Chmelka, B. F. *Curr. Opin. Colloid Interface Sci.* **2009**, *14*, 281.

(47) Yiu, H. H. P.; Wright, P. A. *J. Mater. Chem.* **2005**, *15*, 3690.

(48) Washmon-Kriel, L.; Jimenez, V. L.; Balkus Jr., K. J. *J. Mol. Catal. B Enzym.* **2000**, *10*, 453.

(49) Lei, J.; Fan, J.; Yu, C.; Zhang, L.; Jiang, S.; Tu, B.; Zhao, D. *Microporous mesoporous Mater.* **2004**, *73*, 121.

(50) Renault, C.; Balland, V.; Martinez-ferrero, E.; Nicole, L.; Sanchez, C.; Limoges, B. *Chem. Commun.* **2009**, No. 48, 7494.

(51) Wei, J.; Ren, Y.; Luo, W.; Sun, Z.; Cheng, X.; Li, Y.; Deng, Y.; Elzatahry, A. A.; Al-Dahyan, D.; Zhao, D. *Chem. Mater.* **2017**, *29*, 2211.

(52) Kirmayer, S.; Dovgolevsky, E.; Kalina, M.; Lakin, E.; Cadars, S.; Epping, J. D.; Fernández-Arteaga, A.; Rodríguez-Abreu, C.; Chmelka, B. F.; Frey, G. L. *Chem. Mater.* **2008**, *20*, 3745.

(53) Neyshtadt, S.; Jahnke, J. P.; Messinger, R. J.; Rawal, A.; Peretz, T. S.; Huppert, D.; Chmelka, B. F.; Frey, G. L. *J. Am. Chem. Soc.* **2011**, *133*, 10119.

(54) Corma, A. *Chem. Rev.* **1997**, *97*, 2373.

(55) Granja, L. P.; Martínez, E. D.; Troiani, H.; Sanchez, C.; Soler Illia, G. J. A. A. *ACS Appl. Mater. Interfaces* **2017**, *9*, 965.

(56) He, J.; Song, Z.; Ma, H.; Yang, L.; Guo, C. *J. Mater. Chem.* **2006**, *16*, 4307.

(57) Itoh, T.; Ishii, R.; Matsuura, S.; Mizuguchi, J.; Hamakawa, S.; Hanaoka, T.; Tsunoda, T.; Mizukami, F. *Colloids Surf., B* **2010**, *75*, 478.

(58) Oda, I.; Iwaki, M.; Fujita, D.; Tsutsui, Y.; Ishizaka, S.; Dewa, M.; Nango, M.; Kajino, T.; Fukushima, Y.; Itoh, S. *Langmuir* **2010**, *26*, 13399.

(59) Noji, T.; Kamidaki, C.; Kawakami, K.; Shen, J.-R.; Kajino, T.; Fukushima, Y.; Sekitoh, T.; Itoh, S. *Langmuir* **2011**, *27*, 705.

(60) Hussain, S.; Franck, J. M.; Han, S. *Angew. Chemie Int. Ed.* **2013**, *52*, 1953.

(61) Stone, K. M.; Voska, J.; Kinnebrew, M.; Pavlova, A.; Junk, M. J. N.; Han, S. *Biophys. J.* **2013**, *104*, 472.

(62) Berliner, L. J.; Grunwald, J.; Hankovszky, H. O.; Hideg, K. *Anal. Biochem.* **1982**, *119*, 450.

(63) Altenbach, C.; Flitsch, S. L.; Khorana, H. G.; Hubbell, W. L. *Biochemistry* **1989**, *28*,

7806.

(64) Höfer, P.; Grupp, A.; Nebenführ, H.; Mehring, M. *Chem. Phys. Lett.* **1986**, *132*, 279.

(65) Schweiger, A. *Angew. Chem. Int. Ed. Engl.* **1991**, *30*, 265.

(66) Yang, Q.; Zhou, Q.; Somasundaran, P. *Colloids Surf., A* **2007**, *305*, 22.

(67) Štangar, U. L.; Hüsing, N. *Silicon Chem.* **2003**, *2*, 157.

(68) Reckel, S.; Gottstein, D.; Stehle, J.; Löhr, F.; Verhoefen, M.; Takeda, M.; Silvers, R.; Kainosho, M.; Glaubitz, C.; Wachtveitl, J.; Bernhard, F.; Schwalbe, H.; Güntert, P.; Dötsch, V. *Angew. Chemie Int. Ed.* **2011**, *50*, 11942.

(69) Lakatos, M.; Lanyi, J. K.; Szakács, J.; Váró, G. *Biophys. J.* **2003**, *84*, 3252.

(70) Zhao, D.; Feng, J.; Huo, Q.; Melosh, N.; Frederickson, G. H.; Chmelka, B. F.; Stucky, G. D. *Science* **1998**, *279*, 548.

(71) Sun, H.; Nathans, J. *J. Biol. Chem.* **2001**, *276*, 11766.

(72) Herz, J.; Verhoefen, M. K.; Weber, I.; Bamann, C.; Glaubitz, C.; Wachtveitl, J. *Biochemistry* **2012**, *51*, 5589.

(73) Druckmann, S.; Ottolenghi, M. *Biophys J* **1981**, *33*, 263.

(74) Columbus, L.; Hubbell, W. L. *Trends Biochem. Sci.* **2002**, *27*, 288.

(75) Ježek, P.; Bauer, M.; Trommer, W. E. *FEBS Lett.* **1995**, *361*, 303.

(76) Butterfield, D. A.; Markesbery, W. R. *Neurosci. Lett.* **1983**, *35*, 221.

(77) Shi, L.; Ahmed, M. A. M.; Zhang, W.; Whited, G.; Brown, L. S.; Ladizhansky, V. *J. Mol. Biol.* **2009**, *386*, 1078.

(78) Andersson, M.; Malmerberg, E.; Westenhoff, S.; Katona, G.; Cammarata, M.; Wöhri, A. B.; Johansson, L. C.; Ewald, F.; Eklund, M.; Wulff, M.; Davidsson, J.; Neutze, R. *Structure* **2009**, *17*, 1265.

(79) Dioumaev, A. K.; Brown, L. S.; Shih, J.; Spudich, E. N.; Spudich, J. L.; Lanyi, J. K. *Biochemistry* **2002**, *41*, 5348.

(80) Váró, G.; Brown, L. S.; Lakatos, M.; Lanyi, J. K. *Biophys. J.* **2003**, *84*, 1202.

(81) Váró, G.; Lanyi, J. K. *Biochemistry* **1991**, *30*, 5016.

(82) Singer, S. J. *Annu. Rev. Biochem.* **1974**, *43*, 805.

(83) Hirota, S.; Hattori, Y.; Nagao, S.; Taketa, M.; Komori, H.; Kamikubo, H.; Wang, Z.; Takahashi, I.; Negi, S.; Sugiura, Y.; Kataoka, M.; Higuchi, Y. *Proc. Natl. Acad. Sci.* **2010**, *107*, 12854.

(84) Hüttemann, M.; Pecina, P.; Rainbolt, M.; Sanderson, T. H.; Valerian, E.; Samavati, L.; Doan, J. W.; Lee, I. *Mitochondrion* **2011**, *11*, 369.

(85) Lambeth, D. O.; Campbell, K. L.; Zand, R.; Palmer, G. *J. Biol. Chem.* **1973**, *248*, 8130.

(86) Kurihara, M.; Sano, S. *J. Biol. Chem.* **1970**, *245*, 4804.

Chapter 2 : Proton-based structural analysis of a heptahelical transmembrane protein in lipid bilayers

This chapter is adapted with permission from Lalli, D.; Idso, M. N.; Andreas, B. L.; Hussain, S.; Baxter, N.; Han, S.; Chmelka, B. F.; Pintacuda, G., Proton-based structural analysis of a heptahelical transmembrane protein in lipid bilayers. *Journal of the American Chemical Society* **2017**, Article ASAP.

Abstract

The structures and properties of membrane proteins in lipid bilayers are expected to closely resemble those in native cell-membrane environments, though have been difficult to elucidate. By performing solid-state NMR measurements at very fast (100 kHz) magic-angle spinning rates and at high (23.5 T) magnetic field, severe sensitivity and resolution challenges are overcome, enabling the atomic-level characterization of membrane proteins in lipid environments. This is demonstrated by extensive ^{1}H-based resonance assignments of the fully protonated heptahelical membrane protein proteorhodopsin, and the efficient identification of numerous ^{1}H-^{1}H dipolar interactions, which provide distance constraints, inter-residue proximities, relative orientations of secondary structural elements, and protein-cofactor interactions in the hydrophobic transmembrane regions. These results establish a general approach for high-resolution structural studies of membrane proteins in lipid environments via solid-state NMR.

Introduction

Atomic level characterization of membrane proteins in lipid bilayers is essential for understanding their functions, though extremely challenging. Membrane proteins in lipid

environments generally lack long-range order, and tumble slowly in solutions, which respectively render scattering investigations infeasible and jeopardize liquid-state NMR investigations. Magic-angle spinning (MAS) solid-state NMR spectroscopy is a powerful tool that can reveal both structural and dynamical details of such systems,[1-13] yet its application has been limited by low spectral sensitivity and resolution, as well as by the difficulty in obtaining large (~20 mg) quantities of isotopically labeled proteins.

Many strategies have been employed to overcome the resolution and sensitivity issues that impede structural characterization of membrane proteins by MAS-NMR. Proton detection is a powerful technique that exploits the high gyromagnetic ratio and abundance of proton nuclei to enhance the spectral sensitivity.[14] However, despite encouraging proof-of-principle studies performed on fully-protonated model systems,[15-18] applications of ^{1}H-detection to membrane proteins in native-like lipid environments have been hindered by the low ^{1}H spectral resolution under moderate MAS rates (<40 kHz). Higher spectral resolution[19-20] can be achieved in part by proton dilution strategies (typically perdeuteration and back-protonation at the exchangeable sites) to quench the ^{1}H-^{1}H dipolar couplings that broaden NMR signals.[21-28] This strategy, however, is problematic during protein expression, due to anemic growth in deuterium oxide which sometimes is even incompatible with protein expression, as for example in mammalian cells. When feasible, it allows reintroduction of ^{1}H species exclusively at sites that are exchangeable and accessible to solvent, which notably do not include the extensive hydrophobic transmembrane regions, thereby precluding their analyses by ^{1}H-detected spectroscopy.[29] Unfolding and refolding membrane proteins leads to the introduction of ^{1}H species at the exchangeable sites of transmembrane regions, however such protocols are not general, and specific examples are rare.[11,24,30-31] To address this in part, isotopic labeling

strategies have been developed in which membrane proteins are expressed in H_2O in the presence of deuterated ^{13}C glucose, such that $^{1}H/^{2}H$ species are homogeneously distributed in both water-accessible and inaccessible regions.[32] Nevertheless, in such cases the $^{1}H/^{2}H$ isotopomeric distributions often result in poorly resolved ^{13}C resonances from side-chain moieties that are crucial for structure determination.

The advent of MAS-NMR probes capable of spinning at rates of 100 kHz or greater has reduced the amount of sample required,[14,5-6,33] and, most importantly, reduced the need for proton dilution.[10] This has opened unprecedented opportunities for structural investigations of biosolids by using sensitive ^{1}H-detected methods,[34-36] with a dramatic reduction in homogenous line broadening to improve the resolution of ^{1}H resonances. However, even at the fastest (~100 kHz) sample spinning rates and the highest magnetic fields (23.5 T) currently available, membrane proteins in lipid bilayers remain challenging to study by NMR (or other methods), because of their inherently heterogeneous lipid bilayer environments in which they are naturally diluted and which limit spectral resolution and signal sensitivity.

Transmembrane proteins, in particular, are incorporated into lipid bilayers and perform sensing, transport and enzymatic functions in support of cellular viability. One example is the green variant of proteorhodopsin, a light-activated H^{+}-ion pump of 240 residues that in solution has an archetypical heptahelical transmembrane protein structure with a retinal cofactor.[37-38] While the structure of monomeric proteorhodopsin in detergents has been determined by solution NMR (pdb code: 2L6X),[39] the structure of the protein in native-like lipid environments remains unknown. This is complicated further by the tendency of proteorhodopsin molecules in bilayers to assemble into pentamers and hexamers, which are thought to mediate protein function.[40-42] Conventional ^{13}C-detected MAS-NMR methods have

enabled the extensive assignment of backbone and side-chain ^{13}C and ^{15}N resonances of proteorhodopsin oligomers in lipids.[43-44] However, only a partial assignment of the solvent-exposed amide ^{1}H resonances was possible with ^{1}H-detected measurements on perdeuterated protein, due to incomplete solvent exchange.[29]

Here, we demonstrate very fast (100 kHz) MAS-NMR to be a general approach for structural analyses of fully-protonated membrane proteins in near-native lipid environments. Notably, we show that the use of fast 100 kHz MAS conditions expedites sequence-specific resonance assignments and facilitates the detection of ^{1}H-^{1}H proximities in hydrophobic transmembrane regions, which are essential features of protein structure and for their function.

Materials and Methods

Sample preparation. Expression of isotopically-labeled proteorhodopsin was carried out as described by Ward et al.[29] with a few differences. Following overnight growth of *E. Coli* cells in the 25 mL culture, the cells were pelleted by centrifugation at ~5,000 RPM and resuspended in 75 mL of M9 minimal media with all labels present. Subsequently, the 75 mL culture was grown at 37°C to an $O.D._{600}$ of 1.0-1.5 (approximately 6 hours) and then added to 925 mL of M9 media (all labels present). Protein expression was induced at an $O.D._{600}$ of 0.8 by the addition of IPTG to a concentration of 1 mM and allowed to proceed for ~24 hours at room temperature without shaking. Protein purification was carried out using methods described previously[40] with a few modifications. Cells were lysed by a freeze fracture step with three freeze-thaw cycles using liquid nitrogen in addition to probe tip sonication and incubation with DNAse, lysozyme and $MgCl_2$. Then, the large cell fragments containing proteorhodopsin were pelleted by centrifugation at 5,000 RPM and then washed with 250 mL of phosphate buffered

solution (150 mM KCl and KH_2PO_4, pH ~ 8.7) by repeatedly suspending the cell pellet in 40 mL of buffer, shaking the solution for 5 minutes, and pelleting cells by centrifugation. Subsequently, proteorhodopsin was extracted from lysed *E. coli* membranes by overnight incubation of the washed cell fragments in a phosphate buffered solution containing 4% (w/v) n-dodecyl-*β,D*-maltoside surfactant. Following the Ni-NTA resin binding, washing and elution steps,[2] the optical purities of the proteorhodopsin samples, as measured by the ratio of absorbances at 280 nm to 520 nm, typically ranged between 1.8 and 2.2. The concentration of proteorhodopsin was estimated based on the absorbance at 520 nm, using an extinction coefficient of 49,000 $M^{-1}cm^{-1}$. Proteorhodopsin was reconstituted into 1,2-dimyristoyl-sn-glycero-3-phosphate (DMPA) and 1,2-dimyristoyl-sn-glycero-3-phosphocholine (DMPC) liposomes using procedures described previously, except using a 10 mM HEPES buffer that was titrated to a pH 6.2 using dilute HCl.[44]

NMR Spectroscopy. All experiments were carried out on a Bruker Avance III 1 GHz standard bore spectrometer operating at a static field of 23.4 T, equipped with a triple channel H, C, N, 0.7 mm probe, at a MAS rate $\omega_r/2\pi$ of 100 kHz. Sample temperature was maintained at about 305K using a Bruker cooling unit with regulated N_2 gas directed at the rotor. The temperature of this gas measured just before reaching the sample was 280 K. Chemical shifts were referenced to adamantane (^{1}H signal at 1.87 ppm).

The non-selective pulses were set to 1.1 μs at 227 kHz rf-field amplitude (^{1}H), 5.5 μs at 45 kHz rf-field amplitude (^{15}N) and 3.1 μs at 81 kHz rf-field amplitude (^{13}C). The dipolar-based ^{15}N,^{1}H and ^{13}C,^{1}H CP-HSQC experiments (H)CH and (H)NH follow, with little modifications, those introduced by Rienstra and coworkers.[16,21] (H)NCAHA,

(H)N(CO)CAHA, (H)CANH, (H)(CO)CA(CO)NH and (H)CONH experiments were performed as described recently.[25,36] The ^{1}H-^{15}N and ^{1}H-^{13}C cross-polarization (CP) were performed using a constant RF frequency applied to ^{15}N and ^{13}C of 40 kHz and a pulse linearly ramped from 90% to 100% of a maximum RF frequency of 130 kHz on ^{1}H. The ^{13}C-^{15}N CP was performed using a constant RF frequency of 60 kHz on ^{13}C and a 10% tangent ramp of 40 kHz on ^{15}N for 10 ms. Low power WALTZ-16 decoupling of 10 kHz was applied for heteronuclear decoupling. Swept low-power TPPM (slTPPM)[45] decoupling was used during ^{13}C, ^{15}N chemical shift evolution with a ^{1}H RF frequency of 25 kHz and a pulse-length duration of 20 μs. DIPSI-2 of $\gamma B_1/2\pi$=20 kHz was used for ^{13}C decoupling during acquisition due to the presence of homonuclear ^{13}C-^{13}C *J*-couplings. Suppression of solvent signals[19] was applied using the MISSISSIPPI scheme[46] without the homospoil gradient for 200 ms. The interscan recycle delay was 1 s.

The (H)CCH experiment follows that reported recently.[34,36] The composite ^{13}C pulses of 25 kHz were applied for the TOCSY mixing for 15 ms. In the 3D (H)CHH experiment, ^{1}H-^{1}H RFDR recoupling[16] was applied after the back-CP at a ^{1}H RF frequency of 200 kHz, for 1.4 ms. No loss of water from the sample was observed during the acquisition of the spectra. Spectra were apodized in each dimension with 60- to 90-degree shifted squared sine-bells ('qsine 3' or 'qsine 2' in Bruker Topspin), and zero-filled to at least twice the number of points in the indirect dimensions. Where linewidths are reported, no apodization was applied for the reported frequencies. Spectra were processed with Topspin3.5, and their analysis was performed using Cara.

Results and discussion

A dipolar-mediated 2D ^{1}H-^{15}N correlation spectrum (Figure 1, blue) of fully protonated U-[^{13}C,^{15}N] proteorhodopsin acquired at 100 kHz MAS shows highly resolved signals from the amide moieties of the protein backbone. These correlations have an average proton linewidth of 190 Hz fwhm that is significantly narrower than in a spectrum acquired on an identical sample at 60 kHz MAS rates in a 1.3 mm probe (Appendix B, Figure B5). Surprisingly, these spectra show comparable signal sensitivities, despite the significantly lower sample quantity (~0.5 mg, 0.7 mm rotor) at 100 kHz MAS, compared to 60 kHz MAS (~2.0 mg, 1.3 mm rotor). Deuterated proteorhodopsin re-protonated at the amide sites by exchange

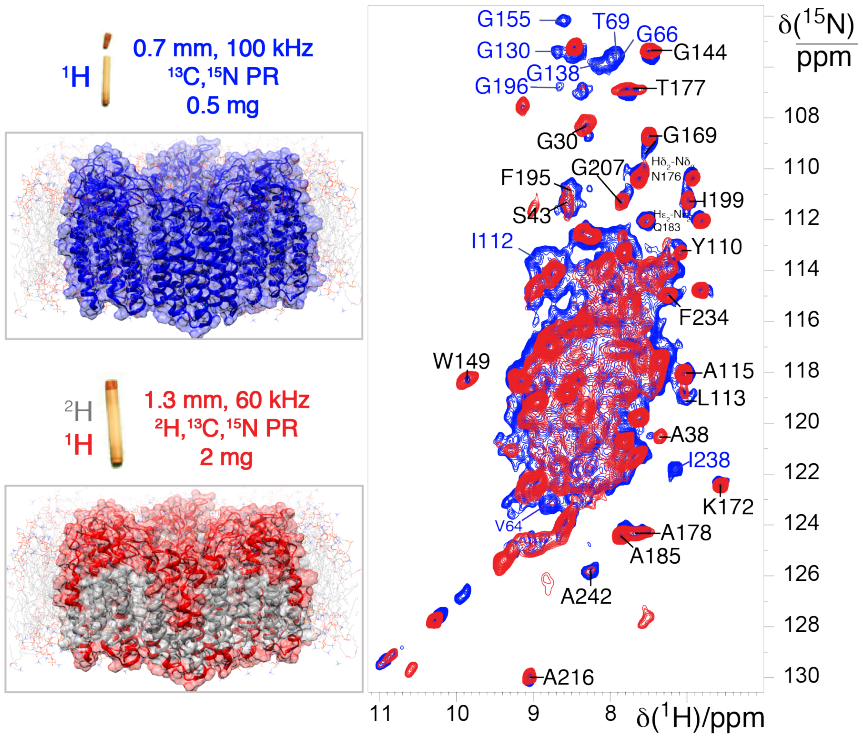

Figure 10. (A) Comparison of 2D ^{1}H-^{15}N CP-HSQC MAS-NMR spectra acquired at 305 K on (blue trace) fully protonated U-[^{13}C,^{15}N] proteorhodopsin in DMPC:DMPA lipids at 100 kHz MAS, and (red trace) U-[^{2}H,^{15}N,^{13}C] proteorhodopsin, re-protonated in 100% protonated buffer, in the same lipids at 60 kHz MAS and a field strength of 23.5 T. **(B)** Schematic diagrams of proteorhodopsin oligomers, modeled from the monomeric protein structure (pdb code: 2L6X, see SI), in which residues with ^{1}H^{N} species are highlighted in blue and red for the fully protonated and perdeuterated samples, respectively. (Figure courtesy of Dr. Daniela Lalli)

in 100% protonated buffers, yields enhanced resolution in a ^{1}H-^{15}N correlation spectrum (Figure 1, red) acquired under conventional 60 kHz MAS rates, showing average linewidths of 140 Hz fwhm. However, the spectrum acquired on the perdeuterated sample at 60 kHz MAS has far fewer cross-peaks (Figure 1, red) than that from the fully protonated (Figure 1, blue) protein at 100 kHz MAS. This reflects an incomplete reintroduction of H^{N} species in perdeuterated proteorhodopsin, predominantly at residues in the hydrophobic transmembrane regions, which precludes their detection and structural analysis. By comparison, the ubiquity of ^{1}H species in fully protonated proteorhodopsin allows the entire biomolecule to be probed by ^{1}H-detected spectroscopy, in particular moieties on the aliphatic side-chains from which critical structural constraints are derived.

For example, the 2D ^{13}C-^{1}H CP-HSQC spectra of fully protonated proteorhodopsin at 60 kHz (Figure 2, left) and 100 kHz (Figure 2, right) MAS show correlated signals from ^{1}H and ^{13}C nuclei in the side-chains (top panel) and α positions (bottom panel). Substantially enhanced proton resolution is observed under the faster MAS conditions, as established by the larger number of fully resolved correlations that appear only in the spectrum recorded at 100 kHz; these include many $^{1}H\alpha$ resonances labeled in Figure 2, bottom panels, as well as ^{1}H methyl resonances (Figure 2, top panels). For several peaks resolved even at 60 kHz, the linewidths are observed to be 50–100 Hz broader (Figure 2). The dramatic improvements in resolution enable the use of aliphatic side-chain protons as crucial reporters of protein structure. The significant increase in spectral resolution observed at 100 kHz MAS is surprising. While microcrystalline proteins, capsids, and fibrils often are homogeneous samples with rigid architectures that are amenable to MAS-averaging of homonuclear dipolar interactions, membrane proteins are less homogeneous, comparably flexible and undergo a

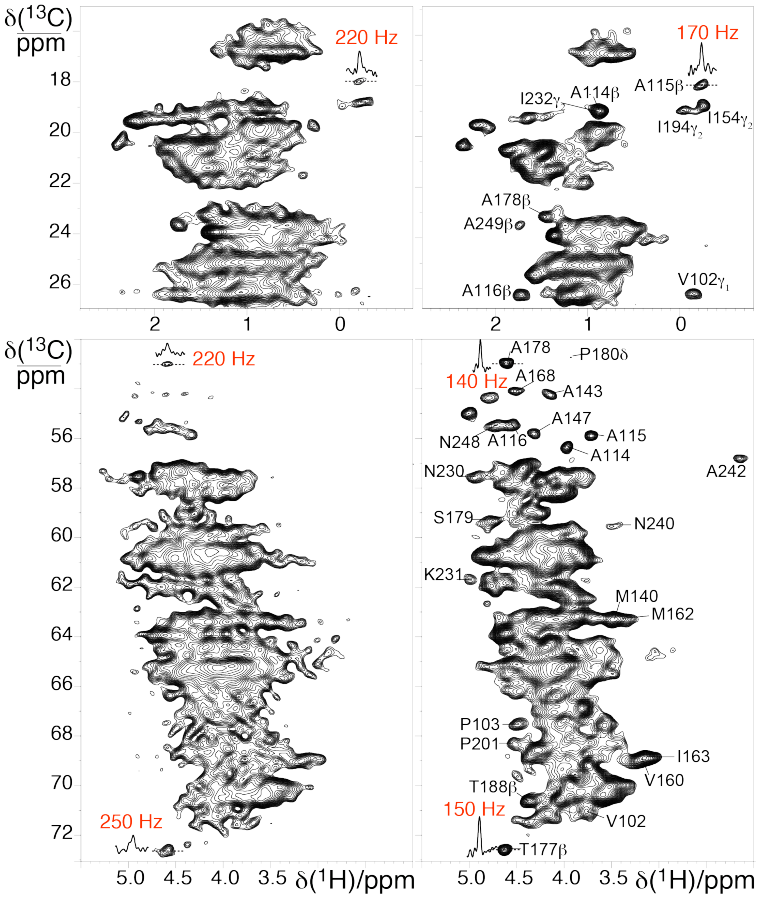

Figure 11. 2D ^{1}H-^{13}C CP-HSQC MAS-NMR spectra acquired at 305 K and 23.5 T on fully protonated U-[^{13}C, ^{15}N] proteorhodopsin in lipids at MAS rates of 60 kHz (left) and 100 kHz (right). The side chain and alpha regions of the spectra are shown in the top and bottom panels, respectively. (Figure courtesy of Dr. Daniela Lalli)

range of motions[47] that could reduce the benefits of faster MAS rates in improving signal resolution.

Nevertheless, in spectra from fully protonated proteorhodopsin in lipids, the average ^{1}H linewidth of ^{15}N-^{1}H correlations from amide moieties is ~190 Hz fwhm at 100 kHz MAS, compared to ~280 Hz fwhm at 60 kHz MAS. Greater resolution improvements are observed for aliphatic ^{1}H signals, where average linewidths are approximately 145 Hz fwhm at 100 kHz MAS, versus about 235 Hz fwhm estimated from the few resolved signals at 60 kHz. The bulk ^{1}H coherence lifetimes were measured to be 2.5 ms on the fully protonated protein at 100 kHz MAS, which corresponds to residual homogeneous components of ~125 Hz that suggest

inhomogeneous linewidths of 155 and 70 Hz for the $^{1}H^{N}$ and $^{1}H\alpha$ signals, respectively. The larger inhomogeneous components for the $^{1}H^{N}$ species likely arise from a distribution of hydrogen bonding environments, consistent with the larger range of amide $^{1}H^{N}$ shifts reported generally for proteins in the BMRB. The substantial homogeneous broadening remaining even at 100 kHz MAS conditions indicates that further narrowed ^{1}H linewidths could be obtained for faster MAS rates and/or higher magnetic fields.[14,48]

Additionally, the ^{1}H signal resolution of fully protonated proteorhodopsin at 100 kHz MAS is comparable to that obtained with state-of-the-art partial isotopic labeling schemes. These labeling strategies, including fractional deuteration,[28,49] isoleucine-leucine-valine labelling,[35-36,50] proton clouds[27] and stereospecific array isotopic labeling (SAIL),[51] selectively introduce ^{1}H side-chains into a deuterated protein matrix. Spectra of fully protonated proteorhodopsin in lipids at 100 kHz MAS show 20% higher ^{1}H resolution than for the similar α-helical transmembrane K^{+} channel Kcsa in lipid bilayers labeled with an inverse fractional deuteration approach and using 60 kHz MAS rates.[32] Importantly, while this labeling scheme yields $^{1}H/^{2}H$ isotopomers that can account for up to 0.3 ppm dispersions in ^{13}C chemical shifts,[52-53] such effects are negligible in fully protonated proteins probed using 100 kHz MAS.

To facilitate rapid and global sequence-specific resonance assignments, judicious selections of 3D correlation experiments are essential for high sensitivity, in addition to high spectral resolution. Between the two different types of protein backbone ^{13}C species, the coherence lifetimes are longest for $^{13}C'$ species ($T_2' = 21$ ms, compared to $^{13}C\alpha$ $T_2' = 12.5$ ms), yielding considerable sensitivity advantages for 3D NMR measurements that rely on evolution of $^{13}C'$ versus $^{13}C\alpha$ coherences. Thus, for sequential resonance assignments of fully protonated proteorhodopsin, we chose the combination of two strategies that leverage the longer lifetimes

of the ^{13}C' spins by using *J*-mediated ^{13}C'-^{13}Cα coherence transfers[54] and detection of either HN[5d] or Hα resonances.[36] These two approaches, respectively, use (H)CANH and (H)(CO)CA(CO)NH spectra to correlate signals from ^{1}H-^{15}N amide pairs to ^{13}Cα resonances of adjacent residues, or use (H)NCAHA and (H)N(CO)CAHA to correlate the signals of ^{1}Hα-^{13}Cα pairs to intra and inter-residue ^{15}N species.[11b] Sequential backbone assignments are achieved by simultaneously linking correlations of both ^{1}H-^{15}N or ^{1}Hα-^{13}Cα pairs through their mutual ^{13}Cα or ^{15}N chemical shifts established in the amide or α proton-detected spectra, respectively, as depicted in Figure 3. Here, representative portions of the four spectra that demonstrate sequential linking of amide and alpha pairs are reported. The choice of these pairs of experiments is motivated by the coherence lifetimes, which for membrane proteins are not as long as for microcrystalline samples. For comparison, while these 3D spectra were acquired in less than two weeks, ^{1}H^{N}-detected experiments that rely on the faster decaying ^{13}Cα spins to enable ^{13}C'- or ^{13}Cβ-linking[55] have lower transfer efficiencies and significantly longer acquisition times. The ^{1}Hα-^{13}Cα and ^{1}H-^{15}N pairs also have roughly equal sensitivities, and the narrow dispersion in the ^{1}Hα dimension is offset by the narrow linewidth. This makes both types of spin pairs similarly useful in providing sequence-specific assignments. The backbone resonance assignments are further corroborated by analyses of the ^{13}C-^{13}C-^{1}H TOCSY spectrum (Appendix B, Figure B6) that yields the assignment of the ^{1}H and ^{13}C side-chain resonances, thus enabling the identification of the amino acid types.

Resonance assignments for extensive portions of the proteorhodopsin backbone and side-chains were made based on spectra acquired at 100 kHz MAS. Despite the high degeneracy of aliphatic residues (32 Leu, 32 Ala, 24 Gly, 21 Val, and 19 Ile residues) that account for 49% of the proteorhodopsin sequence and the typically low chemical shift

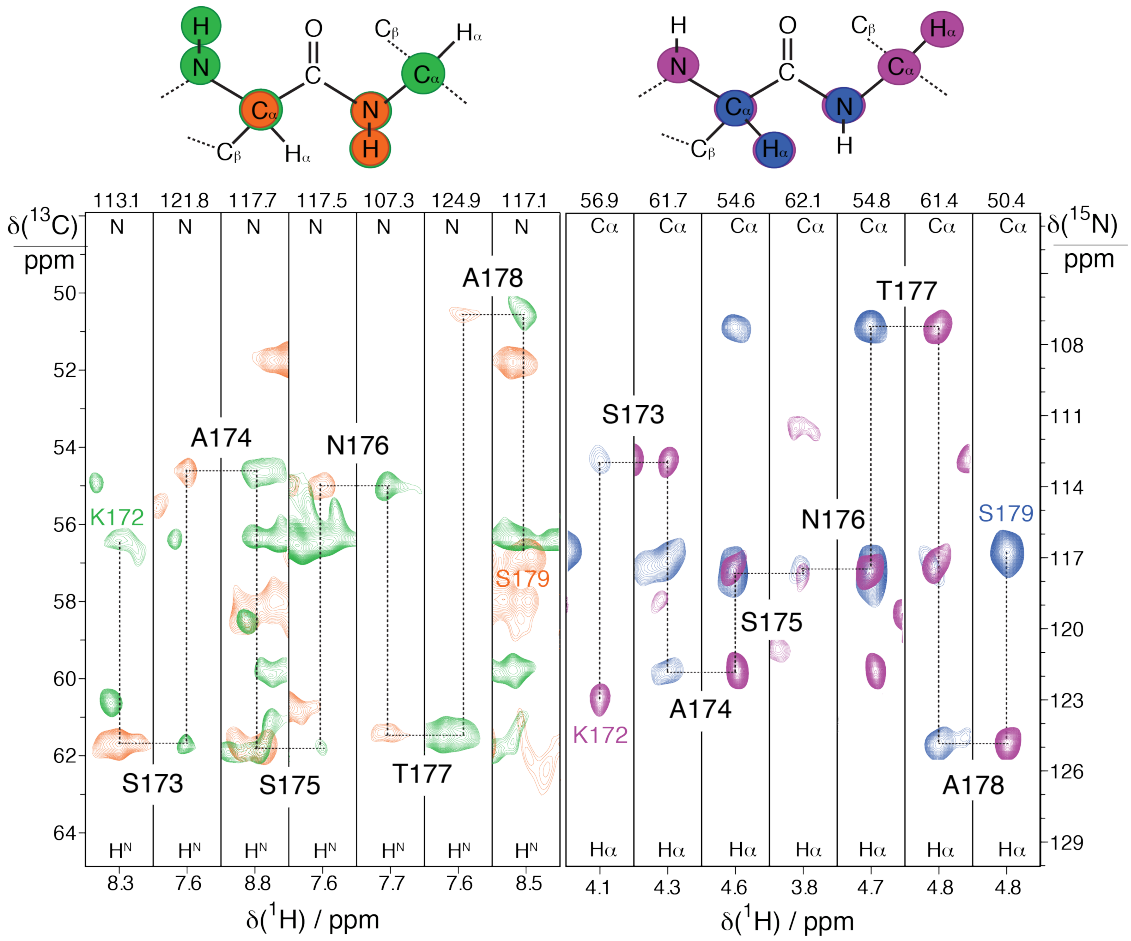

Figure 12. Sequential assignments of intensity correlations for residues 172-179 in fully protonated proteorhodopsin in lipids bilayers. 2D ^{1}Hα-^{13}Cα slices extracted from (H)CANH (green trace) and (H)(CO)CA(CO)NH (orange trace) spectra are shown in the left panel, and 2D ^{1}H-^{15}N slices from (H)NCAHA (magenta trace) and (H)N(CO)CAHA (blue trace) spectra in the right. The four spectra were acquired at 100 kHz MAS and 23.5 T. (Figure courtesy of Dr. Daniela Lalli)

dispersions for helical proteins, the backbone resonances of 146 residues were sequence specifically assigned, as depicted in Figure 4. Continuous linkages through 5 of the 6 proline residues were identified from analyses of ^{1}Hα-detected 3D NMR correlation spectra. These residues are distributed in the transmembrane helices and extra-membrane loop regions. Importantly, resonance assignments were established for 57% of the ^{1}H and ^{13}C moieties of the aliphatic side-chains.

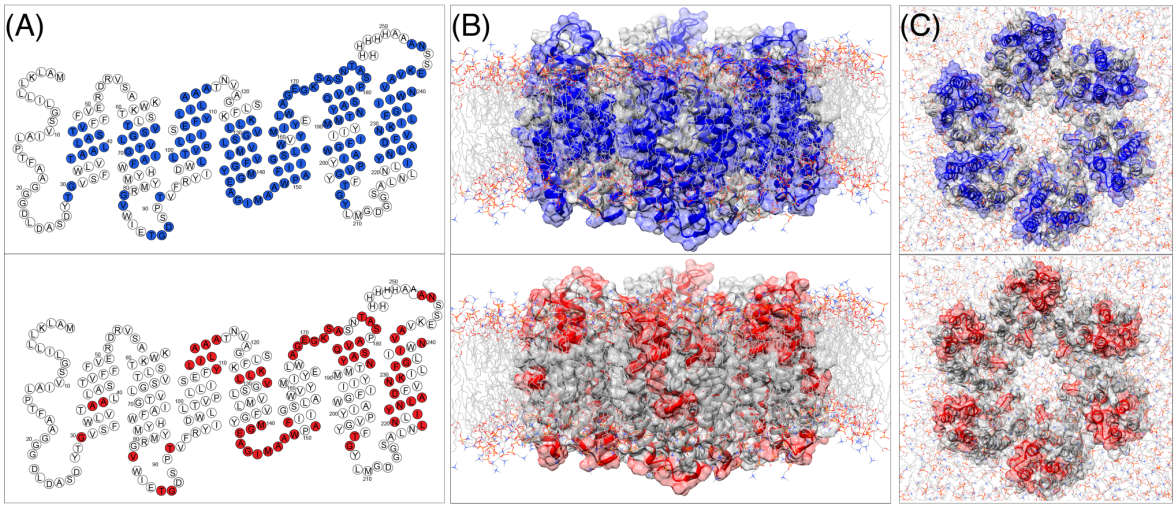

Figure 13. (A) Schematic snake-like diagrams of the amino acid sequence of proteorhodopsin in which amino acids with backbone resonance assignments are colored in blue for the case of $^{13}C,^{15}N$-enriched proteorhodopsin (top), and red for the case of $^{2}H,^{13}C,^{15}N$-enriched proteorhodopsin (bottom). **(B)** and **(C)** show cartoons of the structures of proteorhodopsin hexamers in lipid bilayers, where amino acids colored in red and blue have backbone resonance assignments and those colored in grey do not have assignments. (Figure courtesy of Dr. Daniela Lalli)

Such extensive resonance assignments facilitate the identification of inter-residue ^{1}H-^{1}H proximities that yield detailed site-specific information on proteorhodopsin structure in lipids. Key insights into the intra- and inter-helical proximities between side-chains are obtained from analyses of high-resolution radio-frequency-driven-recoupling (RFDR) spectra. For example, the 3D H(H)CH RFDR spectrum (1.4 ms mixing time, Figure 5) acquired from fully protonated proteorhodopsin shows numerous cross-signals that can be assigned to specific ^{1}H species using the resonance assignments established above. Subsequent analyses yield the identification of structural constraints, several of which are depicted schematically on the protein structure derived by solution NMR data, shown in Figure 5B. These include both intra-helical proximities, such as between the methyl ^{1}H of M134 and $^{1}H\alpha$ of G138 (Figure 5B, right, middle), and inter-helical proximities, including the methyl ^{1}Hs of A116 and V182 (Figure 5B, right, bottom). These inter-nuclear contacts within the transmembrane region

are a direct way to probe the relative orientations of secondary structural elements. Especially important are the ^{1}H-^{1}H proximities of the ^{1}Hα of Gly residues and methyl groups, as these provide extremely useful structural constraints for α-helical proteins. In addition, the spectrum contains ^{1}H-^{1}H cross peaks between ^{1}Hα of Gly155 and two methyl groups with ^{1}H signals at 2.0 and 1.6 ppm, respectively, which are tentatively assigned to the retinal cofactor (Figure 5B, right, top). Such signals are valuable to establish the location, orientation and configuration of the chromophore in the transmembrane region of the protein, which is directly related to the protein functionality. In contrast, similar 3D spectra using perdeuterated and back-exchanged proteorhodopsin can only reveal $^{1}H^{N}$-$^{1}H^{N}$ contacts that primarily provide short- and medium-range intra-helical distance restraints. Importantly, much higher signal sensitivity and resolution were observed from the fully protonated sample at 100 kHz MAS versus an otherwise identical measurement at 60 kHz MAS on a 5-fold larger sample (Figure 5A).

The structures and properties of fully protonated membrane proteins in lipid bilayers are expected to closely resemble those in native cell-membrane environments. Interestingly, all of the ^{1}H-^{1}H contacts between the transmembrane helices reported above can be explained on the basis of the structure of proteorhodopsin in micellar (diheptanoyl-phosphocholine, diC_7PC) surfactant solution.[39] In combination with the ^{13}C chemical shift analysis above, this establishes that for the compositions and conditions investigated, the structure of proteorhodopsin in lipid bilayers and in micellar surfactant solution are very similar, and that even the position of the retinal cofactor within the transmembrane pocket is maintained. While in many cases solubilizing detergents have been observed to alter the structures or functionalities of membrane proteins,[56] that is not the case here. NMR structural analyses of fully protonated membrane proteins in lipids enabled by fast MAS represent an essential step

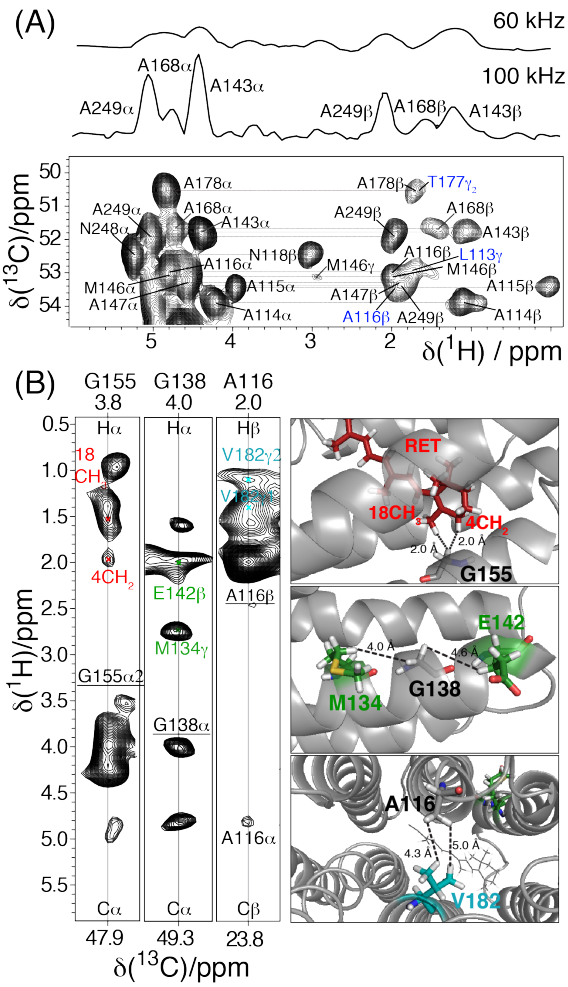

Figure 14. (A) Alanine region of the 2D ^{1}H-^{13}C projection of a 3D H(H)CH RFDR spectrum acquired on U-[^{15}N,^{13}C] proteorhodopsin in lipids at 100 kHz MAS at 305 K and 23.5 T, using a 1.4 ms mixing time during which the RFDR rf-field was 200 kHz. Diagonal peaks are labeled in black and cross peaks in blue. Shown above the 2D projection are 1D ^{13}C slices extracted at the A249 Cα-Hα position (~51.9 ppm in the indirect dimension of the 2D projection) from the 3D RFDR spectrum acquired at 100 kHz and (up 60 kHz MAS. **(B)** 2D cross sections (left) of the 3D RFDR spectrum with ^{1}H-^{1}H correlations assigned to intra/inter-helical and helix-retinal contacts cofactor, as depicted in the schematic 3D structure of the protein (right). (Figure courtesy of Dr. Daniela Lalli)

to validating the conclusions from solution NMR data in detergent micelles. From the present data, the oligomeric state of proteorhodopsin in lipid bilayers cannot be concluded, since it is not possible to identify any inter-monomer cross peak in the 3D H(H)CH RFDR spectrum reflecting the presence of pentamers and/or hexamers. Unambiguous detection of such cross-peaks is extremely challenging due to the partial side chain assignment, the signal degeneracy,

and the sample heterogeneity in terms of oligomeric composition. In order to identify such contacts, different strategies aimed at decreasing the sample heterogeneity and the spectral overlap and increasing the signal sensitivity can be adopted, such as the expression of mutants that stabilize a single oligomeric form to increase the sample homogeneity, or the use of tailored labeling schemes to decrease the spectral crowding, the acquisition of selective proton-proton distance restraints to increase the signal-to-noise, or the acquisition of 4D spectra with increased heteronuclear dimensionality to improve the spectral resolution.

Conclusions

Extensive atomic-level structural insights on a fully-protonated membrane protein in native-like lipid environments are provided by ^{1}H-detected solid-state NMR spectra acquired under 100 kHz MAS conditions and at high (23.5 T) magnetic field. This approach yields highly resolved ^{1}H resonances from moieties throughout the protein, including those from transmembrane amide sites that are generally inaccessible to chemical exchange with water, and that are therefore absent in spectra of perdeuterated samples. This enables the sequential assignments of the protein resonances, including the majority of the aliphatic ^{1}H moieties, and notably the identification of long-range inter-helical ^{1}H-^{1}H contacts between side-chains in transmembrane protein regions. To the best of our knowledge, this is the first report of long-range proximities between side-chain protons in a fully protonated membrane protein. Remarkably, this information was obtained with less than 0.5 mg of sample without the need for deuteration, thus circumventing a major roadblock to the structural characterization of membrane proteins by solid-state MAS-NMR or other methods. This represents an important step toward the determination of membrane protein structures and their relationships to functional interactions in native-like lipid environments. The approach is expected to open

opportunities to investigate a variety of complicated structure-dependent biochemical phenomena, including protein interactions in near-native environments or molecular recognition mechanisms that govern ligand binding to transmembrane receptors.

References

(1) Lange, A.; Giller, K.; Hornig, S.; Martin-Eauclaire, M. F.; Pongs, O.; Becker, S.; Baldus, M. *Nature* **2006**, *440*, 959-962

(2) Xu, J.; Durr, U. H.; Im, S. C.; Gan, Z.; Waskell, L.; Ramamoorthy, A. *Angew. Chem. Int. Ed.* **2008**, *47*, 7864-7867;

(3) Etzkorn, M.; Kneuper, H.; Dunnwald, P.; Vijayan, V.; Kramer, J.; Griesinger, C.; Becker, S.; Unden, G.; Baldus, M. *Nat. Struct. Mol. Biol.* **2008**, *15*, 1031-1039;

(4) Bajaj, V. S.; Mak-Jurkauskas, M. L.; Belenky, M.; Herzfeld, J.; Griffin, R. G. *Proc. Natl. Acad. Sci. U. S. A.* **2009**, *106*, 9244-9249

(5) Cady, S. D.; Schmidt-Rohr, K.; Wang, J.; Soto, C. S.; Degrado, W. F.; Hong, M. *Nature* **2010**, *463*, 689-692

(6) Sharma, M.; Yi, M.; Dong, H.; Qin, H.; Peterson, E.; Busath, D. D.; Zhou, H. X.; Cross, T. A. *Science* **2010**, *330*, 509-512;

(7) Bhate, M. P.; McDermott, A. E. *Proc. Natl. Acad. Sci. U. S. A.* **2012**, *109*, 15265-15270;

(8) Park, S. H.; Das, B. B.; Casagrande, F.; Tian, Y.; Nothnagel, H. J.; Chu, M.; Kiefer, H.; Maier, K.; De Angelis, A. A.; Marassi, F. M.; Opella, S. J. *Nature* **2012**, *491*, 779-783

(9) Shahid, S. A.; Bardiaux, B.; Franks, W. T.; Krabben, L.; Habeck, M.; van Rossum, B. J.; Linke, D. *Nat. Methods* **2012**, *9*, 1212-1217

(10) Wang, S.; Munro, R. A.; Shi, L.; Kawamura, I.; Okitsu, T.; Wada, A.; Kim, S. Y.; Jung, K. H.; Brown, L. S.; Ladizhansky, V. *Nat. Methods* **2013**, *10*, 1007-1012

(11) Wylie, B. J.; Bhate, M. P.; McDermott, A. E. *Proc. Natl. Acad. Sci. U. S. A.* **2014**, *111*, 185-190

(12) Andreas, L. B.; Reese, M.; Eddy, M. T.; Gelev, V.; Ni, Q. Z.; Miller, E. A.; Emsley, L.; Pintacuda, G.; Chou, J. J.; Griffin, R. G. *J. Am. Chem. Soc.* **2015**, *137*, 14877-14886

(13) Becker-Baldus, J.; Bamann, C.; Saxena, K.; Gustmann, H.; Brown, L. J.; Brown, R. C.; Reiter, C.; Bamberg, E.; Wachtveitl, J.; Schwalbe, H.; Glaubitz, C. *Proc. Natl. Acad. Sci. U. S. A.* **2015**, *112*, 9896-9901.

(14) Andreas, L. B.; Le Marchand, T.; Jaudzems, K.; Pintacuda, G. *J. Magn. Reson.* **2015**, *253*, 36-49.

(15) Samoson, A.; Tuherm, T.; Gan, Z. *Solid State Nucl. Magn. Reson.* **2001**, *20*, 130-136

(16) Zhou, D. H.; Shea, J. J.; Nieuwkoop, A. J.; Franks, W. T.; Wylie, B. J.; Mullen, C.; Sandoz, D.; Rienstra, C. M. *Angew. Chem. Int. Ed.* **2007**, *46*, 8380-8383;

(17) Marchetti, A.; Jehle, S.; Felletti, M.; Knight, M. J.; Wang, Y.; Xu, Z. Q.; Park, A. Y.; Otting, G.; Lesage, A.; Emsley, L.; Dixon, N. E.; Pintacuda, G. *Angew. Chem. Int. Ed. Engl.* **2012**, *51*, 10756-10759

(18) Vasa, S. K.; Rovo, P.; Giller, K.; Becker, S.; Linser, R. *Phys. Chem. Chem. Phys.* **2016**, *18*, 8359-8363.

(19) Paulson, E. K.; Morcombe, C. R.; Gaponenko, V.; Dancheck, B.; Byrd, R. A.; Zilm, K. W. *J. Am. Chem. Soc.* **2003**, *125*, 15831-15836

(20) Chevelkov, V.; Rehbein, K.; Diehl, A.; Reif, B. *Angew. Chem. Int. Ed. Engl.* **2006**, *45*, 3878-3881.

(21) Zhou, D. H.; Shah, G.; Cormos, M.; Mullen, C.; Sandoz, D.; Rienstra, C. M. *J. Am. Chem. Soc.* **2007**, *129*, 11791-11801

(22) Knight, M. J.; Webber, A. L.; Pell, A. J.; Guerry, P.; Barbet-Massin, E.; Bertini, I.; Felli, I. C.; Gonnelli, L.; Pierattelli, R.; Emsley, L.; Lesage, A.; Herrmann, T.; Pintacuda, G. *Angew. Chem. Int. Ed.* **2011**, *50*, 11697-11701

(23) Knight, M. J.; Pell, A. J.; Bertini, I.; Felli, I. C.; Gonnelli, L.; Pierattelli, R.; Herrmann, T.; Emsley, L.; Pintacuda, G. *Proc. Natl. Acad. Sci. U. S. A.* **2012**, *109*, 11095-11100

(24) Barbet-Massin, E.; Pell, A. J.; Retel, J. S.; Andreas, L. B.; Jaudzems, K.; Franks, W. T.; Nieuwkoop, A. J.; Hiller, M.; Higman, V.; Guerry, P.; Bertarello, A.; Knight, M. J.; Felletti, M.; Le Marchand, T.; Kotelovica, S.; Akopjana, I.; Tars, K.; Stoppini, M.; Bellotti, V.; Bolognesi, M.; Ricagno, S.; Chou, J. J.; Griffin, R. G.; Oschkinat, H.; Lesage, A.; Emsley, L.; Herrmann, T.; Pintacuda, G. *J. Am. Chem. Soc.* **2014**, *136*, 12489-12497

(25) Lamley, J. M.; Iuga, D.; Oster, C.; Sass, H. J.; Rogowski, M.; Oss, A.; Past, J.; Reinhold, A.; Grzesiek, S.; Samoson, A.; Lewandowski, J. R. *J. Am. Chem. Soc.* **2014**, *136*, 16800-16806

(26) Agarwal, V.; Penzel, S.; Szekely, K.; Cadalbert, R.; Testori, E.; Oss, A.; Past, J.; Samoson, A.; Ernst, M.; Bockmann, A.; Meier, B. H. *Angew. Chem. Int. Ed. Engl.* **2014**, *53*, 12253-12256

(27) Sinnige, T.; Daniels, M.; Baldus, M.; Weingarth, M. *J. Am. Chem. Soc.* **2014**, *136*, 4452-4455

(28) Mance, D.; Sinnige, T.; Kaplan, M.; Narasimhan, S.; Daniels, M.; Houben, K.; Baldus, M.; Weingarth, M. *Angew. Chem. Int. Ed. Engl.* **2015**, *54*, 15799-15803.

(29) Ward, M. E.; Shi, L.; Lake, E.; Krishnamurthy, S.; Hutchins, H.; Brown, L. S.; Ladizhansky, V. *J. Am. Chem. Soc.* **2011**, *133*, 17434-17443.

(30) Zhou, D. H.; Nieuwkoop, A. J.; Berthold, D. A.; Comellas, G.; Sperling, L. J.; Tang, M.; Shah, G. J.; Brea, E. J.; Lemkau, L. R.; Rienstra, C. M. *J. Biomol. NMR* **2012**, *54*, 291-305

(31) Eddy, M. T.; Su, Y.; Silvers, R.; Andreas, L.; Clark, L.; Wagner, G.; Pintacuda, G.; Emsley, L.; Griffin, R. G. *J. Biomol. NMR* **2015**, *61*, 299-310.

(32) Medeiros-Silva, J.; Mance, D.; Daniels, M.; Jekhmane, S.; Houben, K.; Baldus, M.; Weingarth, M. *Angew. Chem. Int. Ed. Engl.* **2016**, *55*, 13606-13610.

(33) Nishiyama, Y. *Solid State Nucl. Magn. Reson.* **2016**, *78*, 24-36.

(34) Andreas, L. B.; Jaudzems, K.; Stanek, J.; Lalli, D.; Bertarello, A.; Le Marchand, T.; Cala-De Paepe, D.; Kotelovica, S.; Akopjana, I.; Knott, B.; Wegner, S.; Engelke, F.; Lesage, A.; Emsley, L.; Tars, K.; Herrmann, T.; Pintacuda, G. *Proc. Natl. Acad. Sci. U. S. A.* **2016**, *113*, 9187-9192.

(35) Mroue, K. H.; Nishiyama, Y.; Kumar Pandey, M.; Gong, B.; McNerny, E.; Kohn, D. H.; Morris, M. D.; Ramamoorthy, A. *Sci. Rep.* **2015**, *5*, 11991

(36) Stanek, J.; Andreas, L. B.; Jaudzems, K.; Cala, D.; Lalli, D.; Bertarello, A.; Schubeis, T.; Akopjana, I.; Kotelovica, S.; Tars, K.; Pica, A.; Leone, S.; Picone, D.; Xu, Z. Q.; Dixon, N. E.; Martinez, D.; Berbon, M.; El Mammeri, N.; Noubhani, A.; Saupe, S.; Habenstein, B.; Loquet, A.; Pintacuda, G. *Angew. Chem. Int. Ed. Engl.* **2016**, *55*, 15504-15509.

(37) Bamann, C.; Bamberg, E.; Wachtveitl, J.; Glaubitz, C. *Biochim. Biophys. Acta* **2014**, *1837*, 614-625

(38) Inoue, K.; Kato, Y.; Kandori, H. *Trends Microbiol.* **2015**, *23*, 91-98.

(39) Reckel, S.; Gottstein, D.; Stehle, J.; Lohr, F.; Verhoefen, M. K.; Takeda, M.; Silvers, R.; Kainosho, M.; Glaubitz, C.; Wachtveitl, J.; Bernhard, F.; Schwalbe, H.; Guntert, P.; Dotsch, V. *Angew. Chem. Int. Ed. Engl.* **2011**, *50*, 11942-11946.

(40) Stone, K. M.; Voska, J.; Kinnebrew, M.; Pavlova, A.; Junk, M. J.; Han, S. *Biophys. J.* **2013**, *104*, 472-481

(41) Edwards, D. T.; Huber, T.; Hussain, S.; Stone, K. M.; Kinnebrew, M.; Kaminker, I.; Matalon, E.; Sherwin, M. S.; Goldfarb, D.; Han, S. *Structure* **2014**, *22*, 1677-1686

(42) Maciejko, J.; Mehler, M.; Kaur, J.; Lieblein, T.; Morgner, N.; Ouari, O.; Tordo, P.; Becker-Baldus, J.; Glaubitz, C. *J. Am. Chem. Soc.* **2015**, *137*, 9032-9043.

(43) Shi, L.; Ahmed, M. A. M.; Zhang, W.; Whited, G.; Brown, L. S.; Ladizhansky, V. *J. Mol. Biol.* **2009**, *386*, 1078-1093

(44) Shi, L.; Lake, E. M.; Ahmed, M. A.; Brown, L. S.; Ladizhansky, V. *Biochim. Biophys. Acta* **2009**, *1788*, 2563-2574.

(45) Bennett, A. E. R., C. M.; Auger, M.; Lakshmi, K. V.; Griffin, R. G. *J. Chem. Phys.* **1995**, *103*, 6951-6958.

(46) Zhou, D. H.; Rienstra, C. M. *J. Magn. Reson.* **2008**, *192*, 167-172.

(47) (a) Good, D. B.; Wang, S.; Ward, M. E.; Struppe, J.; Brown, L. S.; Lewandowski, J. R.; Ladizhansky, V. *J. Am. Chem. Soc.* **2014**, *136*, 2833-2842; (b) Saurel, O.; Iordanov, I.; Nars, G.; Demange, P.; Le Marchand, T.; Andreas, L. B.; Pintacuda, G.; Milon, A. *J. Am. Chem. Soc.* **2017**, *139*, 1590-1597.

(48) Asami, S.; Szekely, K.; Schanda, P.; Meier, B. H.; Reif, B. *J. Biomol. NMR* **2012**, *54*, 155-168.

(49) Asami, S.; Schmieder, P.; Reif, B. *J. Am. Chem. Soc.* **2010**, *132*, 15133-15135.

(50) Huber, M.; Hiller, S.; Schanda, P.; Ernst, M.; Bockmann, A.; Verel, R.; Meier, B. H. *Chemphyschem* **2011**, *12*, 915-918.

(51) Wang, S.; Parthasarathy, S.; Nishiyama, Y.; Endo, Y.; Nemoto, T.; Yamauchi, K.; Asakura, T.; Takeda, M.; Terauchi, T.; Kainosho, M.; Ishii, Y. *PLoS One* **2015**, *10*, e0122714.

(52) Venters, R. A.; Farmer, B. T., 2nd; Fierke, C. A.; Spicer, L. D. *J. Mol. Biol.* **1996**, *264*, 1101-1116

(53) Smith, A. A.; Ravotti, F.; Testori, E.; Cadalbert, R.; Ernst, M.; Bockmann, A.; Meier, B. H. *J. Biomol. NMR* **2017**, *67*, 109-119.

(54) Barbet-Massin, E.; Pell, A. J.; Jaudzems, K.; Franks, W. T.; Retel, J. S.; Kotelovica, S.; Akopjana, I.; Tars, K.; Emsley, L.; Oschkinat, H.; Lesage, A.; Pintacuda, G. *J. Biomol. NMR* **2013**, *56*, 379-386.

(55) Barbet-Massin, E.; Pell, A. J.; Knight, M. J.; Webber, A. L.; Felli, I. C.; Pierattelli, R.; Emsley, L.; Lesage, A.; Pintacuda, G. *Chemphyschem* **2013**, *14*, 3131-3137.

(56) Cross, T. A.; Sharma, M.; Yi, M.; Zhou, H. X. *Trends Biochem. Sci* **2011**, *36*, 117-125.

Chapter 3 : Structure and function of the membrane protein proteorhodopsin incorporated in a synthetic mesostructured silica host

Abstract

We report an atomic-level understanding of the factors that influence the structure, dynamics, and functional activity of the membrane protein light-activated transmembrane protein proteorhodopsin in a mesostructured silica synthetic host material. The materials were synthesized from aqueous solutions by the co-assembly of membrane-protein-stabilizing surfactants, and network-forming silica species into wormlike surfactant mesochannels into which the hydrophobic proteorhodopsin guest species were incorporated with high loading (13 wt%). Three-dimensional (3D) NMR analyses resolved signals associated with the residues of the proteorhodopsin molecules that reflected exceptional uniformity of their local environments and enabled site-specific structural and dynamical insights to be obtained on the membrane protein guests confined in the mesostructured silica host. Comparisons with otherwise identical proteorhodopsin molecules in lipid or micellar solution environments revealed that the preponderance of the membrane protein guests exhibited structures and local dynamics that were nearly identical to the native protein, although with some regions that were perturbed by inclusion in the synthetic hosts. The molecular-level properties are related to the light-activated functional behaviors of proteorhodopsin molecules and establish the efficacy of the synthetic silica host for harnessing membrane protein properties in robust abiological environments.

Introduction.

Membrane proteins perform a broad range of functions, including sensing, catalysis and transport, that would be attractive for technological applications. To exploit membrane proteins for such purposes generally requires protein molecules to be incorporated into synthetic materials that can be integrated into macroscopic devices. This however is exceedingly challenging, as membrane proteins are often unstable outside lipid bilayer environments, substantially limiting the range of synthetic materials that can accommodate functional membrane proteins. Functionally-active membrane proteins have been incorporated into a number of synthetic host materials, including block copolymers,[1–3] in lipids supported by hydrogels,[4] sol-gel-derived silicas[5] and mesostructured silica-surfactant materials,[6] the latter of which also exhibit enhanced thermal stabilities compared to native-like lipids. Despite the technological promise of such materials, the factors that account for retained protein function in these synthetic host materials, such as confinement effects, interactions with surfactants, solvents, or surfaces, remain largely unknown.

The functionalities of membrane proteins are imparted by their structures and dynamics, which are complicated, diverse, and often sensitive to local environments. Most membrane proteins are composed of several structural motifs that arrange through physical and chemical interactions to support their functions. For example, a large subset of transmembrane proteins have α-helical motifs that assemble to form channels to permit the rapid and selective transport of particular ions or molecules,[7–10] promote allosteric effects,[11] or facilitate catalytic reactions.[12,13] In many cases, these functionalities are associated with or require the dynamic motions of structural elements, an example of which are those of the light-activated H^+-ion pump membrane bacteriorhodopsin.[14] The structures of membrane proteins

can also accommodate cofactors that undergo reactions to support function, such as the heme moieties of cytochrome c oxidase,[13] or to enable function to be activated by external stimuli, such the light-responsive retinal and carotenoid antennae of xanthorhodopsin.[7] Furthermore, membrane protein structures can promote inter-protein interactions that result in oligomerization (*i.e.*, changes in quaternary protein structure), which is known to modify or complement protein function.[11,15–17] Besides intra- and inter-protein interactions, protein structures are also stabilized by surfactants (*e.g.*, lipids, detergents) and solvent species that associate with the hydrophobic and hydrophilic regions.[18,19] In many cases, subtle changes to the environment of a membrane protein can cause irreversible unfolding of a protein and permanently deactivate its function. Elucidating the structures of membrane proteins in synthetic materials remains exceedingly challenging, as protein guests generally lack long-range order, are structurally complicated, and undergo dynamic structural changes on multiple length and time scales.

Several techniques can yield high-resolution structural information about membrane proteins. The predominant method for determining protein structures is x-ray crystallography, which relies on diffracted X-rays from crystalline protein samples and can typically establish protein structures down 0.2 Å resolution. Procedures to prepare crystalline membrane protein samples, however, are difficult to develop, not general, and specific examples are limited. By comparison, cryo-electron microscopy (cryo-EM) is a technique capable of determining the structures of crystalline and non-crystalline proteins by analyzing the diffraction of electrons from numerous protein molecules. Since the use of cryo-EM to solve the structure of 2D-crystalline bacteriorhodopsin in purple membranes in 1975,[20] technological advances and pioneering research efforts have enabled the technique to determine protein structures as small

as ~130 kDa.[21,22] Smaller proteins, however, remain difficult due damage and movements induced by exposure to the electron beam, and the resolution of cryo-EM is often lower (~3.5 Å) than that of X-ray diffraction. Notably, the specific sample preparations required for X-ray crystallography and cryo-EM approaches limit the suitability of these techniques for examining the structure of proteins in non-crystalline and compositionally and structurally diverse synthetic hosts.

Solid-state NMR spectroscopy is a powerful means for interrogating the atomic-level structures and dynamics of proteins in synthetic host materials. In proteins, the chemical shifts of ^{1}H, ^{13}C and ^{15}N species are sensitive to local environments and can be correlated and assigned to specific amino acid residues, thereby providing site-specific information. Through-space dipole-dipole and through-bond scalar (*J*) interactions between ^{1}H, ^{13}C and ^{15}N spins can be exploited to determine the proximities and bonding of various nuclei that can be used as intramolecular structural constraints, while separate measurements can yield information about protein dynamics. Similarly, intermolecular interactions of proteins with other molecules, including with ligands,[23] other proteins,[24] or inorganic surfaces[25,26] can be determined. Several limitations of NMR are mitigated by recent advancements in superconducting magnet technologies that provide very high (23.5 Tesla) and homogeneous magnetic fields, probeheads that are capable of very fast (up to 110 kHz) magic-angle-spinning (MAS) rates,[27] pulse sequence design and spectral analyses,[27–30] and isotopic enrichment strategies.[31] Collectively, these advances have also enabled sensitive ^{1}H-detection schemes to be employed for solid-state NMR measurements of biological solids,[32–34] allowing up to 4x improvement in signal sensitivity versus conventional methods that use ^{13}C and ^{15}N detection.

Here, we report an atomic-level analysis of the physicochemical factors that influence the structures, dynamics, and corresponding functionalities of the membrane protein proteorhodopsin in a mesostructured silica synthetic host material. Surfactant species are ubiquitous in protocols that stabilize protein structures and functions outside of native cellular lipid bilayers, such as in micellar solutions or in synthetic host materials. We exploit the properties of such surfactants to stabilize proteorhodopsin (PR) molecules and to co-assemble them at high loadings (~15 wt%) within mesostructured silica. A primary objective is to understand how the protein-stabilizing surfactants and inorganic silica host influence the structures and dynamics of PR guest molecules. Powerful multidimensional solid-state NMR techniques are used to probe and correlate the atomic-level structures and conformational dynamics of the hepta-helical membrane protein proteorhodopsin in synthetic mesostructured silica environments with the photocycle kinetics of PR that account for its light-activated H^+ pumping properties.

Materials and methods

Protein expression and purification: Protein expression and purification were carried out as described previously, but with a few minor differences. These include that *E. Coli* cell membranes were lysed by incubation in lysozyme, DNAse, and $MgCl_2$ for one hour and subsequently freeze fractured using liquid N_2 (three freeze-thaw cycles) and sonicated. Next, lysed membranes were washed 150 mM KCl and 50 mM K_2HPO_4 buffered solution until the solution supernatant became transparent, which required approximately 250 mL of buffered KCl/K_2HPO_4 solution. PR was extracted from lysed cell membranes by incubation in 4% (w/v) n-dodecyl-β,D-maltoside (DDM) overnight.

Size-exclusion chromatography was used to isolate the monomeric fraction of PR. All PR samples were incubated overnight in solutions containing 2% diC_7PC to enrich the monomeric population. The monomeric/dimeric fractions of PR from SEC were concentrated in 50 kDa centrifugal concentrators to a volume of ~1 mL. Then the protein was desalted in a PD-10 desalting column equilibrated with dilute HCl solution (pH ~4) containing 0.05% DDM. The eluate was concentrated using a 50 kDa concentrator to a volume of approximately 200 uL after which 800 uL of D_2O (98%, Cambridge Isotopes) was added. Solution-state ^1H NMR was used to quantify the DDM surfactants in the solution of PR. In particular, the integrated intensities of ^1H NMR peaks at 0.8, 1.2, 1.5 ppm in spectra from the proteorhodopsin sample were compared with a 0.1 wt% DDM in D_2O. The concentration of protein for all measurements was calculated by the absorbance peak at 520 nm with an extinction coefficient of 49,000 M cm^{-1}. The purity of PR was assessed by the A_{280}/A_{520} ratio, which was ~1.9-2.2 for all samples in this study.

To synthesize mesostructured silica materials with high loadings of PR guests required low quantities of DDM and diC_7PC relative to the PR concentration. To remove excess DDM and diC_7PC, the monomeric PR fractions from SEC were bound to Ni-NTA resin, which was subsequently washed with ~150 mL of solutions containing 150 mM KCl, 50 mM K_2HPO_4 and 0.05 wt% DDM. Following these washing steps, PR was eluted from the resin by incubation the same solution but with 500 mM imidazole, desalted in a PD-10 column equilibrated with dilute HCl solution (pH 4) with 0.05 wt% DDM, and concentrated using a 50 kDa centrifugal concentrator (Millipore) to a volume of 200 μL. The sample was diluted with 800 μL of DDM and the DDM concentration determined as described above. Subsequently, the sample was concentrated using a 3 kDa MWCO centrifugal concentrator

(Millipore) to a PR concentration of 150-300 μM, and the DDM concentration calculated based on the volume change of the sample during this concentration step.

Reconstitution of PR into DMPC/DMPA lipids: Proteorhodopsin was reconstituted into DMPC/DMPA lipids using the protocols described previously,[35] except using a 10 mM HEPES buffer titrated to a pH of 6.2 using HCl (aq.).

Material synthesis: 350 mg of tetraethoxysilane (TEOS) was mixed with 1.5 g of water and 10 uL of 400 mM HCl (aq.) and vigorously stirred for approximately two hours until the solution became transparent, indicating that a significant extent of silica precursor has been hydrolyzed. 200 mg of this solution was isolated and mixed with an appropriate amount of n-dodecyl-β,D-maltoside (DDM). The resulting solution was mixed with a solution of proteorhodopsin in an acidic solution containing DDM and diC_7PC surfactants and titrated using small quantities of 1 M HCl (or NaOH) to a pH of ~3.5-4. Solutions were drop-cast onto PDMS stamps (~2.5cm x 2.5cm x 0.5cm) under conditions of 75% relative humidity and room temperature (20 °C) to allow for solvent evaporation. Solvent evaporation was allowed to occur for two days before characterization of the materials.

Time-resolved absorption techniques and analyses: Flash photolysis measurements were acquired using a spectraphysics Nd:YAG laser tuned to a 532 nm pulse with a time constant of 15 μs. A Xenon lamp outfitted with a monochrometer was used to generate the measuring light, and the transient absorbance signals transmitted through the sample were filtered through a monochrometer and collected by an oscilloscope. All measurements were acquired with a 1

s delay time between laser pulses to allow all PR species to achieve equilibrium in its initial state before the next signal-averaging UV-visible measurement. Absorbance data was acquired from times ranging from 1 μs to 1 s on a linear timescale and subsequently averaged to yield evenly spaced data points on a logarithmic time scale. Prior to flash photolysis measurements, samples of monomeric/dimeric PR in surfactant solutions were incubated in appropriate amounts of DDM and diC_7PC overnight for 24 hrs at 4°C to ensure equilibrium of surfactants and PR species. Measurements were conducted on quartz curvettes filled with the PR-containing surfactant solutions that had PR concentrations of approximately 10 μM PR. Before measurement, nanostructured silica films containing monomeric/dimeric PR were incubated in at 100% RH at 4°C for five days to hydrate the materials. The humidity was controlled at 100% RH for nanostructured silica films during the flash photolysis measurements. Global fitting analyses of the transient UV-visible absorbances were performed using a home-written MATLAB code from a recent study.[16]

Results and discussion

Mesostructured silica materials were synthesized from aqueous solutions by the co-assembly of silica precursor species with the protein-stabilizing surfactants *n*-dodecyl-ß,D-maltoside (DDM) and 1,2-diheptanoyl-*s,n*-glycero-3-phosphocholine (diC_7PC). The resulting material had a mechanically robust inorganic silica framework with wormlike surfactant mesochannels ~3 nm in diameter, into which the hydrophobic proteorhodopsin guest species were incorporated [6]. Three-dimensional (3D) NMR analyses identify signals associated with the residues of the PR molecules and subsequently enabled site-specific structural and dynamical information about the protein guests confined in the mesostructured silica host.

Subsequent comparisons with PR in near-native lipid and surfactant environments identified regions of PR that were perturbed by inclusion into the synthetic hosts.

Importantly, this approach relies on high NMR sensitivities and resolutions that are realized by investigating materials with high (13 wt%) loadings of ^{2}H,^{13}C,^{15}N-enriched PR guests (with 100% back-exchange of ^{1}H species at solvent-exposed sites), and the use of sensitive ^{1}H-detection schemes, strong (18.8-23.5 T) magnetic fields, and ultra-fast (60-100 kHz) MAS rates. At such high PR loadings the mesostructured silica materials show a single broad SAXS reflection with a *d*-spacing of 5.2 nm that is greater than that of otherwise identical materials without PR, indicating a swelling of the mesochannels upon incorporation of PR (Appendix B, Figure S8).

Proteorhodopsin function in mesostructured silica.

For mesostructured silica that incorporate macroscopically aligned and functionally-active PR guests, higher loadings of PR would promote greater fluxes of H^{+}-ions across the host material in response to light, translating to more efficient macroscopic solar energy conversion. Should all PR guest species be active, the structures of these species would be uniform and support native function. Such homogeneity, however, is often difficult to achieve in synthetic hosts because the abiological processing conditions and host components may irreversibly destabilize protein structures; moreover, for hosts with anisotropic nanoscale features (e.g., surfactant mesochannels), structural heterogeneities are introduced simply by the mutual orientation of the protein guest and the feature.

Information about the H^{+}-ion pumping functionalities of proteorhodopsin species is obtained from the transient absorbance behaviors of the protein in response to light. Following activation by green light, PR undergoes a series of local and large-scale motions that result in

the net movement of an H^+-ion from the cytoplasmic to periplasmic side of the protein. Some of these motions perturb the retinal chromophore and therefore manifest as changes in absorbance. For example, after a short green (532 nm) laser pulse a mesostructured silica membrane with 13 wt% PR excited exhibits complex transient absorbance behaviors at several wavelengths, as shown in Figure 1(A). At early (10^{-5} s) times, positive difference absorbances are observed at 630 nm and 550 nm while the absorbances at 410 and 500 nm are bleached. As time progresses the difference absorbances at 410, 500 and 630 nm monotonically decay to zero by multiexponential processes, while the 550 nm absorbance becomes negative at times beyond ~$1x10^{-4}$ s and subsequently decays to zero. Qualitatively similar behaviors are observed for PR in lipid environments (Figure 1B), except that the 570 nm absorbance remains bleached over the entire time range investigated. These results provide evidence that PR largely retains native-like photo-responsivities in the synthetic mesostructured silica environments, but suggests slightly different photocycle kinetics for PR in the two environments.

To interpret these subtle kinetic differences, we analyzed the absorption behaviors quantitatively with respect to a well-established kinetic reaction model of PR. Detailed investigations by Varo et al.[36] established that, under acidic conditions, PR undergoes a cyclic photochemical reaction cycle with four intermediates *K*, *L*, *N* and *PR'*, as depicted in Figure 1A. Apparent rate coefficients for this reaction sequence can be obtained by a global fitting routine, in which transient absorbances are collectively fit to a series of irreversible reactions with first-order rate kinetics. Accurate fits to the absorption data require three exponentials that, based on reported rate kinetics for PR under acidic conditions,[36] correspond predominantly to the interconversions of the *K* and *L* intermediates (τ_1), the *L* and *N* (τ_2), and the *N*, *PR'* and *PR* (τ_3) intermediates, as indicated in the schematic photocycles in Figure 1.

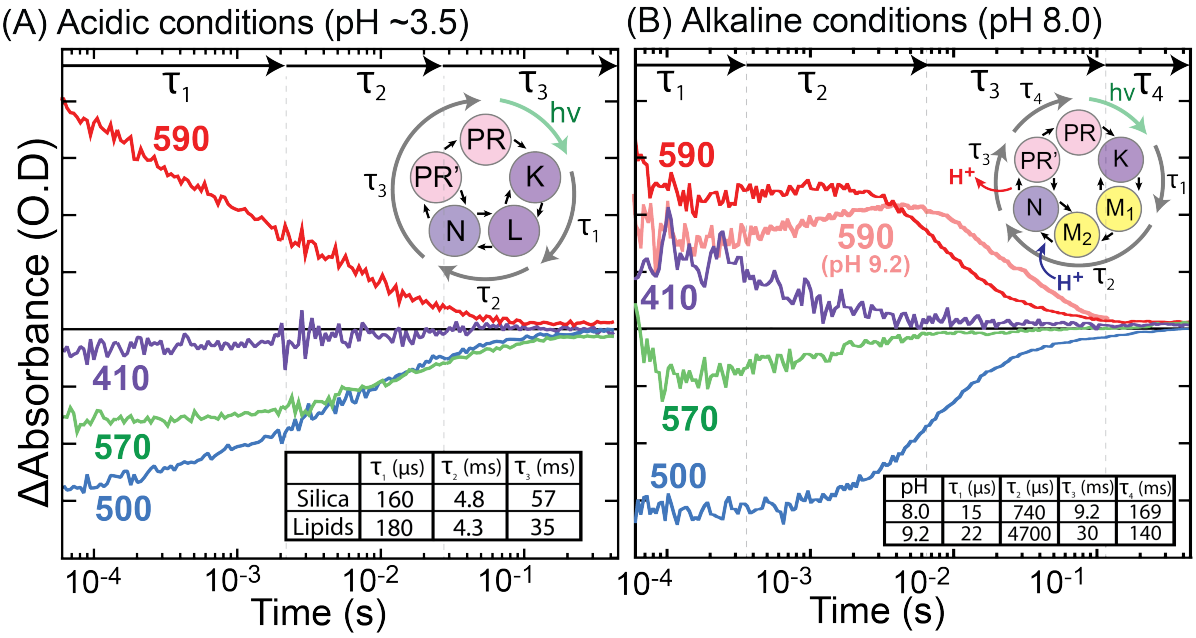

Figure 15. Time-resolved differences in the UV-visible light absorption of proteorhodopsin in mesostructured silica **(A)** hydrated at 100% relative humidity for >1 month or **(B)** exposed to bicine/CHES buffered solutions (aq.) at either pH 8.0 or 9.2. The transient absorbances were measured at different wavelengths: 410 nm (purple), 500 nm (blue), 570 nm (green), and 630 nm (orange) after excitation by a 10 ns laser pulse at 532 nm. The insets show schematic diagrams of the photochemical reaction cycles of proteorhodopsin in lipid membranes as reported by Varo et al.[38]. Measurements under acidic and alkaline conditions were conducted on mesostructured silica films containing 13 wt% and 5 wt% PR, respectively. All measurements were acquired at ~295 K.

Comparisons with the transient absorbance responses of PR in mesostructured silica and near-native lipids (Appendix B, Figure S9) reveal high qualitative and quantitative similarities. Specifically, as shown in Figure 1A the τ_1 and τ_2 timescales are nearly identical for PR in these environments, while the τ_3 timescale is approximately 60% longer for PR in mesostructured silica hosts than in lipids, establishing a slightly slower photocycle for PR in the mesostructured silica hosts. These analyses support that the synthetic mesostructured silica environments support the light-activated conformational changes necessary for H^+-ion pumping function.

To assess whether PR guests in mesostructured silica pump H^+-ions in response to light, we probed the photochemical reaction cycle of PR under alkaline conditions. Light-activated

H^+-ion transport by PR requires a deprotonated carboxylic acid moiety of aspartic acid residue 97,[37] which generally occurs for PR under pH conditions at >7.0. Under such conditions, Váró et al developed a photochemical reaction model (shown in Figure 1B, inset) for PR in lipid environments, which bears similarity to that under acidic conditions but lacks an observable *L* intermediate and includes M_1 and M_2 intermediates that have a blue-shifted absorbance (λ_{max}~410 nm) versus the *PR* state.[38] The transient absorbance responses of PR in mesostructured silica soaked in alkaline (pH 8.0) buffered solutions, shown in Figure 3B, include positive absorbance intensities at 410 nm at early (<20 μs) times that establish the presence of M_1 and/or M_2 intermediates. At subsequent times, the absorbance intensity at 410 nm decays concomitantly with a rise at 590 nm, which can be assigned to an increase in the population of *N* intermediates. These qualitative absorbance trends can be explained and agree well with that photochemical reaction model of PR in near-native lipids under alkaline conditions. Moreover, a global fitting analyses of the absorbance behaviors for PR in mesostructured silica films yields five apparent timescales, assigned to interconversions of intermediates in Figure 3B, that are in close quantitative agreement with those reported for PR in near-native lipid environments.[39] These analyses clearly establish that, following exposure to alkaline solutions, PR guests in mesostructured silica hosts undergo the alkaline photochemical reaction known to support activated H^+-ion pumping.

A crucial step in light-activated H^+-ion transport mechanism of PR is the uptake and subsequent release of H^+-ions from bulk solution, which occur during the M_2 to *N* and *N* to *PR'* transitions, respectively, as shown schematically in the inset of Figure 1B [39]. As a result, at sufficiently high alkalinities the photochemical reaction cycle becomes limited by H^+-ion diffusion to PR species and, accordingly, the *N* intermediate will begin to accumulate at later

times with increasingly alkaline conditions. The transient absorbance behaviors of PR in mesostructured silica soaked in highly alkaline (pH 9.2) buffered solutions show an accumulation of the 590 nm absorbance at longer times (Figure 1B, pink line) versus under conditions of lower pH (8.0), indicating a delayed accumulation of the *N* intermediate with increasing pH. The later accumulation of the *N* intermediate is also borne out quantitatively in the global fitting analyses (Figure 1B, inset), which show a >600% longer τ_2 timescales than for PR films under slightly more neutral (pH 8.0) conditions. As this τ_2 timescale is associated with the conversion of M_1 and M_2 intermediates to *N* intermediates, this signifies a substantially slower conversion of M_2 to *N* intermediates for PR in mesostructured silica at the more alkaline pH. Such pH-dependent absorbance behaviors establish an H^+-ion diffusion limitation in the photocycle of PR in synthetic mesostructured silica hosts, supporting that PR uptakes H^+-ion species in accordance with the native-like H^+-ion transport mechanism of PR. These results provide strong evidence that PR guests pump H^+-ions in response to green light.

Powerful three-dimensional solid-state NMR analyses were employed to assess the distributions of local environments and structures proteorhodopsin guests in mesostructured silica hosts. For example, each intensity in the 3D (H)CANH NMR spectra correlates the signals from ^1H, ^{13}C, and ^{15}N nuclei of individual residues on the PR backbone. The 3D (H)CANH spectrum (Fig. 2A) recorded from hydrated ^2H,^{13}C,^{15}N-enriched PR in mesostructured silica shows numerous highly-resolved signals, also observed in the 2D projections (Figure 2A), that are each associated with one of the 246 backbone residues of the PR guests. Such sharp signals imply low levels of inhomogeneous broadenings, which would arise from a wide distribution of PR environments, establishing that PR guests have highly uniform structures in the hydrated synthetic mesostructured silica materials. Importantly, the

high signal resolutions achieved through hydrating the mesostructured silica materials facilitates the sequence-specific resonance assignments of PR residues.

The assignments of signals in the 3D NMR spectra are essential to probe the site-specific structures and dynamics of proteorhodopsin in synthetic mesostructured silica hosts. While the (H)CANH measurements correlate signals of moieties on the same residue, separate (H)CA(CO)NH measurements employ inter-residue coherence transfers to correlate moieties on adjacent residues. Simultaneous analyses of both spectra allow signals from adjacent residues to be linked by common NH resonances, enabling the signals to be sequentially assigned to residues along the protein backbone. Using as a guide the resonance assignments for PR in surfactant micellar environments,[40] and in lipid bilayers,[41–43] the 3D NMR analyses yielded assignments for 65 residues of the protein backbone, as shown schematically in Figure 2B. These assignments include those on the D-E and E-F loops, which importantly undergo large movements associated with the light-activated H^+-ion pumping mechanisms,[44] as well as residues D227 and K231 in the G loop that are involved with H^+ transport.[39,45] A majority of the residues in the hydrophobic transmembrane region could not be assigned, which is typical of ^2H,^{13}C,^{15}N-enriched membrane proteins, including PR,[43] which have transmembrane backbone ^2H amide groups that do not exchange with the protonated solvent and therefore produce no signals in the ^1H-detected NMR measurements. Nonetheless, the 65 residues for which assignments were made provide deep and meaningful insights into the structures of PR species in mesostructured silica hosts.

Structural comparisons with PR in native-like lipid environments.

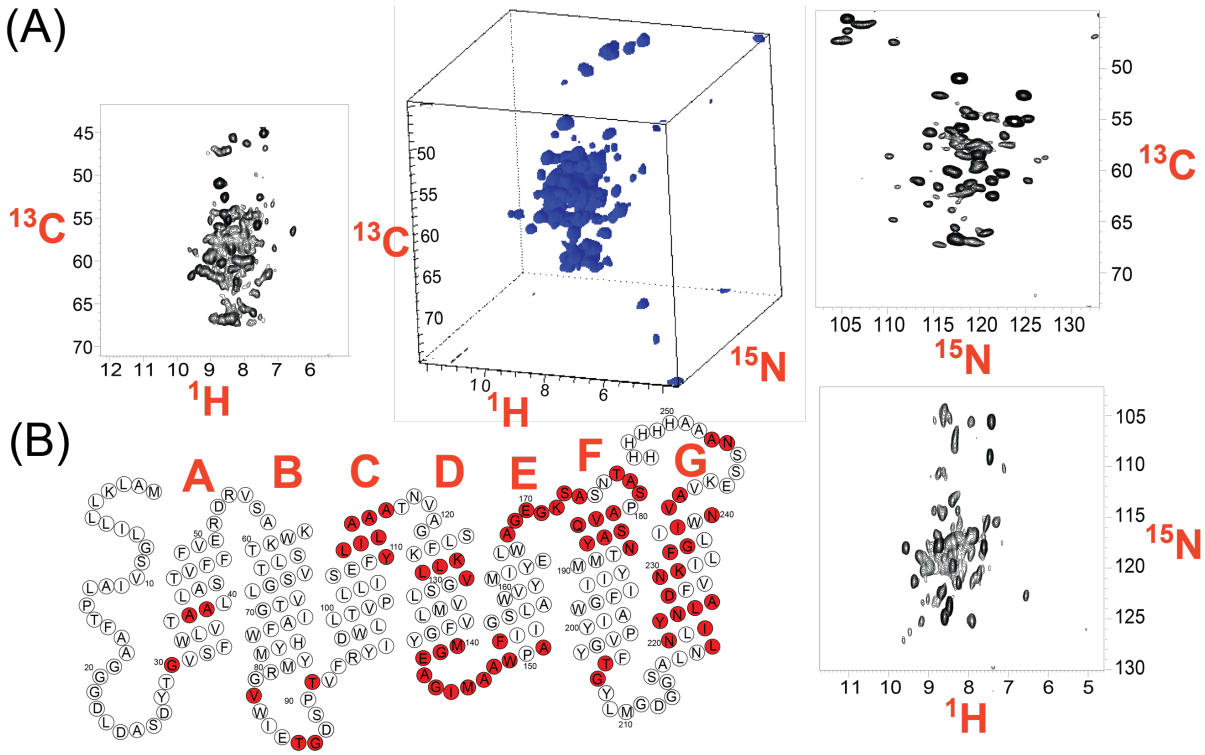

Figure 16. (A) Solid-state 3D (H)CANH NMR spectrum of 13 wt% ^{2}H,^{13}C,^{15}N-labeled proteorhodopsin in hydrated mesostructured silica, with accompanying projections onto the ^{1}H, ^{15}N, and ^{13}C spectral planes; **(B)** Schematic diagram of proteorhodopsin with assigned residues colored in red in which helices A-G are labeled in red above each respective helix. NMR measurements were conducted at 60 kHz MAS at 18.8 T and at a nominal temperature of 300 K.

Key differences among the local environments of proteorhodopsin in synthetic silica and native lipid environments can be distinguished by comparing the chemical shift positions of NMR signals. The structures and dynamics of proteorhodopsin have been characterized extensively by NMR in micellar solutions[40] and reconstituted into lipid environments,[24,35,43,46–49] enabling detailed comparisons with the properties of proteorhodopsin guests in synthetic mesostructured silica membranes. The chemical shift interactions of ^{1}H, ^{13}C and ^{15}N moieties are sensitive to local protein structure and therefore are useful to identify regions on PR molecules that are influenced by the local mesochannel environment. Proteorhodopsin molecules reconstituted into native-like lipids, shown schematically in Figure 1A (top), serve

as a standard by which to assess whether and to what extent PR in synthetic host environments (Figure 1A, bottom) exhibit native-like folding and structures.

A 3D NMR spectrum acquired from $^{2}H,^{13}C,^{15}N$-labeled proteorhodopsin reconstituted into native-like DMPC/DMPA lipids show well-resolved signals, the 2D projections of which are shown in red in Figure 3B. Analyses of (H)CANH and (H)CONH spectra of PR in lipids yielded assignments for all residues shown in Figure 2B. A comparison of the positions and intensities of these signals (Figure 3B, red) with those from PR in mesostructured silica (Figure 3B, black) reveal only small differences for most residues, as evidenced by the many resolved correlations the 2D projections in Figure 3B with nearly identical positions and intensities. A specific region of high spectral similarity is in the NH projection (Figure 3B) at 105-110 ppm in the ^{15}N dimension, where the signals assigned to residues G30, T86, G144 and G169 (Figure 3, blue arrows) overlap precisely among the two spectra. This reflects a high degree of

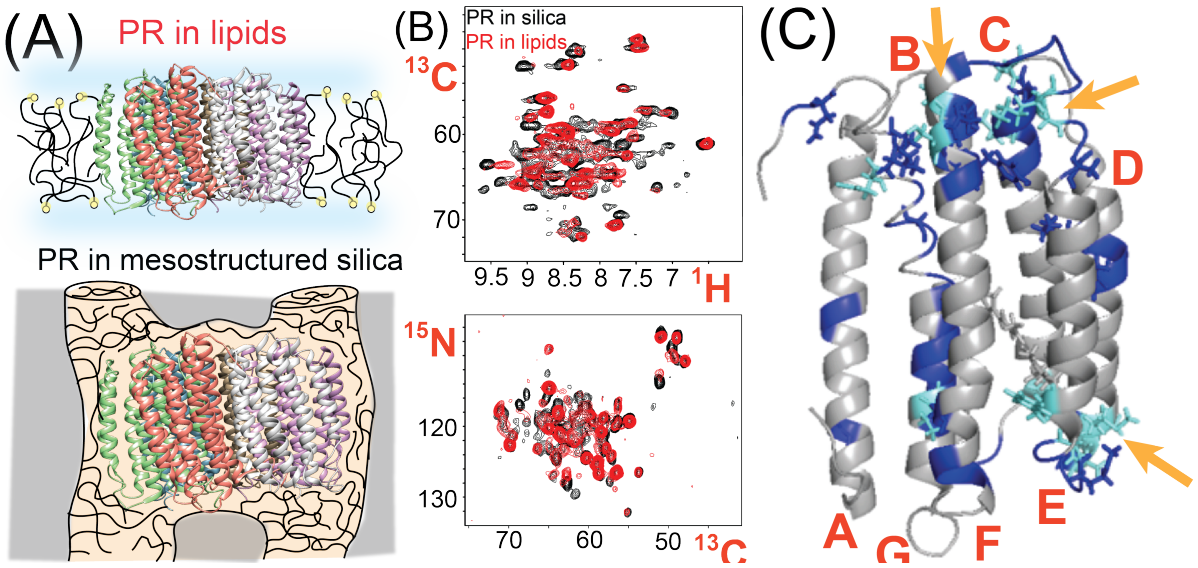

Figure 17. (A) Schematic diagrams of PR in lipid membranes (top) and mesostructured silica-surfactant hosts (bottom). **(B)** 2D projections NCA (top), HN(middle), and HCA (bottom) from solid-state 3D (H)CANH spectra of $^{2}H,^{13}C,^{15}N$-labeled proteorhodopsin in (black) hydrated mesostructured silica (13 wt% protein) and (red) DMPC/DMPA lipids. (C) Schematic structural diagram of proteorhodopsin (from PDB: 2L6X) in which residues colored blue and teal exhibited small and large chemical shift differences, respectively, between (H)CANH spectra collected from PR in mesostructured silica and sedimented DDM+diC_7PC. Helices A-G are labeled in red. Measurements were conducted at 18.8 T, 60 kHz MAS, and 300 K.

structural similarity of PR species in the synthetic mesostructured silica and native-like lipid environment.

Nevertheless, there are several notable differences between the 3D NMR (H)CANH spectra of proteorhodopsin in synthetic mesostructured silica hosts and in lipids. These are in the ^{15}N chemical shift regions of 102-112 ppm and 124-128 ppm, where a few correlated pairs of ^{15}N and ^{1}H signals present in the 2D spectrum of PR in lipids (Fig. 3A, blue) are absent in that of PR in mesostructured silica (Fig. 2A, black). A global chemical shift perturbation analyses reveals that 12 of the 64 mutually resolved signals experience significant (∂_{NH} = >0.1 ppm) displacements, while 22 others exhibit moderate (0.1 ppm > ∂_{NH} > 0.05 ppm) differences between the two spectra, as illustrated schematically in Figure 3C. Regions of PR with particularly high concentrations of strongly perturbed residues are the periplasmic side of the periplasmic side of the G-helix, the D-E loop, and the E-F loop (Figure 3C, orange arrows), establishing that these regions undergo the most significant structural changes upon incorporation into the mesostructured silica materials. No chemical shift perturbations are observed for helices A, B and G that participate in inter-protein interactions responsible for oligomerization,[24] supporting that PR in mesostructured silica and lipids are in the same oligomeric state, likely pentameric or hexameric as evidenced by BN-PAGE analysis of PR prior to incorporation into mesostructured silica (Appendix B, Figure B7) of PR prior to incorporation into mesostructured materials and the proclivity of PR to form pentameric/hexameric assemblies in lipids.[50] The deviations in the structures of PR in synthetic silica versus native lipids could originate from the structure-directing DDM and diC_7PC surfactants, which interact strongly with the hydrophobic transmembrane regions of PR, and the interaction or confinement of PR with the inorganic silica framework, which has a slight

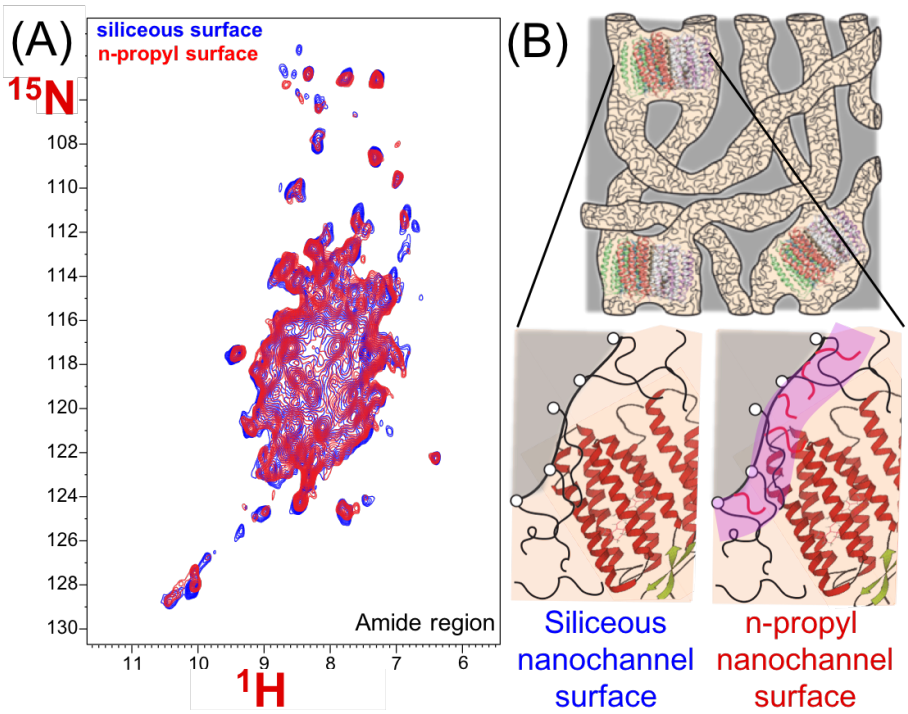

Figure 18. 2D hNH heteronuclear correlation spectra recorded from $^{2}H,^{13}C,^{15}N$-enriched PR in nanostructured silica materials inorganic frameworks that are fully siliceous **(A)** and contain 25% n-propyl-functionalized silica precursor species. **(B)** A schematic diagram of PR in the nanochannels that are fully siliceous (left) and surface-functionalized with n-propyl species (right).(Figure (A) courtesy of Dr. Daniela Lalli)

negative charge and has numerous silanol moieties that could support electrostatic or hydrogen bonding interactions, respectively.

To further investigated the possible influence of interactions with the silica surface with proteorhodopsin guests, the structures of proteorhodopsin in synthetic silica hosts with fully siliceous and n-propyl functionalized nanochannel surfaces. Alkyl n-propyl functionalities were introduced into the silica framework during synthesis by the co-condenstation of n-propyl-functionalized silica precursors and non-functionalized silica precursors. Based on the relatively hydrophobic alkyl n-propyl groups, they are expected to reside at the nanochannel interface, nearby the alky tail groups of the structure-directing surfactants, but still part of the silica framework. In such a configuration, the n-propyl alkyl groups would likely decorate the

surface of the nanochannels, as shown in Figure 4A in red. The 2D hNH spectrum (Figure 4B, red) recorded from 12.5 wt% $^{2}H,^{13}C,^{15}N$-enriched PR in n-propyl surface-functionalized nanostructured silica materials show sharp intensity correlations that reflect fast dynamic motions of the PR guests. A spectrum collected from an otherwise identical material except without n-propyl surface functionalities bears high similarity, with only a few minor differences indicated with orange arrows. Such small dependencies of PR structure on surface functionalization suggest weak interactions with the silica surface and provide additional evidence that the effects of structure-directing surfactants, as opposed to the silica walls, most predominantly adjust protein structure in nanostructured host materials.

Conclusion

The functionalities and structures of the membrane protein proteorhodopsin in synthetic nanostructured silica hosts are correlated. Functionally-active proteorhodopsin species in nanostructured silica hosts are shown to have native-like transient absorption behaviors in response to green light, that provide clear evidence that proteorhodopsin guests retain native light-activated H^{+}-ion pumping functionalities. Interestingly, however, the kinetics of the photochemical reaction cycles are different from those of PR in near-native lipid and micellar surfactant environments. To explain these differences, powerful three-dimensional NMR techniques were employed to interrogate the structures of proteorhodopsin species in separate lipid, surfactant, and nanostructured silica environments. Subsequent comparisons revealed similarly native-like PR structures in each environment, but with subtle differences that were suggested to arise from effects of the structure-directing surfactants, rather than the silica nanochannel walls.

References

(1) Liang, H.; Whited, G.; Nguyen, C.; Stucky, G. D. *Proc. Natl. Acad. Sci. U. S. A.* **2007**, *104*, 8212.

(2) Hua, D.; Kuang, L.; Liang, H. *J. Am. Chem. Soc.* **2011**, *133*, 2354.

(3) Wang, M.; Wang, Z.; Wang, X.; Wang, S.; Ding, W.; Gao, C. *Environ. Sci. Technol.* **2015**, *49*, 3761.

(4) Jeon, T.-J.; Malmstadt, N.; Schmidt, J. J. *J. Am. Chem. Soc.* **2006**, *128*, 42.

(5) Luo, T.-J. M.; Soong, R.; Lan, E.; Dunn, B.; Montemagno, C. *Nat. Mater.* **2005**, *4*, 220.

(6) Jahnke, J. P.; Idso, M. N.; Hussain, S.; Junk, M. J. N.; Han, S.; Chmelka, B. F. *Submitt. J. Am. Chem. Soc.* **2017**.

(7) Balashov, S. P. *Science (80-.).* **2005**, *309*, 2061.

(8) Béjà, O.; Aravind, L.; Eugene, V.; Suzuki, M. T.; Hadd, A.; Nguyen, L. P.; Jovanovich, S. B.; Gates, C. M.; Feldman, R. A.; Spudich, J. L.; Spudich, E. N.; DeLong, E. F. *Science* **2000**, *289*, 1902.

(9) Veatch, W.; Stryer, L. *J. Mol. Biol.* **1977**, *113* (1), 89.

(10) de Groot, B. L.; Grubmüller, H. *Science* **2001**, *294* (5550), 2353.

(11) Ferré, S.; Casado, V.; Devi, L. A.; Filizola, M.; Jockers, R.; Lohse, M. J.; Milligan, G.; Pin, J.-P.; Guitart, X. *Pharmacol. Rev.* **2014**, *66*, 413.

(12) Kaplan, J. H. *Annu. Rev. Biochem.* **2002**, *71*, 511.

(13) Wikström, M. *Biochim. Biophys. Acta - Bioenerg.* **2004**, *1655* (1–3), 241.

(14) Kühlbrandt, W. *Nature* **2000**, *406*, 569.

(15) Hussain, S.; Kinnebrew, M.; Schonenbach, N. S.; Aye, E.; Han, S. *J. Mol. Biol.* **2015**, *427*, 1278.

(16) Idso, M. N.; Baxter, N.; Narayanan, S.; Chang, E.; Fisher, J.; Chmelka, B. F.; Han, S. *Prep. J. Mol. Biol.* **2017**.

(17) Chitnis, P. R. *Annu. Rev. Plant Physiol. Plant Mol. Biol.* **2001**, *52*, 593.

(18) Moller, J. V; Maire, M.; Pierre, I. U.; Paris, C.; Yvette, F.-G.-. *J. Biol. Chem.* **1993**, *268*, 18659.

(19) Le Maire, M.; Champeil, P.; Møller, J. V. *Biochim. Biophys. Acta - Biomembr.* **2000**, *1508* (1–2), 86.

(20) Henderson, R.; Baldwin, J. M.; Ceska, T. a; Zemlin, F.; Beckmann, E.; Downing, K. H. *J. Mol. Biol.* **1990**, *213* (4), 899.

(21) Park, E.; Campbell, E. B.; MacKinnon, R. *Nature* **2016**, *541* (7638), 500.

(22) Kühlbrandt, W. *Science* **2014**, *343*, 1443.

(23) Cala, O.; Guillière, F.; Krimm, I. *Anal. Bioanal. Chem.* **2014**, *406*, 943.

(24) Maciejko, J.; Mehler, M.; Kaur, J.; Lieblein, T.; Morgner, N.; Ouari, O.; Tordo, P.; Becker-Baldus, J.; Glaubitz, C. *J. Am. Chem. Soc.* **2015**, *137*, 9032.

(25) Geiger, Y.; Gottlieb, H. E.; Akbey, Ü.; Oschkinat, H.; Goobes, G. *J. Am. Chem. Soc.* **2016**, *138* (17), 5561.

(26) Gebbie, M. A.; Wei, W.; Schrader, A. M.; Cristiani, T. R.; Dobbs, H. A.; Idso, M.; Chmelka, B. F.; Waite, J. H.; Israelachvili, J. N. *Nat. Chem.* **2017**, *9*, 473.

(27) Stanek, J.; Andreas, L. B.; Jaudzems, K.; Cala, D.; Lalli, D.; Bertarello, A.; Schubeis, T.; Akopjana, I.; Kotelovica, S.; Tars, K.; Pica, A.; Leone, S.; Picone, D.; Xu, Z.; Dixon, N. E.; Martinez, D.; Berbon, M. Ø.; Mammeri, N. El; Noubhani, A.; Saupe, S.; Habenstein, B.; Loquet, A.; Pintacuda, G. *Angew. Chemie* **2016**, *55*, 15504.

(28) Andreas, L. B.; Le Marchand, T.; Jaudzems, K.; Pintacuda, G. *J. Magn. Reson.* **2015**,

253, 36.

(29) Lalli, D.; Schanda, P.; Chowdhury, A.; Retel, J.; Hiller, M.; Higman, V. A.; Handel, L.; Agarwal, V.; Reif, B.; Van Rossum, B.; Akbey, Ü.; Oschkinat, H. *J. Biomol. NMR* **2011**, *51*, 477.

(30) Andreas, L. B.; Jaudzems, K.; Stanek, J.; Lalli, D.; Bertarello, A.; Le Marchand, T.; Cala-De Paepe, D.; Kotelovica, S.; Akopjana, I.; Knott, B.; Wegner, S.; Engelke, F.; Lesage, A.; Emsley, L.; Tars, K.; Herrmann, T.; Pintacuda, G. *Proc. Natl. Acad. Sci. U. S. A.* **2016**, *113*, 9187.

(31) Mance, D.; Sinnige, T.; Kaplan, M.; Sinnige, T.; Kaplan, M.; Narasimhan, S.; Daniëls, M.; Houben, K.; Baldus, M.; Weingarth, M. *Angew. Chemie Int. Ed.* **2015**, *127*, 16025.

(32) Barbet-Massin, E.; Pell, A. J.; Retel, J. S.; Andreas, L. B.; Jaudzems, K.; Franks, W. T.; Nieuwkoop, A. J.; Hiller, M.; Higman, V.; Guerry, P.; Bertarello, A.; Knight, M. J.; Felletti, M.; Le Marchand, T.; Kotelovica, S.; Akopjana, I.; Tars, K.; Stoppini, M.; Bellotti, V.; Bolognesi, M.; Ricagno, S.; Chou, J. J.; Griffin, R. G.; Oschkinat, H.; Lesage, A.; Emsley, L.; Herrmann, T.; Pintacuda, G. *J. Am. Chem. Soc.* **2014**, *136* (35), 12489.

(33) Chevelkov, V.; Rehbein, K.; Diehl, A.; Reif, B. *Angew. Chemie - Int. Ed.* **2006**, *45* (23), 3878.

(34) Zhou, D. H.; Shah, G.; Cormos, M.; Mullen, C.; Sandoz, D.; Rienstra, C. M. *J. Am. Chem. Soc.* **2007**, *129* (38), 11791.

(35) Shi, L.; Lake, E.; Ahmed, M. A. M.; Brown, L. S.; Ladizhansky, V. *Biochim. Biophys. Acta* **2009**, *1788* (12), 2563.

(36) Lakatos, M.; Lanyi, J. K.; Szakács, J.; Váró, G. *Biophys. J.* **2003**, *84*, 3252.

(37) Dioumaev, A. K.; Wang, J. M.; Bálint, Z.; Váró, G.; Lanyi, J. K. *Biochemistry* **2003**, *42*, 6582.

(38) Váró, G.; Brown, L. S.; Lakatos, M.; Lanyi, J. K. *Biophys. J.* **2003**, *84*, 1202.

(39) Dioumaev, A. K.; Brown, L. S.; Shih, J.; Spudich, E. N.; Spudich, J. L.; Lanyi, J. K. *Biochemistry* **2002**, *41*, 5348.

(40) Reckel, S.; Gottstein, D.; Stehle, J.; Löhr, F.; Verhoefen, M.; Takeda, M.; Silvers, R.; Kainosho, M.; Glaubitz, C.; Wachtveitl, J.; Bernhard, F.; Schwalbe, H.; Güntert, P.; Dötsch, V. *Angew. Chemie Int. Ed.* **2011**, *50*, 11942.

(41) Shi, L.; Ahmed, M. A. M.; Zhang, W.; Whited, G.; Brown, L. S.; Ladizhansky, V. *J. Mol. Biol.* **2009**, *386*, 1078.

(42) Shi, L.; Lake, E. M. R.; Ahmed, M. A. M.; Brown, L. S.; Ladizhansky, V. *Biochim. Biophys. Acta* **2009**, *1788*, 2563.

(43) Ward, M. E.; Shi, L.; Lake, E.; Krishnamurthy, S.; Hutchins, H.; Brown, L. S.; Ladizhansky, V. *J. Am. Chem. Soc.* **2011**, *133*, 17434.

(44) Hussain, S.; Franck, J. M.; Han, S. *Angew. Chemie Int. Ed.* **2013**, *52*, 1953.

(45) Herz, J.; Verhoefen, M. K.; Weber, I.; Bamann, C.; Glaubitz, C.; Wachtveitl, J. *Biochemistry* **2012**, *51*, 5589.

(46) Good, D. B.; Wang, S.; Ward, M. E.; Struppe, J.; Brown, L. S.; Lewandowski, J. R.; Ladizhansky, V. *J. Am. Chem. Soc.* **2014**, *136*, 2833.

(47) Pfleger, N.; Wörner, A. C.; Yang, J.; Shastri, S.; Hellmich, U. A.; Aslimovska, L.; Maier, M. S. M.; Glaubitz, C. *Biochim. Biophys. Acta* **2009**, *1787*, 697.

(48) Mao, J.; Do, N. N.; Scholz, F.; Reggie, L.; Mehler, M.; Lakatos, A.; Ong, Y. S.; Ullrich, S. J.; Brown, L. J.; Brown, R. C. D.; Becker-Baldus, J.; Wachtveitl, J.; Glaubitz, C. *J.*

Am. Chem. Soc. **2014**, *136* (50), 17578.

(49) Mehler, M.; Scholz, F.; Ullrich, S. J.; Mao, J.; Braun, M.; Brown, L. J.; Brown, R. C. D.; Fiedler, S. A.; Becker-Baldus, J.; Wachtveitl, J.; Glaubitz, C. *Biophys. J.* **2013**, *105* (2), 385.

(50) Jastrzebska, B.; Maeda, T.; Zhu, L.; Fotiadis, D.; Filipek, S.; Engel, A.; Stenkamp, R. E.; Palczewski, K. *J. Biol. Chem.* **2004**, *279*, 54663.

Chapter 4 : Tuning the function of proteorhodopsin by oligomeric assembly in different surfactant environments

Abstract

The ubiquity and diverse functionalities of membrane proteins in biological systems have garnered much interest in leveraging these biomolecules for technological and biomedical purposes, including as pharmaceutical targets. One challenge of studying membrane proteins for these applications is that many factors modulate their structures and functionalities, including the composition of surfactants that interact with the hydrophobic transmembrane region of the membrane protein or the assembly of the protein as oligomers. As oligomerization offers a means by which proteins could selectively interact among the copious environmental factors in biological environments, we hypothesized that membrane protein function is predominantly modified by oligomerization rather than local surfactants that, by comparison, largely interact with proteins nonspecifically. To test this, we opted to study the membrane protein proteorhodopsin (PR) in micellar surfactant solutions because it is functionally active in monomeric and oligomeric forms, while its light-activated functionalities can be assessed in rich detail. The effects of bulk surfactant composition and oligomerization of PR were rigorously correlated with protein function, as measured by the protonation behaviors of aspartic acid residue 97 of PR, which mediates light-activated H^+ transport, and the photocycle kinetics associated with the light-activated H^+-ion transport. The results demonstrate that oligomerization generally tunes PR function across different surfactant environments, but suggest that some surfactants can modify the H^+-ion pumping kinetics. This work underscores the importance of understanding and controlling oligomerization of membrane proteins to study and exploit their function.

Introduction

Membrane proteins are biomacromolecules with functionalities that impart transport,[1,2] catalytic,[3] sensing[4] and structural [5] properties to biological lipid membranes to facilitate cellular functions. Such proteins have extensive hydrophobic transmembrane regions that interact with surfactants (e.g., lipids or detergents) as well as other protein constructs, which can result in the formation of oligomeric protein assemblies[6–10] typically by weak interactions. Numerous studies have shown that membrane protein (MP) oligomerization can enhance protein stability,[11] modify protein function,[7,8,12–14] and enable more complex functional processes versus the monomeric protein components.[15,16] Fewer studies suggest that the surfactant environment also plays a significant role in adjusting MP function.[12,17–19] However, no study has directly addressed the question whether MP function is dominantly tuned by oligomerization or the variation in the MP's surfactant environment. A key challenge in comparing the functional role of oligomerization and the surfactant environment is that these factors are often interdependent,[11,12] making it difficult to parse their effects on protein function.

In a biological context, the protein-specific interactions in MP oligomers could serve to selectively perturb protein characteristics amidst the copious environmental factors (i.e., lipids, salts, water, etc.) present nearby cellular lipid bilayers. Therefore, we hypothesize that oligomerization governs functional tuning rather than the surfactant environment, which by comparison supports largely hydrophobic and non-specific interactions with MPs. To test this hypothesis, we (1) select a MP system in which the surfactant environment and monomer/oligomer populations can be adjusted while retaining protein function, and (2) subsequently correlate changes in MP function with the difference in oligomer distributions

and surfactant environments. We chose the heptahelical transmembrane protein proteorhodopsin (PR) in a surfactant-solubilized state. In these systems, surfactants are known to associate with the surfaces of other MPs[20,21] and exchange with surfactants in solution,[22] which should enable the surfactant composition near the protein surface to be adjusted by the composition of surfactants in the bulk solution. Moreover, surfactant-solubilized PR samples with different distributions of functional monomers and oligomers can be prepared by using size exclusion chromatography[6] or point mutations, e.g. E50Q that enriches the monomeric PR populations versus the wild type protein.[19] Finally, as PR has as a light-activated H^+-ion pumping functionality[23] that is easily probed and yields functional information[24,25] at a level of detail typically not available for many MPs.

The function of surfactant-solubilized PR is known to depend strongly on its oligomeric state, as verified by the photocycle kinetics associated with the H^+-transport process and the pK_a of the functionally-relevant aspartic acid residue 97 (pKa_{D97}). Specifically, Hussain et al. established that monomeric PR underwent a ~5x faster photocycle and had a significantly higher pKa_{D97} value (pKa_{D97}=7.4) than the oligomeric PR (pKa_{D97}=6.7), which was proposed to arise form an inter-protein W34-D97 hydrogen bond.[12] These functional differences were relatively insensitive to the surfactant type present in the solution with PR, specifically n-dodecyl-*β,D*-maltoside (DDM), n-dodecyl phosphocholine (DPC), and diheptanoyl-*s,n*-glycero-3-phosophotidylcholine (diC_7PC).[12] Subsequently, Maciejko et al[19] reported similarly distinct pKa_{D97} values for hexameric PR in DDM (pKa_{D97}=6.9) and monomeric PR in octylglucoside (pKa_{D97}=8.0), consistent with that of Hussain et al.[12] These researchers, however, also observed a surprisingly low pKa_{D97} of 6.9 for PR in monomeric Triton X-100 (TX100) surfactants.[19] If true, this would suggest that some surfactants could also be potent

modifiers of PR function, which would contradict the hypothesis that inter-protein interactions dominate functional tuning.

Our study takes this apparent contradiction as a starting point to test our stated hypothesis with a scope that extends the studies of Hussain et al. and Maciejko et al.[12,19] Functional analyses of monomeric and oligomeric PR in DDM surfactants help establish the degree to which oligomerization modulates the protonation behaviors of the functionally relevant D97 residue and the photocycle kinetics, providing scales by which to compare the effects of the surfactant environment. The same functional parameters were acquired for PR in solutions of Triton X-100 (TX100), Brij-35, or the fluorinated Zonyl FSN-100 surfactant, as well as in mixtures of these surfactants with DDM, and subsequently correlated with the oligomeric distribution of PR species. The collective analyses reveal that oligomerization modifies PR function among all surfactant environments investigated, while changes to the surfactant environment produce relatively subtle effects. While this study focused on PR, we expect the results to apply more broadly to other transmembrane proteins and reflect the general physiological importance of oligomerization in adjusting protein function.

Materials and Methods

Sample Preparation: The expression and purification of green absorbing PR were essentially carried out as described previously,[6] but with a few exceptions. Namely, additional freeze fracture steps (three freeze-thaw cycles) were used to lyse the E. *coli* cells and the lysed cell fragments were collected by centrifugation at ~7,000 *g*, rather than using ultracentrifugation. All protein purification steps were performed in aqueous buffered solutions that consisted of 150 mM KCl and 50 mM K_2HPO_4, which provided a pH of ~8.7, and surfactant quantities are expressed as a weight-per-volume percent. Green PR was cloned into a pET26b(+) plasmid

vector *containing an additional C-terminal HSV sequence and hexahistidine tag for purification*. Moreover, in this study, we use the triple-cysteine mutant of PR, in which the three natural cysteines are mutated to serine residues, and refer to this protein as wild type (WT) PR throughout the manuscript. Additional mutations were introduced to the wild-type green PR template vector via site directed mutagenesis by PCR amplification with mutagenic primers. Vectors were transformed into *E. coli* XL1-Blue competent cells and were plated on LB agar plates containing kanamycin and subsequently grown at 37C overnight. Colonies were picked and grown in LB medium, and the plasmid DNA was isolated using GeneJET Plasmid Miniprep Kit. Sequences were verified with GENEWIZ. Expression of wild type and mutant green PR was carried out in *E. coli* competent BL21 (DE3) cells in LB. Cells were grown to an OD_{600} of 0.8-1 at which point expression was induced by the addition of IPTG to a concentration of 1 mM, and retinal was added such that the final concentration was 10 uM. Cell disruption and Ni-NTA matrix purification was performed as described previously except that a freeze fracture technique using liquid Nitrogen was employed in addition to sonication to further lyse cell membranes. Additionally, for Triton-X 100 solubilized samples, green PR membranes were solubilized from lysed *E. coli* membranes in 1.5% TX100 buffered solutions and the protein was eluted from Ni-NTA resin in 0.1% TX100 buffered solutions. All samples were desalted prior to size-exclusion chromatography (SEC) using Sephadex™ G-25 M PD-10 Columns (GE Healthcare). SEC to isolate the different oligomeric forms of PR and assess the oligomeric state was conducted as described in Stone *et al*.[6] however 0.1% TX100 buffered solution was used as the running buffer for TX100 solubilized samples. PR samples purified in DDM were exchanged into D_2O by concentrating the PR-containing solution in a 50 kDa

MWCO centrifugal concentrator to a volume of ~300 uL and then adding 0.1% DDM alkaline buffer made with D_2O (Cambridge isotopes, 98%) to achieve a final volume of ~1 mL.

Surfactant exchange protocol: To exchange the surfactants that solubilize PR, a solution with 0.5 mg of PR purified in DDM was added to ~10 mL of phosphate buffered solution (50 mM KH_2PO_4, 150 mM KCl) containing appropriate amount of Ni-NTA resin. After PR was completely bound, the resin was allowed to settle and the supernatant was completely removed. The protein-bound resin was then washed with ~120 mL of phosphate buffer with 0.1 wt% of the desired surfactant by repeatedly resuspending the resin in 40 mL of solution, allowing the resin to settle (~15 minute), and then removing the supernatant. Subsequently, the protein-bound resin was resuspended in an additional 40 mL of phosphate buffer with 0.1 of the desired surfactant and incubated overnight (~18 hrs). Following removal of the supernatant, the PR was removed from the resin by incubation in 0.5-1 mL of phosphate buffered solution with 500 mM imidazole and 0.1 wt% of the desired surfactant for ~30 minutes. The imidazole was removed by running the protein-containing solution through a PD-10 desalting column equilibrated in phosphate buffer with 0.1 wt% of the desired surfactant. Solution ^1H NMR analyses establishes the presence of only the desired surfactant in the protein-containing solutions prepared by this surfactant exchange protocol.

Blue-Native polyacrylamide gel electrophoresis: The distributions proteorhodopsin monomers and oligomers in protein samples were assessed by using BN-PAGE. Preparation and electrophoresis of BN-PAGE gels (NativePAGE Novex Bis-Tris Gel 4-16%, 10 wells) were performed according to manufacturer's instructions. Samples were prepared with 3-4 µg of protein, 5 µL sample buffer, 1 µL of 5% Coomassie Brilliant Blue G250 solution, and H_2O adjusted to a total volume of 20 µL. Integration of signal intensities on BN-PAGE gels was

carried out with ImageJ software using first a background subtraction (rolling ball method, 150 pixels) and then integrating along the direction of low to high molecular weight, averaging across the entire width of the respective well.

Optical absorption measurements and analyses: UV-visible absorption spectra of wild type proteorhodopsin and E50Q variants were measured by using a Shimadzu UV-1800 spectrophotometer. The optical absorbance of each sample was recorded over a wavelength range of either 250-750 or 400-750 nm in increments of 0.5 nm. All samples had an initial volume of 750 µL, were buffered with 50 mM KCl and 150 mM K_2HPO_4, and had optical densities of >0.15 at 520 nm. Samples were titrated with 1 M NaOH (aq.) from the initial pH to a pH of 10, and then with 1 M HCl (aq.) to a pH of 4. Approximately 30 µL of 1M HCl or NaOH was used during the titration so the ionic strength changed by ~30 mM during the measurement. The pH was measured by using a low-volume pH probe (Mettler Toledo).

pKa_{D97} analyses

The pKa of proteorhodopsin's D97 residue side chain was determined by analyses of the UV-visible absorption spectra. Briefly, each UV-visible absorption spectrum was adjusted by a zero-order baseline correction such that the absorbance at 750 nm had zero intensity and subsequently normalized to the maximum absorbance intensity between 510 and 550 nm to account for dilution. Then, the absorbance spectrum collected at the most basic pH (~10) was subtracted from each spectrum to yield differential absorbance spectra. The differential absorbance at 570 nm was normalized and fitted to the Henderson-hasselbalch equation using non-linear least-squares regression in a home-built MATLAB code with two fitting parameters, the pKa value and hill coefficient (code available on request). The distribution of monomeric and oligomeric wild type PR in DDM was not affected by incubation for 24 hours

under pH conditions ranging from 3 to 11; also, only subtle differences in monomer and oligomer populations were observed for E50Q PR in various surfactants before and after implementing the pH titration protocol used to probe the protonation behaviors of D97. Measurements were acquired on three samples of as-purified wild type proteorhodopsin in DDM surfactants reveal standard deviations of ~0.05 and ~0.02 for the pKa_{D97} and hill coefficients, respectively. Based on these measurements, we expect the error in the pKa_{D97} and hill coefficients to be approximately 0.1 and 0.05, respectively.

Flash photolysis measurements and analyses

Flash photolysis measurements were conducted using an SpectraPhysics Nd:YAG laser with a monochrometer. Samples were illuminated by a 10 ns 532 nm laser flash and the transient absorbances at several wavelengths were monitored over a timespan of 10 μs to ~0.5 s. For each wavelength measured, 5096 absorbance points were collected with time resolutions of 20 ns, 20 μs, and 2 ms, and subsequently stitched together to yield an absorbance trace. Absorbance data at each wavelength was averaged over approximately 200 logarithmically spaced time points, and was truncated below 40 μs to account for artifacts from the laser. Global fitting analyses and direct kinetic fitting analyses were performed using a home-built MATLAB codes (code available in SI). The direct kinetic fitting procedure used intermediate absorbance spectra reported in Varo et al., and it was assumed that only K and M_1 intermediate species were present at 40 μs following the laser flash.

Solution ^{1}H NMR: Solution ^{1}H single-pulse NMR measurements was used to quantify the surfactants in solutions without and with proteorhodopsin species. ^{1}H NMR measurements were conducted on a Varian NMR spectrometer operating at a field strength of 14.1 T, which corresponds to a ^{1}H Larmor frequency of 600 MHz. Samples were prepared by diluting 50 μL

of the proteorhodopsin containing solution in 950 μL D_2O (Cambridge isotopes, 98%) in a 1-in-20 dilution Each ^1H NMR medasurement used an acquisition time of 6 s, a delay time of 10 s, and between 16 and 64 signal-averaging scans. The amounts of surfactants in proteorhodopsin-containing solutions were determined by comparing the integrated areas of ^1H NMR peaks of DDM of spectra from the protein-containing solutions and a solution containing 0.1% (w/v) DDM in D_2O. All of the resolved peaks in the ^1H NMR spectra of proteorhodopsin-containing solutions can be assigned to DDM, indicating that DDM was the predominant organic species in these solutions.

Results and discussion

To compare the effects of the surfactant environment and oligomerization on proteorhodopsin (PR) function, we employ a combination of complementary characterization methods to quantify the surfactant compositions of micellar solutions containing surfactant-PR complexes, isolate monomeric and oligomeric PR species, and yield insight into the distributions of PR monomers and oligomers in micellar solutions. Information derived from these techniques are correlated with PR function, including the protonation characteristics of residue D97 and the photocycle kinetics of PR at microsecond time resolution, as probed by using visible absorbance spectroscopy.

Selection of PR-stabilizing surfactants

The surfactants explored in this study were judiciously selected to span a range of molecular architectures to allow insights into how the types of headgroup and tail moieties influence PR function. Surfactants are amphiphilic molecules that have a hydrophilic headgroup and hydrophobic tail moiety and can interact with PR species in aqueous solutions.

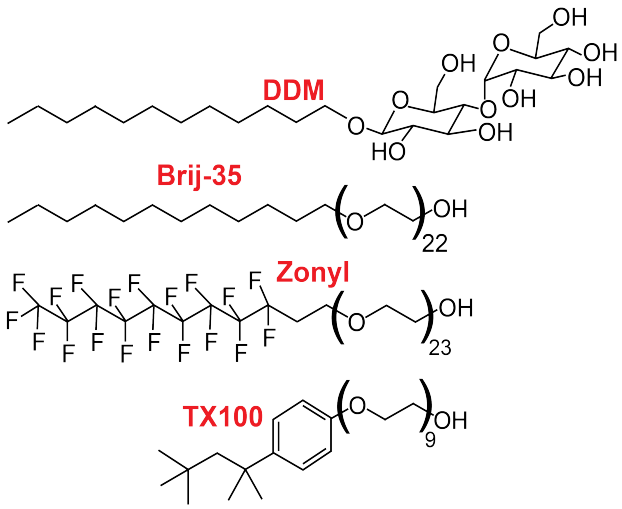

Figure 1. Molecular structures of n-dodecyl-β,D-maltoside (DDM), Brij-35, Triton X-100 (TX100) and Zonyl FSN-100 (Zonyl).

This study explores the effects of n-dodecyl-*β,D*-maltoside (DDM), Brij-35, Triton X-100 (TX100) and Zonyl FSN-100 (Zonyl) surfactants, the molecular structures of which are shown schematically in Figure 1. UV-visible absorption spectra (Appendix B, Figure B10) of PR solubilized in solutions containing each of these surfactants show characteristic absorption properties of functionally active PR, suggesting that these surfactants can stabilize functional PR species. Both DDM and Brij-35 have identical 12-membered alkyl tails but different head groups, namely a maltoside headgroup for DDM and a linear ethylene oxide chain for Brij-35. Thus, analyses of PR solubilized by DDM and Brij-35 allow the effects of surfactant head group type to be probed. By comparison, Triton X100 (TX100) and Zonyl FSN 100 (Zonyl) surfactants have linear ethylene oxide headgroups, as with Brij-35, but dramatically different nonaphenolic and linear fluorinated tails, respectively. These surfactants permit the effects of tail group type on PR behaviors to be compared.

Quantifying surfactant compositions of micellar solutions containing PR

To establish how surfactants influence PR function, it is necessary to understand the surfactant compositions in the micellar solutions in which PR are stabilized. Solution ^{1}H NMR

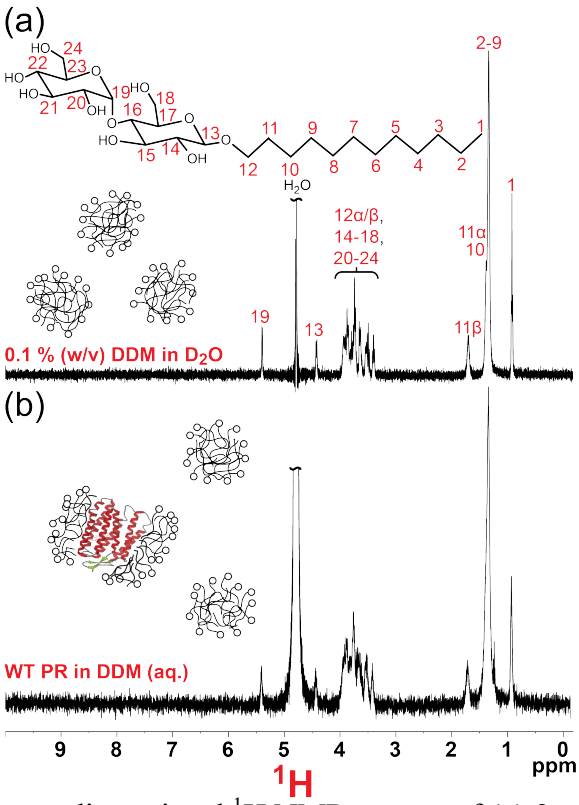

Figure 2. Solution-state one-dimensional ^{1}H NMR spectra of **(a)** 2 mM DDM in D_2O and **(b)** the monomeric fractions of PR from SEC, diluted 20x in D_2O. A comparison of the respective peak areas among these spectra establishes the DDM concentration in the PR-containing solutions.

spectroscopy is a powerful method for quantifying surfactant compositions in PR-containing solutions, yet is scarcely used for such applications.[26] Single-pulse ^{1}H NMR experiments exploit the chemical shift interaction to resolve signals from chemically distinct ^{1}H moieties. For example, the ^{1}H single-pulse solution NMR spectrum (Fig. 2(a)) of 2 mM DDM in D_2O shows peaks at 0.8, 1.3, 1.6, 3.5-4, 4.4 and 5.4 ppm that are confidently assigned to the various ^{1}H moieties of the alkyl tail and maltoside head group of DDM. Moreover, the integrated areas of these assigned ^{1}H signals correspond stoichiometrically to the ^{1}H species of a DDM molecule, corroborating the ^{1}H signal assignments. A ^{1}H single-pulse NMR spectrum (Fig. 2(b)) acquired on a solution containing wild-type (WT) PR purified in DDM shows the same ^{1}H NMR signals, indicating that DDM is the only surfactant present in this solution. Notably,

signals associated with PR molecules are entirely absent in the spectrum in Figure 1B, likely because the PR species are too dilute (~10 μM) to be detected or undergo too slow of motions to be resolved by this measurement. A comparison of these ^{1}H NMR signal areas to those from a 0.1 wt% DDM solution, which serves as a quantitative external ^{1}H reference, reveals that this PR sample contains 17.6 mM DDM. Interestingly, this DDM concentration is substantially higher than in the 1 mM DDM buffers used to purify of this very protein sample, suggesting that DDM surfactants accumulate during purification, possibly during centrifugal concentration or due to the strong association of surfactants with the PR molecules. The ^{1}H NMR spectra recorded from Triton X-100 (TX100), Brij-35 and Zonyl FSN 100 (Zonyl) surfactants in D_2O solutions also show distinct sets of ^{1}H signals, enabling ^{1}H NMR analyses to quantify these surfactants as well.

Isolating PR monomers and oligomers in micellar solutions

Critical to evaluating how the surfactant environment and oligomerization influence PR function is comparing the function of both monomeric and oligomeric PR in various surfactant environments; however, preparing such samples is often challenging because the monomer/oligomer distribution of PR are often surfactant dependent. Subsequently, we exploit solution ^{1}H NMR spectroscopy and blue-native polyacrylamide gel electrophoresis (BN-PAGE) techniques, which provide information about the populations of PR monomers and oligomers,[27] to yield insights about how PR monomers and oligomers can be stabilized in different surfactant environments.

Separation of PR species with size-exclusion chromatography (SEC)

Monomeric and oligomeric PR species can be isolated in identical surfactant environments by using size-exclusion chromatography, demonstrated here in micellar DDM

solutions. A BN-PAGE gel (Fig. 3(a), well 1) of WT PR that, by ^{1}H NMR, has 8 mM of DDM surfactants shows an intense band at ~242 kDa that is assignable to pentameric/hexameric PR assemblies.[19] As described previously by Hussain et al,[12] incubation of this pentameric/hexameric WT PR sample in solutions of ~40 mM diheptanoyl-*s,n*-glycero-3-phosophotidylcholine (diC_7PC) surfactants enriches the monomer PR population, which can be subsequently isolated using an SEC column equilibrated with a running buffer of 1 mM DDM without diC_7PC. The monomeric PR fractions from SEC have approximately 49 mM DDM by solution ^{1}H NMR, and the BN-PAGE analysis (Fig. 3(a), well 2) shows a strong signal at ~60 kDa that corresponds to monomeric PR with a relatively weaker band at ~242 kDa. Interestingly, the solution ^{1}H NMR spectrum of the monomeric sample shows no ^{1}H signals assignable to diC_7PC, suggesting that diC_7PC molecules elute separately from the monomers during SEC. These results clearly demonstrate SEC as a valuable tool for isolating monomeric and oligomeric PR in the same surfactant type, enabling the influence of oligomerization on PR function to be probed independently of the surfactant environment.

Tuning the surfactant environment of PR monomers and oligomers

The populations of monomeric or oligomeric PR can be largely maintained in micellar solutions of various surfactants by judiciously selecting the types of surfactants in these solutions. For example, monomeric PR should be stable in micellar solutions with any combination of surfactants that each mutually promote the formation of monomeric PR. Therefore, we sought to identify how DDM, TX100 and Brij-35 surfactants influence the oligomerization behaviors of PR in micellar solutions. First, we explore the effects of TX100 surfactants. Solutions of oligomeric WT PR in 3 mM DDM (aq.) were incubated overnight with TX100 concentrations ranging from 1-10 mM and subsequently characterized by using

BN-PAGE, which is shown in Figure 3. Oligomeric WT PR incubated in solutions of 3 mM DDM without and with 1 mM TX100 are primarily pentameric/hexameric with some higher-order oligomers (Fig. 3(c), wells 1,2), but samples with TX100 concentrations of 5 and 20 mM show increasing populations of monomeric and dimeric PR (Fig. 3(c), wells 3,4). This establishes a proclivity of PR to form monomers or dimers in the presence of TX-100 surfactants.

Importantly, this understanding can be exploited to prepare micellar solutions that have similar distributions of PR monomers and oligomers but different surfactant compositions. For example, leveraging the monomer/dimer forming proclivities of TX-100, we incubated monomeric WT PR in DDM (and obtained from SEC) in solutions containing 40 mM DDM+20 mM TX100 and 60 mM DDM. BN-PAGE analyses of these samples (Fig. 3(b), well 2,3) show nearly identical signal patterns that indicate high populations of monomers with lower quantities of larger oligomers. These results demonstrate that monomeric PR in DDM micellar solutions can be largely preserved in the presence of TX100 surfactants. By comparison, similar analyses of DDM and Brij-35 surfactants reveal that, at least at surfactant concentrations below 10 mM, these surfactants individually and in mixtures stabilize pentameric/hexameric PR (SI, Fig. 5).

Adjusting PR oligomerization behaviors by point mutations

Point mutations that alter PR oligomerization behaviors can exploited to enable informative comparisons with the wild-type protein. In this case, the mutated and WT proteins would have different monomer and oligomer distributions in identical surfactant environments, so any differences in protein function would arise from oligomerization. Recently, Maciejko et al[19] used powerful solid-state NMR techniques to identify several residues at the oligomeric

interface that mediate PR oligomerization. These mutations include the R51A and D52N mutation that promotes the formation of hexameric versus pentameric PR and the E50Q mutation that enriches the population of monomeric PR in DDM and TX100 surfactants with respect to the WT protein. Of specific interest is the monomer-forming E50Q variant, as this mutant should promote higher monomer populations versus the WT protein in any given surfactant environment. To test this, we separately exchanged E50Q and WT PR from micellar DDM solutions into new micellar solutions containing exclusively TX100, Brij-35, Zonyl or DDM (as a control) surfactants, and used BN-PAGE to compare their monomer/oligomer distributions by using BN-PAGE. The BN-PAGE results (Fig. 3(d)) for E50Q PR exchanged into each surfactant environment show strong signals associated with monomeric and dimeric PR, but weaker signals from higher-order oligomers, which are most intense for E50Q PR solubilized in Brij-35. Importantly, though the E50Q mutation alone could not eliminate oligomer formation, each E50Q PR sample shows higher monomer/dimer contents than WT PR exchanged into the same respective surfactants (Appendix B, Figure B11). Thus, comparisons of the monomer-forming E50Q and WT PR could effectively establish how oligomerization tunes protein function in various surfactant environments.

Adjustments to the protonation behavior of D97

The protonation behaviors of the carboxylic acid sidechain moiety of aspartic acid residue 97 (pKa_{D97}) is a key functionally-relevant property of proteorhodopsin that provides a sensitive measure by which to compare how surfactants and oligomerization influence protein function. Under alkaline conditions, the anionic carboxylic acid moiety of the D97 side-chain

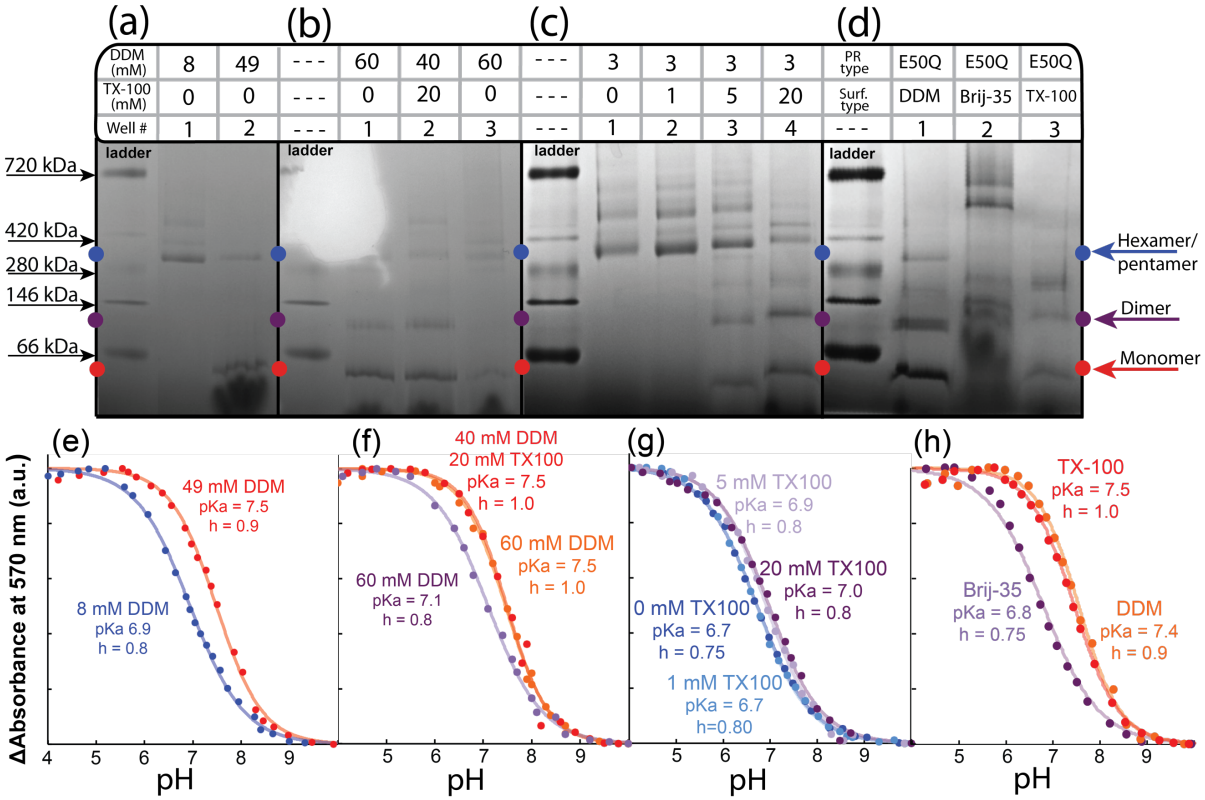

Figure 3. Surfactant compositions and blue-native PAGE gels **(a-d)** with corresponding pKa_{D97} titration results **(e-h)**. The PR samples analyzed in (a) and (e) are solubilized exclusively in DDM surfactants but have distinct monomer and oligomeric distributions. In (b) and (f), PR is solubilized in the same total quantity of surfactants, but with different DDM and TX100 compositions. Proteorhodopsin species in samples (c) and (g) are solubilized in low concentrations of DDM but with various TX100 concentrations. Finally, the E50Q PR in (d) and (h) is solubilized exclusively in either DDM, Brij-35 or TX100 surfactants. Samples in (b-c, f-g) were incubated at 4°C in surfactant solutions for overnight before conducting BN-PAGE and pKa_{D97} titration measurements.

serves as the primary proton acceptor for the Schiff base,[28] and is crucial for mediating activated H^+-ion transport by PR.[29] As D97 is nearby the retinal chromophore, changes in the protonation state of D97 produce a substantial ~25 nm shift in the visible absorbance of the retinal, from ~515 nm when deprotonated to ~540 nm when protonated.[28] This wavelength shift can be equivalently expressed as the difference absorbance at 570 nm (ΔA_{570}), which is the difference in absorbance intensity at 570 nm between PR at a pH of interest and under alkaline (~pH 10) conditions at which D97 is fully deprotonated. For example, as shown in Figure 3(e) for in monomeric WT PR in 49 mM DDM, ΔA_{570} decreases sigmoidally from 1.0

under acidic pH conditions to 0.0 at basic pH (Fig. 3(e), red dots). A fit of this data to the Henderson-Hasselbalch equation (Fig. 3(a), well 1 & Fig. 3(e), red line) yields a pKa_{D97} of 7.5 and hill coefficient of 0.9. By comparison, pentameric/hexameric PR in 8 mM DDM (Fig. 3(a), well 2 & Fig. 3(e) blue) has a substantially lower pKa_{D97} of 6.9 and moderately reduced hill coefficient of 0.8. As the PR in both samples are solubilized exclusively by DDM surfactants, the dissimilar protonation behaviors cannot be due to the presence of different surfactant types and, thus, strongly correlate with differences in monomeric and oligomeric populations. Therefore, these results imply that the carboxylic moiety D97 residues of PR oligomers are more acidic and undergo uncooperative protonation compared to monomeric PR in micellar solutions.

The influence of TX-100 on the protonation behaviors of D97 are assessed by interrogating monomeric and oligomeric WT PR in solutions of identical surfactant concentrations but different TX100 compositions. Primarily monomeric/dimeric WT PR incubated overnight in 60 mM DDM and 40 mM DDM+20 mM TX100 (Fig. 3(b), well 2) exhibit identical pKa_{D97} and hill coefficient values of 7.5 and 1.0, respectively (Fig. 3(f)). These values agree well with those of monomeric PR at a different surfactant concentration of 49 mM DDM (pKa_{D97} = 7.5, hill coefficient = 0.9). Thus, the presence of TX-100 at a 1:3 molar ratio with DDM provided no change in pKa_{D97} and a minor difference in the associated hill coefficient, supporting that TX100 plays a minor role in tuning the protonation behaviors of D97. To explore in greater detail the effect of TX100 on PR function, the D97 protonation behaviors were assessed for PR incubated in solutions with higher TX100-to-DDM ratios, in which any effects of TX100 on PR function would be intensified. The WT PR in micellar solutions of 3 mM DDM and TX100 concentrations of 0 mM and 1 mM TX100 have identical

pKa_{D97} values of 6.7, while WT PR in 5 mM and 10 mM TX100 exhibit relatively higher pKa_{D97} values of 6.8 and 7.0, respectively. These data show that the pKa_{D97} values concomitantly increase with monomer/dimer PR populations. Thus, these results support that oligomerization predominantly tunes the protonation behaviors of D97, while the presence of TX100 has a comparatively smaller influence.

D97 protonation behaviors of the monomer-forming E50Q PR variant

The monomer-forming E50Q mutant can be exploited to provide additional insights into how the pKa_{D97} is tuned by PR oligomerization and surfactant environment. As E50Q PR was shown to have higher monomer/dimer content than WT PR in micellar solutions of DDM, TX100 and Brij-35, any differences in the pKa_{D97} among E50Q and WT PR in the same surfactant environment would arise from oligomerization. As shown in Figure 3(h), E50Q PR in micellar DDM and TX100 solutions have similar pKa_{D97} values of 7.4 and 7.5, respectively, while E50Q PR solubilized in Brij-35 solutions exhibit a significantly lower pKa_{D97} of 6.8 and hill coefficient of ~0.75 (Fig. 3(h)). By comparison, wild-type PR exchanged into micellar DDM, TX100 and Brij-35 solutions have pKa_{D97} values of 6.9, 6.8 and 6.6, respectively, (Appendix B, Figure B11) which are consistently lower than for E50Q PR in each respective surfactant environment. These analyses strongly correlate pKa_{D97} values with greater monomer populations for PR in DDM, TX100 and Brij-35 surfactant environments, thus supporting that oligomerization tunes pKa_{D97} regardless of surfactant environment.

Quantitative correlations of pKa_{D97} and BN-PAGE signals

Correlation of the pKa_{D97} and BN-PAGE signals provides semi-quantitative insights into whether oligomerization or surfactant environment predominantly modify the protonation behaviors of D97. We hypothesize that the W34-D97 inter-protein hydrogen bond accounts

for the difference in pKa_{D97} for monomeric (pKa_{D97} ~7.5) and oligomeric (pKa_{D97}~6.9) PR. Should this be the case, assuming that PR oligomers larger than dimers are cyclic and can support W34-D97 hydrogen bonding among each PR subunit, then monomeric PR and one protein subunit of the dimeric PR species could not accept an inter-protein W34-D97 hydrogen bond; correspondingly, these species would be expected to have a high pKa_{D97} value (~7.5) while other oligomers would have lower (~6.9) pKa_{D97} values. To test this, we correlate the summed contents of monomers and one half of the dimers, estimated by their integrated BN-PAGE signals, and pKa_{D97} values measured from the same sample, as shown in Figure 4 for thirty-eight WT or E50Q PR samples. A best-fit linear line through the data points obtained from PR exclusively in DDM surfactants (blue points) has a Pearson's correlation coefficient of +0.93 that indicates a strong positive correlation of pKa_{D97} with monomer/dimer content. Notably, the data points obtained from PR samples in DDM concentrations had surfactant concentrations ranging from 3 to 60 mM, suggesting that DDM concentration has little influence over the pKa_{D97}. The correlated data of PR in micellar DDM solutions (Figure 4, blue) also shows reasonable agreement with the data from PR in micellar TX100 (Fig. 4, red) and Brij-35 (Fig. 4, orange) solutions. A best-fit linear line (not shown) fit to every data point shown in Figure 4 has a Pearson's correlation coefficient of +0.86 that is slightly lower than for PR in DDM solutions, but nonetheless supports a strong correlation of pKa_{D97} with monomer/dimer content. Interestingly, a correlation of the hill coefficient with monomer/dimer contents (data not shown) shows a poor correlation with monomer/dimer content, indicating that the hill coefficient of D97 is tuned only partially or not at all by oligomerization.

Another important feature of the correlation plot are the variations in data along the abscissa, which arise from differences in oligomerization, and along the ordinate, where effects

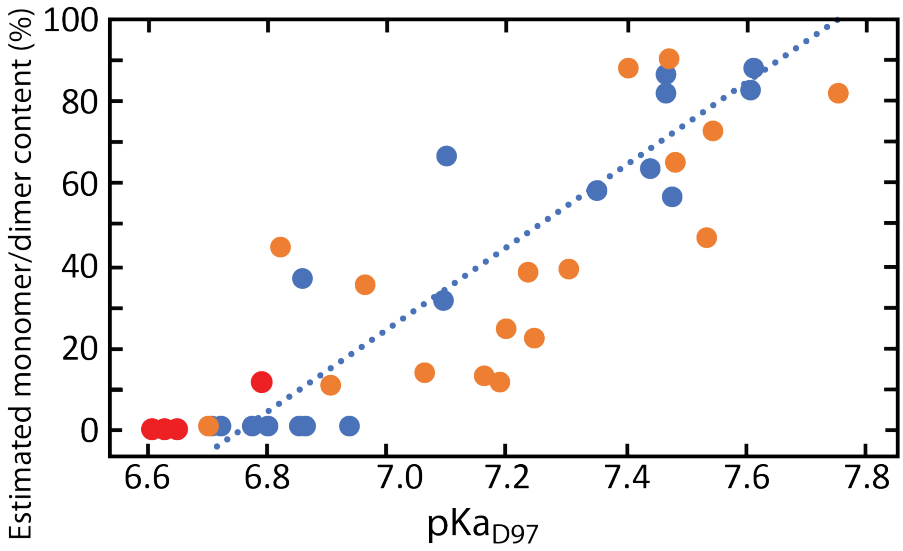

Figure 4. Correlation of pKa_{D97} values with the estimated monomer/dimer contents of WT or E50Q PR in micellar solutions that contain (blue) exclusively DDM, or (orange) TX100 and (red) Brij-35 surfactants either exclusively or in mixtures with DDM. Monomer/dimer content was estimated as the sum of the integrated BN-PAGE signals of monomers and one-half that of dimers, normalized by the total integrated intensity. The dotted blue line is a best-fit to the pKa_{D97} and BN-PAGE data from PR in exclusively DDM (blue dots), which has a Pearson correlation coefficient of 0.93 that reflects a strong correlation of monomer/dimer content with pKa_{D97} value. Moreover, the linear fit shows reasonable correlation with data from PR in the presence of TX100 (orange dots) and Brij-35 (red dots).

of surfactant on pKa_{D97} would manifest. The pKa_{D97} values range from 6.6 to 7.7 (1.1 pH units) along the abscissa, while the pKa_{D97} values deviate by an average of 0.2 from the best-fit line in the ordinate direction. This supports that oligomerization plays a more dominant role in tuning the pKa_{D97} than the surfactant environment. The predominance of oligomerization in modifying pKa_{D97} is borne out by the sparse population of data in regions of the correlation plot with high (>7.3) pKa_{D97} values and low (<50%) monomer/dimer signals (region contains 1 point) and low (<7.3) pKa_{D97} values and high (>50%) monomer/dimer signals (region contains 2 points). An important note about assigning populations based on BN-PAGE intensities is that it assumes that a PR molecule binds similar amounts of Coomassie blue dye molecules regardless of oligomeric state; this, however, would be expected considering that PR subunits in any oligomer should be chemical identical and thus have similar extents

covalent or electrostatic interactions with dye molecules. Nonetheless, should the dye molecules bind at the oligomeric interface, or some region influenced by oligomerization, then the number of bound dye molecules per PR subunit would likely reduce proportionally with the area of the oligomeric interface. A correlation plot (Appendix B, Figure B12) in which oligomer contents from the BN-PAGE are adjusted by an estimate of the oligomeric interfacial area also shows a strong correlation of pKa_{D97} and monomer/dimer content.

The pKa_{D97} behaviors reported here are in general agreement with the literature for green-absorbing PR. The pKa_{D97} values reported in literature for green-absorbing PR in micellar solutions generally range from 6.9 to 8.2,[19,30,31] but higher values have been observed in the presence of certain anions.[32] While few studies have explored the effects of different surfactants on the pKa_{D97} of PR, one recent example is Maciejko et al, which reported a pKa_{D97} of ~6.8 for pentameric PR in DDM and ~8.0 for monomeric PR in octyl glucoside surfactants that are entirely consistent with the results here. The same study, however, reports a pKa_{D97} value of ~6.8 for monomeric PR in micellar TX100 surfactant solutions that is much lower than would be expected should oligomerization dominate the functional tuning of PR as observed in this study. This apparent inconsistency could be explained by two possible differences: (1) in this study we investigate a triple-cysteine PR mutant whereas Maceijko et al uses PR that has the three natural cysteines, the oxidations of which can influence the pKa_{D97} and photocycle,[29] or (2) in our experience samples of PR in micellar TX100 solutions stored at -20°C partially aggregate and the supernatant is primarily pentameric/hexameric. Given these factors and the general agreement of our results with Maciejko et al, it appears likely that the unusually low pKa_{D97} reported for PR in micellar TX100 solutions would agree with our data and analyses, should we have used consistent sample preparation methods.

Effect of oligomerization on photocycle kinetics

Given the distinct dependence of the protonation behaviors of D97 on oligomerization, we interrogated how oligomerization influences the H^+-ion pumping kinetics of PR by probing the light-activated responses of monomeric and oligomeric PR in micellar DDM solutions. Following the absorption of green light, PR undergoes a cyclic sequence of small and large-scale motions that result in the net transport of an H^+-ion from the cytoplasmic to extracellular sides of PR. Several of these motions perturb the local environment of the retinal chromophore and alter its absorbance, enabling the H^+-ion pumping kinetics to be analyzed by transient optical absorbance spectroscopy. Monomeric PR in alkaline DDM solutions activated by a 10 ns green laser show complex absorption behaviors (Fig. 5(a), solid lines) over the μs to 100 ms timescales. Importantly, though the transient absorbance responses of pentameric/hexameric PR in 8 mM DDM (Fig. 5(a), dotted lines) appear qualitatively similar to those of the monomeric PR, they occur over dramatically different timescales that reflect key functional differences attributable only to oligomerization.

Qualitative insights into the different light-activated kinetic behaviors of PR monomers and oligomers are available by interpreting the absorbance responses in terms of the photochemical reaction cycle developed by Varo et al for PR.[25] This sequential reaction model, depicted in Figure 5(b), includes five intermediates (*K*, M_1, M_2, *N*, and *PR'*) with distinct absorption signatures and lifetimes[25] that enable the transient absorbance behaviors to be assigned to changes in intermediate populations. For example, positive intensities at 570, 590, and 630 nm at early (~10 μs) times arise from the *K* intermediate that absorbs maximally at ~555 nm. The subsequent decay of these intensities is concomitant with a rise in absorbance

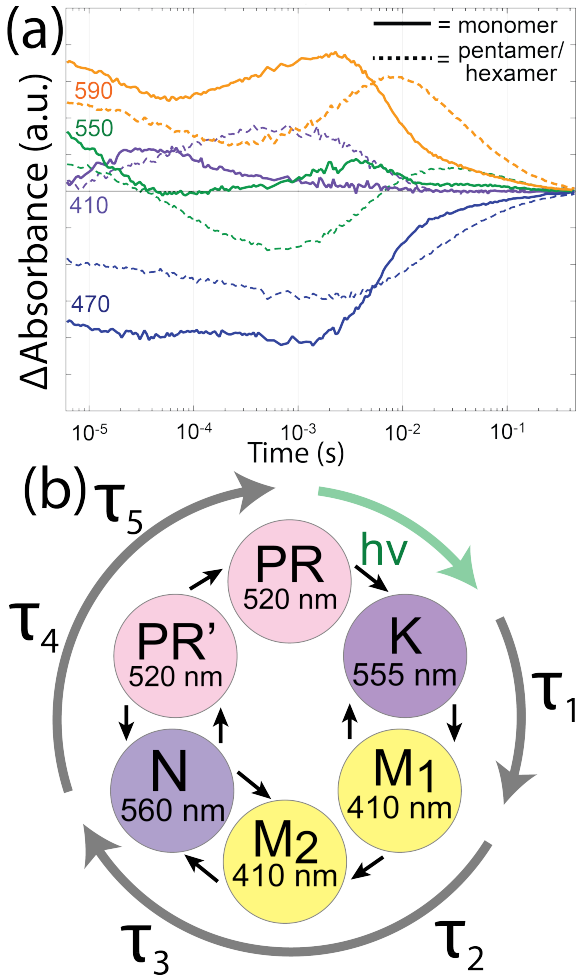

Figure 5. (a) A schematic diagram of the photochemical reaction cycle of proteorhodopsin under basic conditions, which includes *K*, M_1, M_2, *N* and *PR'* intermediates.[25] **(b)** Transient visible absorbance data collected from samples in Figure 2(a) that contain mostly (solid lines) monomeric and (dotted lines) pentameric/hexameric in alkaline (pH 8.5) DDM solutions and ~20 °C.

at ~410 nm, signifying the conversion of the *K* to M_1 intermediates. At times >20 μs the absorbance at 410 nm decays while those at 570, 590 and 630 nm increase, reflecting a rising populations of the *N*, and all intensities decay to zero by ~300 ms as the *N* and *PR'* intermediates convert to the non-activated *PR* state. A key difference among monomeric (Fig. 4(a), solid lines) and pentameric/hexameric (Fig. 5(a), dashed lines) PR is that the 410 nm absorbance peaks at much shorter times (~30 μs) for monomeric PR than for pentameric/hexameric PR (~500 μs). Moreover, the relative intensity of the absorbance at 410

nm to 590 nm is generally much larger for pentameric/hexameric than for monomeric PR. These observations establish that M_1 and/or M_2 intermediates accumulate in greater quantities, relative to other intermediates, and at longer times for pentameric/hexameric PR versus monomeric PR. Furthermore, the 590 nm absorbance peaks at much shorter times (~1 ms) for monomeric PR than pentameric/hexameric PR (~8 ms), revealing that the *N* and *PR'* intermediates accumulate at much later times for PR oligomers.

More detailed quantitative comparisons are enabled by global fitting analyses of the transient absorbance data. A global fitting routine approximates the intensities at each wavelength as a sum of mono-exponential decays with wavelength-dependent pre-exponential factors and mutual (wavelength-independent) exponential time constants. Accurate global fits to the absorbance data of monomeric and oligomeric PR required five exponentials, the exponential time constants (Table 1) of which reflect the apparent timescales for interconversions among two or more intermediates. In particular, for monomeric PR (Fig 5A, solid lines) the τ_1 largely characterizes the decay of the *K* and rise of the *M* intermediates, while τ_2 and τ_3 are associated with a decrease in the populations of *M* species and rise in *N* intermediates, as well as the equilibria among the M_2 and *N* intermediates, as shown schematically in Figure 5(b). The time constants τ_4 and τ_5 reflect the interconversions among the *N* and *PR'* intermediates and the non-activated *PR* state. Importantly, the apparent time constants τ_1-τ_4 are two to three times lower for monomeric compared to pentameric/hexameric PR, indicating that monomeric PR species undergo H^+-ion pumping at 2-3 times faster rates. These results and analyses underscore the substantial dependence of oligomerization on PR function.

Table 1. Apparent time constants for the photochemical reaction cycle of proteorhodopsin from global fitting analyses of time-resolved UV-visible absorbance data

	τ_1 (μs)	τ_2 (μs)	τ_3 (ms)	τ_4 (ms)	τ_5 (ms)
Monomer (49 mM DDM)	13	130	1.6	5.2	89
Oligomer (8 mM DDM)	47	380	3.9	14	103

Photocycle of PR in different surfactants

To compare the effects of oligomerization and surfactant environment on PR photocycle kinetics, we investigate the light-activated absorbance responses of the monomer-forming E50Q PR variant in different micellar surfactant environments, which include DDM, TX100, Brij-35 and Zonyl FSN-100. The transient absorbance intensities at 410 nm and 590 nm of E50Q PR in each micellar surfactant solution bear qualitative similarities to those of WT PR in DDM solutions, namely an initial decay at 590 nm and concomitant rise at 410 nm is followed at longer (>1 ms) times by a rise and subsequent decay of the 590 nm absorbance. Nonetheless, there are quantitative differences among these absorbance data. The absorbance behaviors (Fig. 6(a)) of primarily monomeric E50Q PR in micellar DDM solutions shows intensity maxima for 410 nm and 590 nm at ~$4x10^{-5}$ s and $2x10^{-3}$ that correspond well to those of monomeric WT PR in 49 mM DDM (Fig. 6(a)). By comparison, for E50Q PR in Brij-35 (Figure 6(b)), which is a distribution of monomer, dimers and higher order oligomers, the maximum intensities at 410 and 590 nm occur at much longer times (~$2x10^{-4}$ s and ~$1x10^{-3}$ s, respectively), roughly agree with those of petameric/hexameric WT PR in DDM (~$6x10^{-4}$ s and ~$8x10^{-3}$ s) except with a slightly faster accumulation of 410 nm absorbances for E50Q PR in Brij-35 surfactants. Thus, for E50Q PR in micellar TX100 and Brij-35 solutions, faster

kinetics correlate with higher monomer populations, as observed for WT PR in DDM (Figure 6A). These transient absorbance results and analyses establish oligomerization tunes the light-activated H^+-ion pumping function of PR similarly in DDM and Brij-35 surfactant environments.

The absorbance behaviors of E50Q PR in TX100 and Zonyl surfactant environments also show characteristics attributable to oligomerization, but others that cannot. For example, for E50Q PR in TX100, while the early ($4x10^{-5}$ s) accumulation of the 410 nm absorbance would be expected based on the high monomer and dimer contents (Fig. 6(c), inset), there is an additional local maximum in the 410 nm absorbance appears at much longer times ($5x10^{-3}$ s) and is unique to all the samples studied here. Such a late accumulation of 410 nm absorbance could not be manufactured from any linear combination of the absorbance behaviors of monomeric and pentameric/hexameric PR in DDM (Figure 5A), and thus is confidently

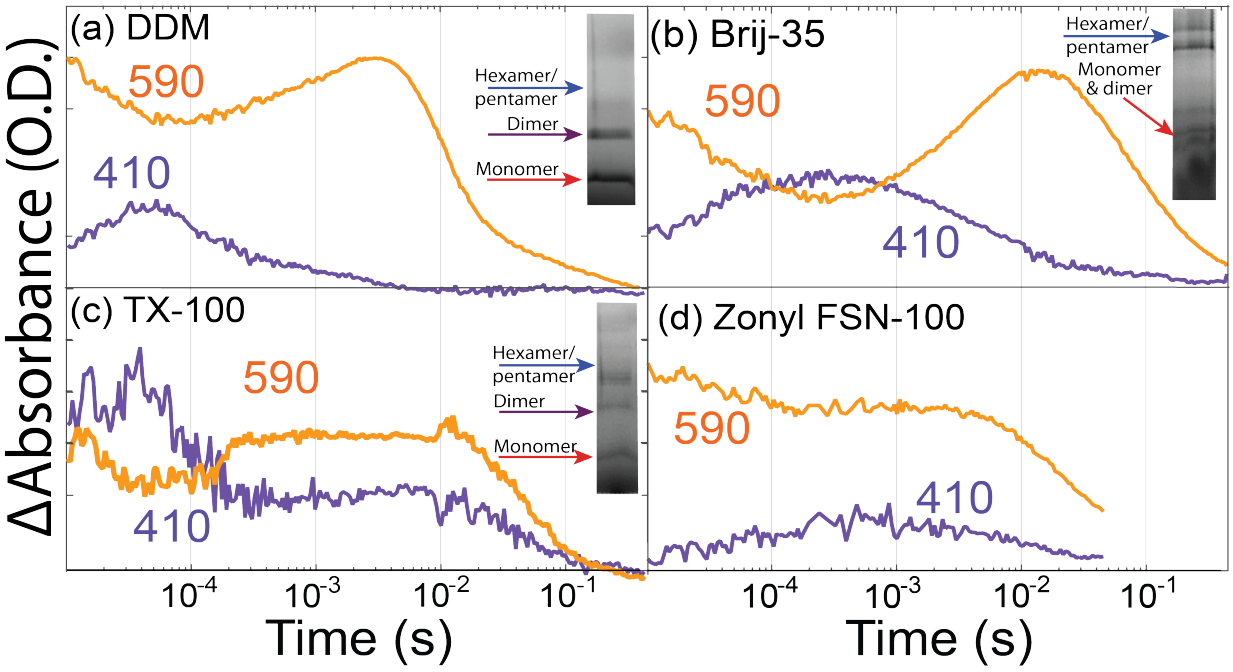

Figure 6. Transient visible absorbances of surfactant-solubilized PR-E50Q exchanged from DDM into **(a)** DDM, **(b)** Brij-35 and **(c)** TX100 surfactants. The PR-E50Q samples exchanged into DDM and TX100 surfactants showed a distribution of monomers and dimers, while PR-E50Q in Brij-35 surfactants was primarily oligomeric. Measurements were conducted at pH ~8.5.

assigned as an effect of the TX100 surfactant environment. Similarly, the absorbance behaviors of E50Q PR in micellar Zonyl solutions, which based on the pKa_{D97} of this sample has high oligomer populations, also exhibit contributions attributable to oligomerization and the surfactant environment.[1] For example, the 410 nm absorbances of E50Q PR in Zonyl surfactants (Fig. 6(d)) accumulate at late ($1x10^{-3}$ s) times that are quantitatively consistent with those observed for pentameric/hexameric WT PR (Fig. 5A) in micellar DDM solutions. Surprisingly, the 590 nm absorbance accumulates at early (~$3x10^{-3}$ s) times, like those observed for monomeric WT PR in DDM (Figure 5(a)). Moreover, the ratio of 590 nm to 410 nm absorbances for E50Q PR in Zonyl surfactants is generally lower than for oligomeric WT PR in DDM (Fig. 5(a), dotted), establishing lower relative populations of *M* intermediates during the photocycle. These data support that oligomerization effects appear to persist under different surfactant conditions, but that the surfactant environment can also modify the light-activated responses of PR.

Collectively, the photocycle and BN-PAGE analyses suggest that the hydrophobic surfactant tail is a more important feature than the headgroup in tuning the photocycle kinetics of PR. Both DDM and Brij-35 have identical dodecyl alkyl chains but vastly different head groups, one a maltoside and the other a linear 23-unit polyethylene oxide chain. As differences among the light-activated kinetics of PR in DDM and Brij-35 could be explained entirely by oligomerization, it appears that the disparities among the surfactant headgroups of DDM and Brij-35 do not account for substantial differences in protein function.

[1] Sensitivity issues prevented BN-PAGE analyses of E50Q PR in Zonyl surfactants, though pKa_{D97} of this sample was 6.5 (hill coefficient = 0.5), suggesting a predominantly pentameric/hexameric PR population

The absorbance data of E50Q PR in Zonyl FSN and TX100 surfactants, however, revealed unique transient absorbance characteristics attributable to each surfactant environment. Both TX100 and Zonyl surfactants have similar ethylene oxide headgroups, albeit with different lengths, but dramatically different nonaphenolic and linear fluorinated tail groups. The transient absorbance data from PR in micellar TX100 and Zonyl solutions suggest the presence of surfactant-dependent effects on function originate mainly from the architecture of the surfactant tail group.

Conclusions

The influence of oligomerization and surfactant environment on the functionality of the membrane protein proteorhodopsin in micellar solutions are compared. The combined use of solution ^{1}H NMR and blue-native PAGE techniques enabled the rigorous correlation of surfactant compositions, PR oligomerization behaviors and PR function, as measured by the protonation behaviors of the D97 residue and photocycle kinetics associated with H^{+}-ion transport. The pK_a and hill coefficient for D97 were unanimously higher for monomeric PR (pKa_{D97}~7.5, h~0.9) compared to oligomeric (pKa_{D97}~6.9, h~0.8), regardless of the concentration and type of solubilizing surfactant, which in this study included DDM, TX100, Brij-35 and Zonyl FSN-100. Similarly, under alkaline (pH~8.5) conditions the kinetics associated with the H^{+}-ion transport were 2-3 times faster for PR monomers than pentamers/hexamers in DDM-containing solutions. Further analyses of WT PR and the monomer-forming E50Q PR variant supported that these substantial differences persisted in different surfactant environments, establishing oligomerization as a general mechanism by which PR function is adjusted. Yet, in a few cases, the surfactant environment modifies the light-activated kinetics associated with H^{+}-ion transport by PR, which is attributed mainly to

the molecular structure of the surfactant tail. While the analyses here focused on PR, these findings are expected to apply more broadly to other transmembrane proteins that have important physiological or therapeutic roles.

References

(1) Nagelhus, E. A.; Ottersen, O. P. *Physiol. Rev.* **2013**, *93*, 1543.

(2) Berndt, A.; Lee, S. Y.; Wietek, J.; Ramakrishnan, C.; Steinberg, E. E.; Rashid, A. J.; Kim, H.; Park, S.; Santoro, A.; Frankland, P. W.; Iyer, S. M.; Pak, S.; Ährlund-Richter, S.; Delp, S. L.; Malenka, R. C.; Josselyn, S. A.; Carlén, M.; Hegemann, P.; Deisseroth, K. *Proc. Natl. Acad. Sci. U. S. A.* **2016**, *113*, 822.

(3) Kaplan, J. H. *Annu. Rev. Biochem.* **2002**, *71*, 511.

(4) Lefkowitz, R. J. *Trends Pharmacol. Sci.* **2004**, *25*, 413.

(5) Rampelt, H.; Bohnert, M.; Zerbes, R. M.; Horvath, S. E.; Warscheid, B.; Pfanner, N.; van der Laan, M. *J. Mol. Biol.* **2017**, *429*, 1162.

(6) Stone, K. M.; Voska, J.; Kinnebrew, M.; Pavlova, A.; Junk, M. J. N.; Han, S. *Biophys. J.* **2013**, *104*, 472.

(7) Tsukamoto, T.; Demura, M.; Sudo, Y. *J. Phys. Chem. B* **2014**, *118*, 12383.

(8) Ferré, S.; Casado, V.; Devi, L. A.; Filizola, M.; Jockers, R.; Lohse, M. J.; Milligan, G.; Pin, J.-P.; Guitart, X. *Pharmacol. Rev.* **2014**, *66*, 413.

(9) Schonenbach, N. S.; Rieth, M. D.; Han, S.; Malley, M. A. O. *FEBS Lett.* **2016**, *590*, 3295.

(10) Klyszejko, A. L.; Shastri, S.; Mari, S. A.; Grubmüller, H.; Muller, D. J.; Glaubitz, C. *J. Mol. Biol.* **2008**, *376*, 35.

(11) Jastrzebska, B.; Maeda, T.; Zhu, L.; Fotiadis, D.; Filipek, S.; Engel, A.; Stenkamp, R.

E.; Palczewski, K. *J. Biol. Chem.* **2004**, *279*, 54663.

(12) Hussain, S.; Kinnebrew, M.; Schonenbach, N. S.; Aye, E.; Han, S. *J. Mol. Biol.* **2015**, *427*, 1278.

(13) Schonenbach, N. S.; Hussain, S.; Malley, M. A. O. **2015**, *7* (June).

(14) Veenhoff, L. M.; Heuberger, E. H. M. L.; Poolman, B. *Trends Biochem. Sci.* **2002**, *27* (5), 242.

(15) Veatch, W.; Stryer, L. *J. Mol. Biol.* **1977**, *113* (1), 89.

(16) Chitnis, P. R. *Annu. Rev. Plant Physiol. Plant Mol. Biol.* **2001**, *52*, 593.

(17) Rosevear, P.; VanAken, T.; Baxter, J.; Ferguson-Miller, S. *Biochemistry* **1980**, *19*, 4108.

(18) Lund, S.; Orlowski, S.; de Foresta, B.; Champeil, P.; le Maire, M.; Møller, J. V. *J. Biol. Chem.* **1989**, *264*, 4907.

(19) Maciejko, J.; Mehler, M.; Kaur, J.; Lieblein, T.; Morgner, N.; Ouari, O.; Tordo, P.; Becker-Baldus, J.; Glaubitz, C. *J. Am. Chem. Soc.* **2015**, *137*, 9032.

(20) Garavito, R. M.; Ferguson-Miller, S. *J. Biol. Chem.* **2001**, *276*, 32403.

(21) Moller, J. V; Maire, M.; Pierre, I. U.; Paris, C.; Yvette, F.-G.-. *J. Biol. Chem.* **1993**, *268*, 18659.

(22) Casey, J. R.; Reithmeier, R. A. F. *Biochemistry* **1993**, *32*, 1172.

(23) Béjà, O.; Aravind, L.; Eugene, V.; Suzuki, M. T.; Hadd, A.; Nguyen, L. P.; Jovanovich, S. B.; Gates, C. M.; Feldman, R. A.; Spudich, J. L.; Spudich, E. N.; DeLong, E. F. *Science* **2000**, *289*, 1902.

(24) Lakatos, M.; Lanyi, J. K.; Szakács, J.; Váró, G. *Biophys. J.* **2003**, *84*, 3252.

(25) Váró, G.; Brown, L. S.; Lakatos, M.; Lanyi, J. K. *Biophys. J.* **2003**, *84*, 1202.

(26) Maslennikov, I.; Kefala, G.; Johnson, C.; Riek, R.; Choe, S.; Kwiatkowski, W. *BMC*

Struct. Biol. **2007**, *12*, 1.

(27) Heuberger, E. H. M. L.; Veenhoff, L. M.; Duurkens, R. H.; Friesen, R. H. E.; Poolman, B. *J. Mol. Biol.* **2002**, *317* (4), 591.

(28) Dioumaev, A. K.; Brown, L. S.; Shih, J.; Spudich, E. N.; Spudich, J. L.; Lanyi, J. K. *Biochemistry* **2002**, *41*, 5348.

(29) Dioumaev, A. K.; Wang, J. M.; Bálint, Z.; Váró, G.; Lanyi, J. K. *Biochemistry* **2003**, *42*, 6582.

(30) Friedrich, T.; Geibel, S.; Kalmbach, R.; Chizhov, I.; Ataka, K.; Heberle, J.; Engelhard, M.; Bamberg, E. *J. Mol. Biol.* **2002**, *321*, 821.

(31) Hempelmann, F.; Hölper, S.; Verhoefen, M. K.; Woerner, A. C.; Köhler, T.; Fiedler, S. A.; Pfleger, N.; Wachtveitl, J.; Glaubitz, C. *J. Am. Chem. Soc.* **2011**, *133* (12), 4645.

(32) Sharaabi, Y.; Brumfeld, V.; Sheves, M. *Biochemistry* **2010**, *49* (21), 4457.

Chapter 5 : Co-assembly of proteorhodopsin species into mesostructured silica-surfactant composites

Abstract

Membrane proteins are biomacromolecules with versatile transport, sensing and catalytic functionalities that could be exploited for practical purposes by incorporation into synthetic materials. Recently, high concentrations of functionally-active membrane proteins have been co-assembled into mesostructured surfactant-silica composites that are mechanically robust, optically transparent, and processable in a variety of morphologies; this co-assembly procedure, however, involved six components and multiple kinetic processes that make it difficult to understand and manage the roles of individual components to optimize material properties. Here, biophysical and materials characterization techniques are employed to develop a detailed understanding about the co-assembly and properties of the transmembrane protein proteorhodopsin in mesostructured surfactant-silica composites. Solution ^{1}H NMR, UV-visible absorption and X-ray diffraction techniques provide insight into the protein-stabilizing and structure-directing roles of surfactant species, which is leveraged to synthesize self-supporting mesostructured silica materials with high (20%) protein loadings, mechanical durabilities and optical transparencies. Solid-state nuclear magnetic resonance spectroscopy provides molecular-level information about the local structures and interactions of surfactant, silica and protein species in the nanochannel environments. The protein structure and dynamics are shown to be highly dependent on hydration and, moreover, correlate with the light-activated functionalities of proteorhodopsin guests. The synthetic, structural and functional insights are exploited to demonstrate that monomeric and oligomeric

proteorhodopsin species can be selectively incorporated into the mesostructured silica host materials. As proteorhodopsin has an archetypical transmembrane protein structure, the new understanding developed here is expected to serve as general guidelines for co-assembling other membrane proteins into mesostructured surfactant-silica materials.

Introduction

Membrane proteins are evolutionarily optimized to perform a broad variety transport, sensing and catalytic functionalities at high rates and selectivities that could be exploited for technological purposes in synthetic materials. As an example, in native lipid bilayers the transmembrane protein aquaporin selectively transports water at rates of nearly 3 billion molecules per second,[1,2] which exceeds the water flux of state-of-the-art water purification membranes by a factor of 100.[3,4] Other proteins undergo activated processes, *e.g.* the transmembrane protein proteorhodopsin absorbs either green or blue light to translocate an H^+-ion from the intracellular to extracellular regions of lipid bilayers,[5–7] which could be useful for solar-to-chemical energy conversion. Moreover, the functionalities of membrane proteins can be tailored through mutagenesis, as demonstrated by using directed evolution to tune the absorbance properties of light-activated H^+-ion pumping rhodopsins.[8] However, while native lipid bilayers support membrane protein function and stability, these membranes are small, not easily scaled and lack the mechanical and chemical robustnesses necessary to exploit protein function over macroscopic scales.

Mechanically robust synthetic membrane materials that incorporate high concentrations of functionally-active membrane proteins could harness membrane protein function in durable macroscopic devices. The highly hydrophobicities, complex structures and limited stabilities of membrane proteins make them difficult to process into synthetic materials.

As a result, many synthetic materials that include membrane proteins are designed to incorporate and support lipid bilayers that include the active protein;[9–11] though, as lipid bilayers are components of these materials they likely would exhibit comparable or marginally reduced susceptibilities to mechanical and chemical damage with respect to neat lipid bilayers. Other groups have self-assembled functionally-active membrane proteins into multi-component lipid or block-copolymer arrays,[12–14] yet such materials have small dimensions that would make them challenging to integrate with macroscopic devices. Finally, membrane proteins can be incorporated into a synthetic host by adsorption, but this approach often leads to inhomogeneous distributions and low loadings of proteins.[15]

Recently, mesostructured silica has emerged as a new material with high promise to enable membrane protein function to be exploited for technological applications. Such inorganic-organic hybrid materials are synthetized from solutions by the co-assembly of amphiphilic surfactants with silica precursors that cross-link into a mechanically and chemically robust matrix. The resulting material is ordered on the mesoscale (2-50 nm), the dimensions and topologies of which can be adjusted by the synthesis compositions and conditions, and can include molecular guests, such as polymers,[16] small molecular dyes,[17–19] nanoparticles[20] and globular proteins.[21] By careful selection of synthesis conditions, Jahnke et al co-assembled high concentrations of functionally-active proteorhodopsin and cytochrome c membrane proteins into mesostructured silica.[22] Critical aspects of this synthetic protocol are the uses of protein-stabilizing and structure-directing surfactants, aqueous solvent conditions, and mildly acidic pH conditions that collectively stabilize and solubilize the membrane proteins during the co-assembly process. This synthesis requires up to six different chemical components and involves multiple kinetic processes, which provides great difficulties in

understanding and managing the roles of individual synthesis components. Parsing their effects, however, would allow the judicious selection of synthesis compositions and conditions to generate materials with properties important for harnessing membrane proteins in macroscopic devices.

This study seeks to understand the co-assembly and properties of synthetic mesostructured surfactant-silica host materials that incorporate membrane protein species. As surfactants stabilize functionally-active membrane proteins in non-native micellar environments, it is hypothesized that understanding and managing the structure-directing and protein-stabilizing roles of surfactants would enable materials to be synthesized with high protein loadings, optical transparencies, and mechanically robustnesses. To test this, the membrane protein proteorhodopsin is investigated because it has an archetypical transmembrane structure with seven α-helices, can be stabilized in various micellar surfactant solutions, and has light-activated behaviors that provide rich functional information. Complementary analyses by solution NMR and UV-vis spectroscopies interrogate how the surfactant-to-protein ratio influences the capacity to which proteorhodopsin can be loaded into self-supporting, optically transparent mesostructured silica membranes. Subsequently, powerful two-dimensional solid-state NMR techniques are used to probe the local environments and structures of the surfactant-silica nanochannels into which proteorhodopsin guests are incorporated. These molecular-level insights are then correlated with proteorhodopsin function, as measured by the transient light-activated and pH-dependent absorbance behaviors. The knowledge developed here is employed to incorporate either monomeric or oligomeric proteorhodopsin into mesostructured silica films.

Materials and Methods

Protein purification and preparation. Protein purification was carried out as described previously,[23] but with a few differences. Specifically, cell lysis was carried out with incubation overnight in lysis buffer (20 mg/mL lysozyme, DNAse and 20 mM $MgCl_2$), three freeze fracture freeze-thaw cycles (using liquid nitrogen), and low-power probe tip sonication. All solutions used to purify proteorhodopsin were buffered at pH ~8.7 by a phosphate buffer of 50 mM K_2HPO_4 and 150 mM KCl. Prior to incorporation into materials, the ionic strength of the PR-containing solutions was lowered by using a PD-10 desalting column (Millipore) and then concentrating the eluate to centrifugal concentration (50 kDa MWCO, Amicon Ultra) to the desired protein concentration, generally >100 μm. Protein concentration was determined using the absorbance at 515 nm using an extinction coefficient of 49,000 M^{-1}•cm and a molecular weight of 29,000 g/mol.

Size-exclusion fast protein liquid chromatograph (FPLC) was used to separate and isolate monomeric and oligomeric proteorhodopsin species. Prior to FPLC, the PR sample was incubated overnight in a solution of 2 wt% 1,2-diheptanoyl-s,n-glycero-3-phosphocholine (diC_7PC) and subsequently filtered through a PTFE syringe filter with 0.2 μm pore size. The running buffer for FPLC measurements was a solution containing 50 mM K_2HPO_4,150 mM KCl and 0.05 wt% DDM. The monomeric and oligomeric proteorhodopsin fractions from the FPLC were collected and subsequently concentrated using centrifugal concentrators (50 kDa MWCO, Amicon Ultra). Before incorporation into materials, these samples were desalted using a PD-10 column and then concentrated to the desired protein concentration (>100 μm).

Materials synthesis. Mesostructured silica materials were prepared by mixing 350 mg of tetraethylorthosilicate (TEOS, Acros Organics) with 1.5 g of H_2O and 10 uL of 400 mM HCl.

The solution was stirred vigorously for 2 hours, at which point the solution was transparent. 200 mg of this solution was removed and mixed with an appropriate amounts of DDM and 9.1 wt% solution of diC_7PC and subsequently vortexed until the DDM was completely dissolved. This solution was mixed in an appropriate volume of the desalted PR-containing solution and subsequently titrated to a pH of 3.5-4 by using 100 mM NaOH. Solutions were cast onto PDMS stamps (~2 cm x 2 cm) under ambient temperature and 75% relative humidity conditions. Solvent evaporation was allowed to proceed for 2 days before the materials were characterized. For materials synthesized with n-propyl silica functionalities, an appropriate amount (usually 25 wt%) of TEOS was replaced with n-propyltriethoxysiline (97%, Alfa Aesar) in the material precursor solution prior to hydrolysis.

UV-visible absorbance spectroscopy. Static visible absorption spectroscopy was conducted on a Shimadzu UV-1800 spectrophotometer. For measurement of the pKa of D97, free-standing films of mesostructured silica were inserted into a home-built sample holder that fit into a transparent plastic cuvette. The sample was incubated initially in a solution containing 50 mM K_2HPO_4 and 150 mM KCl (pH ~8.7) for 15 minutes before UV-vis absorbance measurements were taken. Subsequently, the solution in the cuvette was removed and replaced with 2 mL of new buffered solution that had been titrated to the desired pH, one minute was allowed for incubation, the pH of the solution was measured, and the UV-visible absorbance of the film was taken. To determine the amount of time required for soaked films to equilibrate with the buffered solution, we monitored the visible absorbance of PR in the mesostructured silica after exposure to different buffered solutions; these measurements indicated that soaking as-synthesized films for 15 minutes and, following this initial soak, incubation times of 1 minute in a new buffer were sufficient to allow equilibrium among PR species in the synthetic

host and the buffered solution. Using an initial incubation time of 15 minutes and allowing 1 minute of exposure to a new buffered solution between pH This process was repeated using at least 11 buffered solutions that were at different pH values.

The absorbance data acquired from films soaked in different buffered solutions was analyzed using a home-built MATLAB to yield the acid dissociation constant for residue D97. In short, the program adjusts each spectrum such that the absorbance intensity at 700 nm is zero, then normalizes each absorption spectrum such that the absorbance maximum between 500-550 nm has an absorbance intensity of 1. Subsequently, the wavelength of maximum absorbance intensity is extracted and plotted as a function of pH. The resulting data is then fit to the Henderson-hasselbalch equation using a non-linear fitting algorithm with two fitting constants, the pKa value and the hill coefficient.

Transient UV-visible absorption data was acquired using a SpectraPhysics Quanta-ray Nd:Yag INDI series laser with a halogen lamp measuring light and single wavelength detector. Mesostructured silica films that incorporate proteorhodopsin were placed into quarts cuvettes and subsequently pulsed with a 10 ns green laser. The absorbance intensities at 410, 500, 550 and 570 nm were recorded over timescales ranging from 1 μs to 0.2 s. The absorption data at each wavelength were stitched together from three acquisitions in which 5120 absorbance datum were measured over timescales of 200 μs, 200 ms and 500 ms starting at 20 μs, 20 ms and 50 ms prior to the laser pulse. The absorbance data at each wavelength were averaged over 200 equally spaced bins on a logarithmic scale. The points were averaged over 200 equally spaced regions on a log scale. Global fitting analyses was performed with a home-build MATLAB code with initial guesses of 0.0001, 0.05 and 0.1 s. Fitting analyses used increasing numbers of exponential terms until a reasonable fit was obtained.

Blue-native Polyacrylamide Gel Electrophoresis (BN-PAGE). Blue-native polyacrylamide gel electrophoresis techniques were used to assess the distributions of proteorhodopsin monomers and oligomers in micellar surfactant solutions, prior to incorporation into mesostructured silica materials. Preparation and electrophoresis of BN-PAGE gels (NativePAGE Novex Bis-Tris Gel 4-16%, 10 wells) were carried according to manufacturer's instructions. Proteorhodopsin samples were prepared by mixing a micellar solution containing 3-4 μg of protein with 5 μL sample buffer, 1 μL of 5% Coomassie Brilliant Blue G250 solution, and a variable amount of H_2O such that the total volume of the solution was 20 μL. Integration of signal intensities on BN-PAGE gels was carried out with ImageJ software using first a background subtraction (rolling ball method, 150 pixels) and then integrating along the direction of low to high molecular weight, averaging across the entire width of the respective well.

Solution ^{1}H NMR spectroscopy. Solution ^{1}H NMR was used to determine the concentration of surfactants in micellar solutions containing proteorhodopsin. Single-pulse ^{1}H NMR measurements were acquired on a small-bore Bruker Avance NMR spectrometer operating at 11.74 T and at room temperature. Samples were prepared by adding 50 μL of the proteorhodopsin-containing solution to 950 μL of D_2O (99.9%, Cambridge Isotopes). The single-pulse measurements used a 30º pulse with a pulse length of 13.8 μs, a 6 s acquisition time, a recycle delay time of 1 s, and between 16 and 64 signal-averaging scans.

Solid-state NMR spectroscopy. Solid-state NMR measurements were used to probe the local structures of silica nanochannels and proteorhodopsin structures. Samples were packed into zirconia rotors that had 4 mm outer diameters, inserted into a double-resonance variable-temperature Bruker probehead, and rotated at a rate of 12.5 kHz at the magic angle.

Measurements were conducted on a Bruker Avance NMR spectrometer operating at 11.74 T, which provided nutation frequencies of 500.24 MHz, 125.79 MHz, and 99.38 MHz for ^{1}H, ^{13}C, and ^{29}Si nuclei, respectively. The ^{13}C{^{1}H} and ^{29}Si{^{1}H} heteronuclear correlation (HETCOR) measurements used hard ^{1}H 90º 100 kHz pulses and achieved cross-polarization (CP) by adiabatic passage at the Hartmann-Hahn condition using either a 3 ms or 1.0 ms contact time for the ^{13}C{^{1}H} and ^{29}Si{^{1}H} HETCOR experiments, respectively .[24] High-power ^{1}H homonuclear decoupling was achieved during the evolution period by application of an eDUMBO-1_{22} decoupling pulse sequence using a high-power ^{1}H pulses that were phase-modulated but of constant amplitude (100 kHz).[25] Heteronuclear decoupling during the acquisition period was achieved by applying the SPINAL-64 pulse sequence at a ^{1}H nutation frequency of 100 kHz.[26] Signal detection was realized by quadrature detection using time-proportional phase incrementation (TPPI) in the indirect (^{1}H) dimension.[27] The τ_1 dimensions of the ^{13}C{^{1}H} and ^{29}Si{^{1}H} HETCOR measurements were incremented by 128 μs with 256 signal-averaging per τ_1 increment, respectively. An eDUMBO-1_{22} scaling factor of 0.575 was applied based on a ^{1}H spin-diffusion measurements with zero mixing time, and a scaling factor of 0.58 was obtained for the ^{13}C{^{1}H} HETCOR spectrum by scaling a ^{13}C{^{1}H} HETCOR spectrum acquired from a ^{13}C,^{15}N-isotopically enriched glycine sample such that the three ^{1}H chemical shifts resonated at 3.2, 4.3 and 8.4 ppm. Isotropic ^{1}H, ^{13}C, and ^{29}Si chemical shifts were referenced neat tetramethyl-silane (TMS, 0 ppm) by using an external reference of either tetrakis-methylsilane (with ^{13}C and ^{1}H chemical shifts of 3.52 and 0.25 ppm relative to TMS, respectively) or ^{13}C,^{15}N-isotopically enriched glycine (with respective ^{13}C shifts of 176.46, 43.67 ppm).[28]

Results and Discussion

The co-assembly of membrane proteins into mesostructured silica materials is a multicomponent non-equilibrium process in which surfactant aggregates, protein molecules, solvent and silica precursors interact and self-assemble. To incorporate functionally-active proteorhodopsin into transparent and self-supporting mesostructured silica materials requires that material synthesis conditions are compatible with protein stability and solubility; this necessitates complex synthesis compositions and conditions and make it difficult to parse the influences of individual components. Here, the parameters important for co-assembling functional proteorhodopsin molecules into mesostructured silica materials are explored in detail, and these new insights are exploited to yield materials with desirable macroscopic properties.

Protein-stabilizing surfactants as structure-directing agents

Protein-stabilizing surfactants play necessary roles in solubilizing and stabilizing functionally-active proteorhodopsin species during co-assembly into materials. The solubility of PR molecules throughout the material synthesis is crucial for generating mesostructured silica as self-supporting films morphologies rather than as powders. However, only a few types of surfactants are known to solubilize PR species. Thus, the mesostructure-directing capabilities of surfactants that solubilize proteorhodopsin, including Brij-78, n-dodecyl-β,D-maltoside (DDM) and 1,2-diheptanoyl-s,n-glycero-3-phosphocholine (diC_7PC), were investigated. Insights into the mesostructural (2-50 nm) ordering of materials can be obtained by using small-angle X-ray scattering (SAXS) techniques, which exploit X-ray diffraction from regions of contrasting electron densities that exhibit long-ranged mesoscale (2-50 nm) ordering; using Bragg's law, the reflections in such patterns can be related to characteristic

length scales and indexed to identify the mesostructural topology. For example, the SAXS pattern (Figure 2B, top) of silica materials directed by Brij-35 surfactants that include 5 wt% PR show a single reflection at ~1.15° 2θ (full-width half maximum, fwhm 0.32°), with associated *d*-spacing of 7.6 nm. Based on broadness of this reflection, lack of higher-order Bragg reflections, and proclivity of Brij-78 molecules to direct wormlike mesostructures,[29] this reflection likely is assigned to the *(100)* reflection of a wormlike mesostructure, as depicted in the inset of Figure 2B. By comparison, silica materials directed by a combination of DDM and diC_7PC with 5 wt% PR exhibits a SAXS reflections at ~1.8° 2θ (fwhm 0.5°), with an associated *d*-spacing of 4.6 nm, and a broad shoulder at ~2.2° 2θ (Figure 1B), suggesting a small quantity of mesochannels with a 4.4 nm channel-to-channel distance. The slightly larger *d*-spacing observed for Brij-78-directed mesostructured silica materials versus those directed by DDM likely originates from the longer alkyl chain (16 carbon chain) and ethylene oxide (~20 units) headgroup than that of DDM (12 carbon chain tail, maltoside headgroup. Importantly, both the Brij-78- and DDM+diC_7PC-directed silica materials have absorption properties of native-like PR under acidic conditions, establishing the maintained photoactivities of PR guests. Additionally, both materials are optically transparent, indicating that PR species remain soluble throughout the synthesis.

Mesostructured silica materials with functionally-active proteorhodopsin can be synthesized using surfactants that are proficient in directing mesostructure formation but tend to destabilize proteorhodopsin molecules. For example, cationic surfactants often destabilize membrane proteins through strong electrostatic interactions but have high hydrophilic-hydrophobic contrast that make them effective structure-directing agents. We hypothesized that the use of mixtures of protein-stabilizing and cationic surfactants could promote high

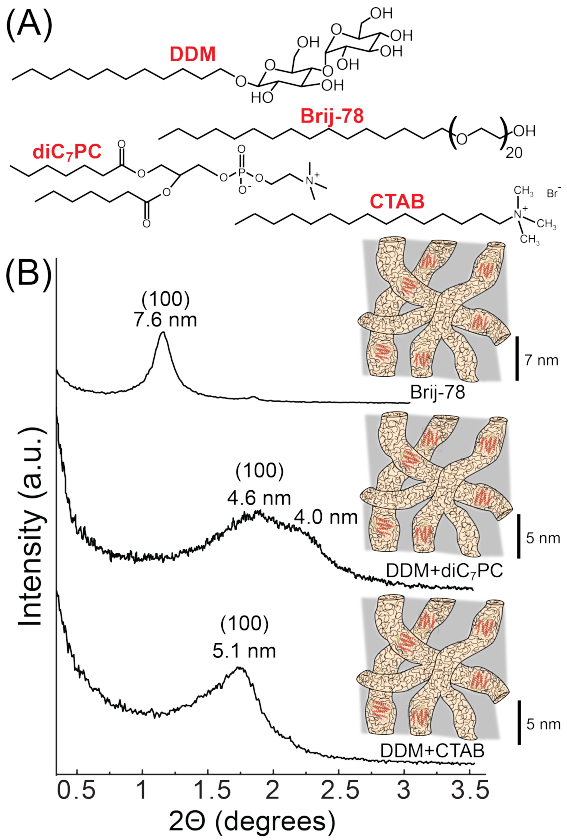

Figure 7. (A) Molecular structures of the surfactants n-dodecyl-β,D-maltoside (DDM), Brij-78, 1,2-diheptanoyl-s,n-glycero-3-phosphocholine (diC7PC), and cetyltrimethylammonium bromide (CTAB). (B) Small-angle X-ray scattering patterns of mesostructured silica with 5 wt% proteorhodopsin using (top) Brij-78, (middle) DDM+diC7PC and (top) DDM+CTAB as structure-directing surfactants.

degrees of mesostructural ordering while also stabilizing membrane protein guests. The SAXS patterns of materials synthesized using a mixture of DDM and CTAB that include 5 wt% PR have a single reflection at ~1.75° 2Θ (fwhm 0.35°), with associated d-spacing of 5.1 nm. While this *(100)* reflection of the CTAB+DDM-directed materials is sharper (fwhm = 0.35°) than those directed by DDM+diC$_7$PC (fwhm ~0.5°), a much narrower *(100)* SAXS reflection of 0.15° is observed for the Brij-35 directed materials. Though CTAB+DDM-directed materials can have sharper *(100)* SAXS reflections at higher CTAB contents, when PR was included in such materials an increasingly yellow coloration was observed, indicating that PR guests were denatured. Despite the typically effective structure-directing qualities of CTAB surfactants,

high extents of mesostructural ordering were not achieved under synthesis conditions compatible with PR stability.

Controlling membrane protein loadings in mesostructured silica

The solubility of proteorhodopsin molecules during co-assembly is critical for the optical transparencies of the resulting materials and requires appropriate amounts of surfactants that can influence material compositions. Proteorhodopsin is a highly hydrophobic molecule that requires intimate interactions with surfactants, specifically at the transmembrane surfaces, to remain soluble in aqueous solutions. For example, soluble and functional bacteriorhodopsin molecules in micellar solutions reportedly adsorb 120-200 surfactants per BR molecule, or approximately 2-4 times the mass of the bacteriorhodopsin molecule, depending on the type of surfactant.[30] Should such surfactant-to-protein ratios be required to solubilize PR, then co-assembling PR into mesostructured silica would demand surfactant quantities that substantially contribute to the final material composition and thus limit protein loading.

To understand the solubility of proteorhodopsin molecules during mesostructured silica co-assembly, the concentrations of surfactant and soluble PR species were investigated in micellar DDM solutions directly prior to incorporation using solution ^{1}H NMR and UV-vis spectroscopies. Each functional PR molecule binds a single chromophore that absorbs visible light (510-545 nm) and allows the PR concentration to be determined via the Beer-Lambert law; DDM surfactants have no such visible absorption, but rather yield multiple well-resolved ^{1}H NMR signals that can be quantified by analyses by single-pulse ^{1}H NMR measurements.[31] Comparison of the DDM and PR concentrations for numerous samples of PR in micellar solutions yielded DDM-to-PR ratios ranging from 0.9 to 6.2 (w/w) with an average value of 3.2 ± 1.8. This is in reasonable agreement with the DDM-to-protein ratio of 4.1 (w/w) reported

for bacteriorhodopsin,[30] likely owing to its structural homology with PR. Moreover, the large range of DDM-to-PR ratios, however, is unexpected and could originate varying distributions of PR monomers, dimers, pentamers and hexamers among samples; larger oligomers are expected to have more protein-protein contacts that would reduce transmembrane surface area available for interactions with surfactants. Corroborating this hypothesis are complementary blue-native polyacrylamide gel electrophoresis analyses that correlate higher DDM-to-PR ratios of 2.7-6.2 with high monomer+dimer contents and lower ratios of 0.9-2.1 with pentameric/hexameric PR. It should be noted, though, that the increased surfactant contents for monomeric samples could also reflect that surfactant micelles were not separated from monomeric PR-surfactant complexes during size exclusion chromatography based on their similar molecular weights. While DDM-to-PR ratios as low as 0.9 appear suitable to solubilize PR, it remains unclear whether this reflect a lower surfactant limit for stability. Separate measurements (Appendix B, Figure B13) in which the DDM-to-PR ratio in micellar solutions of monomeric/dimeric PR (with E50Q mutation) were reduced from 3.9 to 1.0 by using bio-beads show that PR precipitates sharply upon changing the DDM-to-PR ratio from 1.7 to 1.0; though 80% of the PR remained soluble at a DDM-to-PR ratio of 1.0. These suggest that a DDM-to-PR ratio of 1.0 is near the boundary of PR solubility in DDM, with PR becoming less soluble at lower DDM-to-PR ratios.

The DDM-to-PR ratios yield estimates for the highest loading of proteorhodopsin that can be co-assembled into optically transparent mesostructured silica materials, as represented by the line labeled “PR solubility” in the ternary composition diagram in Figure 2A. The ternary composition diagram in Figure 2A includes the non-volatile components of the material synthesis, which remain after solvent evaporation, that include the surfactants, silica and

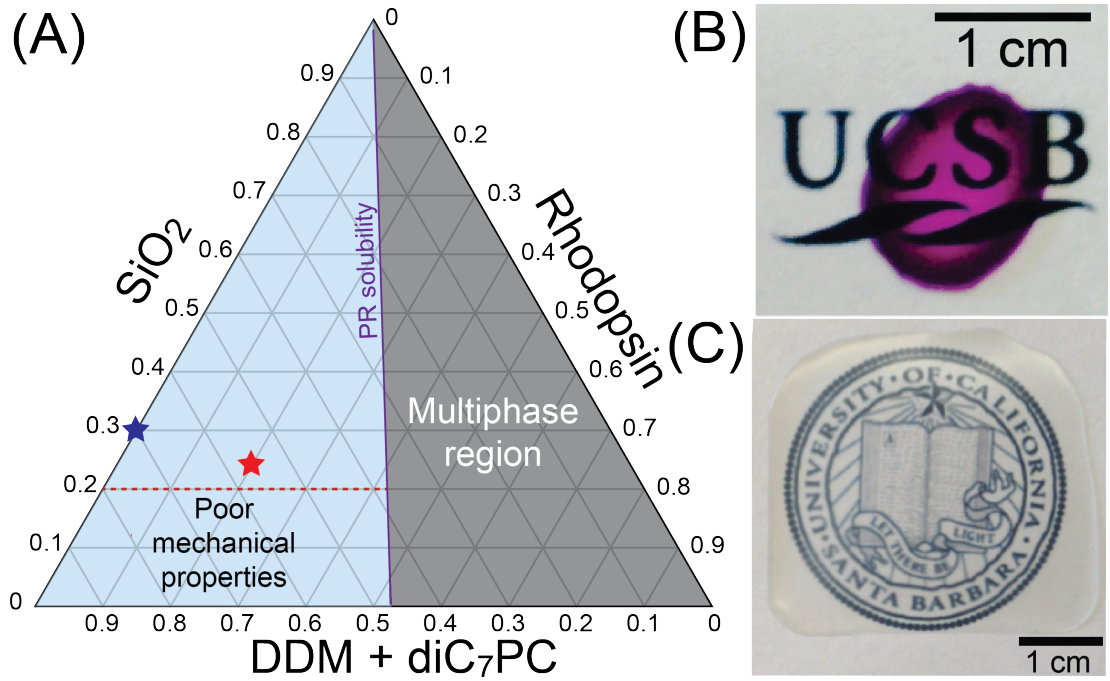

Figure 8. (A) Ternary composition diagram for mesostructured silica materials without or with proteorhodopsin/rhodopsin guests synthesized by using solvent evaporation induced co-assembly. Material with compositions to the left of the line titled "PR solubility" can be synthesized as optically transparent membranes, while at other compositions PR is expected to precipitate from solution during material synthesis. Generally, materials with less then 20% silica show poor mechanical properties, as defined by the dotted red line. **(B,C)** DDM-diC_7PC-directed mesostructured silica free-standing materials synthesized (B) with 20 wt% rhodopsin and (C) as a larger 3x3 cm film but without rhodoposin. The materials in (B) and (C) were ~100 μm thick.

proteorhodopsin species. The blue-colored region to the left of the "PR solubility" line indicates mesostructured silica compositions that have sufficient quantities of surfactants render all PR molecules soluble during co-assembly. By comparison, the gray-colored region to the right of the "PR solubility" boundary represents material compositions in which PR is expected to precipitate during co-assembly and yield disordered powders. DDM+diC_7PC-directed mesostructured silica materials synthesized with rhodopsin loadings up to 20% at a DDM-to-PR ratio of 2.8 (red star in Figure 2A) are optically transparent, as shown in the macroscopic image in Figure 2B, indicating the rhodopsin species remain soluble throughout co-assembly. Higher protein loadings can be achieved with lower DDM-to-PR ratios. For

example, at a DDM-to-PR ratio of 0.9, the highest PR loading in optically transparent films should be approximately 53 wt%, with the balance of the material composition being surfactant. Such materials, however, would have poor mechanical properties and dissolve upon exposure to water, making them unsuitable for technological applications.

Correlating mesostructured silica composition with material properties

Appropriate choice of silica content is important to provide mechanical robustness to self-supporting mesostructured silica films that include proteorhodopsin guests. The presence of an interconnected silica framework imparts mechanical robustness to mesostructured silica materials, yet higher silica contents also lower the maximum loading of PR in self-supporting mesostructured silica materials. To optimize the mechanical robustness and PR loading, the influence of silica content on the mechanical properties of mesostructured silica films with PR guests was investigated. Observations also generally suggest that materials with >20 wt% silica content are mechanically robust and will not dissolve upon incubation in aqueous solutions, as indicated by the "Poor mechanical properties" region in Figure 1A. However, films with >20 wt% silica content were highly susceptible to brittle fracture that would hinder their integration into macroscopic devices. Though such membranes are self-supporting (~50 μm-1 mm thick), they were moderately susceptible to brittle fracture, which indicate poor mechanical flexibilities.

To improve the mechanical flexibilities of mesostructured silica hosts, the inorganic silica framework was modified with hydrophobic alkyl functional groups that reduce the silica cross-linking density. It is hypothesized that lower degrees of silica cross-linking will yield higher macroscopic flexibilities. While hydrolyzed tetraethylorthosilicate silica precursor species can form four Si-O-Si linkages, silica precursors in which some –OH moieties are

replaced with non-reactive moieties, such as alkyl groups, support lower degrees of cross linking. Mesostructured silica membranes with ~30% total silica content, but with 25% of the Si atoms having one alkyl n-propyl functionality, but without PR (Figure 2A, blue star) can be synthesized as optically transparent self-supporting membranes that exhibit high mechanical flexibilities (Figure 3). Materials of the same composition can be easily synthesized as large (3x3 cm) self-supporting mesostructured silica membranes (Figure 2C), likely because the increased flexibilities reduce mechanical stress on the material as the silica framework condenses. Such membranes can also accommodate up to 20 wt% of functionally active rhodopsin species in transparent self-supporting film morphologies (Figure 2B). The fact that n-propyl functionalities influences macroscopic material properties suggests that these species distribute throughout the silica framework. Based on the amphiphilicity of these species, however, it is expected that the nanochannel surfaces will be enriched in the n-propyl-functionalized silica species and in close contact with incorporated hydrophobic PR guests.

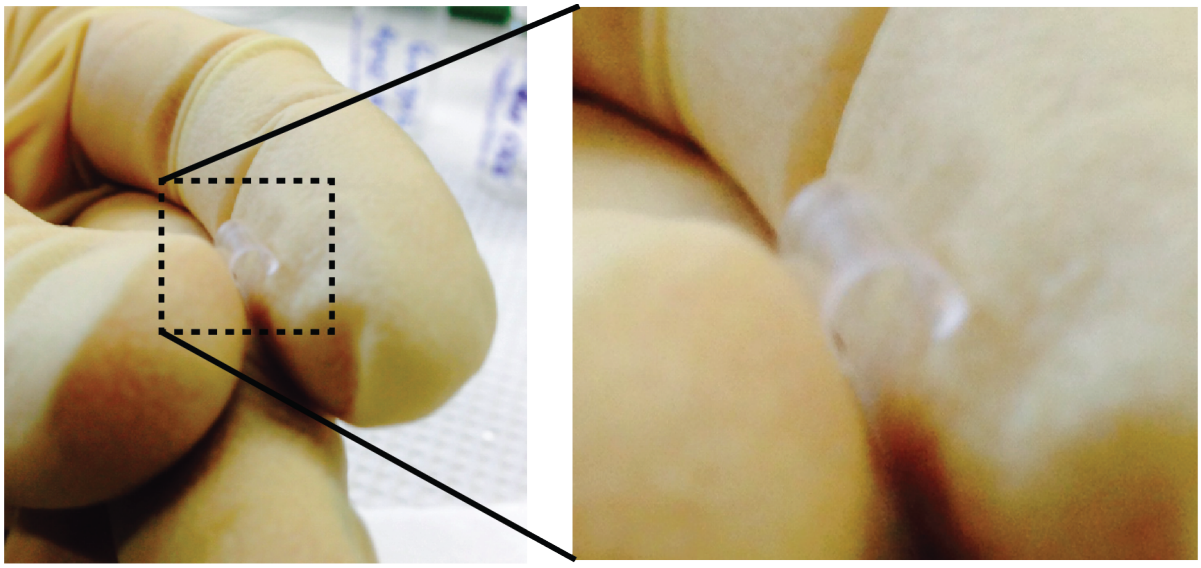

Figure 9. Optical image (left) of an as-synthesized free-standing mesostructured silica film without PR that is bent at approximately 180° without macroscopic cracking. The image on the right shows a zoomed in version of the mesostructured silica membrane. Deformation of membranes to angles greater than ~180° fractured the materials. The compositions of this film were 71 wt% DDM, 22% SiO_2, and 7% n-propyl-$SiO_{1.5}$.

Structure of silica-surfactant mesochannels

Insight into the co-assembly process of mesostructured silica materials can be derived from the structures of the silica nanochannel environments, as probed by using solid-state nuclear magnetic resonance (NMR) spectroscopy. Solid-state NMR experiments exploit the chemical shift interaction to resolve various chemical moieties based on their isotropic chemical shifts, which are sensitive to the local bonding environment. For example, the 1D $^{29}Si\{^{1}H\}$ cross-polarization magic-angle spinning (CPMAS) spectrum shown at the top of Figure 4A shows five resolved signals at approximately -57, -67, -90, -100 and -110 ppm; based on the literature, these can be assigned to the ^{29}Si atoms in T^i or Q^i bonding configurations, where i refers to the number of bridging Si-O-Si bonds of the associated ^{29}Si atom. Similarly, signals in the 1D ^{1}H single-pulse and ^{13}C CPMAS spectra Figure 2A (left and top right, respectively) can be assigned to the various atomic moieties of DDM, diC_7PC and n-propyl functionalities, based on solid-state NMR measurements of their neat components and the literature.[32]

While 1D NMR analyses yield signal assignments for various atomic moieties, solid-state 2D heteronuclear correlation (HETCOR) experiments provide information about the structures of the inorganic framework and nanochannels. Solid-state 2D $^{29}Si\{^{1}H\}$ heteronuclear correlation (HETCOR) NMR measurements employ through-space dipolar couplings among nearby (<1 nm) ^{29}Si and ^{1}H nuclei to probe their proximities. The 2D $^{29}Si\{^{1}H\}$ HETCOR of DDM+diC_7PC-directed mesostructured silica in Figure 4A shows many correlations that arise from nearby ^{1}H and ^{29}Si species, such as those at ca. 0.9 ppm in the ^{1}H dimension of the propyl functionalities with ^{29}Si signals at -57 and -67 of the T^2 or T^3 silica species to which the propyl alkyl chains are covalently bound. While the covalent bonding of

n-propyl groups to ^{29}Si atoms accounts for these correlated intensities, other correlations are observed for the same ^{1}H signals and ^{29}Si signals at -100 and -110 ppm from Q^3 and Q^4 sites, unambiguously establishing the close (<1 nm) proximities of the T and Q silica sites in the framework. This supports that n-propyl-functionalized and non-functionalized silica species co-condense to form the inorganic silica matrix. The relatively strong correlation at ca. 7.8 ppm in the ^{1}H dimension and -100 ppm in the ^{29}Si dimension is assignable to silanol groups of the Q species that participate in hydrogen bonds, likely with adsorbed water in the silica framework. No such correlation is observed with the ^{29}Si resonance of the T^3 silicon species, likely because these species are not directly bonded to silanol groups and their hydrophobic n-propyl group doesn't interact strongly with relatively hydrophilic silanols.

Analyses of ^{29}Si{^{1}H} and ^{13}C{^{1}H} 2D HETCOR NMR spectra clearly reflect close proximities of structure-directing surfactants with moieties in the silica framework. The 2D ^{13}C{^{1}H} HETCOR NMR spectrum (Figure 4A) shows many highly-resolved signals that can be assigned to the ^{1}H and ^{13}C moieties of the DDM, diC_7PC and n-propyl-silica species based on NMR of the neat components and the literature.[33] Especially sharp NMR signals are observed in the alkyl region (10-35 ppm) that indicate the fast motions of alkyl tails relative to the 100 μs timescale of the NMR measurement. By comparison, in the same spectrum the ^{13}C signals between 70-80 ppm associated with the hydrophilic headgroups of DDM molecules are relatively broad, suggesting relatively lower mobilities or less uniform environments. These ^{13}C signals correlate with the ^{1}H signals at ca. 3.5 ppm assigned to moieties 12, 14-18 and 20-24 of the DDM headgroups and moieties i moieties of the diC_7PC headgroups, as these ^{13}C and ^{1}H moieties are directly bonded; interestingly, in the ^{29}Si{^{1}H} spectrum, ^{1}H signals at the same resonance correlate strongly with ^{29}Si signals at -100 and -110 of the Q^3 and Q^4 silica species,

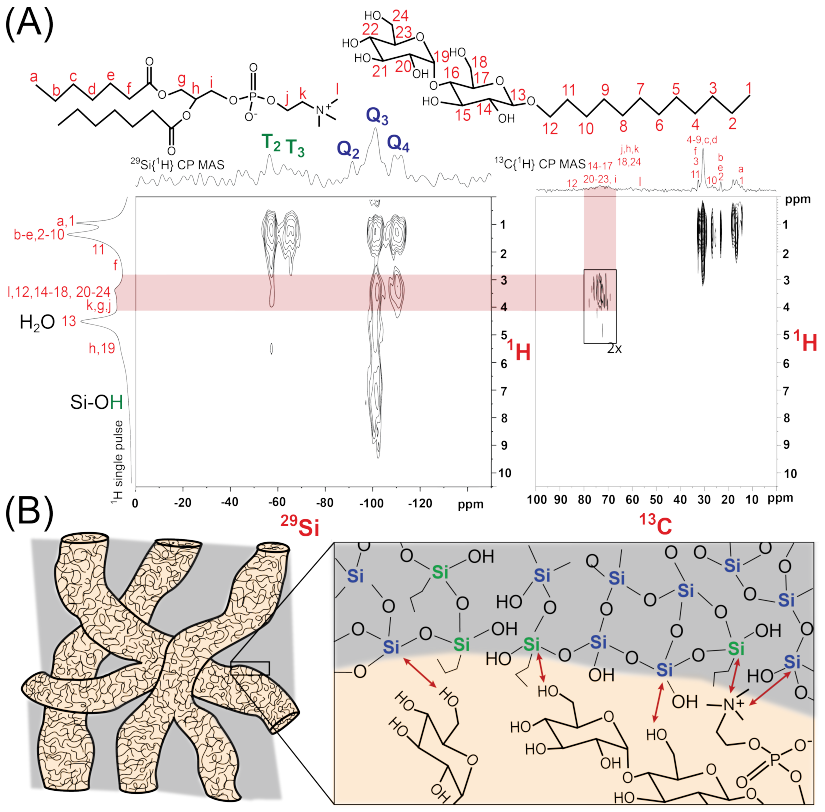

Figure 10. Two-dimensional (2D) solid-state **(A)** ^{29}Si{^{1}H} HETCOR and **(B)** ^{13}C{^{1}H} NMR spectra acquired from DDM-diC_7pC-directed mesostructured silica materials with 25% of the inorganic framework having n-propyl-silica. Red bands indicate correlations that establish the close proximities of the ^{13}C species of the maltoside headgroups of DDM species with ^{29}Si groups of T^3, Q^3, and Q^4 silica sites. ^{1}D ^{29}Si{^{1}H} and ^{13}C{^{1}H} CP MAS spectra are shown on the top axes of the spectra, while a 1D ^{1}H single-pulse spectrum is shown on the left axis. All measurements were conducted at 11.7 T under 12.5 kHz MAS conditions at 20 °C.

respectively, while a much weaker correlation is observed with ^{29}Si signals at -57 of the T^3 sites. This establishes the close proximities and interactions of the DDM and diC_7PC headgroups with Q^3 and Q^4 silicon species, as depicted schematically in Figure 4B, likely through hydrogen bonding, and comparably weaker interactions with T^2 sites, probably because these species are relatively hydrophobic versus the Q^i sites.

Structure and function of protein guests in nanochannel environments

It is widely believed that membrane proteins require hydration to support their structure and dynamics necessary for their function. As a result, the effect of hydration on the

structures and functionalities of PR guests in synthetic mesostructured silica hosts was interrogated. Proteorhodopsin has 249 amino acid residues that interact to form a complex heptahelical structure in which many residues have unique chemical environments and mobilities, to which solid-state NMR spectroscopy are highly sensitive. The solid-state 2D $^{15}N\{^{1}H\}$ magic-angle spinning (MAS) NMR correlation spectrum in Figure 5A recorded from non-hydrated mesostructured silica materials with 12.5 wt% of ^{2}H,^{13}C,^{15}N-isotopically enriched PR shows correlated intensities that arise from the close proximiites of ^{1}H and ^{15}N species on the PR backbone. Though a few well-resolved correlations are observed, such as at ca. 105 in the ^{15}N dimension and approximately 7.3 ppm in the ^{1}H dimension, this spectrum shows generally poor signal resolution, as evidenced by the lack of resonances observed in the glycine region (104-112 ppm) that typically observed in spectra of functional PR in near-native lipids.[34,35] Moreover, most correlated intensities in this spectrum contribute to a broad, poorly resolved feature centered at ~118 ppm in the ^{15}N dimension and 8.2 ppm in the ^{1}H dimension. These spectral features suggest that PR guests have either undergo slow motions relative to the ~60 μs timescale of the NMR measurement or a broad distribution of local environments.

By comparison, a spectrum recorded from this same material but after incubation at 100% relative humidity for >1 month shows many strong and well-resolved correlations. Based on resonance assignments of PR in the literature,[34,35] these resolved intensities are tentatively assigned to amino acid residues G141, G144, G169, G171 and K172. As hydration is strongly coupled to protein dynamics,[36] the hydration dependences of these correlated signals likely arises from the faster dynamics of PR backbone moieties in hydrated versus non-hydrated materials. Due to the high density of the silica framework and hydrophobicity of the surfactant nanochannel core, it's likely that water molecules incorporated during hydration will

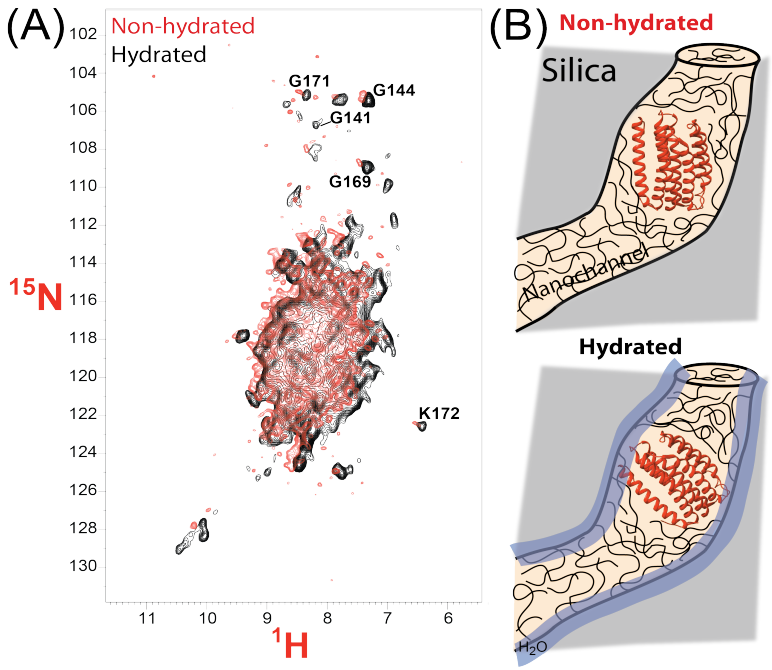

Figure 11. (A) ^{1}H-detected 2D ^{15}N{^{1}H} magic-angle spinning (MAS) heteronuclear correlation spectra acquired from mesostructured silica materials that incorporate 12.5 wt% proteorhodopsin (red) without and (black) with hydration at 100% relative humidity for >1 month. (B) Cartoons of the local nanochannel environments for non-hydrated and hydrated mesostructured silica materials in which the additional water from hydration is depicted along the nanochannel surface, which has high densities of hydrophilic surfactant headgroups and silanol species.

reside at the nanochannel interface and thus interact mainly with the hydrophilic loops of PR guests, as shown in Figure 5B. The strong correlation of material hydration and the dynamics of PR guests underscores the importance of water in supporting fast protein dynamics, which are generally thought to be coupled with membrane protein function.

Correlating the structure and function of proteorhodopsin guests

As protein dynamics and function are closely coupled, the substantial sensitivity of proteorhodopsin dynamics to material hydration of mesostructured silica suggests that hydration is important to proteorhodopsin guest function. Following excitation by green light, PR undergoes a series of conformational changes that result in the net movement of an H^{+}-ion across the transmembrane region of PR. Under acidic conditions, the light-activated function of PR proceeds by a cyclic reaction with five sequential intermediates (*K*, *L*, *N*, *PR'* and *PR*),[37]

each of which can be resolved by their distinct visible absorbances and lifetimes. Thus, the light-activated absorbance behaviors of PR in mesostructured silica hosts can yield detailed insights into the kinetics of PR function.

Non-hydrated mesostructured silica films with proteorhodopsin show complex transient absorbance behaviors in response to green light that are depicted in Figure 6A as difference absorbance, which is the difference in absorbance at a certain time versus in the non-photoactivated PR state. At early times following green laser excitation, mesostructured silica films with PR show increased difference absorbance intensity at 590 nm, and bleached intensity at 410, 500 and 550 nm. The difference intensities at all wavelengths decay monatonically towards zero at long (>0.1 s) times. These absorbance behaviors are qualitatively similar to those observed for PR in DDM micellar solutions and E. coli lipids under aqueous acidic conditions,[37] which also show positive difference intensities at 590 nm and negative intensities for 410, 500 and 550 nm. Moreover, these absorption behaviors can be related to the photochemical reaction cycle model for PR shown in Figure 6B, which was developed by Lakatos et al for PR in E. coli lipids.[37] All three of the *K*, *L* and *N* intermediates have absorbances that are bathochromically shifted with respect to the non-activated PR state, which has a maximum absorbance at ~540 nm. Thus, the positive and negative difference absorbances above and below 540 nm, respectively, in Figure 6A originate from increased populations of *K*, *L* and *N* intermediates relative to the non-photoactivated PR. These results and analyses provide evidence that PR in non-hydrated mesostructured silica materials undergo a native-like photochemical reaction cycle.

Global fitting analyses of the transient absorbance data yield quantitative information about the kinetics of the photochemical reaction cycle, which show a strong dependence on

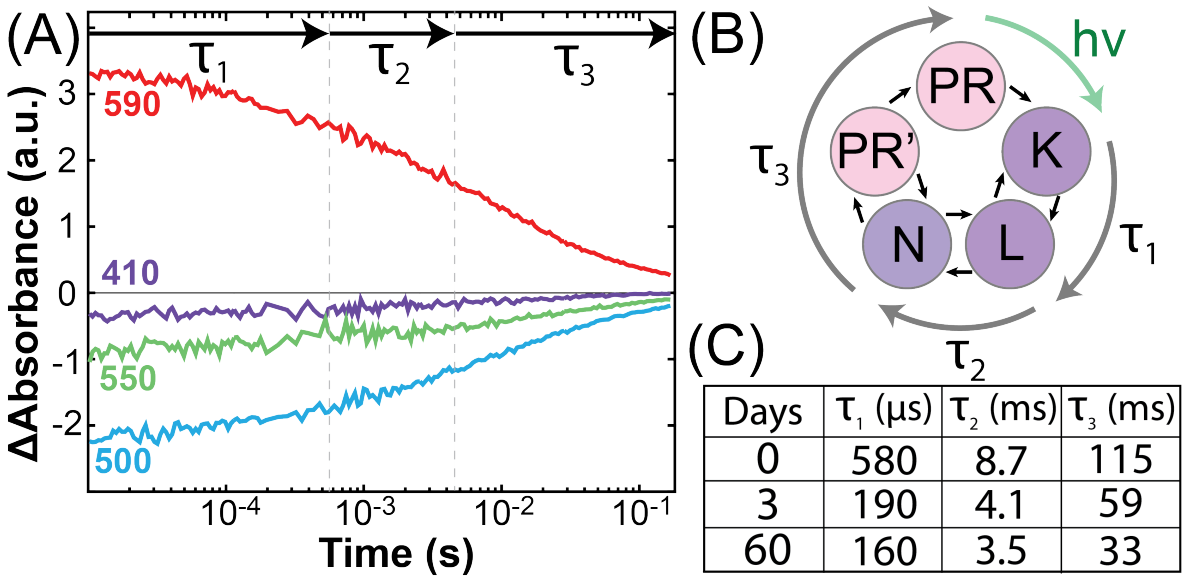

Days	τ_1 (μs)	τ_2 (ms)	τ_3 (ms)
0	580	8.7	115
3	190	4.1	59
60	160	3.5	33

Figure 12. (A) Time-resolved difference absorbances at 410 (purple), 500 (blue), 550 (green) and 590 (red) nm recorded from a non-hydrated mesostructured silica material containing 12.5 wt% PR following excitation by a ~10 ns laser pulse at 532 nm. **(B)** Schematic diagram of the photochemical reaction cycle of PR developed by Lakatos et al.,[37] with three global fitting time constants shown over associated processes in the reaction cycle. **(C)** Tabulated values of global fitting time constants affiliated with non-hydrated materials and those exposed to 100% relative humidity at 4 °C for 3 or 60 days. All transient absorbance measurements were conducted at approximately 20 °C.

material hydration. Such analyses involve simultaneously fitting the absorbance data at all wavelengths with a sum of multiexponentials that have wavelength-dependent pre-factors and wavelength-independent exponential time constants; the time constants are the apparent rate coefficients of the photochemical reaction cycle of PR. Accurate fits to the absorbance data from PR in non-hydrated mesostructured silica were obtained with three exponentials (τ_1, τ_2, and τ_3) with time coefficients of 578 μs, 8.7 ms, and 115 ms, as shown in Figure 6C. Guided by photocycle analyses of PR in E. coli membranes in the literature,[37] the first time constant, τ_1, is assignable to the conversions among *K* and *L* intermediates, while τ_2 mainly correlated with conversions between *L* and *N* intermediates, while the final τ_3 time constant is affiliated with *N*-to-*PR'* and irreversible *PR'*-to-*PR* steps. Interestingly, analyses of absorbance data from same mesostructured silica film but incubated at 100% RH for either 3 or 60 days show

a monatonic decrease of τ_1, τ_2 and τ_3 time constants (Figure 6C) with increasing hydration time. The most hydration-dependent time constant is the rate-limiting τ_3 value (115 ms for non-hydrated materials, and 33 ms for 60 day hydration), which establishes 3.5 times faster photocycles for PR guests in hydrated mesostructured silica. Moreover, the photocycle timescales for materials hydrated for 60 days agree well with those reported for PR in near-native DMPC/DMPA lipid environments under acidic aqueous solutions,[38] indicating that PR guests in hydrated materials have more native-like responses to light than those in non-hydrated materials. Along with the 2D NMR analyses, the hydration of PR in mesostructured silica materials yields pronounced structural, dynamical and functional changes of PR that are all correlated, highlighting the critical role of hydration in harnessing the functionality of membrane proteins in synthetic mesostructured silica materials.

Co-assembly of monomeric and oligomeric PR into mesostructured silica hosts

The insights into proteorhodopsin co-assembly, structure and function in mesostructured silica was extended to selectively incorporate monomeric and oligomeric proteorhodopsin into optically transparent self-supporting mesostructured silica materials. Many transmembrane protein species natively associate, typically by weak non-covalent interactions,[39] to form oligomers that can have augmented stabilities or enhanced functionalities versus their monomeric forms. In fact, PR in micellar solutions readily forms as monomers, dimers, pentamers and hexamers that exhibit oligomer-dependent functionalities; for example, the carboxylic acid moiety of aspartic acid residue 97 (D97) serves a key role in light-activated H^+-ion transport by PR and exhibits a higher acid dissociation constant in monomeric/dimeric ($pKa_{D97} \approx 7.4$-5) versus oligomeric ($pKa_{D97} \approx 6.7$-6.9) PR species.[40,41] This functional difference persisted for PR in various micellar surfactant

environments, making it a suitable property by which to assess the content of monomeric/dimeric and oligomeric PR in mesostructured silica hosts.

Mesostructured silica films that include the monomeric/dimeric and oligomeric PR species show pH-dependent absorbance behaviors consistent with changes in the protonation state of D97. As D97 is close in proximity to the retinal chromophore, changes to its protonation state alter the visible absorbance of PR. As shown in Figure 7A, mesostructured silica films synthesized with 2.5 wt% monomeric PR exhibit a maximum absorbance (λ_{max}) of 518 nm in alkaline (pH 8) solutions, in which the D97 should be deprotonated, and at 537 nm under acidic conditions (pH 3) in which D97 is protonated. These absorption maxima agree

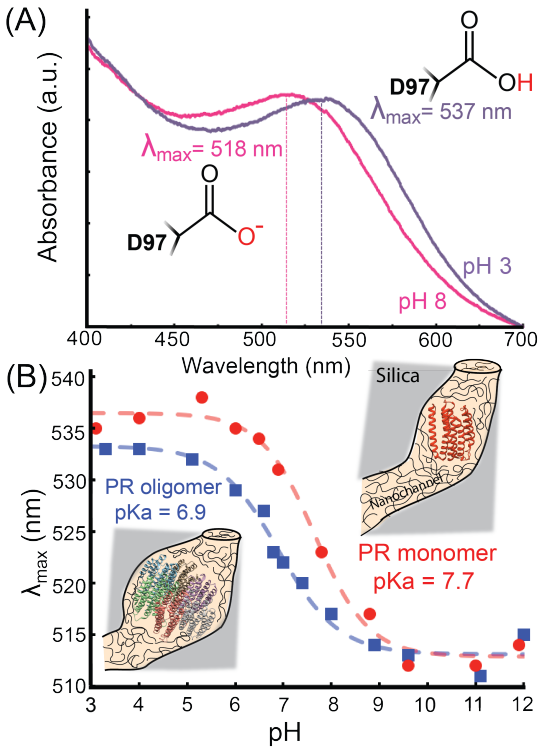

Figure 13. (A) UV-visible absorbance spectra recorded from free-standing mesostructured silica films with 2.5 wt% oligomeric PR soaked in aqueous solutions at pH 3 (pink line) and pH 8 (purple line). **(B)** The wavelength at maximum absorbance for mesostructured silica films synthesized with predominantly (red, circles) monomeric/dimeric and (blue, squares) oligomeric PR soaked in solutions of various pH. Best fit lines to the Henderson-hasselbalch equations are shown in dashed lines and establish pKa_{D97} values of 6.8 and 7.3 for materials with monomeric and oligomeric PR. All solutions used here contained 150 mM KCl and 50 mM K_2HPO_4 and were titrated to the desired pH using HCl (aq.) and NaOH (aq.).

well with those reported in the literature for PR in micellar DDM solutions.[42] Subsequent measurements on the same materials but under pH conditions ranging from 3 to 12 reveal a sigmoidal dependence of λ_{max} on pH (Figure 6B, red circles), as observed for PR in micellar surfactant solutions.[40] Fitting the λ_{max} data to the Hendersson-Hasselbalch equation yields a pKa value of 7.7 for PR films synthesized using monomeric PR, while same analyses of mesostructured films synthesized with 2.5 wt% oligomeric PR provides a much lower pKa_{D97} of 6.9. The differences in pKa values observed here align well with those of PR monomer/dimers (pKa ~7.4-7.5) and oligomers (pKa ~6.7-6.9) in micellar solutions, respectively,[40,41] and indicate that monomeric/dimeric and oligomeric PR can be selectively incorporated into mesostructured silica materials, as depicted schematically in the insets of Figure 7B.

Conclusions

Mesostructured silica has emerged a promising host materials to harness the unique and diverse functionalities of membrane proteins in macroscopic devices. This work develops a deep understanding of the protein-stabilizing and structure-directing roles of surfactant species critical to co-assemble membrane proteins into the mesostructured silica hosts. The new understanding is exploited to synthesize materials that are optical transparent, mechanically robust and flexible, accommodate high (20 wt%) protein loadings, and processable as self-supporting membranes. Subsequent interrogation by powerful multidimensional solid-state NMR correlation techniques provide molecular-level insights into the interactions and structures of surfactant and silica species in the mesostructured composite materials, which suggest that co-assembly proceeds by hydrogen bonding among the hydrophilic headgroups and surface silanol species. Complementary solid-state NMR and

time-resolved UV-visible absorption spectroscopies reveal a significant hydration dependence of the structures, dynamics and functionalities of proteorhodopsin, which appear necessary for the native-like function of proteorhodopsin in the synthetic mesostructured hosts. The synthetic, structural and functional insights are further exercised to selectively incorporate either monomeric or oligomeric proteorhodopsin species into mesostructured silica materials, which demonstrates that protein tertiary structure is largely unperturbed during the co-assembly process. Based on the archetypical seven α-helical structure proteorhodopsin, the understanding presented here is expected apply to other transmembrane membrane proteins and provide useful guidelines for synthesizing materials that harness protein function on macroscopic scales.

References

(1) de Groot, B. L.; Grubmüller, H. *Science* **2001**, *294* (5550), 2353.

(2) Zeidel, M. L.; Ambudkar, S. V.; Barbara, S. L.; Agre, P. *Biochemistry* **1992**, *31*, 7436.

(3) Tang, C. Y.; Zhao, Y.; Wang, R.; Hélix-nielsen, C.; Fane, A. G. *Desalination* **2013**, *308*, 34.

(4) Tang, C. Y.; Kwon, Y.; Leckie, J. O. *Desalination* **2009**, *242*, 168.

(5) Béjà, O.; Spudich, E. N.; Spudich, J. L.; Leclerc, M.; DeLong, E. F. *Nature* **2001**, *411*, 786.

(6) Sabehi, G.; Massana, R.; Bielawski, J. P.; Rosenberg, M.; DeLong, E. F.; Beja, O. *Environ. Microbiol.* **2003**, *5*, 842.

(7) Béjà, O.; Aravind, L.; Eugene, V.; Suzuki, M. T.; Hadd, A.; Nguyen, L. P.; Jovanovich, S. B.; Gates, C. M.; Feldman, R. A.; Spudich, J. L.; Spudich, E. N.; DeLong, E. F. *Science* **2000**, *289*, 1902.

(8) Engqvist, M. K. M.; McIsaac, R. S.; Dollinger, P.; Flytzanis, N. C.; Abrams, M.; Schor, S.; Arnold, F. H. *J. Mol. Biol.* **2015**, *427*, 205.

(9) Nordlund, G.; Boon Sing Ng, J.; Ng, S.; Bergström, L.; Brzezinski, P. *ACS Nano* **2009**, *3*, 2639.

(10) Janshoff, A.; Steinem, C. *Anal. Bioanal. Chem.* **2006**, *385*, 433.

(11) Petkova, V.; Benattar, J.; Zoonens, M.; Zito, F.; Popot, J.; Polidori, A.; Jasseron, S.; Pucci, B.; Drecam, D. S. M.; V, F.-G. Y.; Uni, V.; Physico-chimique, I. D. B.; Frc, C.; Curie, M.; Paris, F.-; Pasteur, L.; F-, A. V. **2007**, No. 10, 4303.

(12) Liang, H.; Whited, G.; Nguyen, C.; Stucky, G. D. *Proc. Natl. Acad. Sci. U. S. A.* **2007**, *104*, 8212.

(13) Liang, H.; Whited, G.; Nguyen, C.; Okerlund, A.; Stucky, G. D. *Nano Lett.* **2008**, *8*, 333.

(14) Hua, D.; Kuang, L.; Liang, H. *J. Am. Chem. Soc.* **2011**, *133*, 2354.

(15) Blin, J. L.; Carteret, C.; Bleta, R.; Stébé, M. J. *Colloids Surfaces A Physicochem. Eng. Asp.* **2010**, *357* (1–3), 128.

(16) Neyshtadt, S.; Jahnke, J. P.; Messinger, R. J.; Rawal, A.; Segal Peretz, T.; Huppert, D.; Chmelka, B. F.; Frey, G. L. *J. Am. Chem. Soc.* **2011**, *133*, 10119.

(17) Melosh, N. a.; Steinbeck, C. a.; Scott, B. J.; Hayward, R. C.; Davidson, P.; Stucky, G. D.; Chmelka, B. F. *J. Phys. Chem. B* **2004**, *108* (32), 11909.

(18) Segal-peretz, T.; Jahnke, J. P.; Berenson, A.; Neeman, L.; Oron, D.; Rossini, A. J.; Chmelka, B. F.; Frey, G. L. *J. Phys. Chem. C* **2014**, *118*, 25374.

(19) Phan, H.; Jahnke, J. P.; Chmelka, B. F.; Nguyen, T.-Q. *Appl. Phys. Lett.* **2014**, *104*, 233305.

(20) Granja, L. P.; Martínez, E. D.; Troiani, H.; Sanchez, C.; Soler Illia, G. J. A. A. *ACS Appl. Mater. Interfaces* **2017**, *9*, 965.

(21) Blin, J. L.; Gérardin, C.; Carteret, C.; Rodehüser, L.; Selve, C.; Stébé, M. J. *Chem. Mater.* **2005**, *17*, 1479.

(22) Jahnke, J. P.; Idso, M. N.; Hussain, S.; Junk, M. J. N.; Han, S.; Chmelka, B. F. *Submitt. J. Am. Chem. Soc.* **2017**.

(23) Stone, K. M.; Voska, J.; Kinnebrew, M.; Pavlova, A.; Junk, M. J. N.; Han, S. *Biophys. J.* **2013**, *104*, 472.

(24) Hediger, S.; Meier, B. H.; Kurur, N. D.; Bodenhausen, G.; Ernst, R. R. *Chem. Phys. Lett.* **1994**, *223*, 283.

(25) Elena, B.; de Paëpe, G.; Emsley, L. *Chem. Phys. Lett.* **2004**, *398* (4–6), 532.

(26) Fung, B. M.; Khitrin, a K.; Ermolaev, K. *J. Magn. Reson.* **2000**, *142* (1), 97.

(27) Marion, D.; Wüthrich, K. *Biochem. Biophys. Res. Commun.* **1983**, *113*, 967.

(28) Hayashi, S.; Hayamizu, K. *Bull. Chem. Soc. Jpn.* **1991**, *64*, 685.

(29) Kim, S.; Pauly, T. R.; Pinnavaia, T. J. *Chem. Commun.* **2000**, 835.

(30) Moller, J. V; Maire, M.; Pierre, I. U.; Paris, C.; Yvette, F.-G.-. *J. Biol. Chem.* **1993**, *268*, 18659.

(31) Maslennikov, I.; Kefala, G.; Johnson, C.; Riek, R.; Choe, S.; Kwiatkowski, W. *BMC Struct. Biol.* **2007**, *12*, 1.

(32) Pfleiderer, B.; Albert, K.; Bayer, E. *J. Chromatogr.* **1990**, *506*, 343.

(33) Ferrer, M.; Ballesteros, A. O. *Tetrahedron* **2000**, *56*, 4053.

(34) Lalli, D.; Idso, M. N.; Andreas, L. B.; Hussain, S.; Baxter, N.; Emsley, L.; Han, S.; Chmelka, B. F.; Pintacuda, G. *Submitt. J. Am. Chem. Soc.* **2017**.

(35) Ward, M. E.; Shi, L.; Lake, E.; Krishnamurthy, S.; Hutchins, H.; Brown, L. S.; Ladizhansky, V. *J. Am. Chem. Soc.* **2011**, *133*, 17434.

(36) Pieper, J.; Hauss, T.; Buchsteiner, A.; Baczyński, K.; Adamiak, K.; Lechner, R. E.; Renger, G. *Biochemistry* **2007**, *46*, 11398.

(37) Lakatos, M.; Lanyi, J. K.; Szakács, J.; Váró, G. *Biophys. J.* **2003**, *84*, 3252.

(38) Idso, M. N.; Lalli, D.; Andreas, L. B.; Lanyi, J. K.; Emsley, L.; Han, S.; Pintacuda, G.; Chmelka, B. F. *Prep. Sci.* **2017**.

(39) Maciejko, J.; Mehler, M.; Kaur, J.; Lieblein, T.; Morgner, N.; Ouari, O.; Tordo, P.; Becker-Baldus, J.; Glaubitz, C. *J. Am. Chem. Soc.* **2015**, *137*, 9032.

(40) Idso, M. N.; Baxter, N.; Narayanan, S.; Chang, E.; Fisher, J.; Chmelka, B. F.; Han, S. *Prep. J. Mol. Biol.* **2017**.

(41) Hussain, S.; Kinnebrew, M.; Schonenbach, N. S.; Aye, E.; Han, S. *J. Mol. Biol.* **2015**, *427*, 1278.

(42) Köhler, T.; Weber, I.; Glaubitz, C.; Wachtveitl, J. *Photochem. Photobiol.* **2017**, *93*, 762.

Chapter 6 : Correlating surface-functionalization of mesoporous silica with adsorption and release of pharmaceutical guest species

---

This chapter is adapted with permission from Morales, V.; Idso, M. N.; Balabasquer, M.; Chmelka, B. F.; García-Muñoz, R. A. Correlating surface-functionalization of mesoporous silica with adsorption and release of pharmaceutical guest species. *Journal of Physical Chemistry C* **2016**, 120, 16887-16898.

Abstract

Presented here is a detailed molecular-level understanding of the interactions among surface-functionalized mesoporous SBA-15 silica and pharmaceutical guests that influence macroscopic adsorption and release behaviors. A model drug species, methylprednisolone sodium succinate, was adsorbed on the surfaces of functionalized mesoporous SBA-15 silica materials with aminopropyl species and without or with C_{60} fullerene moieties. Zeta potential measurements show that the electrostatic interactions among methylprednisolone species and modified silica surfaces are important for the adsorption and release of the methylprednisolone molecules. Complementary one and two-dimensional (2D) solid-state $^{13}C\{^{1}H\}$ NMR measurements provide evidence for specific intermolecular interactions between adsorbed methylprednisolone species and different types of functionalized silica surfaces. In particular, correlated ^{13}C and ^{1}H signal intensities from the methylprednisolone alkyl moieties and the aminoalkyl groups of the functionalized silica surfaces unambiguously establish their close (<1 nm) molecular proximities and strong interactions. The molecular-level insights are correlated with macroscopic adsorption and release behaviors of methylprednisolone, providing detailed

new understanding of the interactions responsible for the high loadings and slow release of this important pharmaceutical agent from surface-functionalized mesoporous materials.

Introduction

The biocompatibilities, robustness, high specific surface areas, and facile surface functionalization of mesoporous silicas make these materials promising for applications in drug delivery.[1,2] Drug delivery systems (DDSs) aim to improve therapeutic efficacies and prevent the overdoses of pharmaceutical species by providing site-specific delivery of pharmaceuticals at controlled rates within the body. An additional objective for DDSs is to increase patient compliance by reducing the frequency of doses during the course of treatment, which is achieved by extending the duration over which DDSs deliver effective quantities of pharmaceuticals. Consequently, DDSs are engineered to maximize the adsorption capacities and control the release of pharmaceutical species under biological conditions (e.g., in the bloodstream, sinuses, etc.). Mesoporous silicas are promising as DDSs, because their high surface areas enable large pharmaceutical adsorption capacities and the robust silica frameworks render chemical and mechanical stability under biological conditions. By comparison, the relatively large (2−30 nm) pore sizes of mesoporous silicas allow pharmaceutical guests of large sizes to access the interior mesoporous surfaces. Furthermore, both the internal mesochannel and external particle surfaces of mesoporous silicas can be functionalized with a variety of pharmaceutically inactive chemical moieties that interact with molecular guests and thereby influence the adsorption and release properties of guest species.[3−5] Combined with the large pores, high surface areas and biocompatibilities, the ability

to easily adjust material properties by surface functionalization enables mesoporous silicas to be highly effective DDSs for a variety of chemically distinct pharmaceuticals.

Functionalities at mesoporous silica surfaces can promote the adsorption of molecular guests to enable a variety of technological applications and are especially relevant in mesoporous silica-based drug delivery systems. In most cases, the adsorption of molecular guests to mesoporous silica surfaces involves hydrophobic, hydrogen-bonding, electrostatic, or covalent interactions among the guests and moieties at the silica surface. The strengths and extents of these distinct intermolecular interactions depend on the types and compositions of the surface functional groups, which significantly influence the chemical activities, acid−base properties, and hydrophobicities[6−14] of mesoporous silicas. For example, mesoporous silica grafted with alkyl, haloalkyl, or aryl moieties exhibit increased surface hydrophobicity compared to non-functionalized mesoporous silica.[15−18] Such hydrophobic materials enable enhanced chromatographic performance when used as the stationary phase in reverse-phase high performance liquid chromatography columns, relative to commonly used silica gels.[19] By comparison, hydrophilic non-functionalized mesoporous SBA-15 silicas have high concentrations of surface silanol groups that interact with ibuprofen species by hydrogen-bonding, enabling high quantities of these pharmaceutical molecules to be adsorbed to such non-functionalized mesoporous silica surfaces.[20] Covalent interactions also result in the strong adsorption of guest molecules to functionalized mesoporous silicas and can facilitate the capture of dilute radionuclide,[21] boron,[22] or ibuprofen[23] species from solution by functionalized mesoporous materials. Molecular adsorption can also be influenced by electrostatic interactions, which enable the high adsorption capacities of poorly water-soluble prednisolone species to polyethylenimine-functionalized mesoporous silica materials.[24]

The release rates of pharmaceutical guests from mesoporous silica materials are strongly influenced by adsorption behaviors of the guest species near surface functional groups, which are mediated by site-specific molecular interactions. Specifically, slower transport of molecular species within silica mesochannels can result from adsorption interactions and steric effects between the guest species and surface moieties. Moreover, molecular release rates can also be influenced by the hydrophobicities of the mesoporous materials, which determine the rates at which aqueous biological media (e.g., blood) partition into materials and subsequently solubilize molecular guests. As a result, several previous studies have relied on modifying mesoporous materials with hydrophobic and/or bulky surface groups to control molecular release. Mesoporous SBA-15 silica materials functionalized with octyl or octadecyl groups exhibit erythromycin release rates that are 1 order of magnitude lower than from mesoporous silicas without surface functionalization.[25] Similarly, slow release rates have been reported for captopril[26] and ibuprofen[27] from mesoporous silicas with high degrees of surface silylation, which yields high surface hydrophobicities and correspondingly strong adsorption of pharmaceutical guests. Molecular simulations by Vallet-Regi´ and co-workers have suggested that a combination of electrostatic and hydrogen-bonding interactions are responsible for drug adsorption, desorption, and diffusion behaviors of pharmaceutical guests within surface-functionalized mesoporous silica hosts.[28,29] However, until now, direct molecular-level experimental measurements of such interactions and properties have been limited or absent.

The objective of this investigation is to understand the molecular interactions that mediate the adsorption and desorption of the pharmaceutical species methylprednisolone from the functionalized surfaces of mesoporous SBA-15 silicas to establish design criteria for

controlled release applications. The incorporation of C_{60} into mesoporous silica materials is expected to yield a combination of hydrophobic, π–π, and steric interactions that enable high methylprednisolone adsorption capacities and reduced rates of macroscopic release. Functionalization of similar mesoporous MCM-41 materials with fullerene C_{60} species has been achieved by covalently attaching C_{60} species to grafted amino organosilica groups;[30] however, the resulting materials were not evaluated for the adsorption and release of pharmaceutical guests. Corticoids, including a variety that are synthetically manufactured, are commonly used for medicinal purposes because of their broad relevances in physiological processes, including regulation of stress and immune responses, inflammation, carbohydrate metabolism, protein catabolism, and blood electrolyte levels. The synthetic corticoid methylprednisolone was chosen as a representative pharmaceutical guest for this study, because it is often prescribed to treat a number of different health conditions including arthritis, sinusitis, bronchitis, and cancer.

The molecular interactions among adsorbed methylprednisolone guests and fullerene (e.g., C_{60}) functional groups at the mesoporous silica surfaces are established and correlated with methylprednisolone adsorption and release at the macroscopic level. The quantities of amino organosilica, HC_{60}, and methylprednisolone species incorporated into mesoporous SBA-15 silica hosts are established by using solid-state NMR spectroscopy, elemental analysis, and thermogravimetry, while the textural properties (i.e., surface areas, pore sizes, etc.) of materials were obtained from N_2 adsorption analyses. Zeta potential values for bulk functionalized materials indicate electrostatic interactions among methylprednisolone guests and the silica surface, the magnitudes of which correlate qualitatively with methylprednisolone adsorption capacities. Moreover, hydrogen-bonding and hydrophobic interactions of adsorbed

methylprednisolone species with groups at the mesoporous silica surface are manifested directly by one- and two-dimensional solid-state $^{13}C\{^{1}H\}$ NMR spectroscopy. Insights regarding these intermolecular interactions are correlated with and explain the macroscopic release rates of methylprednisolone from functionalized mesoporous silica hosts into simulated body fluids at neutral and acidic conditions, which correspond to biological environments of the bloodstream and proximate to tumors, respectively. The surface-functionalized mesoporous SBA-15 silica materials in this study show higher methylprednisolone adsorption capacities and exhibit substantially longer release times compared to other non-functionalized mesoporous silicas and zeolite materials.[31] This detailed understanding of C_{60}-functionalized mesoporous silica loaded with methylprednisolone guests at molecular and macroscopic levels provides new opportunities for designing mesoporous silica-based materials for controlled pharmaceutical release.

Materials and methods

Synthesis of SBA-15-APS Silica. The synthesis of mesoporous SBA-15 silica materials was accomplished using the method described previously by Zhao et al.[32] Mesoporous SBA-15 silica materials functionalized with organosilica species were synthesized as follows: 2.0 g of calcined SBA-15 silica was held under vacuum (200 mbar) at a temperature of 150 °C overnight to eliminate residual water. Next, these materials were added to 250 mL of anhydrous toluene stored under a nitrogen atmosphere and the mixture was stirred for 30 min at 110 °C. Then, 5.6 mmol of an organosilica precursor, specifically 3-aminopropyl trimethoxysilane (APS), was added to this mixture, and the resulting mixture was stirred at 110 °C for 24 h. The solids were washed twice with toluene and acetone, filtered, and then dried overnight under vacuum (200 mbar). SBA-15 materials with grafted aminopropyl organosilica

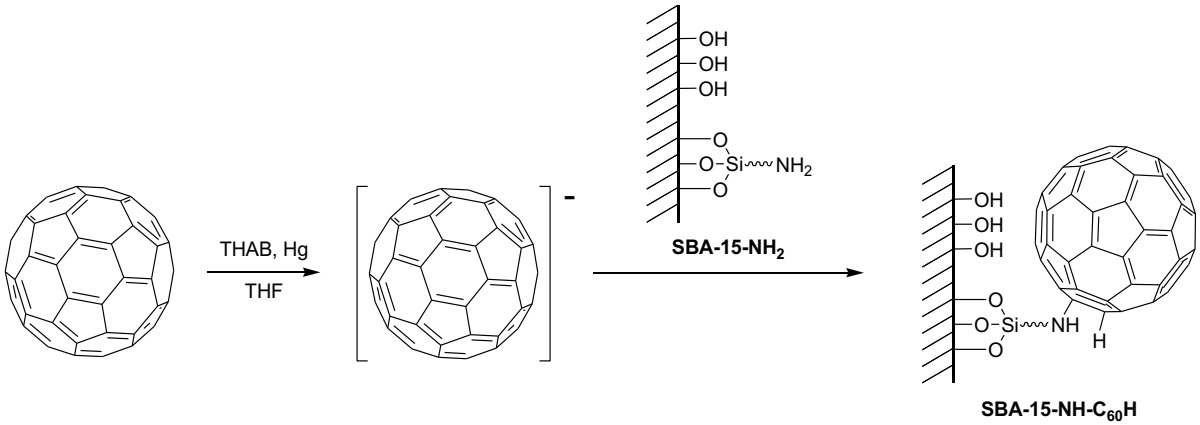

Figure 14. A schematic diagram that shows the principal steps and intermediates involved in the preparation of SBA-15-APS-HC_{60} materials. Fulleride $[C_{60}]^-$ anions are formed as a product by mixing C_{60} fullerene species with THF in the presence of THAB and Hg (left arrow). This solution is exposed to the SBA-15-APS materials (right arrow), which results in the covalent attachment of fulleride species to the primary amine groups of the amino organosilica species to yield SBA-15-APS-HC_{60} materials. (Figure courtesy of Dr. Victoria Morales)

species are referred to as SBA-15-APS materials to reflect the type of organosilica incorporated.

Preparation of SBA-15-APS-C_{60}H Materials. A solution containing fulleride anion $[C_{60}]-$ was prepared by mixing C_{60} fullerene (86 mg, 0.12 mmol) with tetrahexylammonium bromide (THAB, 261 mg, 0.60 mmol) in 32 mL of anhydrous tetrahydrofuran (THF) and 2−3 drops of mercury. The mixture was heated and maintained at 80 °C in a nitrogen atmosphere for 3 h after which the solution became dark red in color, which is the characteristic color of C_{60} radical ions. Subsequently, 400 mg of SBA-15-APS was added to the solution containing C_{60} radical ions and the mixture stirred for 20 h under a nitrogen atmosphere. The solids were then filtered and then washed twice with toluene and acetone to remove unreacted C_{60} radical ions and THAB. Finally, these materials were dried under vacuum overnight to achieve the target materials. A schematic diagram of the C_{60} preparation and attachment procedure is shown in Scheme 1. Materials with C_{60} species are termed SBA-15-APS-C_{60}H to reflect the propyl moieties of the incorporated organosilica species. Such C_{60}-functionalized mesoporous SBA-

15 silica materials are expected to be nontoxic, based on the low cytotoxicities reported for fullerene-containing polymers in vitro,[33,34] the lack of acute toxicities for water-soluble fullerenes in vivo,[35] and the lack of cytotoxic or genotoxic effects for cancer cells exposed to aminopropyl-functionalized silica nanoparticles.[36]

Loading of Methylprednisolone Sodium Succinate onto SBA-15-Derived Silica. Methylprednisolone sodium succinate was loaded into the SBA-15, SBA-15-APS, and SBA-15-APS-C_{60}H materials by exposing materials to an aqueous solution containing dissolved methylprednisolone species. Specifically, SBA-15 or functionalized SBA-15 materials (200 mg) were added to an aqueous solution containing methylprednisolone at a concentration of either 15 or 50 mg mL^{-1}, and was stirred vigorously at room temperature for 24 h. The materials were filtered, washed and dried under vacuum at 70 °C overnight. As soaking materials in the 50 mg mL^{-1} methylprednisolone solution yielded the greater pharmaceutical loadings (data not shown here), materials used for drug release experiments were prepared using solutions at this concentration.

In Vitro Release of Methylprednisolone Sodium Succinate from SBA-15-Derived Silica. Sterilized dialysis bags (molecular-weight cutoff 10,000 Da) were pretreated prior to use by immersion into a boiling aqueous mixture of 50% ethanol (v/v) for 1 h. Then the dialysis bags were washed with water up to 40 °C for 1 h and then immersed in a simulated body fluid (SBF) at 37 °C for 2 h. For pharmaceutical release experiments at neutral conditions the SBF consisted of a phosphate buffered saline (PBS) solution (pH 7.4), while an acetate buffered solution (pH 4.6) was used for experiments under acidic conditions.

Methylprednisolone release from materials into SBF was monitored to understand pharmaceutical release properties of these materials. SBA-15, SBA-15-APS, or SBA-15-APS-

$C_{60}H$ material (100 mg) loaded with methylprednisolone species was dispersed into 2 mL of SBF. This suspension was subsequently added to a pretreated dialysis bag, which was sealed and placed into bottles containing 100 mL of SBF (referred to as release media). Bottles were shaken at 100 rpm at 37 °C. At designated time points, every 15 min for the first 2 h, 1 h for the next 8 h, and 3 h until the released drug concentration remained constant, 1 mL of the SBF release media was withdrawn and a UV−vis absorption spectrum of this sample was collected, using neat SBF as baseline absorption. The 1 mL of the SBF sample was then returned to the original SBF release media directly after the UV−vis measurement. The concentration of methylprednisolone species in the SBF release media was calculated by applying the Beer−Lambert law to its UV absorbance intensity at 248 nm, an adsorption wavelength associated with methylprednisolone species, using an extinction coefficient of 12,400 M^{-1} cm^{-1}. Exposure of surface-functionalized silica materials to an additional 100 mL of methylprednisolone-free simulated body fluid resulted in the release of more methylprednisolone, suggesting that its release from these materials may be limited by adsorption/desorption equilibrium under the conditions used.

X-ray diffraction and N_2 sorption. Small-angle X-ray diffraction (XRD) measurements enable characterization of mesoscopic ordering in SBA-15 derived silica materials and were obtained with a Philips XPERT MPD diffractometer using Cu Kα radiation.

The textural properties of the mesoporous silica materials were established by analysis of nitrogen adsorption−desorption isotherms at −196 °C obtained using a Micromeritics TRISTAR 3000 porosimiter. Prior to measurement, mesoporous SBA-15 silica materials were outgassed under vacuum at 300 °C, while materials with incorporated amino organosilica or C60 fullerene species were outgassed at 100 °C under vacuum. The adsorption−desorption

isotherm measurements were performed according to the B.E.T. method using nitrogen adsorption points in the range P/P0 = 0.05−0.2. Pore size distributions were determined by applying the Barret−Joyner− Halenda model (B.J.H.) to the adsorption branch of the isotherm assuming a cylindrical pore geometry. For each sample, the average pore diameter was estimated as the value associated with the maximum intensity of the pore size distribution curve. Total pore volume was calculated at a relative pressure P/P0 of 0.985.

Nuclear magnetic resonance spectroscopy

NMR measurements conducted at Rey-Juan Carlos University, including one-dimensional (1D) solid-state $^{13}C\{^{1}H\}$ cross-polarization magic-angle-spinning (CP-MAS) and single-pulse ^{29}Si MAS NMR experiments, were performed on a Varian Infinity 400 MHz spectrometer fitted with a 9.4 T magnetic field. At this field strength, the ^{13}C and ^{29}Si nuclei Larmor frequencies are 100.53 and 79.41 MHz, respectively. Samples were packed in 7.5 mm zirconia rotors and experiments were conducted at room temperature under MAS conditions of 6 kHz using an H/X double-resonance 7.5 mm MAS probehead. For solid-state $^{13}C\{^{1}H\}$ CP-MAS experiments, the cross-polarization time was determined by the Hartmann−Hann[37] condition with 4.25 μs π/2 pulses, 2000 transients, a recycle delay of 3 s, and a CP contact time of 1 ms. ^{29}Si MAS single-pulse experiments had 3.5 μs π/2 pulse, 3000 transients, and recycle delay time of 60 s. ^{13}C and 29Si chemical shifts were externally referenced to adamantane and tetramethylsilane, respectively.

Solid-state 1D and two-dimensional (2D) ^{1}H and ^{13}C NMR measurements were carried out on mesoporous SBA-15-APS-$C_{60}H$ silica samples without and with methylprednisolone guest species to understand intermolecular interactions among the guest species, organic surface moieties, and silica walls. Approximately 80 mg of sample was loaded into 4 mm

zirconia MAS rotors for solid-state 1D and 2D NMR measurements. Solid-state 1D $^{13}C\{^{1}H\}$ CP measurements were conducted by a 4 mm double-resonance variable-temperature Bruker MAS probehead at 11.7 T using a Bruker AVANCE II spectrometer with operating frequencies of 500.24 MHz for ^{1}H and 125.79 MHz for ^{13}C. Cross-polarization was used to transfer magnetization from ^{1}H to ^{13}C nuclei by adiabatic passage according to the Hartmann−Hahn condition.37 Solid-state 1D $^{13}C\{^{1}H\}$ CP measurements were conducted at room temperature under 12.5 kHz MAS conditions with a 2 ms CP contact time, recycle delay of 1 s, 1000 transients, and with SPINAL-64 heteronuclear ^{1}H decoupling.[38]

Solid-state 2D $^{13}C\{^{1}H\}$ heteronuclear correlation (HETCOR) measurements were conducted using a 4 mm triple-resonance Bruker MAS probehead using a Bruker ASCEND-III NMR spectrometer at 9.4 T with operating frequencies of 400.02 MHz for ^{1}H and 100.64 MHz for ^{13}C. The 2D $^{13}C\{^{1}H\}$ HETCOR spectrum was acquired under 10 kHz MAS conditions, using a 2 ms CP contact time and 5 s recycle delay with 12 t_1 increments at an incremental size of 96 μs and 3072 transients each. Quadrature detection in the indirect (^{1}H) dimension was achieved using time-proportional phase-incrementation.[39] High power (100 kHz) $^{1}H-^{1}H$ homonuclear decoupling using the eDUMBO-1_{22} sequence was applied during the ^{1}H t_1 evolution period to enhance resolution in the ^{1}H dimension.[40] For the indirect dimension, a scaling factor of 0.60 was calibrated from a separate 2D $^{13}C\{^{1}H\}$ NMR spectrum of 99% ^{13}C- and ^{15}N-enriched glycine sample conducted under identical experimental conditions. During signal acquisition, heteronuclear ^{1}H decoupling was achieved using a SPINAL-64 pulse sequence[38] at a ^{1}H nutation frequency of 100 kHz. Separate 1D $^{13}C\{^{1}H\}$ CP-MAS and single-pulse ^{1}H spectra are shown at the top and alongside the 2D spectrum, respectively, and were acquired under identical experimental conditions as those of the

associated 2D. Contour levels in the 2D spectra correspond to 5, 15, 25, 40, 55, and 75% of the maximum signal intensity. ^{1}H and ^{13}C chemical shifts in all 1D and 2D measurements were referenced to neat tetramethylsilane (TMS, 0 ppm), using tetrakismethylsilane as an external secondary reference (with ^{13}C and ^{1}H chemical shifts of 3.52 and 0.25 ppm relative to TMS, respectively).[41]

Zeta potential measurements

Amino organosilica and pharmaceutical guest loadings were determined by thermogravimetric analysis (TGA) with a Star System Mettler Thermobalance and, separately, elemental microanalyses with a Vario EL III apparatus. Zeta potentials were calculated based on measurements of the electrophoretic mobilities of bulk mesoporous materials using a zeta potential analyzer (Zetasizer Nano ZS, Iesmat).

Results and Discussion

The quantities of aminopropyl organosilica species grafted to the silica surface of SBA-15-APS silica and adsorption properties of these materials are obtained from elemental analyses, TGA, solid-state NMR spectroscopy, and N_2 adsorption measurements. The carbon contents of SBA-15-APS materials can be directly related to the amounts of grafted organosilica species and establish aminopropyl organosilica loadings of 1.6 mmol per gram of SBA-15-APS material. Corroborative evidence for these organosilica loadings is provided by 1D single-pulse ^{29}Si NMR and TGA data, which indicate organosilica loadings of 1.0 and 1.1 mmol per gram of SBA-15-APS materials, respectively. Analyses of

N_2 adsorption data reveal significantly reduced BET surfaces areas (Table 1) for SBA-15-APS (391 $m^2\ g^{-1}$ material) materials with respect to SBA-15 silica (582 $m^2\ g^{-1}$ material), which results, in part, from the added mass associated with grafted aminopropyl organosilica species.

Normalizing the specific surface area to the mass of silica framework in SBA-15-APS materials provides an adjusted surface area of 455 m^2 g^{-1} silica, reflecting that grafted aminopropyl organosilica species block mesopores and/or prevent N_2 adsorption to the silica surface.17 However, pore blockage by incorporated organosilica species is unlikely, based on the highly similar pore volumes of SBA-15-APS materials (0.85 cm^3 g^{-1} silica) and mesoporous SBA-15 silica (0.78 cm^3 g^{-1} silica). These results establish that the surface areas of SBA-15-APS materials are similar to those of mesoporous SBA-15 silica materials, though are somewhat reduced by the presence of the grafted aminopropyl organosilica species. Interestingly, the average pore diameter of SBA-15-APS silica is nearly identical to that of mesoporous SBA-15 silica (Table 1). The high quantities of incorporated aminopropyl organosilica species, minimal pore blockage, and mesochannel pore sizes of SBA-15-APS materials are expected to enable incorporation of relatively high amounts of HC_{60} species.

Table 1. Adsorption properties, zeta potential values at pH 7.4 and 4.6 and methylprednisolone loading capacities of SBA-15 silica materials with and without functionalities. (Table courtesy of Dr. Victoria Morales)

Sample	S_{BET}[a]		V_P[b]		D_p[c]	Zeta potential		Drug loading[d]
	m^2 g^{-1} material	m^2 g^{-1} silica	cm^3 g^{-1} material	cm^3 g^{-1} silica	(Å)	pH 7.4 (mV)	pH 4.6 (mV)	mg g^{-1} sample
SBA-15	582±16	582±16	0.78±0.10	0.78±0.10	82±11	-15.9	-4.85	93
SBA-15-APS	391±11	455±13	0.73±0.10	0.85±0.11	82±11	6.58	26.2	137
SBA-15-APS-C_{60}H	313±9	376±10	0.42±0.06	0.50±0.07	44±6	-1.1	10.7	118
Neat Methylprednisolone	-	-	-	-	-	-23.0	-19.4	-

[a]BET surface area and [b]pore volume normalized to material or silica masses. [c]Modal pore size distribution. [d]Quantity of methylprednisolone sodium succinate loadings achieved by soaking materials in aqueous solutions containing methylprednisolone at concentrations of 50 mg mL^{-1}.

The quantities of C_{60} incorporation and N_2 adsorption properties of SBA-15-APS-C_{60}H materials are established by elemental analysis, TGA, solid-state NMR spectroscopy, and N_2 adsorption. A comparison of the carbon contents of SBA-15-APS materials without and with HC_{60} species establishes C_{60} loadings of 0.17 mmol per gram of SBA-15-APS-C_{60}H material, which is in agreement with the 0.26 mmol C_{60} per gram obtained by analyses of TGA data . Importantly, these incorporated C_{60} species appear to be covalently attached to aminopropyl organosilica species based on solid-state 1D $^{13}C\{^1H\}$ CP-MAS NMR spectra (Figure 1A) of SBA-15-APS-C_{60}H materials, which show a broad (full-width half-height of 10 ppm) ^{13}C signal at 135−155 ppm assignable to C_{60} moieties (Figure 1A, blue dot). A similarly broad ^{13}C NMR signal was attributed C_{60} species covalently bound to surface aminopropyl moieties in mesoporous MCM-41 silica, while sharp signals were observed for nonattached and mobile C_{60} species.[42] Therefore, the 1D NMR analysis provides strong evidence that C_{60} species incorporated into SBA-15-APS-C_{60}H materials are, in fact, attached to surface aminopropyl groups. Based on these results, approximately 31% of aminopropyl groups at the silica surface have covalently bound C_{60} functionalities, most of which likely reside at mesochannel surfaces nearby the silica particle surface because these regions are most accessible to solutions containing radical C_{60} species during the post-synthetic attachment process. Interestingly, despite the partial yield of HC_{60} attachment, incorporated HC_{60} groups considerably influence the N_2 adsorption properties of SBA-15-APS-C_{60}H materials. For example, SBA-15-APS-C_{60}H materials have dramatically reduced average pore diameters relative to SBA-15-APS materials (Table 1). The adjusted average pore volume (modified to account for incorporated organosilica and HC_{60} species) of SBA-15-APS-C_{60}H materials (0.50 $cm^3\ g^{-1}$ silica) is reduced

compared to mesoporous SBA-15 materials (0.78 cm^3 g^{-1} silica), which could reflect either an excluded volume effect from incorporated C_{60} species or pore blockage by C_{60} species. The adjusted BET surface areas of SBA-15-APS-C_{60}H materials (376 m^2 g^{-1} silica support) are slightly lower than those of SBA-15-APS materials (433 m^2 g^{-1} silica support). The high hydrophobicities and surface areas of mesoporous silica functionalized with C_{60} species make these materials promising for the incorporation of large quantities of methylprednisolone species.

The methylprednisolone adsorption capacities of SBA-15, SBA-15-APS, and SBA-15-APS-C_{60}H materials are determined and shown to correlate qualitatively with the strengths of electrostatic interactions between methylprednisolone and the silica surfaces. Adsorption of methylprednisolone species was achieved by exposing mesoporous SBA-15, SBA-15-APS and SBA-15-APS-C_{60}H materials to aqueous solutions containing methylprednisolone at concentrations of 50 mg mL^{-1}. Subsequent elemental analyses establish methylprednisolone loadings (Table 1) of 93mg g^{-1} of mesoporous SBA-15 silica, and relatively greater loadings of 137 and 118 mg g^{-1} of SBA-15-APS and SBA-15-APS-C_{60}H materials, respectively. Differences in methylprednisolone loadings among these materials can be explained by the electrostatic interactions among the methylprednisolone and silica surfaces. As the zeta potential of pure methylprednisolone sodium succinate is −23 mV (measured at pH 7.4), these species will have stronger attractive electrostatic interactions with, and greater adsorption to, silica surfaces having greater positive charge. As expected, SBA-15-APS materials have the most positive zeta potential (6.58 mV at pH 7.4, Table 1) and greatest methylprednisolone adsorption capacity, while mesoporous SBA-15 silicas with the most negative zeta potential (−15.9 mV at pH 7.4) exhibit the lowest capacities. These results demonstrate that attractive

electrostatic interactions are important, though not solely responsible for, methylprednisolone adsorption, as significant methylprednisolone adsorption is observed on surfaces that have negative surface charge and thus, on average, electrostatically repel methylprednisolone species (i.e., mesoporous SBA-15 silica). Therefore, attractive hydrogen-bonding and/or hydrophobic interactions also appear to influence methylprednisolone adsorption to silica surfaces.

Specific insights on intermolecular interactions between adsorbed methylprednisolone species and moieties at the functionalized mesoporous silica surfaces are provided by solid-state ^{13}C and ^{1}H NMR spectroscopy. For example, the solid-state 1D $^{13}C\{^{1}H\}$ CP-MAS NMR spectrum (Figure 1A) of SBA-15-APS-$C_{60}H$ materials without methylprednisolone reveals well-resolved ^{13}C signals associated with ^{13}C moieties of the HC_{60}-aminopropyl groups.42 For example, the ^{13}C signals at 10, 20, 34, 52, and 135−155 ppm are assigned to ^{13}C moieties a, b, c, d, and those of the C_{60} fullerene (blue dot), respectively. Importantly, the $^{13}C\{^{1}H\}$ CP-MAS NMR spectrum (Figure1B) of materials with low methylprednisolone loadings yields ^{13}C signals at 45, 70, 119, and 127 ppm (dotted red lines) that are not associated with ^{13}C moieties of the HC_{60}-aminopropyl groups (or THAB impurities). These signals, and others, correspondingly increase in intensity (Figure 1C) for materials with higher methylprednisolone loadings, and are confidently assigned to the ^{13}C moieties of the methylprednisolone species.[43] The ^{13}C signals associated with the alkyl moieties of the methylprednisolone guest have narrow line widths and reflect the relatively uniform ^{13}C molecular environments of these ^{13}C moieties for materials with both low and high methylprednisolone loadings, as shown in Figure 1B,C, respectively. A separate static (non-MAS) 1D $^{13}C\{^{1}H\}$ CP NMR spectrum of the sample with low methylprednisolone loading yields no resolved ^{13}C signals, which are broadened beyond

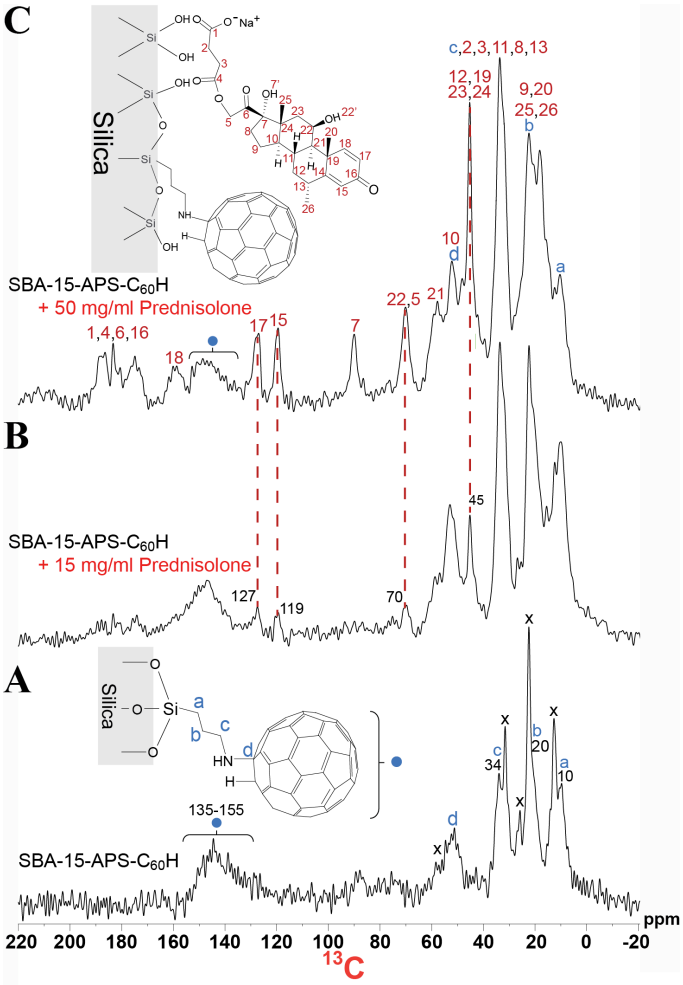

Figure 15. Solid-state 1D $^{13}C\{^{1}H\}$ CP-MAS spectra of mesoporous SBA-15 silica functionalized with HC_{60}-aminopropyl groups **(A)** without methylprednisolone, and with different loadings of methylprednisolone guest species achieved by exposing materials to **(B)** 15 mg mL^{-1}, and (C) 50 mg mL^{-1}. The spectra were all acquired at room temperature under MAS conditions of 12.5 kHz with a 2 ms CP contact time ("X" indicates signals from THAB impurities).

detection (data not shown). Hence, the narrow ^{13}C signals associated with the alkyl moieties of the methylprednisolone and HC_{60}-aminopropyl species can be concluded to result from relatively uniform MAS-averaged environments, rather than high molecular mobilities (relative to the 100 μs time scale of the NMR measurement). Interestingly, not all of the ^{13}C signals associated with the methylprednisolone species are narrow, in particular those at 170−190 ppm from the carboxylic or ketone groups (1, 4, 6, and 16) in Figure 1C. These results suggest that the adsorption of the methylprednisolone guests occurs via hydrogen-bonding of

carboxylate moieties to surface silanol sites, as depicted in the schematic diagram in Figure 1C. Combined with analysis of zeta potential data, these results indicate that methylprednisolone species adsorb to the silica surface of SBA-15-APS-$C_{60}H$ materials based on electrostatic and hydrogen-bonding interactions.

While the solid-state 1D $^{13}C\{^{1}H\}$ CP-MAS NMR measurements yield molecular-level information about the HC_{60}-aminopropyl and methylprednisolone species, 2D $^{13}C\{^{1}H\}$ HETCOR measurements provide complementary insights on intermolecular interactions between these two species. Specifically, 2D $^{13}C\{^{1}H\}$ HETCOR measurements exploit through-space dipole−dipole couplings of locally proximate (<1 nm) ^{13}C and ^{1}H nuclei to correlate their isotropic chemical shifts. This provides direct information on intra- and intermolecular interactions among the chemically distinct ^{13}C and ^{1}H moieties of the HC_{60}-aminopropyl groups and methylprednisolone guests. In the 2D solid-state $^{13}C\{^{1}H\}$ HETCOR spectrum of Figure 3A, most of the observed intensity correlations are of intramolecular origin. These correlations corroborate the ^{13}C and ^{1}H signal assignments to specific moieties of the HC_{60}-aminopropyl group and methylprednisolone guests,[44−47] as labeled in the respective 1D single-pulse ^{1}H MAS and $^{13}C\{^{1}H\}$ CP-MAS spectra in Figure 3A.

Intensity correlations in the solid-state 2D $^{13}C\{^{1}H\}$ HETCOR spectrum in Figure 3 also arise from intermolecular interactions between HC_{60}-aminopropyl and methylprednisolone species and provide evidence for preferential association of the methylprednisolone guests with the aminopropyl, as opposed to the HC_{60}, moieties. Despite many of the overlapping ^{13}C signals of the HC_{60}-aminopropyl and methylprednisolone species, the ^{13}C signal associated with the a (8−9 ppm) methylene moieties of the HC_{60}-aminopropyl group are well-resolved. Importantly, correlated ^{13}C signals (8−9 ppm) associated with the *a* groups of the HC_{60}-

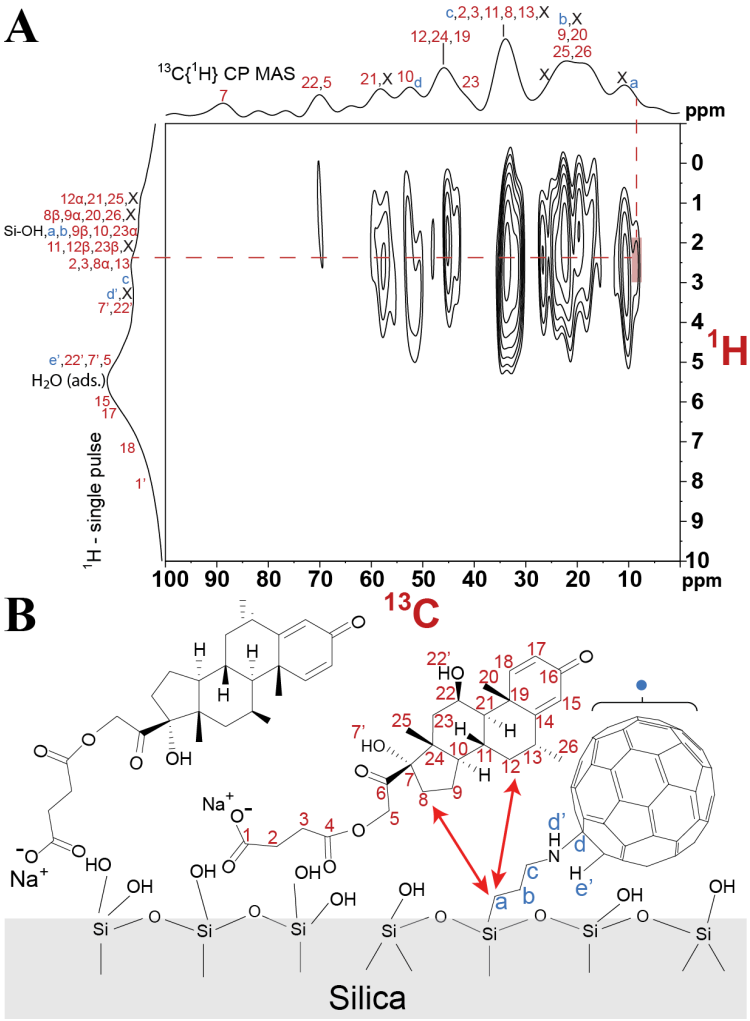

Figure 16. Solid-state 2D ^{13}C{^{1}H} dipolar-mediated HETCOR spectrum **(A)** of SBA-15-APS-C60H materials exposed to aqueous solutions containing 50 mg mL^{-1} methylprednisolone guest species. 1D ^{13}C{^{1}H} CP-MAS and single-pulse ^{1}H MAS spectra are shown along the top horizontal axis and the left vertical axis, respectively. The spectra were all acquired at room temperature under MAS conditions of 12.5 kHz with a 2 ms CP contact time. Schematic diagram **(B)** of methylprednisolone species at the HC-aminopropyl-functionalized silica surface with red and blue arrows that indicate intermolecular interactions consistent with the 2D NMR intensity correlations.

aminopropyl moieties and ^{1}H signals (1.9−2.6 ppm, red shading) from the methylprednisolone alkyl moieties establishes the mutual interactions among HC_{60}-aminopropyl groups and methylprednisolone guests. Although intensity correlations associated with the ^{13}C signals of the alkyl moieties (<80 ppm) are observed, the 2D ^{13}C{^{1}H} HETCOR spectrum yields no correlated intensities in the ^{13}C region 140−148 ppm (not shown in Figure 3A) associated with

the ^{13}C signals of the HC_{60} moieties. This may reflect relatively weak hydrophobic or π−π interactions between methylprednisolone guests and the HC_{60} moieties, or a relatively broad distribution of local interaction environments with the C_{60} fullerene. Due to the many overlapping ^{13}C signals of the HC_{60}-aminopropyl group and methylprednisolone guest in this 2D $^{13}C\{^{1}H\}$ HETCOR spectrum (Figure 3A) a specific configuration of the interacting methylprednisolone guest cannot be inferred and likely reflects a distribution of methylprednisolone configurations. Analysis of the 2D $^{13}C\{^{1}H\}$ HETCOR spectrum (Figure 3A) establishes the close (<1 nm) molecular proximities of HC_{60}-aminopropyl groups and methylprednisolone guests, providing direct evidence for intermolecular interactions among the amino- propyl groups and methylprednisolone alkyl moieties, as depicted in the schematic diagram in Figure 3B. We hypothesize that such interactions influence the release properties of methylprednisolone molecular guests.

The fractions and rates of methylprednisolone released from SBA-15, SBA-15-APS and SBA-15-APS-C_{60}H materials into simulated body fluids are quantified and analyzed to understand how surface aminopropyl and C_{60} moieties influence the release behaviors of methylprednisolone species. The amounts of methylprednisolone species released from mesoporous silica hosts into simulated body fluids under near neutral conditions (pH 7.4), corresponding to those in the bloodstream, can be estimated by using UV−visible spectroscopy to measure the absorbance intensity at 248 nm, which is associated with methylprednisolone molecules.[48] Specifically, the quantities of methylprednisolone released from mesoporous SBA-15, SBA-15-APS, or SBA-15-APS-C_{60}H silica materials were determined by applying the Beer−Lambert law to the absorbance intensities at 248 nm in UV−visible spectra acquired for simulated body fluids that were exposed for various time periods to these mesoporous silica

host materials. Normalizing the amounts of released methylprednisolone species to the initial mass of methylprednisolone contained in the mesoporous SBA-15, SBA-15-APS, or SBA-15-APS-C_{60}H silica material yields the cumulative fractions of methylprednisolone released from these materials, as depicted in Figure 4A. After exposure to simulated body fluids, large fractions of the methylprednisolone species were released from all three of the mesoporous silica materials at times <500 min (Figure 4A). At times >500 min, the fractions of methylprednisolone released from these mesoporous hosts approach constant values that are lower than 100%, indicating incomplete extents of methylprednisolone release, due to diffusion resistances or sorption equilibrium of methylprednisolone species with the mesoporous silica surfaces. In particular, similar fractions of methylprednisolone (~80−90%) were released from mesoporous SBA-15, SBA-15-APS, and SBA-15-APS-C_{60}H silica materials, indicating that surface aminopropyl and C_{60} groups do not significantly influence the fractions of methylprednisolone released from functionalized mesoporous silica materials. However, methylprednisolone species were observed to release from the non-functionalized and functionalized mesoporous silica hosts at significantly different rates (Figure 4B), which were determined from the derivative of the cumulative methylprednisolone release profiles at specific points in time. For example, higher rates of methylprednisolone release were observed for aminopropyl-functionalized SBA-15-APS materials, compared to non-functionalized mesoporous SBA-15 silica materials, which arise in part from the higher loadings of methylprednisolone in the former (137 mg g^{-1} material versus 93 mg g^{-1} material). More specifically, materials with higher methylprednisolone loadings are expected to have larger release rates because of the increased prevalence of relatively weak drug−drug intermolecular interactions, versus stronger drug-host interactions, that facilitates methylprednisolone release

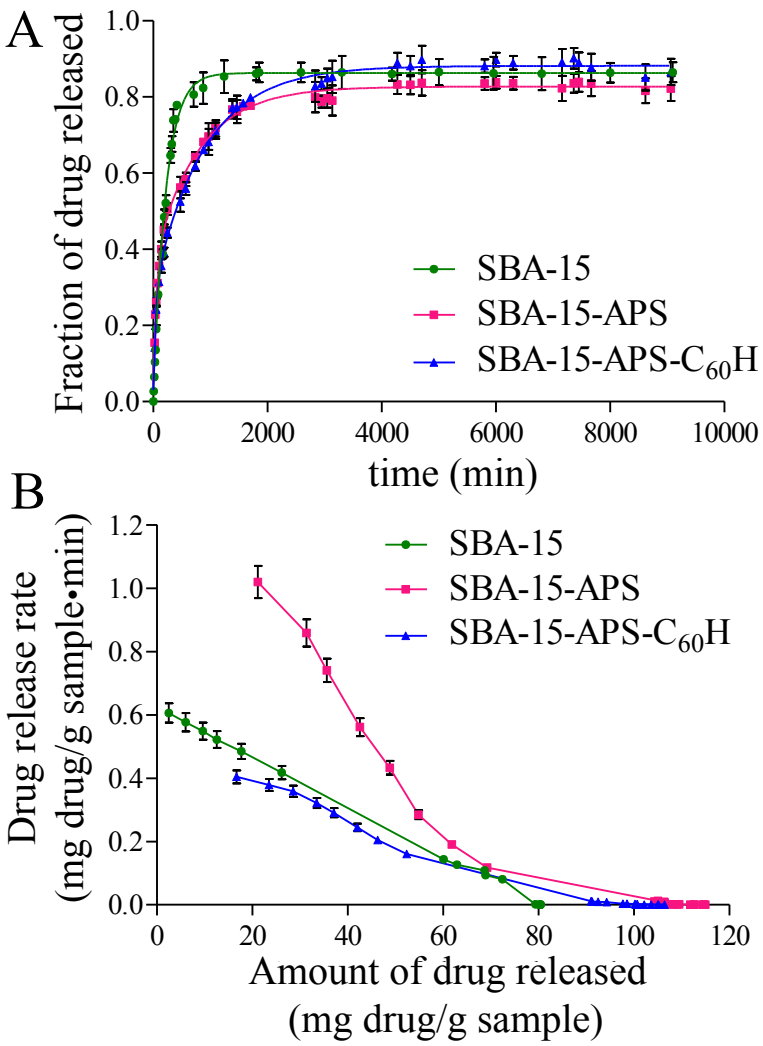

Figure 17. The **(A)** fractions of methylprednisolone released and **(B)** instantaneous release rates of methylprednisolone from non-functionalized mesoporous SBA-15 silica (green, circles), SBA-15-APS (pink, squares) and SBA-15-APS-C_{60}H (blue, triangles) materials into simulated body fluid (PBS buffer) at pH=7.4 and 37 ºC. The instantaneous release rate values in (B) represent the derivative of a given cumulative release profile at a specific point in time, approximated by using a two-point finite difference formula. (Figure courtesy of Dr. Victoria Morales)

into simulated body fluid. Additionally, the high loadings of methylprednisolone species yield large concentration gradients for the transport of methylprednisolone from the host to simulated body fluid, which likely contribute to the large release rates.[49] Importantly, Figure 4B also shows lower methylprednisolone release rates from SBA-15-APS-C_{60}H materials than from non-functionalized SBA-15 silica, despite the higher methylprednisolone loadings for the

C_{60}-functionalized materials (118 mg g^{-1} material), compared to non-functionalized mesoporous SBA-15 silica (93 mg g^{-1} material). These results establish that the release of methylprednisolone species from mesoporous silica materials is mediated by surface-grafted C_{60} moieties, presumably due to steric effects[31] that are also evidenced by the significantly reduced pore diameters (Table 1) for SBA-15-APS-C_{60}H materials relative to SBA-15 and SBA-15-APS silica materials. The high hydrophobicities of C_{60} species may also inhibit the influx of aqueous simulated body fluids into mesoporous SBA-15-APS-C_{60}H materials, thereby reducing methylprednisolone transport within the mesochannels.

The methylprednisolone release from the aminopropyl-functionalized mesoporous SBA-15-APS and SBA-15-APS-C_{60}H silica materials into simulated body fluids can be described by using first-order and Korsmeyer-Peppas[50] kinetic models. The first-order kinetic model for drug release assumes that the rate of methylprednisolone release from a mesoporous silica host material is proportional to the concentration of pharmaceuticals in the simulated body fluid. Smaller first-order rate coefficients (the constants of proportionality) correspond to lower release rates of methylprednisolone from the mesoporous silica hosts. Analyses of the cumulative methylprednisolone release profiles using the first-order kinetic model reveal that the lowest first-order rate coefficients (0.0072 min^{-1}) are associated with the SBA-15-APS-C_{60}H materials, compared to non-functionalized mesoporous SBA-15 (0.0080 min^{-1}) and SBA-15-APS silica (0.0201 min^{-1}). These relative values are consistent with mediated transport of methylprednisolone within the mesochannels by C_{60} moieties grafted to the silica surface. By comparison, the Korsmeyer−Peppas kinetic model for drug release provides complementary insight about the diffusion of methylprednisolone molecules within mesoporous silica materials, in particular whether diffusion occurs by Fickian or non-Fickian processes.

Assuming spherical particle geometries for the SBA-15-APS and SBA-15-APS-C_{60}H materials, the Korsmeyer-Peppas fitting analyses suggest non-Fickian diffusion for methylprednisolone molecules within these functionalized mesoporous materials, within the standard errors associated with the analyses. Such diffusion processes are consistent with the impeded diffusion of methylprednisolone within functionalized mesoporous materials by the nanoscale pore dimensions and/or the interactions among methylprednisolone and moieties at the silica surfaces.

Exposure of C_{60}-functionalized mesoporous silica materials to simulated body fluids under acidic conditions (pH 4.6), corresponding to those nearby tumors, yields lower fractions and rates of methylprednisolone release compared to under near neutral conditions (pH 7.4). For example, while approximately 85% of the total methylprednisolone species were released from SBA-15-APS-C_{60}H materials under near neutral conditions, lower fractions of ~70% were released from identical materials under acidic conditions, as shown in Figure 5A. The lower fractions of methylprednisolone released from these C_{60}-functionalized silica materials are consistent with the increased attractive electrostatic interactions among methylprednisolone and the functionalized silica surfaces under acidic versus near neutral conditions, as evidenced by the zeta potential measurements (Table 1) of the corresponding materials. Similarly, the reduced rates of methylprednisolone release from SBA-15-APS-C_{60}H materials under acidic conditions, as shown in Figure 5B, are also consistent with the increased attractive electrostatic interactions. Analyses of methylprednisolone release profiles into acidic simulated body using the Korsmeyer-Peppas kinetic model reveal non-Fickian diffusion processes for methylprednisolone SBA-15-APS-C_{60}H materials, as observed under near neutral conditions. The reduced rates of methylprednisolone release from C_{60}-functionalized

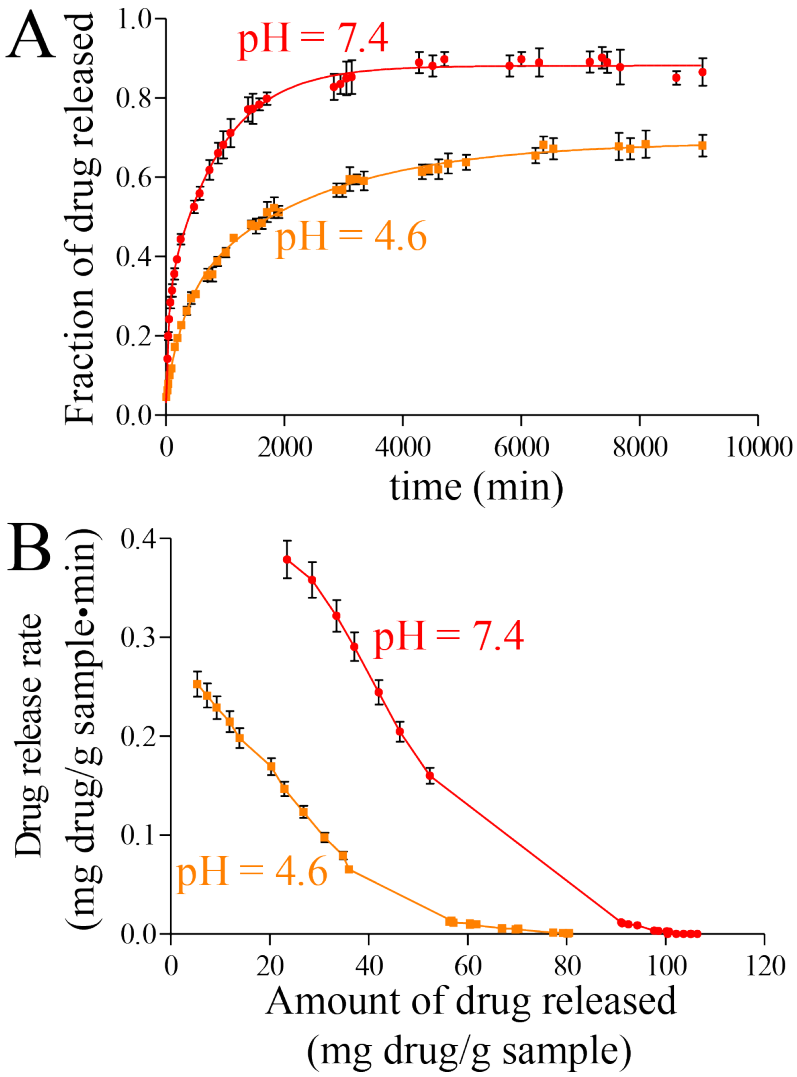

Figure 18. The **(A)** fractions of methylprednisolone released and **(B)** instantaneous release rates of methylprednisolone from SBA-15-APS-C_{60}H into simulated body fluids at pH 7.4 (red, circles) and pH 4.6 (orange, squares). The simulated body fluids at pH 4.6 were acetate buffered solutions, while those at pH 7.4 were PBS buffered solutions, and all release experiments were conducted at 37°C. The instantaneous release rate values in (B) represent the derivative of a given cumulative release profile at a specific point in time, approximated by using a two-point finite difference formula. (Figure courtesy of Dr. Victoria Morales)

materials under acidic conditions would promote longer durations of pharmaceutical release from these materials in the vicinity of tumors. Therefore, if used for tumor treatment, the C_{60}-functionalized materials could allow the pharmaceutical to be administered less frequently to patients, which could subsequently improve patient compliance.

Conclusions

The molecular-level interactions among a representative pharmaceutical species, methylprednisolone sodium succinate, and moieties on the interior surfaces of mesoporous SBA-15 silica materials were established and correlated with bulk adsorption properties. Specifically, mesoporous SBA-15 silica materials with aminopropyl surface moieties without and with C_{60} species were characterized and evaluated for the adsorption of methylprednisolone species. Methylprednisolone adsorption to these materials was shown to depend strongly on the electrostatic interactions among methylprednisolone molecules and the functionalized silica surfaces, which correlate with the different loadings for the functionalized materials. Complementary solid-state 1D $^{13}C\{^{1}H\}$ CP-MAS NMR measurements provided evidence for hydrogen-bonding between methylprednisolone species and the silica surface, while 2D $^{13}C\{^{1}H\}$ HETCOR NMR techniques established the close molecular proximities of the alkyl moieties of methylprednisolone species and aminopropyl functionalities at the silica surface, suggesting attractive hydrophobic interactions among these species. These results indicate that the adsorption of methylprednisolone to SBA-15 materials functionalized with HC_{60}-amino organosilica species involves contributions from electrostatic, hydrogen-bonding, and hydrophobic interactions.

The transient release of methylprednisolone from functionalized mesoporous SBA-15 silica materials into simulated body fluids was monitored to understand the influence of the different surface functionalities on methylprednisolone release behaviors. The surface-grafted aminopropyl, aminobutyl, and C_{60} surface moieties of functionalized mesoporous silica materials appear to reduce the rates of methylprednisolone release by a combination of electrostatic, hydrophobic and steric effects. Indeed, C_{60}-functionalized SBA-15-APS-C_{60}H

materials showed the slowest methylprednisolone release rates of all materials investigated. Methylprednisolone release from these functionalized mesoporous silica materials was evaluated under acidic and near neutral pH conditions, which correspond to conditions nearby tumors and in the bloodstream, respectively. Lower fractions and rates of methylprednisolone release were observed from C_{60}-functionalized mesoporous silica materials under acidic conditions (pH 4.6) versus near neutral conditions (pH 7.4), which were attributed to stronger electrostatic interactions among methylprednisolone and the surfaces of the C_{60}-functionalized SBA-15 silica. These results demonstrate that surface-grafted alkylamino and C_{60} functionalities can mediate pharmaceutical release from functionalized mesoporous silica materials. The detailed understanding of molecular-level properties and interactions of methylprednisolone and C_{60}-functionalized mesoporous silicas developed here provides important information for designing effective silica-based drug-delivery systems.

References

(1) Wang, S. Microporous Mesoporous Mater. **2009**, *117* ,1.

(2) Slowing, I. I.; Vivero-Escoto, J. L.; Wu, C. W.; Lin, V. S. Y. *Adv. Drug Delivery Rev.* **2008**, *60*, 1278.

(3) Calvillo, L.; Celorrio, V.; Moliner, R.; Cabot, P. L.; Esparbé, I.; Lázaro, M. J. *Microporous Mesoporous Mater.* **2008**, *116*, 292.

(4) Izquierdo-Barba, I.; Sousa, E.; Doadrio, J. C.; Doadrio, A. L.; Pérez-Pariente, J.; Martínez, A.; Babonneau, F.; Vallet-Regí, M. *J. Sol-Gel Sci. Technol.* **2009**, *50*, 421.

(5) Gignone, A.; Delle Piane, M.; Corno, M.; Ugliengo, P.; Onida, B J. *Phys. Chem. C* **2015**, *119*, 13068.

(6) Lei, C.; Shin, Y.; Liu, J.; Ackerman, E. J. *J. Am. Chem. Soc.* **2002**, *124*, 11242.

(7) Maria-Chong, A. S.; Zhao, X. S. *J. Phys. Chem. B* **2003**, *107*, 12650.

(8) Liu, Y. H.; Lin, H. P.; Mou, C. Y. *Langmuir* **2004**, *20*, 3231.

(9) Shimojima, A.; Umeda, N.; Kuroda, K. *Chem. Mater.* **2001**, *13*, 3610.

(10) Jia, M.; Seifert, A.; Thiel, W. R. *Chem. Mater.* **2003**, *15*, 2174.

(11) Hoffmann, F.; Cornelius, M.; Morell, J.; Fröba, M. *Angew. Chem., Int. Ed.* **2006**, *45*, 3216.

(12) Lin, V. S. Y.; Lai, C. Y.; Huang, J.; Song, S. A.; Xu, S. *J. Am. Chem. Soc.* **2001**, *123*, 11510.

(13) Mal, N. K.; Fujiwara, M.; Tanaka, Y.; Taguchi, T.; Matsukata, M. *Chem. Mater.* **2003**, *15*, 3385.

(14) Mal, N. K.; Fujiwara, M.; Tanaka, Y. *Nature* **2003**, *421*, 350.

(15) García, N.; Benito, E.; Guzmán, J.; Tiemblo, P.; Morales, V.; García, R. A. *Microporous Mesoporous Mater.* **2007**, *106*, 129.

(16) Matsumoto, A.; Tsutsumi, K.; Schumacher, J.; Unger, K. K. *Langmuir* **2002**, *18*, 4014.

(17) Anwander, R.; Nagl, I.; Widenmeyer, M.; Engelhardt, G.; Groeger, O.; Plam, C.; Röser, T. *J. Phys. Chem. B* **2000**, *104*, 3532.

(18) Inumura, K.; Inoue, Y.; Kakii, S.; Nakano, T.; Yamanaka, S. *Phys. Chem. Chem. Phys.* **2004**, *6*, 3133.

(19) Martin, T.; Galarneau, A.; Di Renzo, F.; Brunel, D.; Fajula, F.; Heinisch, S.; Crétier, G.; Rocca, J. L. *Chem. Mater.* **2004**, *16*, 1725.

(20) Song, S.-W.; Hidajat, K.; Kawi, S. *Langmuir* **2005**, *21*, 9568.

(21) Trens, P.; Russell, M. L.; Spjuth, L.; Hudson, M. J.; Liljenzin, J. O. *Ind. Eng. Chem.*

Res. **2002**, *41*, 5220.

(22) Rodríguez-López, G.; Marcos, M. D.; Martínez-Máñez, R.; Sancenón, F.; Soto, J.; Villaescusa, L. A.; Beltrán, D.; Amorós, P. *Chem. Commun.* **2004**, *19*, 2198.

(23) Tourné-Péteilh, C.; Brunel, D.; Bégu, S.; Chiche, B.; Fajula, F.; Lerner, D. A.; Devoisselle, J. M. *New J. Chem.* **2003**, *27*, 1415.

(24) Martín, A.; García, R. A.; Sen Karaman, D.; Rosenholm, J. M. *J. Mater. Sci.* **2014**, *49*, 1437.

(25) Doadrio, J. C.; Sousa, E. M. B.; Izquierdo-Barba, I.; Doadrio, A. L.; Pérez-Pariente, J.; Vallet-Regí, M. *J. Mater. Chem.* **2006**, *16*, 462.

(26) Qu, F.; Zhu, G.; Huang, S.; Li, S.; Qiu, S. *ChemPhysChem* **2006**, *7*, 400.

(27) Tang, Q.; Xu, Y.; Wu, D.; Sun, Y. *Chem. Lett.* **2006**, *35*, 474.

(28) Diao, X.; Wang, Y.; Zhao, J.; Zhu, S. *Chin. J. Chem. Eng.* **2010**, *18*, 493.

(29) Doadrio, A. L.; Salinas, A. J.; Sánchez-Montero, J. M.; Vallet-Regí, M. *Curr. Pharm. Des.* **2015**, *21*, 6213.

(30) Lee, C.; Lin, T.; Lin, H.; Zhao, Q.; Liu, S.; Mou, C. *Microporous Mesoporous Mater.* **2003**, *57*, 199.

(31) García-Muñoz, R. A.; Morales, V.; Linares, M.; González, P. E.; Sanz, R.; Serrano, D. P. *J. Mater. Chem.* B **2014**, *2*, 7996.

(32) Zhao, D.; Feng, J.; Huo, Q.; Melosh, N.; Frederickson, G. H.; Chmelka, B. F.; Stucky, G. D. *Science* **1998**, *279*, 548.

(33) Nakamura, E.; Isobe, H.; Tomita, H.; Sawamura, M.; Jinno, S.; Okayama, H. *Angew. Chem., Int. Ed.* **2000**, *39*, 4254.

(34) Uritu, C. M.; Varganici, C. D.; Ursu, L.; Coroaba, A.; Nicolescu,

A.; Dascalu, A. I.; Peptanariu, D.; Stan, D.; Constantinescu, C. A.; Simion, V.; et al. *J. Mater. Chem. B* **2015**, *3*, 2433.

(35) Yamago, S.; Tokuyama, H.; Nakamuralr, E.; Kikuchi, K.; Kananishl, S.; Sueki, K.; Nakahara, H.; Enomoto, S.; Ambe, F. *Chem. Biol.* **1995**, *2*, 385.

(36) Lankoff, A.; Arabski, M.; Wegierek-Ciuk, A.; Kruszewski, M.; Lisowska, H.; Banasik-Nowak, A.; Rozga-Wijas, K.; Wojewodzka, M.; Slomkowski, S. *Nanotoxicology* **2012**, *7*, 235.

(37) Hediger, S.; Meier, B. H.; Kurur, N. D.; Bodenhausen, G.; Ernst, R. R. *Chem. Phys. Lett.* **1994**, *223*, 283.

(38) Fung, B. M.; Khitrin, A. K.; Ermolaev, K. *J. Magn. Reson.* **2000**, *142*, 97.

(39) arion, D.; Wüthrich, K. *Biochem. Biophys. Res. Commun.* **1983**, *113*, 967.

(40) Elena, B.; de Paëpe, G.; Emsley, L. *Chem. Phys. Lett.* **2004**, *398*, 532.

(41) Hayashi, S.; Hayamizu, K. *Bull. Chem. Soc. Jpn.* **1991**, *64*, 685.

(42) Lee, C.; Lin, T.; Lin, H.; Zhao, Q.; Liu, S.; Mou, C. *Microporous Mesoporous Mater.* **2003**, *57*, 199.

(43) Valliant, J. F.; Schaffer, P.; Britten, J. F.; Davidson, A.; Jones, A. G.; Yanch, J. C. *Tetrahedron Lett.* **2000**, *41*, 1355.

(44) Cheng, J.; Xenopoulos, A.; Wunderlich, B. *Magn. Reson. Chem.* 1992, 30, 917− 926.

(45) Zhang, Z. G.; Li, H.; Qi, B.; Chi, D.; Jin, Z.; Qi, Z.; Hou, J.; Li, Y.; Wang, J. *J. Mater. Chem. A* **2013**, *1*, 9624.

(46) Dzhemilev, U. M.; Ibrahimov, A. G.; Tuktarov, A. R.; D'yakonov, V. A.; Pudas, M.; Bergmann, U. *Russ. J. Org. Chem.* **2007**, *43*, 375.

(47) Spielmann, H. P.; Wang, G. W.; Meier, M. S.; Weedon, B. R. *J. Org. Chem.* **1998**, *63*, 9865.

(48) Vree, T. B.; Lagerwerf, A. J.; Verwey-van Wissen, C. P. W. G. M.; Jongen, P. J. H. *J. Chromatogr., Biomed. Appl.* **1999**, *732*, 337.

(49) Vallet-Regí, M.; Izquierdo-Barba, I.; Colilla, M. *Philos. Trans. R. Soc*., A **2012**, *370*, 1400.

(50) Korsmeyer, R. W.; Gurny, R.; Doelker, E.; Buri, P.; Peppas, N. A. *J. Pharm. Sci.* **1983**, *72*, 1189.

(51) Doadrio, A. L.; Sánchez-Montero, J. M.; Doadrio, J. C.; Salinas, A. J.; Vallet-Regí, M. *Microporous Mesoporous Mater.* **2014**, *195*, 43.

Chapter 7 : Importance of the Donor:Fullerene Intermolecular Arrangement for High-Efficiency Organic Photovoltaics

---

This chapter is adapted with permission from Graham, K. R. ; Cabanetos, C.; Jahnke, J. P.; Idso, M. N.; El Labban, A.; Ndjawa, G. O. N.; Heumueller, T.; Vandewal, K. ; Salleo, A. ; Chmelka, B. F. ; Amassian, A. ; Beaujuge, P. M. ;Mcgehee, M. D. Importance of the Donor:Fullerene Intermolecular Arrangement for High-Efficiency Organic Photovoltaics. *Journal of the American Chemical Society* **2014**, 136, 9608-9618.

Abstract

The performances of organic photovoltaic (OPV) material systems are believed to depend strongly on the intermolecular interactions, proximities and arrangements at the polymer:fullerene interface. A key factor hypothesized to influence molecular arrangements at polymer:fullerene interfaces is the structure of the conjugated polymer species; namely, that polymer sidechains can sterically direct the fullerene species into specific arrangements with respect to the polymer. However, as there are relatively few molecules at the polymer:fullerene interface in any given heterojunction material, it is often challenging to interrogate these interfaces using conventional spectroscopic techniques. Here, judicious selections of the type and concentrations of conjugated polymer species in bulk polymer:fullerene heterojunction materials enabled the interface to be probed. Powerful two-dimensional solid-state NMR measurements support that the interactions and arrangements of polymer species are dictated by steric effects associated with the polymer sidechains. These molecular-level insights correlate with and explain macroscopic photovoltaic performances of the heterojunction

materials. These analyses yield new understanding about interfaces in photovoltaic polymer:fullerene heterojunctions that is broadly useful for designing high-efficiency photovoltaic devices.

Introduction

Organic photovoltaics (OPVs) are a promising energy conversion technology because they are light weight, can be processed on large and flexible substrates, and can possibly be produced at low-cost.[1–3] Most high-performing photovoltaic materials are processed into so-called heterojunction morphologies in which two immiscible components, usually a photo-sensitive conductive polymer and a fullerene species, are mixed and form separate phases. The interface of these two phases is critical for the photovoltaic properties of the material, as it mediates the separation of photo-generated excitons into free electrons and holes that can produce an electrical current. As a result, many studies conclude that heterojunction interfaces with nanostructured morphologies, which consequently have relatively high interfacial areas, can improve photovoltaic performance significantly versus devices non-structured heterojunction interfaces.[4–7] Besides the interfacial morphology, simulations indicate that the molecular arrangement at the interface influences exciton dissociation, charge separation, and charge recombination processes.[8] However, the importance of polymer and fullerene arrangements on photovoltaic performance remains to be established.

Despite major research progress in organic photovoltaics, there remain many questions about which factors are responsible for the high performances of these materials. Some factors known to support high solar conversion efficiencies in photovoltaic materials include broad solar absorbances, high charge carrier mobilities, appropriate energy level matching of the electron-donating polymer and electron-accepting fullerene species. However, in some cases

heterojunctions that exhibit these properties yield moderate or low solar conversion efficiencies,[9–11] suggesting that other unmeasured properties limit performance; one such property could possibly be the arrangement of polymer and fullerene species. In fact, simulations show that the interfacial energetics, exciton binding energies, and charge separation probabilities can vary substantially with the arrangement of molecules at the interface. Such interfacial properties, however, prove exceedingly challenging to characterize experimentally and thus have been addressed primarily through theoretical investigations.

A recent breakthrough in the organic photovoltaic community was the advent of donor-acceptor (D-A) polymers, which have yielded heterojunction devices with very high (>7%) solar conversion efficiencies.[12–14] These photo-responsive conjugated polymers have two repeating moieties, called the donor (D) and acceptor (A), the types and chemistries of which can be precisely controlled through synthesis; this synthetic versatility allows judicious tuning of the D-A properties, including the band-gap and energy levels of the frontier molecular orbitals.[15–17] The characteristic feature of D-A polymers is that the electron density of the LUMO is concentrated on the D moiety, while electron density in the HOMO predominantly resides on the A moiety.[18] As a result, in a polymer:fullerene heterojunction, photo-generated excitons would be more prone to dissociate if the electron-accepting fullerene species was nearby the A moiety versus the D moiety. Based on their synthetic versatility, chemically distinct moieties, and high performances, D-A appear to be promising polymer species for elucidating the importance of interfacial molecular arrangement.

A detailed literature review by Graham et al[14] uncovered a strong trend of the D-A polymer sidechain architectures with photovoltaic efficiencies of D-A polymer:fullerene heterojunction devices. Namely, with few exceptions, heterojunctions made with D-A

polymers with bulky alkyl sidechains on the D moieties generally showed higher solar conversion efficiencies. Based on this correlation, it is hypothesized that polymer sidechains sterically promote the preferential interactions and arrangements of fullerene species with specific polymer moieties (e.g., the D or A moieties) at the heterojunction interface.

To test this hypothesis, the macroscopic photovoltaic properties of heterojunction materials that included D-A polymers with identical backbones but different sidechain types were correlated with molecular-level proximities of polymer and fullerene species. For this study, the D-A polymer poly-benzo[1,2-b:3,4-b']dithiophene-thieno[3,4-c]pyrrole-4,5-dione (BDT-TPD), with benzodithiophene (BDT) donor and thienopyrroledione (TPD) acceptor moieties,[19–21] was selected because this polymer could be synthesized with various alkyl sidechains, particularly linear C_8H_{17} (C_8) and $C_{14}H_{29}$ (C_{14}) or branched 2-ethylhexyl (EH) chains, but with polydispersities (1.7-2.0) and optical band-gaps.[14] Polymer backbone moieties with linear C8 and C14 sidechains are expected to be more accessible to fullerene species than those with branched ethyl-hexyl (EH) species, and with shorter C8 providing less steric hindrance than longer C14 chains. The photovoltaic performances of various polymer:fullerene heterojunctions showed a strong trend with polymer sidechain type, which correlated with and explained by solid-state NMR analyses of the heterojunction materials.

Materials and Methods

Polymer synthesis, device preparation and macroscopic testing: Details of the synthesis of BDT-TPD polymers, preparation of heterojunctions and photovoltaic cells, and macroscopic device testing are described in Graham et al.[14]

Solid-state NMR measurements: Solid-state 2D $^{13}C\{^1H\}$ HETCOR NMR experiments were conducted at 11.7 T using a Bruker AVANCE II NMR spectrometer operating at frequencies

of 500.24 MHz for ^{1}H and 125.79 MHz for ^{13}C. Experiments were conducted at room temperature under magic-angle spinning (MAS) conditions using a 4-mm double-resonance variable-temperature Bruker MAS probehead. Time-proportional-phase-incrementation (TPPI) was used for quadrature detection in the indirect (^{1}H) dimension.[22] Cross-polarization (CP) was used to transfer magnetization from ^{1}H to ^{13}C nuclei by adiabatic passage according to the Hartmann-Hahn condition.[23] Heteronuclear ^{1}H decoupling was applied during signal acquisition using the SPINAL-64 pulse sequence at a ^{1}H nutation frequency of 100 kHz.[24] The 2D $^{13}C\{^{1}H\}$ HETCOR spectra were acquired under 12.5 kHz MAS conditions with 1, 2, or 8 ms CP contact times. Longer contact times (8 ms) were required to resolve the mobile molecular species in the heterojunction blends, while shorter contact times (1 or 2 ms) were adequate for assigning peaks of the neat compounds. High power ^{1}H-^{1}H homonuclear decoupling using the eDUMBO-1_{22} sequence was applied during the ^{1}H evolution time with a phase-modulated radio frequency pulse of constant amplitude (100 kHz).[25] In the indirect dimension, scaling factors between 0.567 and 0.610 were calibrated from separate 2D $^{1}H\{^{1}H\}$ spin diffusion NMR experiments for EH/C8 and C14/EH blends, respectively. All experiments were conducted using a recycle delay of 1 s, and 1024 and 1536 transients were signal-averaged for each of the 72 t_1 increments for the EH/C8 and C14/EH heterojunction materials, respectively. Separate 1D $^{13}C\{^{1}H\}$ CP MAS and single-pulse ^{1}H spectra are shown at the top and alongside each 2D spectrum, respectively. These 1D spectra were acquired under identical experimental conditions as those of the associated 2D, with the exception of the single-pulse ^{1}H experiments for the heterojunction materials, which were conducted at 18.8 T using a Bruker Avance II NMR spectrometer with a corresponding ^{1}H frequency of 800.24 MHz at 40 kHz MAS. Contour levels in the 2D spectra correspond to 5, 10, 20, 40, and 70% of the

maximum signal intensity. Isotropic ^{13}C and ^{1}H chemical shifts were referenced to neat tetramethyl-silane (TMS, 0 ppm), using tetrakis-methylsilane as an external secondary reference (with ^{13}C and 1H chemical shifts of 3.52 and 0.25 ppm relative to TMS, respectively).[26]

Results and Discussion

The photovoltaic performances of **pBDT-TPD** polymers with various linear and branched alkyl sidechains yield insight about the influences of sidechain sterics. Polymer moieties with shorter linear sidechains are comparatively accessible to fullerene $PC_{61}BM$ species versus those with bulky branched sidechains. Bulk heterojunction materials were generated using **pBDT-TPD** polymers with different permutations of straight chain C_8H_{17} (**C8**) and $C_{14}H_{29}$ (**C14**) or branched 2-ethylhexyl (**EH**) alkyl chains on the BDT donor or TPD acceptor moieties, as shown schematically in Figure 1A. Of the various sidechain permutations on **pBDT-TPD**, the polymer with branched **EH** groups on the BDT donor moiety and straight **C8** group on the TPD acceptor moiety, referred to as **EH/C8**, would be expected to promote $PC_{61}BM$ fullerene access to the TPD acceptor moiety, as illustrated in Figure 1B, and thus support the highest photovoltaic performance. By comparison, the **C14/EH** should promote fullerene interactions with the donor moiety and is expected to have the lowest performance of the polymers synthesized.

Analyses of standard photovoltaic performance characteristics for conventional bulk heterojuction materials reveal strong trends with **pBDT-TPD** alkyl sidechain substitution. Conventional bulk heterojunction materials contain continuous interpenetrating polymer and fullerene phases that have similar volume fractions, as shown in Figure 1C. The phtovoltaic performance metrics include short-circuit current (J_{SC}), open-circuit voltage (V_{OC}) and fill

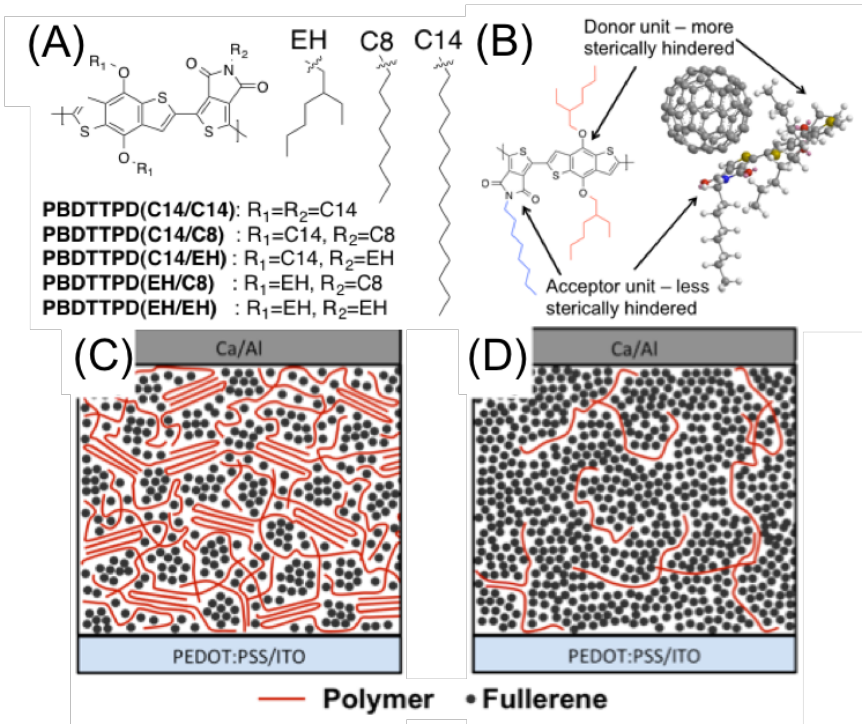

Figure 1. (A) Molecular structures of pBDT-TPD polymer backbone and ethylhexyl (EH), octyl (C8), and tetradecyl (C14) sidechain moieties. **(B)** Schematic illustration of fullerene arrangements with respect to the polymer backbone based on the hypothesis that sidechains sterically direct the fullerene to specific moieties on the polymer backbone. Cartoons of polymer:fullerene heterojunctions in **(C)** bulk heterojunction morphologies[27–29] and **(D)** with low polymer contents. (Figure courtesy of Dr. Ken Graham)

factor (FF), the product of which is the power conversion efficiency (PCE) of the heterojunction material, or the percentage of incident solar energy that is converted into electricity. Heterojunctions with **EH/C8** polymers show 40-170% higher short-circuit current, 1-38% greater fill factors and similar open-circuit voltages compared to heterojunctions made from other polymers. As a result, the calculated power conversion efficiency (PCE) of the **EH/C8** bulk heterojunction devices is 60-250% higher than the other heterojunctions compared. Owing to the highly similar molecular properties (e.g., molecular weight, polydispersity, and optical bandgap) of the polymers, these results establish a large influence of sidechain on macroscopic photovoltaic performance. Moreover, the **EH/C8** polymer performed best while the **C14/EH** polymer had the lowest performance, as expected based on

Table 1. Performance of organic photovoltaic cells based on bulk heterojunction morphologies with standard deviations indicated. (Table courtesy of Dr. Ken Graham)

Material	J_{SC} (mA/cm^2)	V_{OC} (V)	FF	PCE (%)
C14/C14	6.3±0.1	0.94±0.01	0.65±0.07	3.8±0.1
C14/C8	6.9±0.3	0.90±0.02	0.53±0.02	3.3±0.2
C14/EH	3.6±0.2	0.97±0.01	0.48±0.03	1.7±0.2
EH/C8	9.6±0.2	0.94±0.01	0.66±0.01	6.0±0.3
EH/EH	6.6±0.4	0.96±0.03	0.50±0.03	3.2±0.3

the hypothesis that fullerene species access the TPD acceptor in **EH/C8** heterojunctions and BDT donor moiety in **C14/EH** heterojunctions. While these performance measurements suggest that different interfacial polymer:fullerene arrangements influence photovoltaic performance, the observed performance trends could also arise from different nanoscale morphologies or polymer-polymer interactions in the various heterojunction materials.

By comparison, polymer:fullerene heterojunctions with low (<10 wt%) polymer contents are expected to yield heterojunctions with isolated polymer species, as depicted in Figure 1D, thus reducing the effect of polymer-polymer and nanoscale morphology effects on performance. The performances of heterojunctions with **pBDT-TPD** polymer concentrations of 1 to 8% reveal dramatic dependencies on polymer alkyl sidechain architecture, with **EH-C8** again outperforming other polymers in terms of J_{SC} (Figure 2A) and PCE (Figure 2B) over all polymer concentrations. Importantly, using X-ray diffraction, TEM and photoluminescence, Graham et al established that these trends could not originate from polymer aggregation or disparities in the number of excitons that reach the polymer:fullerene interface.[14] These results provide strong evidence that polymer sidechain type and organization can promote preferential interactions with fullerene species that significantly influence photovoltaic performance.

Solid-state nuclear magnetic resonance (NMR) spectroscopy complements the performance measurements by providing molecular-level insights on the interactions of the fullerene with the donor and acceptor moieties in the conjugated polymers. Specifically, solid-state two-dimensional (2D) $^{13}C\{^{1}H\}$ heteronuclear correlation (HETCOR) NMR measurements exploit through-space dipole-dipole couplings of locally proximate (< 1 nm) ^{13}C and ^{1}H nuclei to correlate their isotropic chemical shifts. This provides direct information on intra- and key intermolecular interactions among the chemically distinct polymer and fullerene moieties shown in Figure 6a and b, which depicts the $PC_{61}BM$ functional groups (orange), the linear alkyl chains (blue), the branched EH alkyl groups (red), and the polymer backbone (brown). In particular, the 2D $^{13}C\{^{1}H\}$ HETCOR spectra of the neat **EH/C8** and **C14/EH** conjugated polymers and $PC_{61}BM$ (Appendix B, Figure B14) yield well-resolved ^{1}H and ^{13}C signals that are confidently assigned to the specific polymer and $PC_{61}BM$ moieties, labeled in Figure 6a, as indicated above the respective 1D ^{1}H and ^{13}C MAS spectra in Figure 6c.

To gain insight into the polymer-fullerene intermolecular arrangement, 8 wt. % polymer, 92% $PC_{61}BM$ blends were probed with 2D $^{13}C\{^{1}H\}$ HETCOR NMR. Although some aggregation is evident at 8 wt. % polymer, these higher polymer concentrations are necessary to maximize the 2D $^{13}C\{^{1}H\}$ HETCOR signal arising from polymer-fullerene interactions. For the 8 wt.% **EH/C8** in $PC_{61}BM$ blend, the 2D $^{13}C\{^{1}H\}$ HETCOR spectrum acquired at room temperature also yields well-resolved correlated signals, most of which reflect the same intramolecular contributions as for the neat components. Importantly, however, additional 2D intensity correlations are observed in Figure 6c that directly establish intermolecular interactions between the $PC_{61}BM$ and **EH/C8** polymer moieties. Specifically, ^{13}C signals

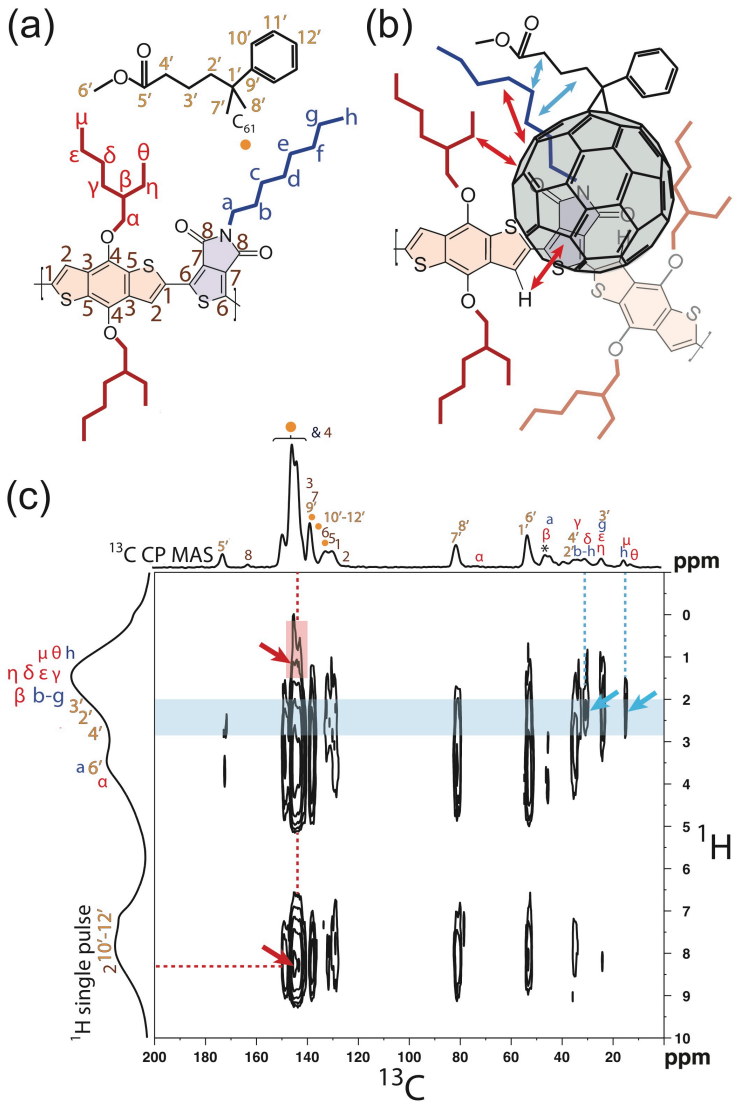

Figure 2. Molecular structures of (a) EH/C8 and $PC_{61}BM$, with their respective moieties labeled and (b) schematic showing red and blue arrows that indicate intermolecular interactions between the conjugated polymer and $PC_{61}BM$ moieties that are consistent with the 2D NMR intensity correlations. (c) Solid-state 2D $^{13}C\{^{1}H\}$ dipolar-mediated heteronuclear correlation (HETCOR) NMR spectrum acquired at room temperature for an 8 wt% EH/C8 in $PC_{61}BM$ blend under MAS conditions of 12.5 kHz, with an 8-ms CP contact time. 1D $^{13}C\{^{1}H\}$ CPMAS and single-pulse ^{1}H MAS spectra are shown along the top horizontal axis and the left vertical axis, respectively.

associated with the C_{60} fullerene group at 140-148 ppm are strongly correlated with the ^{1}H signals at *ca.* 1.2 ppm and *ca.* 8.3 ppm (Figure 6c, red arrows) associated with the alkyl and aromatic ^{1}H moieties of the polymer, respectively. It is noteworthy that the only ^{1}H atoms on the polymer backbone are associated with carbon site *2* of the BDT unit, each of which is

adjacent to a TPD moiety. Similar correlated intensities are observed in the 2D $^{13}C\{^{1}H\}$ spectrum (Appendix B, Figure B15) of the 8 wt.% **C14/EH** in $PC_{61}BM$ blend. These 2D intensity correlations unambiguously establish the close (< 1 nm) proximities of the C_{60} moieties of the $PC_{61}BM$ molecules to the polymer backbone for both of the **EH/C8** and **C14/EH** heterojunction blends, as required for efficient charge transfer.

The 2D NMR results furthermore suggest that the type and placement of the alkyl groups influence the local configurations of the $PC_{61}BM$ moieties near the polymer backbone. In particular, the ^{13}C signals at 31 ppm and 14 ppm that are associated with carbon atoms *b-f* and *h*, respectively, of the linear C8 alkyl chains on the TPD acceptor moiety are strongly correlated (Figure 6c, blue arrows) with the ^{1}H signals at 2-3 ppm from moieties *2'-4'* of the $PC_{61}BM$ functional group (Figure 6c, blue band). While the ^{13}C signal at 31 ppm contains overlapping signals from carbon atoms *b-f* of the linear C8 alkyl chain and δ of the branched EH alkyl groups, most of this signal intensity appears to arise from the ^{13}C atoms of the C8 chains (5/TPD moiety), as opposed to those of the EH groups (2/BDT moiety). This is evident from comparison with the 2D $^{13}C\{^{1}H\}$ HETCOR spectrum (Appendix B, Figure B15) for the 8 wt% **C14/EH** in $PC_{61}BM$ blend, in which significantly greater intensity is observed in the correlated signals at 31 ppm in the ^{13}C dimension and at 2-3 ppm in the ^{1}H dimension (Appendix B, Figure B16). This is consistent with the greater population of interior ^{13}C atoms of the linear C14 chains (22/BDT moiety) relative to the δ-type carbon atoms in the branched EH alkyl groups (1/TPD moiety) and also compared to the **EH/C8** blend. Moreover, the association of the ^{13}C signals at 31 ppm with linear alkyl moieties is also evidenced by the different relative intensities of the weaker correlated signals at 14 ppm (^{13}C) and 2-3 ppm (^{1}H), which are consistent with the comparable populations of moieties μ, *h*, and *n* in the two blends

(Appendix B, Figure B16). These results collectively indicate that, in both blend materials, the $PC_{61}BM$ functional groups interact to greater extents with the linear C8 or C14 alkyl chains of the polymers, compared to the branched EH alkyl groups. As the polymer alkyl chains are covalently bonded to either the TPD or BDT moieties of the polymer backbone, the strong intensity correlations between the linear alkyl chains and $PC_{61}BM$ functional groups suggest that $PC_{61}BM$ species are in closer proximity to moieties of the polymer backbone that have linear alkyl chains, as opposed to those with branched EH groups. The 2D NMR analyses thus establish close (<1 nm) proximities of the $PC_{61}BM$ molecules with the polymer backbone and the linear alkyl chains, which provide evidence of preferential interactions of the $PC_{61}BM$ species and the TPD acceptor moieties in the **EH/C8** blend, as depicted in the schematic diagram of Fig. 6b. Such close proximities of the fullerene and acceptor polymer moieties would facilitate efficient charge separation and promote high photovoltaic performance, which explains the high solar conversion efficiencies of the **EH/C8**:fullerene heterojunctions versus the other polymer variants.

Conclusions

This work underscores the importance of molecular arrangements at polymer:fullerene interfaces for achieving high-efficiencies in organic photovoltaic materials. It was hypothesized that the arrangement of polymer and fullerene molecules could be influenced by the types and organization of alkyl sidechains on the polymer backbone, with fullerene species interacting more with sterically accessible polymer backbone moieties. To test this hypothesis, the photovoltaic performances of polymer:fullerene heterojunctions made with pBDT-TPD donor-acceptor polymers with various linear and branched alkyl sidechains, but otherwise similar molecular properties (i.e., polydispersity, optical bandgaps) were characterized and

compared. The macroscopic device performances of heterojunctions with standard and low polymer contents show a strong dependence with the polymer sidechain type and organization, suggesting that molecular arrangements at the polymer:fullerene interface are important for photovoltaic energy conversion. Powerful two-dimensional solid-state NMR spectroscopy established intermolecular interactions among polymer and fullerene species that support specific polymer:fullerene arrangements based on the alkyl sidechain organization on the polymer. The NMR results correlated with and explained the macroscopic performance measurements of the polymer:fullerene heterojunction materials. These insights provide crucial molecular-level insights that are broadly important for designing polymers for high performance organic photovoltaics. é

References

(1) Darling, S. B.; You, F. *RSC Adv.* **2013**, *3*, 17633.

(2) Dou, L.; You, J.; Hong, Z.; Xu, Z.; Li, G.; Street, R. A.; Yang, Y. *Adv. Mater.* **2013**, *25*, 6642.

(3) Angmo, D.; Gevorgyan, S. A.; Larsen-olsen, T. T.; Søndergaard, R. R.; Hösel, M.; Jørgensen, M.; Gupta, R.; Kulkarni, G. U.; Krebs, F. C. *Org. Electron.* **2013**, *14*, 984.

(4) Marsh, R. A.; Groves, C.; Greenham, N. C. *J. Appl. Phys.* **2007**, *101*.

(5) Castro, F. A.; Benmansour, H.; Graeff, C. F. O.; Nüesch, F.; Tutis, E.; Hany, R. *Chem. Mater.* **2006**, *18*, 5504.

(6) Weickert, J.; Dunbar, R. B.; Hesse, H. C.; Wiedemann, W.; Lukas, S.-M. *Adv. Mater.* **2011**, *23*, 1810.

(7) Neyshtadt, S.; Jahnke, J. P.; Messinger, R. J.; Rawal, A.; Peretz, T. S.; Huppert, D.; Chmelka, B. F.; Frey, G. L. *J. Am. Chem. Soc.* **2011**, *133*, 10119.

(8) Beljonne, D.; Cornil, J.; Muccioli, L.; Zannoni, C.; Brédas, J.; Castet, F. *Chem. Mater.* **2000**, *12*.

(9) Hong, Y.; Wong, H.; Moh, L. C. H.; Tan, H.; Chen, Z. *Chem. Commun.* **2011**, *49*, 4920.

(10) Guo, X.; Zhou, N.; Lou, S. J.; Hennek, J. W.; Ponce Ortiz, R.; Butler, M. R.; Boudreault, P.-L. T.; Strzalka, J.; Morin, P.-O.; Leclerc, M.; López Navarrete, J. T.; Ratner, M. A.; Chen, L. X.; Chang, R. P. H.; Facchetti, A.; Marks, T. J. *J. Am. Chem. Soc.* **2012**, *134* (44), 18427.

(11) Li, Y.; Zou, J.; Yip, H.; Li, C.; Zhang, Y.; Chueh, C.; Intemann, J.; Xu, Y.; Liang, P.; Chen, Y.; Jen, A. K. *Macromolecules* **2013**, *46*, 5497.

(12) Wang, M.; Hu, X.; Liu, P.; Li, W.; Gong, X.; Huang, F.; Cao, Y. *J. Am. Chem. Soc.* **2011**, *133*, 9638.

(13) Liang, B. Y.; Xu, Z.; Xia, J.; Tsai, S.; Wu, Y.; Li, G.; Ray, C.; Yu, L. *Adv. Mater.* **2014**, *22*, E135.

(14) Graham, K. R.; Cabanetos, C.; Jahnke, J. P.; Idso, M. N.; Labban, A. El; Ndjawa, G. O. N.; Heumueller, T.; Vandewal, K.; Salleo, A.; Chmelka, B. F.; Amassian, A.; Beaujuge, P. M.; Mcgehee, M. D. *J. Am. Chem. Soc.* **2014**, *136*, 9608.

(15) Zhou, Q.; Hou, Q.; Zheng, L.; Deng, X.; Yu, G.; Cao, Y.; Zhou, Q.; Hou, Q.; Zheng, L.; Deng, X.; Yu, G.; Cao, Y. *Appl. Phys. Lett.* **2004**, *84*, 1653.

(16) Beaujuge, P. M.; Amb, C. M.; Reynolds, J. R. *Acc. Chem. Res.* **2010**, *43*, 1396.

(17) Ellinger, S.; Graham, K. R.; Shi, P.; Farley, R. T.; Steckler, T. T.; Brookins, R. N.; Taranekar, P.; Mei, J.; Padilha, L. A.; Ensley, T. R.; Hu, H.; Webster, S.; Hagan, D. J.; Stryland, E. W. Van; Schanze, K. S.; Reynolds, J. R.; States, U. *Chem. Mater.* **2011**, *23*, 3805.

(18) Risko, C.; McGehee, M. D.; Brédas, J.-L. *Chem. Sci.* **2011**, *2*, 1200.

(19) Zou, Y.; Najari, A.; Berrouard, P.; Beaupré, S.; Aïch, B. R.; Tao, Y.; Leclerc, M. *J. Am. Chem. Soc.* **2010**, *132* (15), 5330.

(20) Piliego, C.; Holcombe, T. W.; Douglas, J. D.; Woo, C. H.; Beaujuge, P. M.; Fréchet, J. M. J. *J. Am. Chem. Soc.* **2010**, *132* (22), 7595.

(21) Zhang, Y.; Hau, S. K.; Yip, H.-L.; Sun, Y.; Acton, O.; Jen, A. K.-Y. *Chem. Mater.* **2010**, *22* (9), 2696.

(22) Marion, D.; Wüthrich, K. *Biochem. Biophys. Res. Commun.* **1983**, *113*, 967.

(23) Hediger, S.; Meier, B. H.; Kurur, N. D.; Bodenhausen, G.; Ernst, R. R. *Chem. Phys. Lett.* **1994**, *223*, 283.

(24) Fung, B. M.; Khitrin, a K.; Ermolaev, K. *J. Magn. Reson.* **2000**, *142* (1), 97.

(25) Elena, B.; de Paëpe, G.; Emsley, L. *Chem. Phys. Lett.* **2004**, *398* (4–6), 532.

(26) Hayashi, S.; Hayamizu, K. *Bull. Chem. Soc. Jpn.* **1991**, *64*, 685.

(27) Bartelt, J. A.; Beiley, Z. M.; Hoke, E. T.; Mateker, W. R.; Douglas, J. D.; Collins, B. A.; Tumbleston, J. R.; Graham, K. R.; Amassian, A.; Ade, H.; Fréchet, J. M. J.; Toney, M. F.; McGehee, M. D. *Adv. Energy Mater.* **2013**, *3*, 364.

(28) Shoaee, S.; Subramaniyan, S.; Xin, H.; Keiderling, C.; Tuladhar, P. S.; Jamieson, F.; Jenekhe, S. A.; Durrant, J. R. *Adv. Funct. Mater.* **2013**, *23* (26), 3286.

(29) Westacott, P.; Tumbleston, J. R.; Shoaee, S.; Fearn, S.; Bannock, J. H.; Gilchrist, J. B.; Heutz, S.; deMello, J.; Heeney, M.; Ade, H.; Durrant, J.; McPhail, D. S.; Stingelin, N. *Energy Environ. Sci.* **2013**, *6* (9), 2756.

Conclusions and Future Directions

Conclusions

This thesis contains detailed insights about the interactions of functional species in mesostructured materials that mediate the transport of ions, molecules and charges. The investigation spans several different mesostructured materials in which functional species are directly co-assembled or are present at a surface or interface. Generally, the interactions and arrangements of these functional species were critical to mediate transport properties in these materials. For example, the use of synthesis compositions compatible with protein stability allowed proteorhodopsin guests to be co-assembled into mesostructured silica hosts with retained light-activated H^+-ion pumping function. Separately, the functionalities at the surfaces of mesoporous silica and interfaces of photovoltaic heterojunctions exerted major influence over mass and charge transport, respectively, in these materials.

The judicious selection of synthesis compositions that were compatible with membrane protein stability allowed functionally-active membrane proteins to be co-assembled into mesostructured silica host materials. In particular, the synthesis employed surfactants that serve dual protein-stabilizing and structure-directing roles, as well as silica precursors and mild acidic aqueous conditions that were compatible with protein chemistries. The synthetic protocol allowed high concentrations of proteorhodopsin membrane proteins to be incorporated within the mesochannels of mesostructured silica, where these species showed native-like optical absorbance and local dynamical behaviors. Owing to the generality of these insights, the synthetic protocol was adapted to other light-activated membrane proteins, including the transmembrane protein rhodopsin and peripheral membrane protein cytochrome

c. The generality of this approach makes mesostructured silica promising to harness the diverse range of membrane protein functionalities, such as for semi-permeable membranes, in technological devices.

As membrane protein function relies heavily on the protein structure, understanding the molecular interactions that influence proteorhodopsin structure in synthetic mesostructured silica hosts is critical for optimizing light-activated H^+-ion transport in these materials. The complexities of membrane protein structures, however, provide substantial difficulties in assessing protein structures on the molecular level. Analyses by state-of-the-art solid-state NMR techniques showed that the structures of proteorhodopsin guests in mesostructured silica bear high similarities to those of proteorhodopsin in near-native lipid environments, but with several subtle differences. These differences could be attributed to interactions with the structure-directing surfactants and silica mesochannel walls. Subsequent correlation of this structural information with transient optical spectroscopy data revealed similar light-activated functionalities of PR in synthetic mesostructured silica and lipid environments, with slightly slower kinetics for proteorhodopsin in the synthetic silica hosts. Rigorous correlation of the structures and function of proteorhodopsin species in synthetic mesostructured silica materials establish that the interactions in mesostructured silica hosts largely preserve native-like structures and functions.

The interactions of proteorhodopsin with surfactants and other proteins via oligomerization can modify protein function. Membrane proteins have highly hydrophobic transmembrane regions that can interact with surfactants and, separately, with other membrane proteins to form oligomers, which are known to modify protein function. Comprehensive analyses of the functionalities of proteorhodopsin monomers and oligomers in different

micellar surfactant solutions reveal that oligomerization generally modifies function; though in some specific cases surfactants altered function as well. Importantly, faster light-activated transient absorbance behaviors were observed for monomeric proteorhodopsin species, which would be expected to enable more potent macroscopic light-activated responses in mesostructured silica materials.

An understanding of the interactions among surfactants, proteorhodopsin and silica species can be exploited to prepare transparent self-supporting mesostructured silica films with high proteorhodopsin loadings and desirable mechanical properties. Proteorhodopsin is highly hydrophobic and insoluble in aqueous solutions, but can be rendered soluble by appropriate quantities of surfactants. The use of low surfactant-to-protein ratios enabled record-high (20 wt%) rhodopsin loadings into mesostructured silica host materials. Moreover, appropriate choices of surfactant, silica and proteorhodopsin contents enable mesostructured materials to be processed in self-supporting morphologies with optical transparences and high mechanical robustnesses. Investigation of the local nanochannel environments by solid-state NMR spectroscopy reveals that co-assembly likely proceeds by hydrogen bonding interactions among the surfactants and silica species. Furthermore, hydration in the local nanochannel environment appears critical to support fast proteorhodopsin dynamics and functionalities. The synthetic, structural, functional insights are exploited to selectively incorporate monomeric and oligomeric proteorhodopsin species into mesostructured silica hosts.

Interactions with surface moieties in mesoporous silica materials can play key roles in molecular sorption and diffusion within these materials, which are important for applications in drug delivery. Mesoporous silica materials with aminoalkyl or aminoalkyl-HC_{60} surface moieties adsorb higher quantities and support slower releases of the pharmaceutical guest

methylprednisolone versus non-functionalized mesoporous silicas. Subsequent analyses by solid-state NMR techniques reveal that methylprednisolone guests interact with alkyl moieties of the surface-functionalized mesoporous silica surfaces and surface silanol groups, likely via hydrogen bonding. The molecular-level insights correlate with and explain the macroscopic sorption and release of methylprednisolone species from the surface-functionalized mesoporous silica hosts. These results yield guidelines about how surface functionalities dictate the loading and transport of molecular guests in mesoporous materials.

In addition to molecular transport, interfacial interactions are also crucial for efficient photo-initiated charge separation in organic photovoltaic heterojunctions. In polymer:fullerene heterojunction materials, charge separation occurs at the interface of polymer and fullerene molecules and is widely believed to depend strongly on intermolecular interactions at this interface. Solid-state NMR spectroscopy established that the type and organization of alkyl sidechains on donor-acceptor polymers could promote fullerene species to interact predominantly with either the donor or acceptor polymer moieties. The importance of these insights is underscored by macroscopic device performance measurements, which indicate that heterojunctions in which fullerene species interact with the donor moieties had >3 times higher solar conversion efficiencies than those where fullerene-acceptor interactions predominated.

The contents of this thesis have broader impacts for developing new engineering technologies that exploit functional species, especially membrane proteins, in mesostructured materials. The approach for co-assembling functionally-active proteorhodopsin species into mesostructured silica materials, which included appropriate selections of solvent, surfactant and inorganic precursor species, is expected to be adaptable to other membrane proteins. Extension of the synthetic protocol to other membrane proteins would yield materials with

properties and behaviors useful in an assortment of technological areas, including sensing, enzyme catalysis, separations, energy conversion and optoelectronics. Based on the high rates, selectivities and thermodynamic efficiencies of membrane protein functionalities, the resulting materials could achieve performances superior to those of state-of-the-art synthetic materials.

Future directions

Orientational alignments of mesostructure and proteorhodopsin species

Important objectives for enabling mesostructured silica materials to harness membrane protein function are achieving high orientational ordering of membrane protein guests and the mesostructure of the host. As membrane proteins have inherently anisotropic functionalities, the alignment of these species is necessary to produce effects over macroscopic scales; separately, in mesostructured materials, eliminating the tortuousities of mesochannels would reduce mass transport limitations along the channels and benefit transport mediated by membrane protein guests. Several methods have successfully introduced high orientational alignment of mesochannels, yet these conditions are often incompatible with membrane protein stability and solubility. An important step forward would be to adapt these synthesis protocols to be compatible with membrane proteins. One approach would be to blend protein-stabilizing surfactants with others that are proficient at directing mesostructure formation (i.e., those with high hydrophobic/hydrophilic contrast); appropriate mixtures of surfactants and corresponding conditions (i.e., solvent and pH) could support membrane solubility during synthesis and also achieve high degrees of mesostructural ordering and alignment. Possible choices of structure-directing surfactants could be ionic or fluorinated surfactants as these species would have high hydrophilic-hydrophobic contrast, though may tend to interact

strongly with and destabilize membrane proteins under most synthesis conditions. Should ionic surfactants be pursued as structure-directors, the synthesis pH conditions should be selected so the membrane protein guest and surfactant have the same net charge to prevent strong electrostatic interactions that would destabilize the protein. By comparison, alkyl glucoside (e.g., octylglucoside, decylglucoside) and alkyl polyglucoside surfactants (e.g., dodecylmaltoside, hexadecylmaltoside) generally tend to stabilize membrane proteins; surfactants of this type that have long (>12-carbon) alkyl chains may proficiently direct mesostructure formation while stabilizing membrane protein guests.

The macroscopic alignment of membrane protein species presents a separate challenge, but one that is not necessarily decoupled from mesostructure alignment. Many studies have demonstrated partial bulk alignments of membrane proteins in large lipid bilayers by external magnetic or electric fields; these alignment protocols relied on the additive properties (e.g., electric or diamagnetic susceptibilities) of the many (>1000) membrane protein species or lipids. By comparison, the monomeric or oligomeric membrane protein species that are co-assembled into materials would have orders of magnitude lower susceptibilities to external fields. As a result, based on the dipoles of membrane proteins, external electric or magnetic fields of exceedingly high strengths (>100 kV/cm, >1000 T) would necessary to align these protein species over reasonable (>50 nm) distances in aqueous media of relatively high ionic strengths. Alternatively, surface functionalities could be leveraged for the bulk alignment of membrane protein species in mesostructured materials. As surface functionalities can influence the arrangements of nearby molecules, appropriate choices of functionality type could result in the local alignment of membrane proteins with the mesochannel axis. In these surface-functionalized materials, the macroscopic alignment mesostructure would concomitantly result

in the bulk alignment of the membrane protein species. This approach would not require external fields, though these could be employed to facilitate alignment.

Understanding the H^+-ion pumping process of proteorhodopsin

The photochemical reaction cycle of proteorhodopsin includes several conformational motions and the protonation of the protein from bulk solution to result in the net transport of an H^+-ion across the protein's transmembrane region. Data presented in Chapter 4 of this thesis showed that monomeric proteorhodopsin species undergo substantially faster photocycle kinetics than oligomers. The significant kinetic differences between proteorhodopsin monomers and oligomers could originate from sterics associated with protein-protein interactions, which would be expected to slow the conformational motions of proteorhodopsin during the photocycle. This could be tested by correlating the transient populations of photocycle intermediates (*i.e.*, *K*, *M*, *N*, *O*, *PR'*), available by analyzing transient UV-visible absorbance data, with the site-specific motions of proteorhodopsin structural motifs by electron paramagnetic resonance spectroscopy. A motif of specific interest would be the F-helix, which exhibits significant motions during the M_2 photocycle intermediate in bacteriorhodopsin,[1] a proteorhodopsin homologue. Similar large conformational changes have been observed at the E-F loop of proteorhodopsin that are correlated with the *M* intermediate,[2] suggesting that the F-helix may also undergo large motions during the *M* intermediate in proteorhodopsin. Assuming similar photoactivated motions of the F-helix for proteorhodopsin, the steric effects of protein-protein contacts would manifest in longer timescales for F-helix movement (or nearby residues, such as on the α-helical E-F loop) and, correspondingly, the presence of M_2 intermediates for proteorhodopsin oligomers compared to monomers. Moreover, the

photocycle steps that precede the M_2 intermediate involve retinal isomerization, protonation state changes, and relatively small conformational motions, all of which are not expected to be sensitive to sterics effects originating from oligomerization; therefore, the motions of the F-helix and M_2 intermediates should emerge at approximately the same (100 μs – 1 ms) time for both monomers and oligomers following light-activation. Due to the relatively fast (100 μs) accumulation of *M* intermediates after laser excitation, correlating the photocycle kinetics and F-helix movement will require transient UV-visible absorbance and electron paramagnetic resonance instruments with time resolutions of <10 μs, and the capability to excite proteorhodopsin with laser excitation pulses of <10 μs.

The photocycle analyses by transient absorbance and electron paramagnetic resonance spectroscopies may also benefit from investigations by nuclear magnetic resonance spectroscopy (NMR). As an example, NMR relaxation measurements conducted on non-activated monomeric and oligomeric proteorhodopsin could be used to probe the dynamics of proteorhodopsin moieties with atomic level resolution. Such dynamics information could identify key protein sites or regions influenced by oligomerization, which could be correlated with and help explain the transient absorbance and electron paramagnetic resonance data. Separately, NMR also enables investigations into the local environment of the retinal chromophore, which undergoes a *trans*-to-*cis* isomerization to initiate the photocycle and, for bacteriorhodopsin, drives the large conformational movement of the F-helix.[1] Thus, differences in the structures, orientations and local environments of the retinal chromophore between monomeric and oligomeric proteorhodopsin could lend insight into the origins of the different photochemical reaction cycle kinetics of these species. Interrogation of the retinal chromophore of proteorhodopsin by NMR would benefit substantially from proteorhodopsin

samples containing ^{13}C-isotopically enriched retinal. All-trans retinal can be produced with ^{13}C-enrichment uniformly throughout the molecule, or at specific carbons groups, and can be attached to proteorhodopsin during expression in *E. coli*.

The distinct photocycle kinetics of monomeric and oligomeric proteorhodopsin could also arise from different H^+-ion diffusion limitations for these species, which could be tested by analyzing transient absorption behaviors of proteorhodopsin under multiple pH conditions. In the photocycle of proteorhodopsin, the emergence of the *N* photocycle intermediate coincides with the uptake of an H^+-ion from bulk solution[3] that, under sufficiently alkaline conditions, can limit the photocycle rate. As a photo-activated proteorhodopsin monomer requires one H^+-ion from the bulk during a photocycle (much like in a bi-molecular reaction), hexameric proteorhodopsin needs six H^+-ions from the bulk so that each of its six protomer sub-units can complete it's respective photocycle (much like a series of bi-molecular reactions). As hexameric proteorhodopsin have six protomer subunits that diffuse together as a single oligomer, one might expect it to require more time for six H^+-ions in the bulk to collide with the six protomers of a hexamer than with six independent proteorhodopsin monomers. Should this be the case, the photocycle of monomeric proteorhodopsin would become H^+-ion diffusion limited at higher pH than oligomeric proteorhodopsin; this phenomena could be experimentally assessed by performing time-resolved UV-visible absorbance measurements on monomeric and oligomeric proteorhodopsin over a range of pH conditions over which the photocycle becomes diffusion limited (*e.g.,* pH 8-10, where at pH 8 the photocycle is not diffusion limited and pH 10 it would be). One key identifier of a H^+-ion diffusion limitation during the photocycle is the time at which the *N* intermediate accumulates, which occurs between 1-10 ms at pH 8.5, and which should increase with pH if the photocycle isn't limited

by H^+-ion diffusion and be relatively insensitive to pH when H^+-ion diffusion limits the photocycle. Particularly helpful in this investigation would be the H75N variant of proteorhodopsin because this variant exhibits a much lower pKa of D97 (~5.3)[4] than WT PR (typically 6.5 - 7.5) that yields a much larger range (6.5-10) of pH conditions over which near 100% of the proteorhodopsin population would undergo a basic photocycle. In this same manner, the H75N variant would help determine whether protein-protein interactions result in the different photocycle kinetics of monomeric and oligomeric proteorhodopsin. Namely, the H75N mutant enables a comparison of the basic photocycles of monomeric and oligomeric proteorhodopsin under relatively acidic pH conditions (pH ~6.3) where H^+-ions are abundant and, therefore, H^+-ion diffusion will not limit the photocycle rate.

Harness the function of multiple proteins in a macroscopic device

A key objective would be to exploit the functionalities of multiple membrane proteins in a single macroscopic device. An interesting example would be to harness the different optical absorbance properties of H^+-ion pumping rhodopsins for solar-to-electrochemical energy conversion. The synthetic protocol for mesostructured silica presented in Chapters 1-3 and 5 was adapted to incorporate multiple types of H^+-ion pumping rhodopsin species that were mutated to have different optical absorbances. Macroscopic devices that integrate mesostructured films that incorporate all of these H^+-ion pumping rhodopsin variants would absorb broader regions of the solar spectrum versus those that include only one variant type, and thus would be expected to promote greater solar-to-chemical energy conversion. Though, to realize the benefits of these distinct optical absorbances for macroscopic solar energy conversion requires a device architecture that stores the energy converted by each type of rhodopsin in an additive manner. Macroscopic H^+-ion transport in a mesostructured silica film

that incorporates multiple types of proteins would presumably be rate limited by the rhodopsin with the slowest H^+-ion pumping kinetics, which could arise from low intrinsic H^+-ion pumping rate or low availability of light that activates that particular rhodopsin species. By comparison, such transport limitations can be circumvented in a device that integrates several mesostructured silica films that each contain a single rhodopsin variant and are arranged so that the energy converted by each film is captured additively. Such a device can be constructed by stacking the mesostructured silica films so that incident light transmits through each film, thus activating all proteins in the device, and flowing a stream of aqueous solution past each film in series such that the stream is acidified upon passing each film. The solar energy converted by each rhodopsin-laden film is additively stored as chemical energy in the outlet stream.

References

(1) Kühlbrandt, W. *Nature* **2000**, *406*, 569.

(2) Hussain, S.; Kinnebrew, M.; Schonenbach, N. S.; Aye, E.; Han, S. *J. Mol. Biol.* **2015**, *427*, 1278.

(3) Dioumaev, A. K.; Brown, L. S.; Shih, J.; Spudich, E. N.; Spudich, J. L.; Lanyi, J. K. *Biochemistry* **2002**, *41*, 5348.

(4) Hempelmann, F.; Hölper, S.; Verhoefen, M. K.; Woerner, A. C.; Köhler, T.; Fiedler, S. A.; Pfleger, N.; Wachtveitl, J.; Glaubitz, C. *J. Am. Chem. Soc.* **2011**, *133* (12), 4645.

Appendix A : Tuning underwater adhesion by cation-π interactions

---

This chapter is adapted with permission from Gebbie, M. A.; Wei, W.; Schrader, A. M.; Cristiani, T. R.; Dobbs, H. A.; Idso, M. N.; Chmelka, B. F.; Waite, J. H.; Israelachvili, J. N. Tuning underwater adhesion by cation-π interactions *Nature Chemistry* **2017**, 9, 473-479.

Abstract

Cation-π interactions are prevalent in many biological systems where they are responsible for self-assembly and cohesion. One interesting example are mussel foots, which biological structures composed of multiple types of proteins that exhibit the extraordinary property of adhesion under aqueous conditions and high ionic strengths (i.e., ocean waters). Such a property would highly useful in synthetic biomaterials for *in vivo* applications, where materials need to remain adhered to biological tissues for extended periods in bodily fluids, e.g. blood. However, very limited information is available about cation-π type interactions in biological macromolecular systems, which has made it difficult to exploit these demonstrably important interactions for practical use. In this chapter, synthetic polypeptides containing cationic lysine and aromatic groups are interrogated for the presence of cation-π type interactions. In combination with surface-forces apparatus measurements, these molecular-level insights provide new understanding important for developing new biologically-based technologies and also to rationalize biological processes.

Introduction

Biologically-based materials have a wide range of applications, including in surgical adhesives, pharmaceutical delivery, cellular scaffolds and sensors. Such materials are

advantageous versus fully inorganic, or inorganic-organic hybrid, materials due to their biocompatibilities, which improves their effectiveness for *in vivo* applications. Many biologically-based materials are inspired from their functionalities in nature. For example, mussels deploy adhesive protein-based structures, called mussel foots, onto surfaces to stabilize themselves in ocean waters. Importantly and interestingly, the mussel foot remains adhered and cohesive despite being underwater, in high ionic strengths, and under transient mechanical stresses. Such material properties would be attractive for many technological applications, such as surgical tools[1] and glues,[2] where adhesion must be maintained in biological fluids, e.g. blood, and usually under changing mechanical stresses.

Cation-π type interactions are broadly important for the self-assembly[3,4] and adhesive/cohesive[5,6] properties in biomolecular systems, including proteins. This interaction is attractive and occurs between the positively charged cation and the delocalized electron-rich π orbitals, and in aqueous solutions can exceed the strength of hydrogen bonding and possibly even electrostatic interactions.[3,7] In proteins, cation-π interactions can occur among positively charged sidechain moieties, such as on lysine and arginine, and aromatic sidechain groups that include tyrosine, phenylalaline and the non-natural amino acid residue dihydroxyphenylalanine. In fact, the sequences of many adhesive proteins[1,8,9] are enriched in these cationic and aromatic moieties of many adhesive proteins, presumably to impart strong cohesion. However, while much is known about cation-π interactions in non-biological systems, such as in gas or solution phases, but far less is understood about the energetics of these interactions in solid biological systems, where multiple cation-π interaction pairs can be present in high densities on single molecule. This lack of understanding prevents the rational design of synthetic biomaterials that exploit cation-π interactions for robust adhesion.

The objective of this study is to understand cation-π interactions in synthetic peptides. It is hypothesized that cation-π type interactions among the positively-charged lysine and aromatic residues of peptides promote cohesion among peptide molecules. To test this hypothesis, synthetic polypeptides with sequences rich in lysine and aromatic residues were characterized in the solid state by using powerful two-dimensional solid-state NMR measurements. The chemical shift interaction of NMR is highly sensitive to the local environments of atomic nuclei and, in particular, aromatic systems, which can manifest as a ring-current shift. Thus, solid-state NMR spectroscopy can be a sensitive technique by which to identify the presence of cation-π type interactions. The NMR analyses supports surface forces apparatus work by Gebbie et al[10] to provide deep molecular understanding cation-π interactions that is useful for controlling and exploiting them in biomaterials.

Materials and methods

Polypeptide synthesis: The polypeptides characterized in this study were prepared as described in Gebbie et al.[10]

Solid-state NMR measurements: Solid-state NMR measurements were conducted on Bruker AVANCE II spectrometer at 11.7 T at which the ^{1}H and ^{13}C nuclear Larmor frequencies are 500.24 and 125.79 MHz, respectively. Approximately 80 mg of each sample was packed into a 4-mm zirconia rotor for NMR characterization. Measurements were conducted at 0°C under magic-angle spinning rates of 10 kHz using a 4-mm variable-temperature double-resonance Bruker probehead. Magnetization transfer from ^{1}H to ^{13}C nuclei was achieved by cross polarization through adiabatic transfer under the Hartman-Hahn condition with a contact time of 1 ms.[11] The 1D $^{13}C\{^{1}H\}$ CP MAS measurements on the PEP-Y and PEP-L samples were collected with 4096 signal-averaging transients, respectively. For the 2D $^{13}C\{^{1}H\}$ HETCOR

measurements, high-power eDUMBO-1_{22} homonuclear decoupling at a radio frequency field strength of 100 kHz was utilized during the evolution of the ^{1}H nuclei.[12] Scaling factors of 0.65 and 0.63 were calculated for the PEP-Y and PEP-L samples from 2D ^{13}C{^{1}H} HETCOR spectra of ^{13}C,^{15}N-enriched glycine acquired under under identical conditions used for each polypeptide sample, applying the constraint that the three ^{1}H signals in the 2D spectra of ^{13}C,^{15}N-enriched glycine resonate at 3.2, 4.3 and 8.4 ppm. The indirect t_1 dimension for each 2D measurement was incremented by 96 μs, while a total of 60 and 77 t_1 increments were collected for the respective PEP-Y and PEP-L samples. A total of 1024 and 512 transients were signal-averaged for each t_1 increment in the PEP-Y and PEP-L sample, respectively. Quadrature detection in the indirect (^{1}H) dimension was achieved by using time-proportional phase incrementation (TPPI).[13] Heteronuclear ^{1}H-^{13}C decoupling was achieved by using the SPINAL-64 decoupling sequence with a radio frequency field-strength of 100 KHz.[14] Line broadening of 30 Hz and 10 Hz was applied the indirect (^{1}H) and direct (^{13}C) dimensions, respectively. For the 2D spectrum of PEP-Y, seven contours levels are shown that correspond to 20%, 25%, 30%, 40%, 55%, 70%, and 90% of the maximum signal intensity, while for the 2D spectrum of PEPL nine contours are shown that correspond to 3%, 5%, 7.5% 12%, 17%, 25%, 40%, 60% and 90% of the maximum signal intensity. The ^{13}C and ^{1}H chemical shifts were referenced to tetramethyl-silane using tetrakis-methylsilane as an external reference with isotropic ^{1}H and ^{13}C chemical shifts of 0.25 ppm and 3.52 ppm respectively.[15]

Results and Discussion

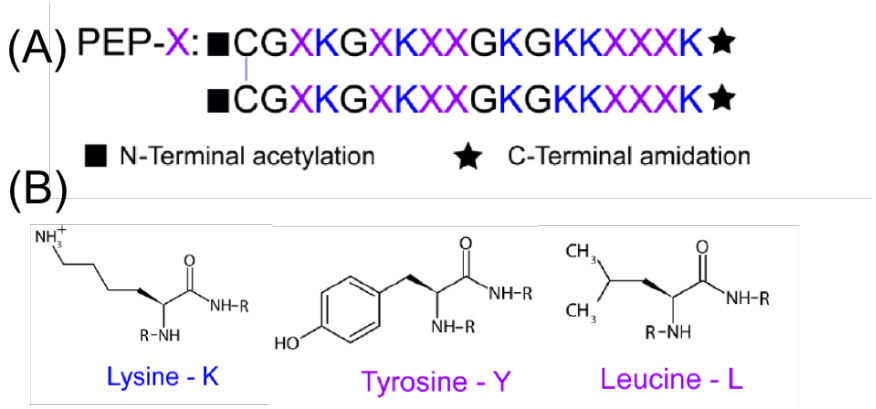

Figure 3. Sequences and molecular structures of the peptides studied. Each of the four peptides included one of the amino acids illustrated in panel **(B)** incorporated in the sequence locations marked by a purple "X" in panel **(A)**. The Lys residues are conserved in each peptide sequence and are marked in blue to emphasize the positive charge of Lys at a pH of 2.5. (Figure courtesy of Dr. Matthew Gebbie)

The synthetic polypeptides in this study were designed to promote high or low extents of cation-π interactions, the molecular structures of which are shown in Figure 1A. Each peptide has two identical chains of eighteen amino acid residues joined by a sulfide bond at the terminal cysteine groups. Each chain contains uncharged cysteine (C) and glycine (G) residues and positively charged lysine ("K") residues, as shown in Figure 1A and B. Additionally, the polypeptides were synthesized with either an aromatic tyrosine ("Y"), called PEP-Y, or alkyl leucine (L) residues, called PEP-L; while lysine and tyrosine residues of PEP-Y can interact via cation-π interactions, the PEP-L has no aromatic residues and therefore cannot support any such cation-π interactions. Using the surface forces apparatus, Gebbie et al established stronger cohesion among surfaces coated with Pep-Y (4.0 ± 0.6 mJ m^{-2}) versus Pep-L (1.3 ± 0.4 mJ m^{-2}) polypeptide, which was suggested to originate from cation-π type interactions in the former.[10] While such SFA measurements have extraordinary spatial resolutions, it cannot directly establish the molecular origins of these force differences.

Solid-state nuclear magnetic resonance (NMR) spectroscopy complements surface forces apparatus measurements by establishing the molecular proximities of the lysine and tyrosine amino acid sidechains, yielding insight into their interactions. Two-dimensional (2D) $^{13}C\{^{1}H\}$ heteronuclear correlation (HETCOR) experiments use through-space dipolar couplings to correlate the isotropic chemical shifts of nearby (<1 nm) ^{1}H and ^{13}C nuclei. For example, the solid-state 2D $^{13}C\{^{1}H\}$ HETCOR spectrum of bulk PEP-Y in Figure 2 shows

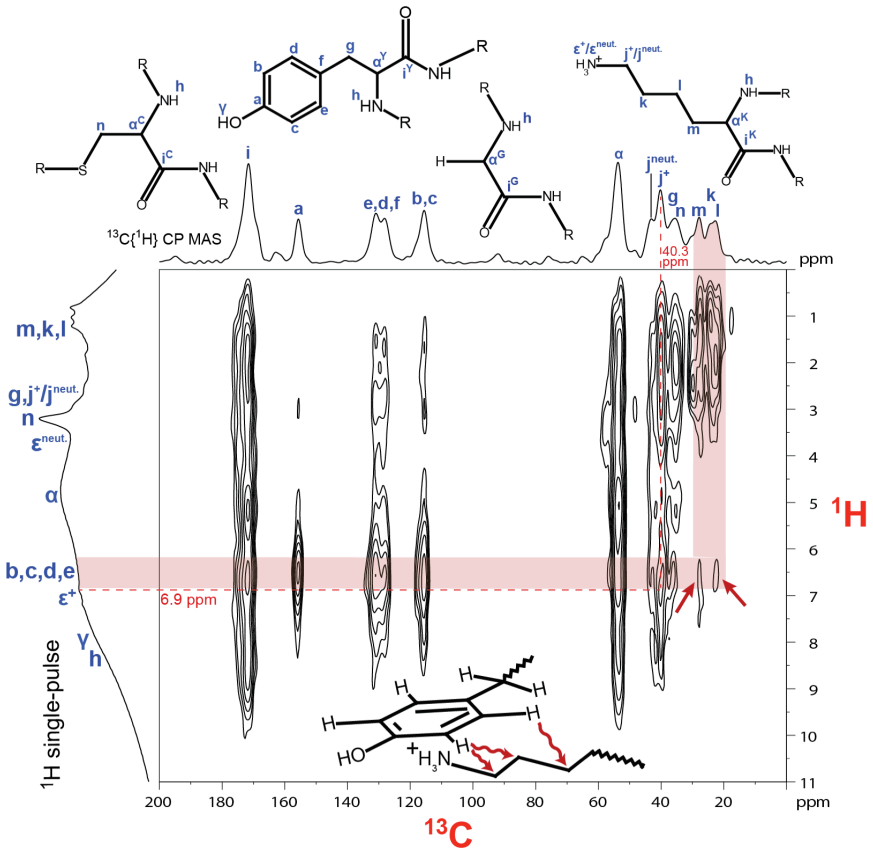

Figure 4. A solid-state 2D $^{13}C\{^{1}H\}$ HETCOR MAS NMR spectrum acquired from bulk PEP-Y polypeptide with a 1D $^{13}C\{^{1}H\}$ CP MAS NMR spectrum along the top axis and ^{1}H single-pulse NMR spectrum along the left axis. Red arrows designate intensity correlations that result from the close (<1 nm) proximities of the aromatic b-e ^{1}H moieties of the tyrosine residues and alkyl l and m ^{13}C moieties of the lysine side chains. The red dotted lines indicate a correlated intensity that arises from proximate alkyl j ^{13}C moieties and protonated amide ε^{+} ^{1}H moieties of lysine residues, which resonates approximately 0.6 ppm up-field in the ^{1}H dimension versus in a PEP-10L sample (SI Figure 3). Such an up-field shift indicates a ring-current effect that would result from a configuration of the lysine and tyrosine sidechains shown schematically in the inset, consistent with inter-residue contact through cation-pi interactions. All NMR measurements were conducted at 11.74 T under 10 kHz MAS conditions at 0°C.

many well resolved intensity correlations that arise from dipolar-coupled ^{13}C and ^{1}H nuclei of the PEP-Y polypeptide. Most intensity correlations in this 2D spectrum originate from ^{1}H and ^{13}C nuclei that are directly bound, allowing their assignment to specific ^{1}H and ^{13}C moieties of the lysine, tyrosine, cysteine and glycine amino acid residues of the PEP-Y molecule. These resonance assignments are corroborated by analyses of solid- and solution-state NMR data of systems with neat peptides and polypeptides reported in the literature.[16–20]

Importantly, the 2D $^{13}C\{^{1}H\}$ HETCOR spectrum (Figure 2) of bulk PEP-Y also includes intensity correlations that result from inter-residue interactions, specifically among the lysine and tyrosine side chains. In particular, ^{1}H signals at ca. 6.6 ppm of the aromatic ^{1}H moieties of the tyrosine residues are correlated with ^{13}C signals between 20 and 30 ppm (Figure 2, red arrows) assigned to the alkyl *l* and *m* moieties of the lysine residues. These correlations unambiguously establish the close proximities of the alkyl groups of the lysine side chains with the aromatic tyrosine moieties. Furthermore, the ^{13}C signals at ca. 40 ppm (Figure 2, red dotted line) from the alkyl j^{+} moieties are correlated with ^{1}H signals at 6.9 ppm of the ε^{+} ^{1}H moieties of the protonated lysine amide groups. By comparison, a 2D $^{13}C\{^{1}H\}$ HETCOR spectrum (Figure 3) collected from a PEP-L sample under otherwise identical conditions shows that the intensity correlation from the same j^{+} ^{13}C and ε^{+} ^{1}H moieties resonates at ca. 7.5 ppm in the ^{1}H dimension. The relative 0.6 ppm up-field shift of this correlation in the PEP-Y spectrum (Figure 2) indicates that the ε^{+} ^{1}H groups experience a ring-current effect resulting from the positioning of these ^{1}H moieties near the center of the aromatic ring on the tyrosine side chain, as shown schematically in the inset of Figure 2. Moreover, the red bands in the 2D HETCOR spectrum in Figure 3 positioned over the exact same regions as in Figure 1 show no correlated intensity at 20-30 ppm, while correlated intensity is observed in the 2D HETCOR spectrum of

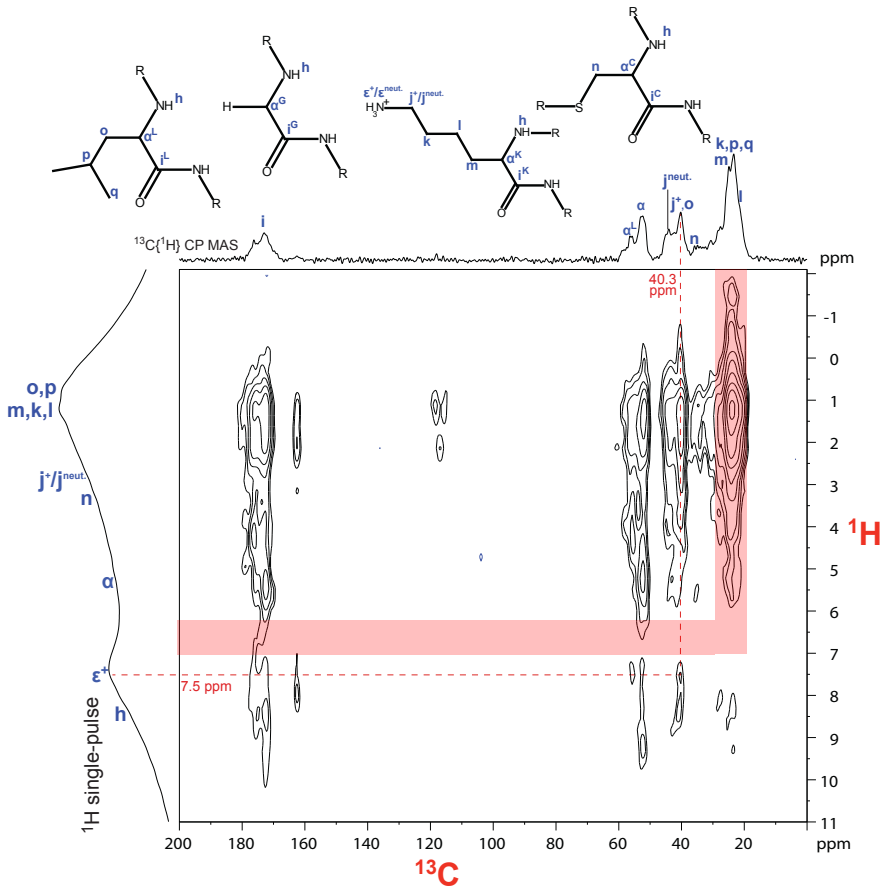

Figure 5. A solid-state 2D $^{13}C\{^{1}H\}$ HETCOR MAS NMR spectrum acquired from bulk PEP-L polypeptide with a 1D $^{13}C\{^{1}H\}$ CP MAS NMR spectrum along the top axis and ^{1}H single-pulse NMR spectrum along the left axis. The red dotted lines indicate correlated intensity that arises from the close (<1 nm) proximities of alkyl j^{+} ^{13}C and amide ε^{+} ^{1}H moieties of protonated lysine side chains, which importantly resonates at 7.5 ppm in the ^{1}H dimension. By comparison, the intensity correlation from the same alkyl j^{+} ^{13}C and ε^{+} ^{1}H moieties resonates up-field at 6.9 ppm in the spectrum of PEP-Y in Figure 1 in the main text, indicating a ring current effect expected from cation-π interactions among protonated lysine and tyrosine sidechains. All NMR measurements were conducted at 11.74 T under 10 kHz MAS conditions at 0°C.

PEP-Y sample. This provides evidence that intensity correlations in this region in the 2D spectrum of PEP-Y arise from the close inter-residue proximities of alkyl ^{13}C moieties on lysine and aromatic ^{1}H moieties of the tyrosine. Collectively, these NMR data support a configuration of the tyrosine and lysine side chains that is consistent with cation-π interactions among the protonated lysine and tyrosine side chains of the PEP-Y molecules.

Conclusions

Cation-π interactions are a promising motif to leverage to develop biomaterials with strong and durable cohesive properties under biological conditions, however little is known about how the nature of these interactions in solid biological materials. Solid-state NMR analyses of a synthetic peptide enriched in cationic lysine and aromatic tyrosine yielded clear evidence for the presence of cation-π interactions between lysine and tyrosine sidechains. These data agree with and can explain separate surface forces apparatus measurements, which show In combination with separate surface forces apparatus measurements, these results highlight the importance of inter-residue cation-π interactions for imparting cohesive properties in biological molecules. Such insights are important for designing biomaterials that have strong and robust cohesive properties *in vivo*, and also for rationalizing biological processes observed in nature.

References

(1) Lee, B. P.; Messersmith, P. B.; Israelachvili, J. N.; Waite, J. H. *Annu. Rev. Mater. Res.* **2011**, *41*, 99.

(2) Wong, C. T. S.; Foo, P.; Seok, J.; Mulyasasmita, W.; Parisi-amon, A.; Heilshorn, S. C. *Proc. Natl. Acad. Sci. U. S. A.* **2009**, *106*, 22067.

(3) Ma, J. C.; Dougherty, D. A. *Chem. Rev.* **1997**, *97*, 1303.

(4) Gallivan, J. P.; Dougherty, D. A. *Proc. Natl. Acad. Sci. U. S. A.* **1999**, *96* (August), 9459.

(5) Kim, S.; Faghihnejad, A.; Lee, Y.; Jho, Y.; Zeng, H.; Hwang, D. S. *J. Mater. Chem. B Mater. Biol. Med.* **2015**, *3*, 738.

(6) Hwang, D. S.; Zeng, H.; Lu, Q.; Israelachvili, J. N.; Waite, J. H. *Soft Matter* **2012**, *8*,

5640.

(7) Deakynet, C. A.; Meot-Ner (Mautner), M. *J. Am. Chem. Soc.* **1985**, *107*, 474.

(8) Shao, H.; Stewart, R. J. *Adv. Mater.* **2010**, *22*, 729.

(9) Kamino, K.; Nakano, M.; Kanai, S. *FEBS J.* **2012**, *279*, 1750.

(10) Gebbie, M. A.; Wei, W.; Schrader, A. M.; Cristiani, T. R.; Dobbs, H. A.; Idso, M.; Chmelka, B. F.; Waite, J. H.; Israelachvili, J. N. *Nat. Chem.* **2017**, *9*, 473.

(11) Hediger, S.; Meier, B. H.; Kurur, N. D.; Bodenhausen, G.; Ernst, R. R. *Chem. Phys. Lett.* **1994**, *223*, 283.

(12) Elena, B.; de Paëpe, G.; Emsley, L. *Chem. Phys. Lett.* **2004**, *398* (4–6), 532.

(13) Marion, D.; Wüthrich, K. *Biochem. Biophys. Res. Commun.* **1983**, *113*, 967.

(14) Fung, B. M.; Khitrin, a K.; Ermolaev, K. *J. Magn. Reson.* **2000**, *142* (1), 97.

(15) Hayashi, S.; Hayamizu, K. *Bull. Chem. Soc. Jpn.* **1991**, *64*, 685.

(16) Guo, C.; Holland, G. P. *J. Phys. Chem. C* **2014**, *118*, 25792.

(17) De Vita, E.; Frydman, L. *J. Magn. Reson.* **2001**, *148*, 327.

(18) Ando, S.; Yamanobe, T.; Ando, I.; Shoji, A.; Ozaki, T.; Tabeta, R.; Saitô, H. *J. Am. Chem. Soc.* **1985**, *107*, 7648.

(19) Martin, P.; Greuter, H.; Belluš, D. *J. Am. Chem. Soc.* **1979**, *101*, 5854.

(20) Gomes, J. A. N. F.; Mallion, R. B. *Chem. Rev.* **2001**, *101*, 1349.

Appendix B : Supporting materials

Chapter 1

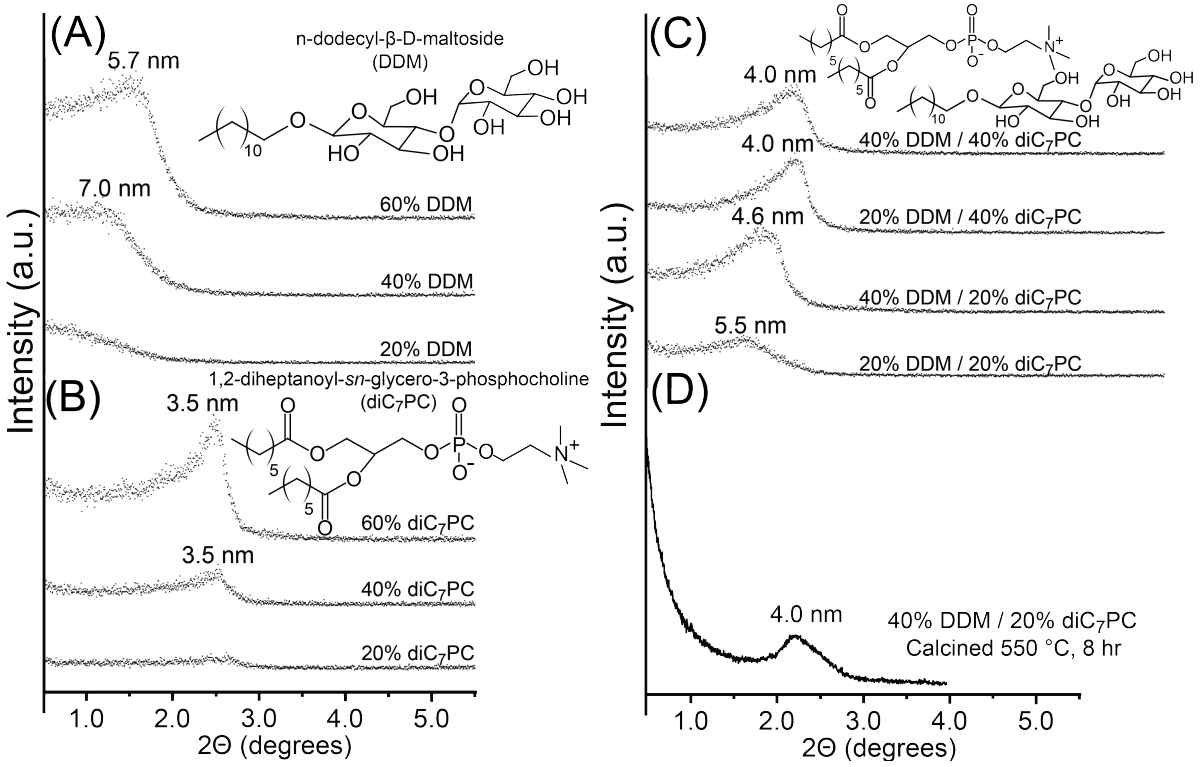

Figure B6. Small-angle X-ray scattering (SAXS) patterns of mesostructured silica materials synthesized using various quantities of **(A)** n-dodecyl-β-D-maltoside (DDM), **(B)** 1,2-diheptanoyl-sn-glycero-3-phosphocholine (diC_7PC), and **(C)** mixtures of DDM and diC_7PC as structure-directing surfactant species. Surfactant quantities are expressed as mass percentages of the final material (silica accounts for the balance), assuming complete solvent removal and silica cross-linking. Material precursor solutions were prepared by adding appropriate quantities of DDM and/or diC_7PC surfactants to aqueous solutions containing tetraethoxysilane silica precursor species, stirred under acidic conditions for 1.5 h. After the surfactants were dissolved, material solutions were titrated to pH 3-4 using 40 mM NaOH (aq.) and cast into Petri dishes under ambient conditions and allowed to dry for 2 days before SAXS characterization. **(D)** SAXS pattern of calcined mesostructured silica synthesized with 40% DDM, 20 % diC_7PC and 40% SiO_2, as described above, then calcined at 550 °C for 8 h; a single broad reflection is present at a d-spacing of 4.0 nm, consistent with contraction that occurs as a result of calcination of the as-synthesized material (d-spacing 4.6 nm, part C, 40% DDM and 20% diC_7PC).

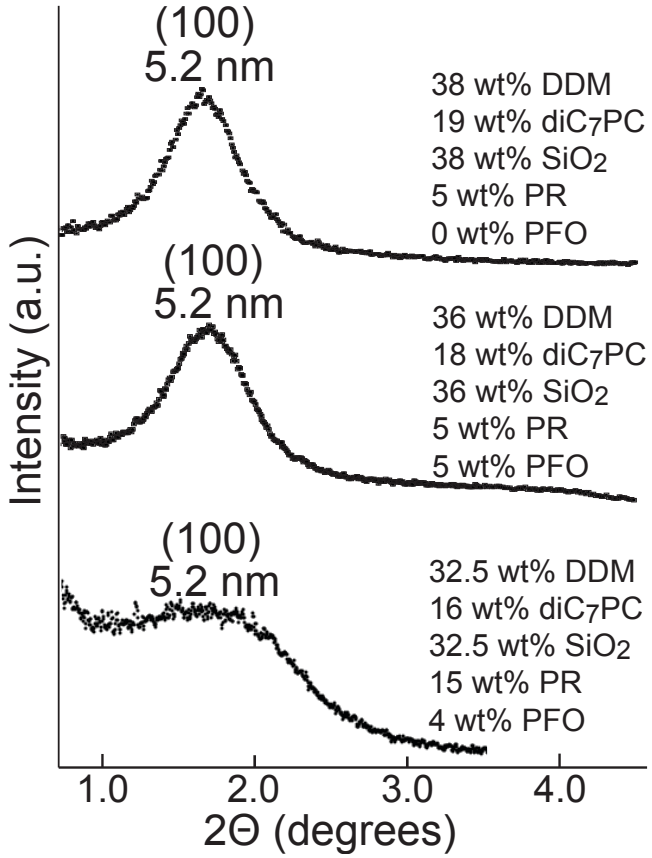

Figure B7. Small-angle X-ray scattering (SAXS) patterns of 50-μm thick DDM- and diC_7PC-directed mesostructured silica films with 5 wt% PR without (top) and with (middle) 5 wt% of PFO. The film that incorporates 5 wt% of PFO yields a primary (100) SAXS reflection at 1.7 ^{o} that is slightly broadened, yet otherwise identical to those of films without PFO, establishing the minor effect of PFO molecules on the co-assembly processes of the silica-surfactant mesostructure. The SAXS reflection pattern (bottom) of a film that incorporates 15 wt% of PR has a primary (100) reflection position shifted to 1.7^{o}, corresponding to a 5.2 nm d-spacing, with a full-width-half-maximum of ~1.0 ^{o}.

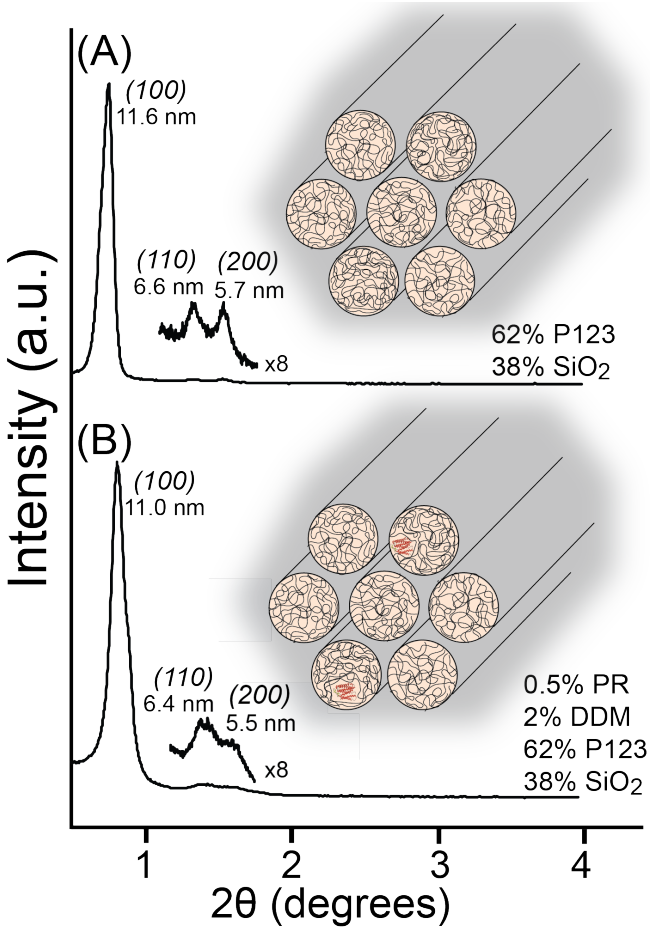

Figure B8. Small-angle X-ray scattering (SAXS) patterns from powders of P123-directed silica films **(A)** without and (B) with 0.5 wt% proteorhodopsin incorporated. Each pattern shows three reflections at ~0.8°, 1.3°, and 1.5° that are indexable to the (100), (110) and (200) reflections, respectively, associated with hexagonal (p6mm) mesostructural order. The patterns are similar, though with broader reflections observed in **(B)** for the film containing dilute PR and DDM, indicating reduced mesostructural order that diminishes further at higher PR loadings (not shown) and is accompanied by eventual loss of transparency of the films. Compared to conventional syntheses of P123-directed mesostructured silica, the somewhat lower extents of mesostructural ordering in these materials likely arises from the use of higher water contents, small quantities of DDM, and mild acidic conditions (pH ~4), which are necessary to stabilize PR molecules during co-assembly.

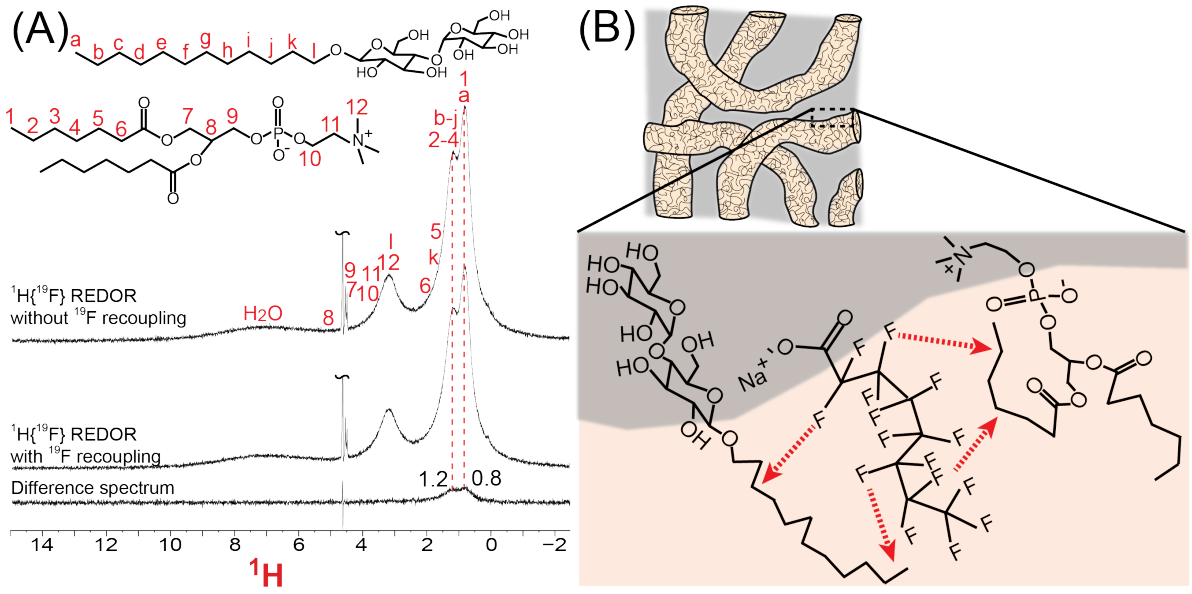

Figure B9. (A) Solid-state ^{1}H{^{19}F} REDOR NMR spectra of DDM- and diC_7PC-directed silica containing 5 wt% PFO, acquired without (A, top) and with (A, middle) reintroduction of ^{19}F-^{1}H dipolar couplings during a recoupling time of 0.11 ms, along with the corresponding difference spectrum (A, bottom). Signal intensities observed at 0.8 and 1.2 ppm (dotted red lines) are assignable to -CH_3 moieties *a* and *1* and -CH_2- moieties *b-j* and *2-4*, respectively, of the DDM and diC_7PC surfactant tails. As the only ^{19}F species in this material are associated with the PFO probe species, these signals unambiguously establish the close proximities (<2 nm) of the PFO molecules to the structure-directing DDM and/or diC_7PC surfactants, as depicted schematically in **(B)**. All spectra were acquired at MAS conditions of 15 kHz at approximately -20 °C.

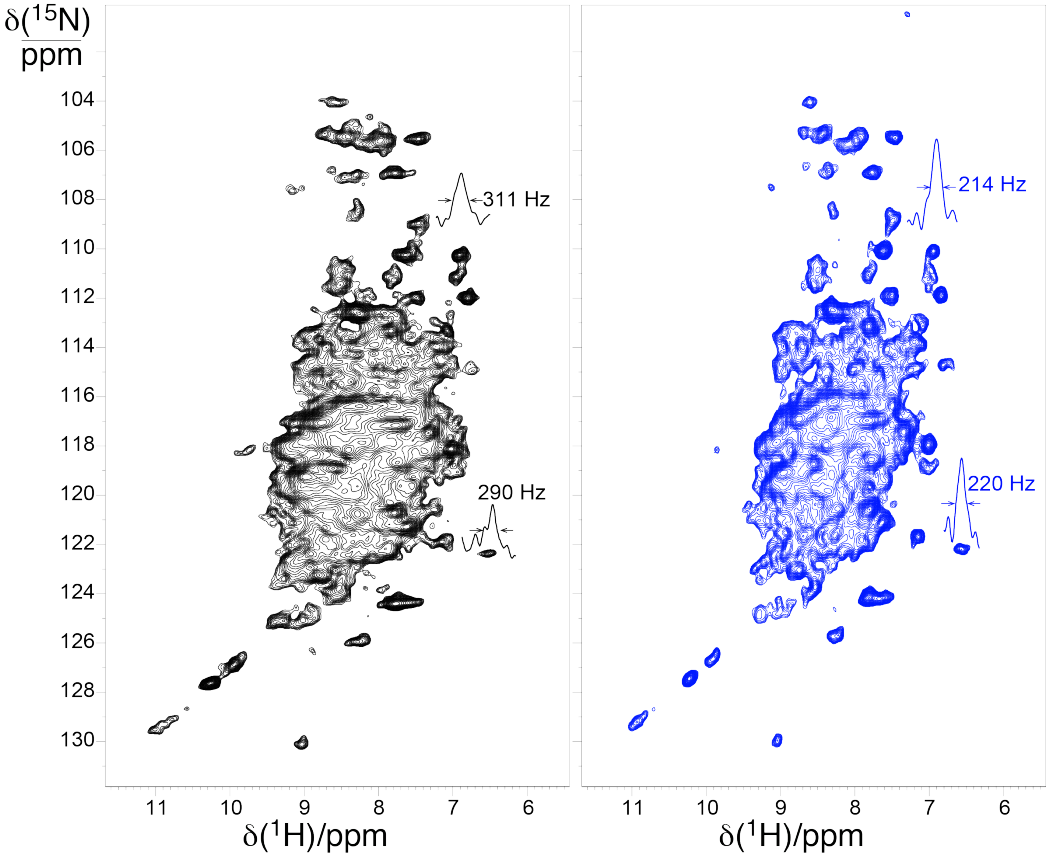

Figure B10. 2D ^{1}H-^{15}N CP-HSQC NMR spectra acquired for U-[^{15}N, ^{13}C] proteorhodopsin in a 1.3 mm probe at 60 kHz (black) and in a 0.7 mm probe at 100 kHz (blue). The spectrum acquired at 100 kHz MAS shows, on average, narrower linewidths than the spectrum recorded at 60 kHz. For example, two correlations on each spectrum (at ~122 ppm and ~109 ppm in the ^{15}N dimension) have linewidths of ~214 Hz and ~220 Hz in the spectrum at 100 kHz MAS spectrum, but ~311 and 290 Hz, respectively, in the spectrum collected at 60 kHz MAS.

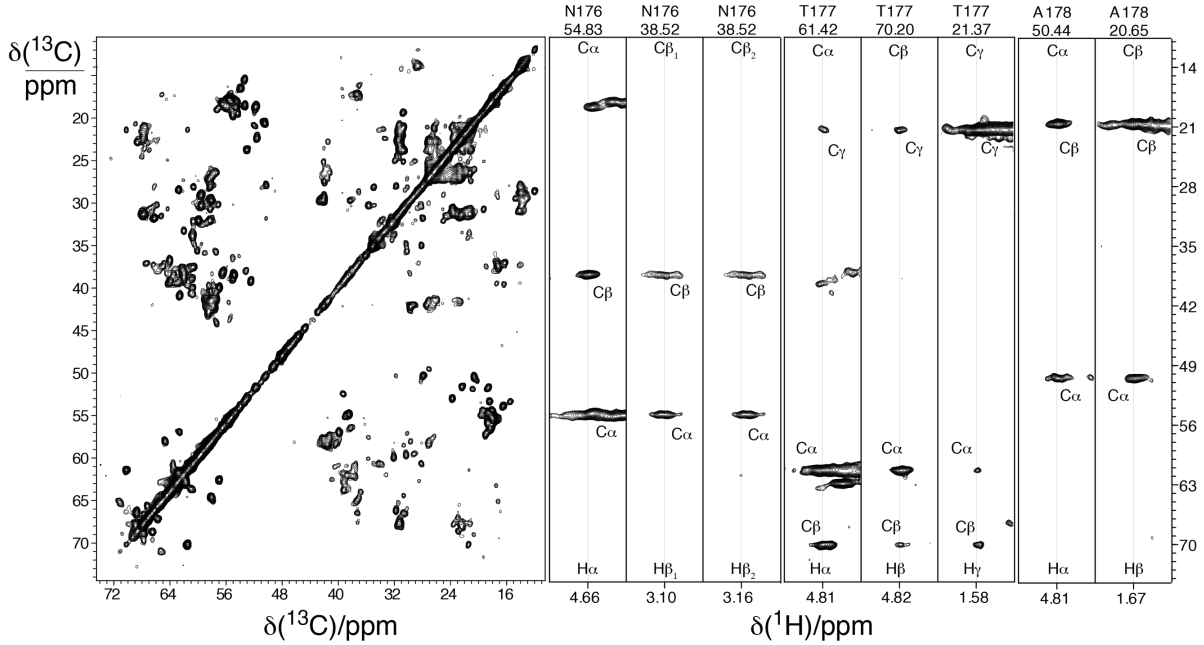

Figure B11. ^{13}C-^{13}C 2D projection of the 3D hCCH-TOCSY spectrum acquired on ^{15}N, ^{13}C proteorhodopsin in lipid bilayers, at the 1 GHz spinning at 100 kHz MAS, in a 0.7 mm probe. WALTZ-16 at 25 kHz was applied for the TOCSY mixing of 15 ms. Examples of carbon and proton side chain assignments are reported for residues 176-178 through strips extracted from the 3D ^{13}C-^{13}C-TOCSY spectrum. (Figure courtesy of Dr. Daniela Lalli)

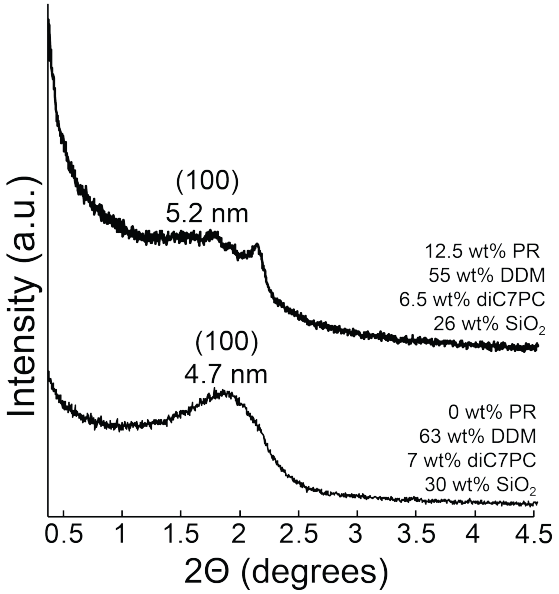

Figure B12. Small-angle X-ray reflection patterns acquired from as-synthesized mesostructured silica **(A)** without and **(B)** with 12.5 wt% PR. Both patterns show broad (reflections with associated d-spacings of 4.7 and 5.2 for materials without and with PR, respectively, that indicate a swelling of the mesochannels upon the incorporation of PR species. The materials with 12.5 wt% PR also show two sharper reflections at approximately 1.75 and 2.25° 2Θ that likely arise from a mixed phase that, based on the sharpness of the reflections, is well ordered and doesn't include the PR guests These X-ray results are in line with those of a previous study in which PR species were incorporated into DDM+diC_7PC mesostructured silica host materials.[1]

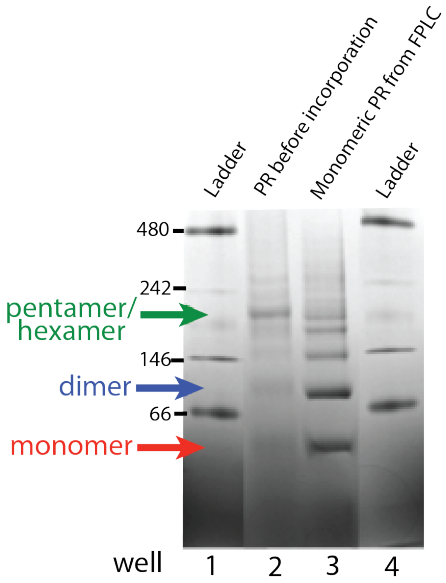

Figure B13. Blue-Native Polyacrylimide Gel electrophoresis of PR in micellar solutions (well 2) directly prior to incorporation into mesostructured silica materials and (well 3) from the monomeric volume fractions of monomeric PR from size-exclusion chromatography (SEC). The PR sample prior to incorporation into synthetic materials (well 2) shows a sharp band associated with pentameric/hexameric PR, suggesting synthetic mesotructured silica materials incorporate predominantly pentameric/hexameric PR species. By contrast, the monomeric PR isolated from SEC (well 3) has sharp bands assignable to both monomeric and dimeric PR species, with much lower intensity bands corresponding to higher order oligomers. These results indicate that, despite separation of monomeric PR by SEC, the post-SEC purification steps used here to remove excess DDM and diC_7PC favor the assembly of PR as pentamers/hexamers. Assignments for monomeric, dimeric and pentameric/hexameric PR were made based on the protein ladders (well 1 and 4) in combination with assignments in previous studies.[2]

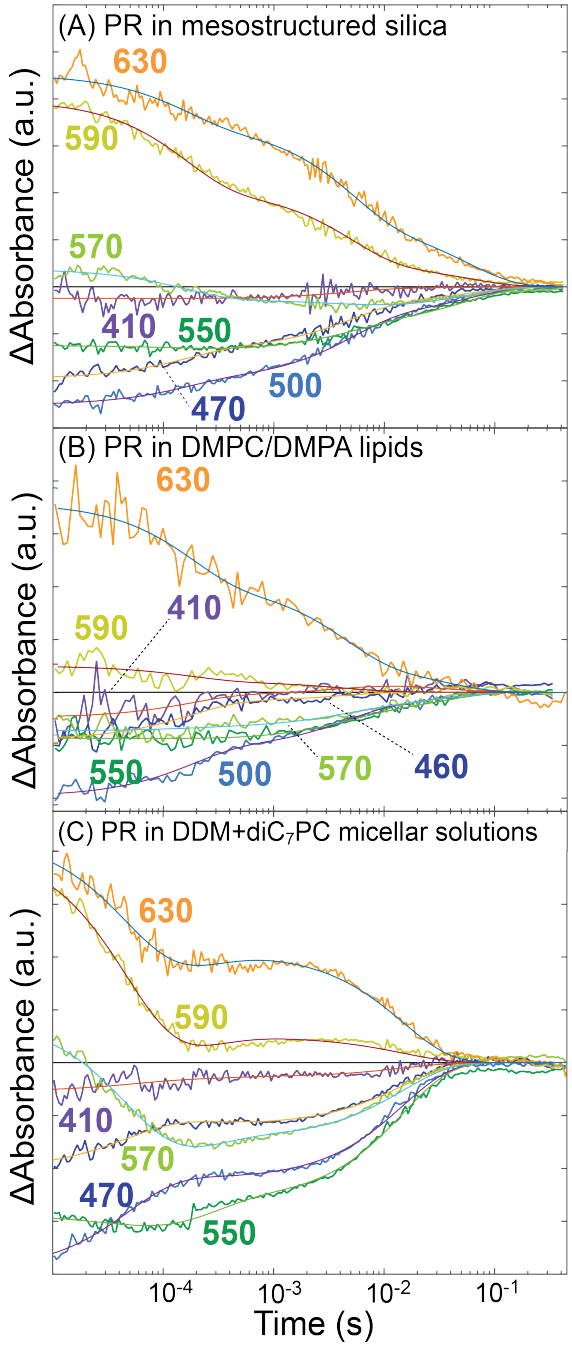

Figure B14. Transient absorbances at various wavelengths from PR in **(A)** mesostructured silica at 12.5 wt% loading (hydrated R.H. 100% for 1 month), **(B)** DMPC/DMPA lipids in solution at pH 3.5, and **(C)** micellar solutions with DDM and diC_7PC. The PR samples were excited with an ~10 ns laser pulse at 532 nm. The smooth lines along each absorbance are the

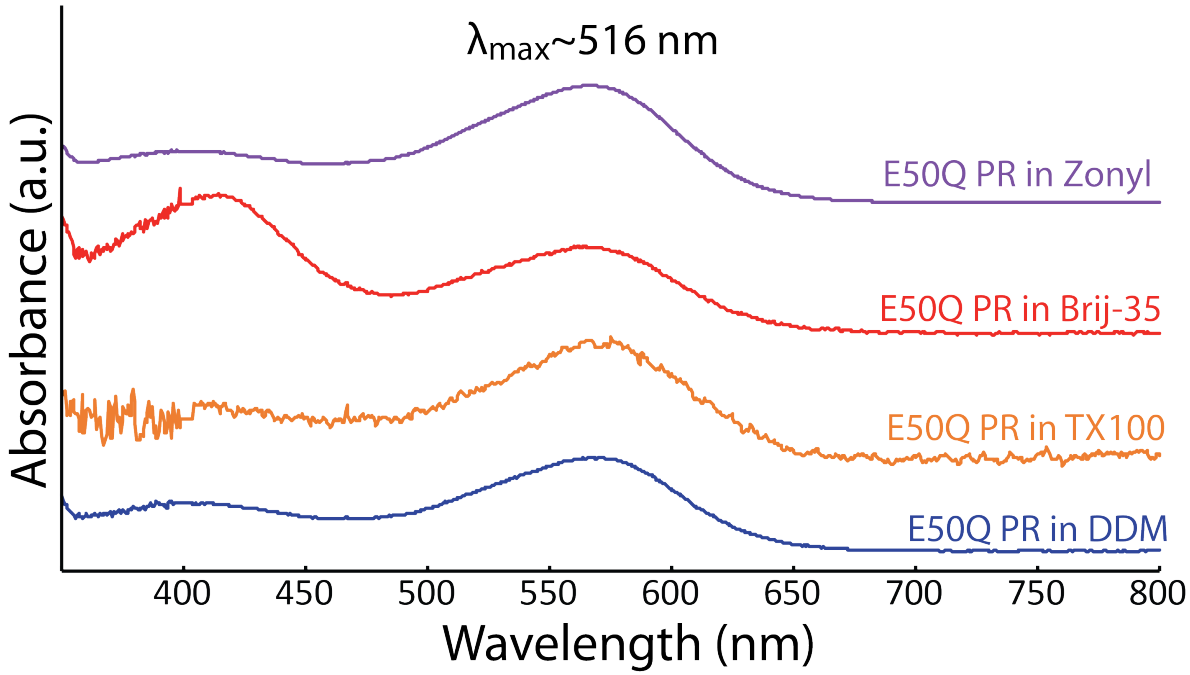

Figure B15. UV-visible absorbance spectra of E50Q PR exchanged into micellar DDM (blue), TX100 (orange), Brij-35 (red) and Zonyl (purple) solutions under alkaline (pH 8.0-8.5) conditions. The wavelength of maximum absorbance for all spectra is approximately 516 nm, which is consistent with that of photoactive PR molecules. An additional absorbance at ~410 nm is also observed for all spectra, but most intensely for E50Q PR in Brij-35 surfactant environments, that is assignable to the beta bands of the retinal chromophore.[3,4]

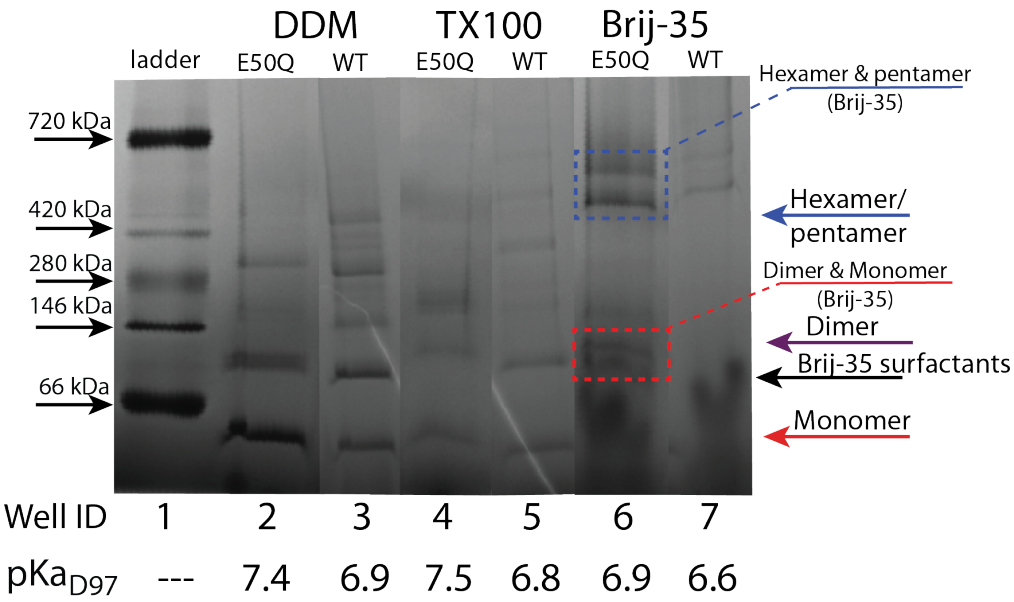

Figure B16. BN-PAGE analyses of E50Q and WT PR in micellar solutions containing exclusively DDM, TX100 or Brij-35 surfactants. For the case of Brij-35 solubilized PR, the signal positions associated with the various monomeric and dimeric PR species appear at higher molecular weights than for TX100 and DDM. This likely originates from the relatively higher molecular weight of Brij-35 (1199.5 g/mol) molecules versus DDM (510.6 g/mol) or TX100 (647 g/mol) that would impart higher molecular weights to all PR-Brij-35 complexes, which would correspondingly appear at higher molecular weights in a BN-PAGE measurements. The E50Q PR samples systematically have greater monomer contents versus the WT PR samples and also exhibit consistently lower pKa_{D97} values (listed below BN-PAGE) than for WT PR. The wells pictured here were taken from two separate gels and rearranged to facilitate comparisons of the E50Q and WT PR samples in different micellar surfactant solutions.

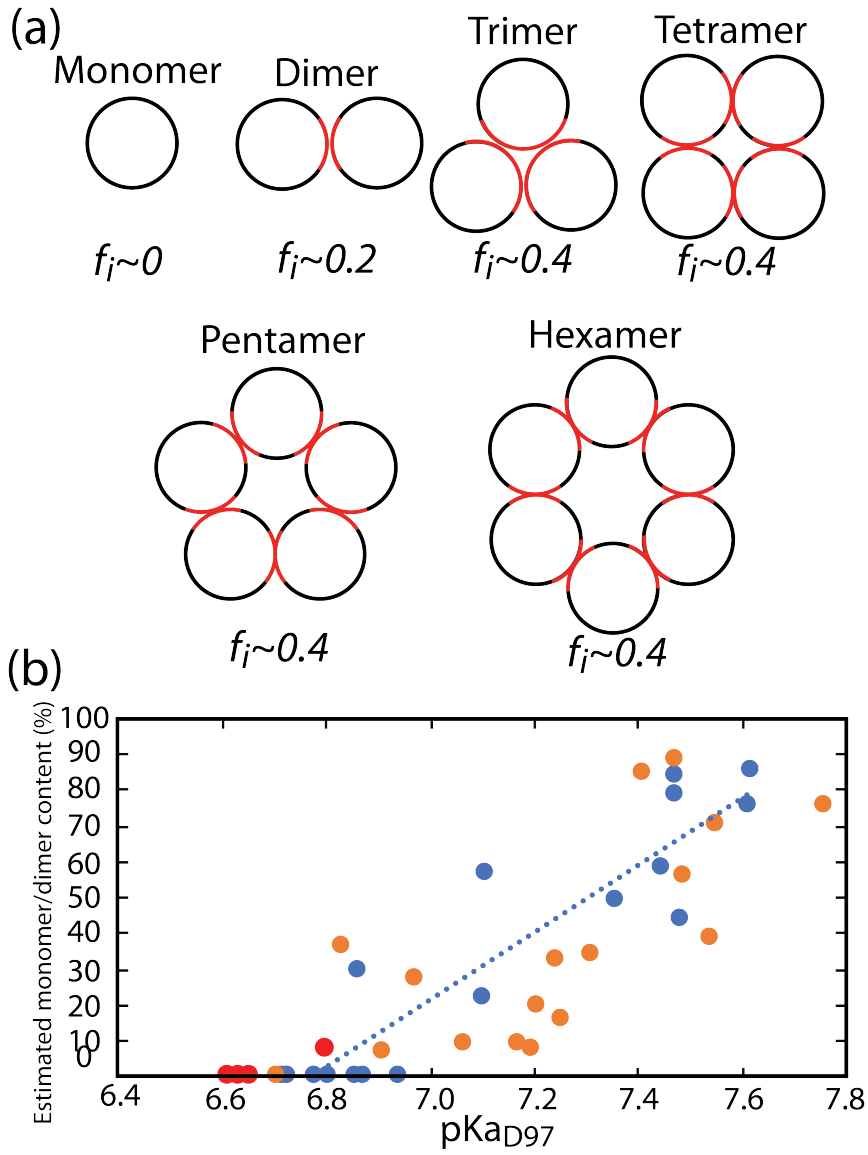

Figure B17. (a) Schematic diagrams of PR molecules (circles), viewed from the cytoplasmic/periplasmic side, in monomeric and various oligomeric assemblies, in which areas of oligomeric contacts are shown in red. The area of oligomeric contact was estimated to be 1/5th of the total perimeter of each PR species, and the total fraction of oligomer interface (f_i) for each PR assembly is shown below each monomer or oligomer. **(b)** A correlation plot of pKa$_{D97}$ value versus the monomer/dimer content, estimated as the sum of 100% and 50% of the integrated BN-PAGE intensities associated with monomer and dimer PR species, respectively. The monomer and oligomer contents were adjusted by a factor of 1-f_i to estimate the surface area of PR molecules that is not part of the oligomeric interface, which may be the only regions accessible to Coomasie blue dye molecules during BN-PAGE measurements. The blue dotted line is a best-fit linear line (Pearson correlation coefficient = 0.92) to the data of PR in micellar DDM solutions (blue dots), which shows reasonable correlation with data from PR in micellar solutions containing TX100 (orange) and Brij-35 (red) either exclusively or in mixtures with DDM.

(A)

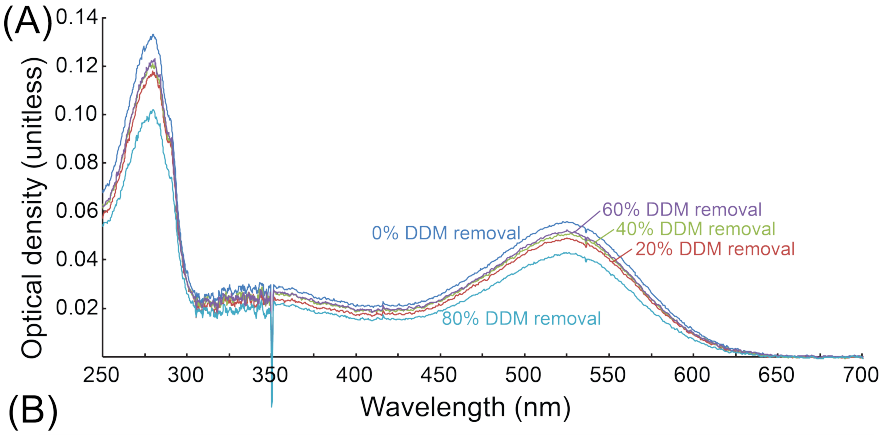

(B)

Estimated DDM removal (%)	0	20	40	60	80
Normalized PR concentration (%)	100	88	91	94	77
Pre-incubation DDM-to-PR ratio (w/w)	4.0	4.0	4.0	4.0	4.0
Post-incubation DDM-to-PR ratio (w/w)	4.0	3.6	2.6	1.7	1.0

Figure B18. (A) UV-visible absorption spectra acquired from micellar DDM solutions containing PR (with the monomer-forming E50Q mutation) incubated overnight with biobeads expected to remove (blue) 0%, (red) 20%, (green) 40%, (purple) 60%, and (teal) 80% of the initial 2.5 wt% of DDM surfactants in the solution. The PR concentration was established by applying the Beer-Lambert law to the absorption maximum at ca. 520 nm, which generally decreases as DDM is removed from the PR-containing solution. **(B)** Tabulated values of the estimated DDM removal, PR concentration, and DDM-to-PR ratios (w/w) before and after overnight incubation in biobeads for various micellar DDM solutions containing PR. The PR concentration decreases with increasing amounts of expected DDM removal, with approximately 77% of PR remaining in solution following an expected removal of 80% of the DDM. As greater quantities of DDM are removed from solution, the DDM-to-PR ratio decreases from an initial 4.0 to 1.0. The initial DDM content in these samples was determined by using solution ^{1}H NMR as described in the methods section in the main text, and the amount of biobeads necessary to remove DDM surfactants was determined empirically by quantifying DDM removal from micellar DDM solutions without PR following incubation in different amounts of biobeads.

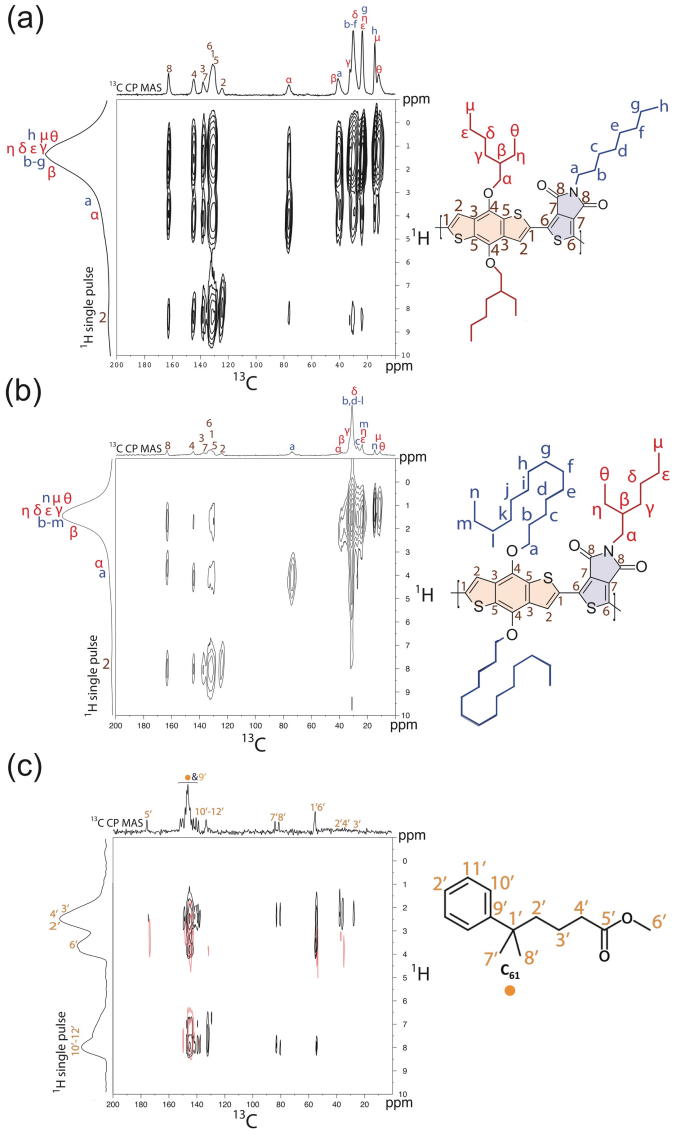

Figure B19. Solid-state 2D $^{13}C\{^{1}H\}$ dipolar-mediated heteronuclear correlation (HETCOR) NMR spectra acquired at room temperature for neat EH/C8 **(A)** and C14/EH **(B)** under MAS conditions of 12.5 kHz, with 2-ms and 1-ms CP contact times respectively. $^{13}C\{^{1}H\}$ HETCOR spectra of neat $PC_{61}BM$ (c) acquired under identical conditions to those in (a) and (b), except with 2-ms (black contours) and 8-ms (red contours) CP contact times. 1D $^{13}C\{^{1}H\}$ CP MAS spectra are shown along the top horizontal axes and single-pulse ^{1}H MAS spectra or projections are shown along the left and vertical axes, respectively. The molecular moieties labeled in the schematic diagrams are shown to the right of each 2D spectrum are assigned by the well-resolved polymer and fullerene signals in the various 2D $^{13}C\{^{1}H\}$ HETCOR and solid-state NMR studies of similar molecules.[5,6] The 2D $^{13}C\{^{1}H\}$ HETCOR spectra of $PC_{61}BM$ was acquired at an 8-ms CP contact time (c, red contours) to help distinguish intermolecular interactions between polymer and fullerene species in polymer:fullerene blends.

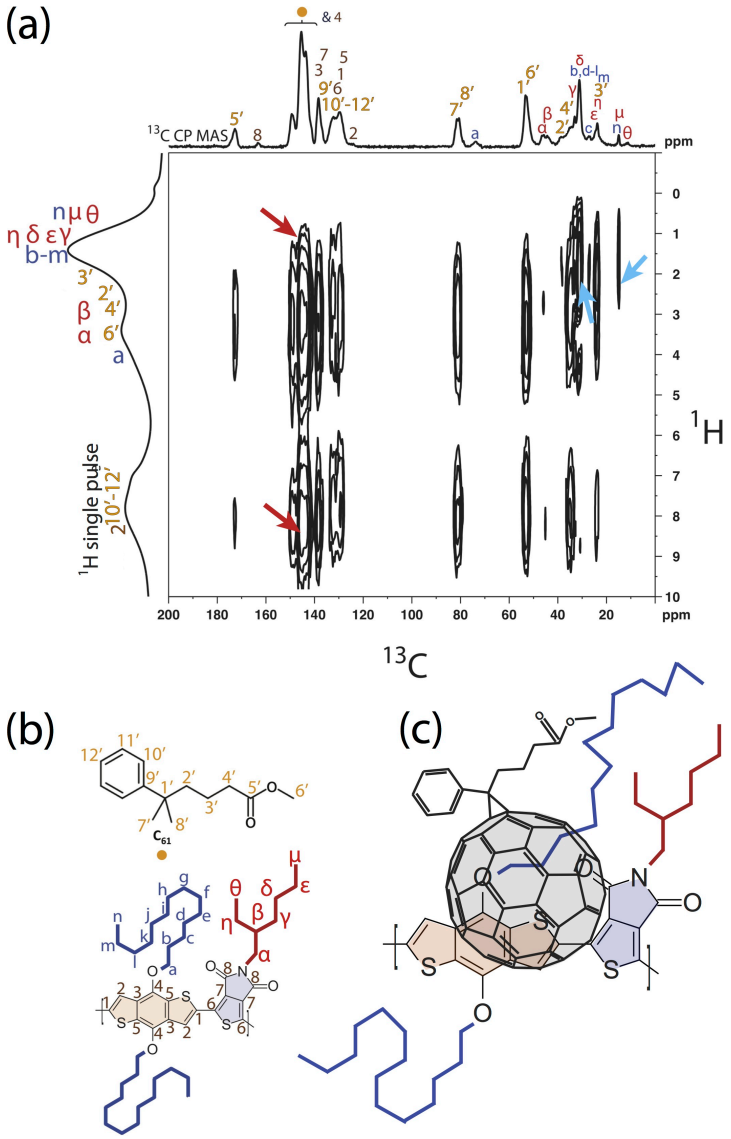

Figure B20. (a) Solid-state 2D $^{13}C\{^{1}H\}$ dipolar-mediated heteronuclear correlation (HETCOR) NMR spectrum acquired at room temperature for a 8 wt% **C14-EH** in $PC_{61}BM$ heterojunction under MAS conditions of 12.5 kHz, with an 8-ms CP contact time. 1D $^{13}C\{^{1}H\}$ CP-MAS and single-pulse ^{1}H MAS spectra are shown along the top horizontal axis and the left vertical axis, respectively. Schematic diagrams of **(b)** the **C14/EH** and $PC_{61}BM$ molecules, with their respective moieties labeled. The correlated signal intensity between 140-148 ppm in the ^{13}C dimension and at ca. 8.3 ppm and ca. 1.2 ppm in the ^{1}H dimension (red arrows) indicate the close intermolecular proximity of the C_{60} fullerene group with polymer backbone and polymer side-group moieties. A selective interaction of the $PC_{61}BM$ species with the BDT group is suggested by the correlated intensity between ^{13}C resonances of moieties *b* & *d-l* and *n* of the linear C14 alkyl chain (ca. 31 ppm) and ^{1}H resonances at 2-3 ppm that are associated with the $PC_{61}BM$ solubilizing group (blue arrows). A schematic diagram is shown in **(c)** that depicts an arrangement of the $PC_{61}BM$ near the BDT group of the polymer that is consistent with the 2D NMR intensity correlations.

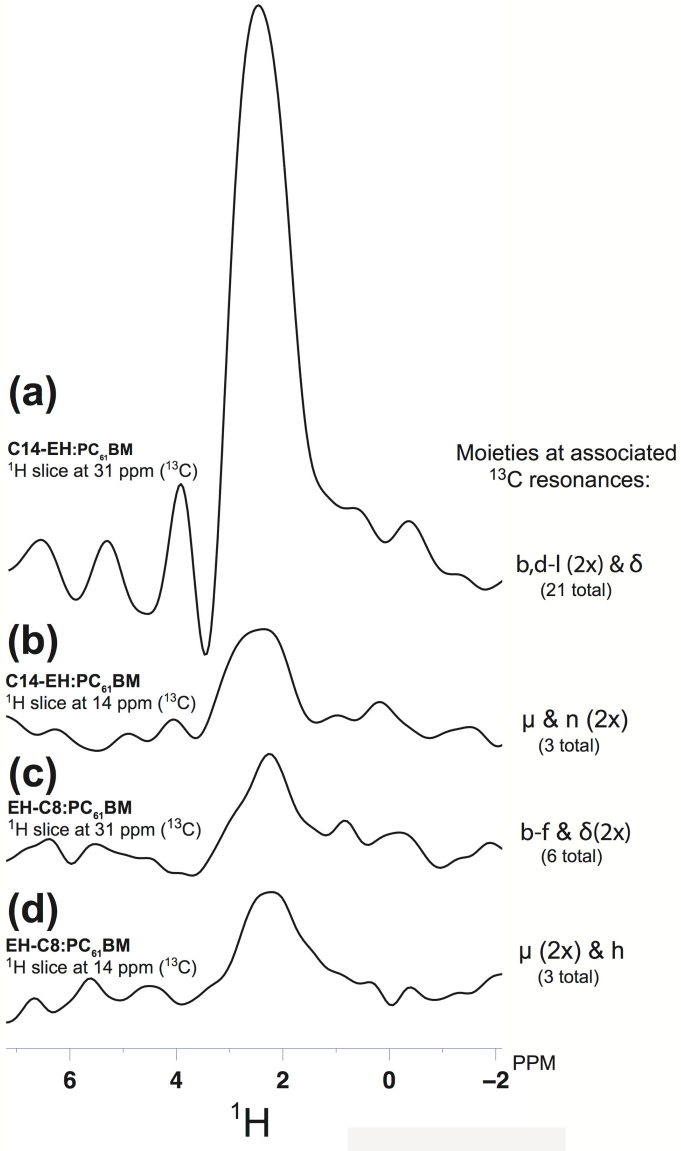

Figure B21. ^{1}H slices taken at **(a,c)** 31 ppm and **(b,d)** 14 ppm in the ^{13}C dimension from the solid-state 2D ^{13}C{^{1}H} HETCOR spectra in Figure S9, a of the C14/EH:$PC_{61}BM$ and in Figure 6, c of the EH/C8:$PC_{61}BM$ heterojunction materials. For the C14/EH:$PC_{61}BM$ heterojunction blend, signal intensity in the ^{1}H slice in **(a)** at 31 ppm arises from ^{13}C species *b,d-l* of the linear C14 alkyl chains and δ of the branched EH alkyl groups, while intensity in the ^{1}H slice in **(b)** at 14 ppm arises from the terminal methyl moieties *n* of the linear C14 alkyl chains and μ of the branched EH group. For the EH/C8:$PC_{61}BM$ heterojunction blend, signal intensity in the ^{1}H slice in **(c)** at 31 ppm arises from ^{13}C species *b-f* of the linear C8 alkyl chains and δ of the branched EH alkyl groups, while intensity in the ^{1}H slice in **(d)** at 14 ppm arises from the terminal methyl moieties *h* of the linear C8 chains and μ of the branched EH groups. The ^{1}H signal intensities at 2-3 ppm in the ^{1}H slice at 31 ppm, relative to that of the ^{1}H slice at 14 ppm, compare well with the relative populations of the associated ^{13}C moieties for each separate blend material. In (a), the oscillatory intensity at >3 ppm results from truncation of the time-domain signals at 31 ppm in the indirect ^{1}H dimension.

References:

(1) Jahnke, J. P.; Idso, M. N.; Hussain, S.; Junk, M. J. N.; Han, S.; Chmelka, B. F. *Submitt. J. Am. Chem. Soc.* **2017**.

(2) Maciejko, J.; Mehler, M.; Kaur, J.; Lieblein, T.; Morgner, N.; Ouari, O.; Tordo, P.; Becker-Baldus, J.; Glaubitz, C. *J. Am. Chem. Soc.* **2015**, *137*, 9032.

(3) Herz, J.; Verhoefen, M. K.; Weber, I.; Bamann, C.; Glaubitz, C.; Wachtveitl, J. *Biochemistry* **2012**, *51*, 5589.

(4) Friedrich, T.; Geibel, S.; Kalmbach, R.; Chizhov, I.; Ataka, K.; Heberle, J.; Engelhard, M.; Bamberg, E. *J. Mol. Biol.* **2002**, *321*, 821.

(5) Kim, H.; Choi, Y.; Jung, J. C.; Zin, W. *Polym. Bull.* **2000**, *45*, 253.

(6) Cossiello, R. F.; Kowalski, E.; Rodrigues, P. C.; Akcelrud, L.; Bloise, A. C.; DeAzevedo, E. R.; Bonagamba, T. J.; Atvars, T. D. Z. *Macromolecules* **2005**, *38*, 925.

(1) Jahnke, J. P.; Idso, M. N.; Hussain, S.; Junk, M. J. N.; Han, S.; Chmelka, B. F. *Submitt. J. Am. Chem. Soc.* **2017**.

(2) Maciejko, J.; Mehler, M.; Kaur, J.; Lieblein, T.; Morgner, N.; Ouari, O.; Tordo, P.; Becker-Baldus, J.; Glaubitz, C. *J. Am. Chem. Soc.* **2015**, *137*, 9032.

(3) Herz, J.; Verhoefen, M. K.; Weber, I.; Bamann, C.; Glaubitz, C.; Wachtveitl, J. *Biochemistry* **2012**, *51*, 5589.

(4) Friedrich, T.; Geibel, S.; Kalmbach, R.; Chizhov, I.; Ataka, K.; Heberle, J.; Engelhard, M.; Bamberg, E. *J. Mol. Biol.* **2002**, *321*, 821.

(5) Kim, H.; Choi, Y.; Jung, J. C.; Zin, W. *Polym. Bull.* **2000**, *45*, 253.

(6) Cossiello, R. F.; Kowalski, E.; Rodrigues, P. C.; Akcelrud, L.; Bloise, A. C.; DeAzevedo, E. R.; Bonagamba, T. J.; Atvars, T. D. Z. *Macromolecules* **2005**, *38*, 925.